Spectral and magnetic properties of copper oxides : towards a theoretical description from first principles

Benjamin Bacq-Labreuil

To cite this version:

Benjamin Bacq-Labreuil. Spectral and magnetic properties of copper oxides : towards a theoretical description from first principles. Strongly Correlated Electrons [cond-mat.str-el]. Institut Polytechnique de Paris, 2022. English. NNT : 2022IPPAX084 . tel-04397326

HAL Id: tel-04397326
https://hal.science/tel-04397326v1

Submitted on 16 Jan 2024

INSTITUT
POLYTECHNIQUE
DE PARIS

NNT : 2022IPPAX084

Thèse de doctorat

ÉCOLE
POLYTECHNIQUE

IP PARIS

Spectral and magnetic properties of copper oxides: towards a theoretical description from first principles

Thèse de doctorat de l'Institut Polytechnique de Paris
préparée à l'École Polytechnique

École doctorale n°626 de l'Institut Polytechnique de Paris (EDIPP)
Spécialité de doctorat: Physique

Thèse présentée et soutenue à Palaiseau, le 23 septembre 2022, par

BENJAMIN BACQ-LABREUIL

Composition du Jury :

Alexander Lichtenstein Professeur, Institute for Theoretical Physics, Universität Hamburg	Président
Michele Casula Directeur de Recherche, Institut de Minéralogie, de Physique des Matériaux et de Cosmochimie, Sorbonne Université	Rapporteur
Simon Moser Group Leader, Physikalisches Institut, Julius-Maximilians-Universität Würzburg	Rapporteur
Marcello Civelli Maître de Conférences, Laboratoire de Phyique des Solides, Université Paris-Saclay	Examinateur
Matteo d'Astuto Chargé de Recherche, Institut Néel	Examinateur
Benjamin Lenz Maître de Conférences, Institut de Minéralogie, de Physique des Matériaux et de Cosmochimie, Sorbonne Université	Co-encadrant de thèse
Silke Biermann Professeure, Centre de Physique Théorique, Ecole Polytechnique	Directrice de thèse

Spectral and magnetic properties of copper oxides: towards a theoretical description from first principles

Benjamin Bacq-Labreuil

Thèse de doctorat de l'Institut Polytechnique de Paris
préparée au Centre de Physique Théorique
à
L'ÉCOLE POLYTECHNIQUE

CONTENTS

PART I

RÉSUMÉ

Si l'oxyde de cuivre peut être une malédiction pour les anciennes casseroles, il serait plutôt une bénédiction pour le monde scientifique. La découverte des cuprates en 1986 par Bednorz et Müller, une famille de matériaux à haute température critique ayant comme élément central les plans 2D CuO_2, a lancé un champ entier de recherche. D'immenses efforts ont été déployés, menant à la découverte d'un diagramme de phase bien plus riche que le seul dôme supraconducteur. Même s'il est établi que les plans 2D de CuO_2 sont responsables des propriétés électroniques à basses énergies, une compréhension globale théorique fait toujours défaut. La raison principale tient dans le fait qu'il est extrêmement difficile de modéliser les cuprates puisqu'ils font partie de la famille des matériaux à fortes corrélations électroniques. Dans ces systèmes, l'énergie d'intéraction de Coulomb est du même ordre de grandeur que l'énergie cinétique, ce qui rend ineffectives les théories de perturbation, et les approximations de couplage faible/fort. Le travail des théoriciens est donc de développer des modèles plus affinés, mais toujours solubles numériquement ou analytiquement.

Dans cette thèse, nous nous concentrons sur l'étude des propriétés spectrales et magnétiques de deux oxydes de cuivre : $Ca_{2-x}Na_xCuO_2Cl_2$ (NaCCOC) et CuO tétragonal (t-CuO). Une grande partie de cette étude est faite en adoptant le modèle de Hubbard à une bande pour capturer l'essentiel de la physique des plans de CuO_2. Malgré son apparente simplicité, ce modèle ne peut être résolu, et nous utilisons donc la théorie du champ dynamique appliquée aux amas (CDMFT). En complément, nous mobilisons la théorie fonctionelle de la densité (DFT). En sus de cet approche théorique, nous avons fait deux campagnes de mesure de spectroscopie par photoémission résolue en angle aux synchrotrons SOLEIL (Saint-Aubain, France) et Photon Factory (Tsukuba, Japon).

Cette combinaison d'outils théoriques et experimentaux nous permet d'étudier en détail les propriétés spectrales de NaCCOC non-dopé, et dopé en trou. Ce matériaux a une structure crystalline simple, et n'est pas supraconducteur à faible dopages ($x < 0.1$, x étant le taux de trous), ce qui le rend intéressant pour l'étude de la phase pseudogap qui survit donc jusqu'à des températures abritrairement basses. Nos calculs et mesures révèlent que les fluctuations antiferromagnétiques de spin jouent un rôle prépondérant. En premier lieu pour le phénomène de "cascade" : nous montrons qu'il s'agit d'un croisement entre une physique de polaron de spin en haut de la bande de valence, et une physique d'électrons localisés à plus haute énergie. Cette explication, mise en évidence par l'utilisation d'un modèle effectif de spin résolu avec l'approximation auto-cohérente de Born pour les polarons de spin et l'approximation Hubbard-I pour les électrons localisés, reste valide à faible dopage en trou. Nous montrons également que les fluctuations de spins sont à l'origine d'interférences destructives supprimant les excitations à basse énergie au point anti-nodal dans la zone de Brillouin. Cela entraîne l'ouverture du pseudogap, que l'on observe également en photoémission. Enfin, nous observons qu'à basse température la fonction de corrélation de spin à temps long ne diminue pas en augmentant le dopage, mais au contraire augmente jusqu'à $x = 0.05$, stagne, puis diminue. Ce phénomène s'étend même aux corrélations de spin entre plus proches voisins, et prochains plus proche voisins.

t-CuO possède une structure cristalline encore plus simple que NaCCOC, puisqu'il est seulement composé de plans 2D CuO qui se superposent dans une symétrie tétragonale sur un substrat de $SrTiO_3$ (STO). Il a été observé expérimentalement que les plans CuO se décomposaient en deux sous-réseaux CuO_2 faiblement couplés. En utilisant la CDMFT avec plusieurs résolveurs d'impurité complémentaires, nous expliquons ce phénomène comment étant la conséquence de l'intéraction de Coulomb locale. La suppression des corrélations entre plus proches voisins, i.e. entre sous-réseaux, entraîne de façon effective une renormalisation des termes de saut qui résulte en un fort découplage. La symétrie du paramètre d'ordre est directement impactée : nous prédisons qu'elle est du type d_{xy}, au lieu du typique $d_{x^2-y^2}$ pour les cuprates.

Enfin, des expériences ont montré récemment l'émergence de moments pamagnétiques de spin et de moments orbitaux fixes sur les atomes de Cu. Compte tenu des connaissances actuelles sur t-CuO, de tels moments sont surprenants. En utilisant la DFT sur de larges cellules unitaires, nous démontrons qu'il est possible d'expliquer les deux types de moment par la formation de lacunes d'oxygène à l'interface t-CuO/STO. En effet, si les lacunes se forment dans le plan interfacial TiO_2, un gaz d'électrons en 2D est généré dans le plan interfacial CuO. Ce gaz d'électrons serait à l'origine des moments paramagnétiques de spin. De plus, la formation de lacunes engendre de fortes distortions dans le plan CuO à l'interface, au point où la symétrie par rotation locale et globale sont brisée. Cela engendre la fixation du moment orbital dans le plan. Notre scenario étant capable d'expliquer l'observation expérimentale, il reste à le confronter à d'autres expériences supplémentaire pour attester de sa validité : nous proposons donc plusieurs expériences qui permettrait de le vérifier.

PART II

INTRODUCTION

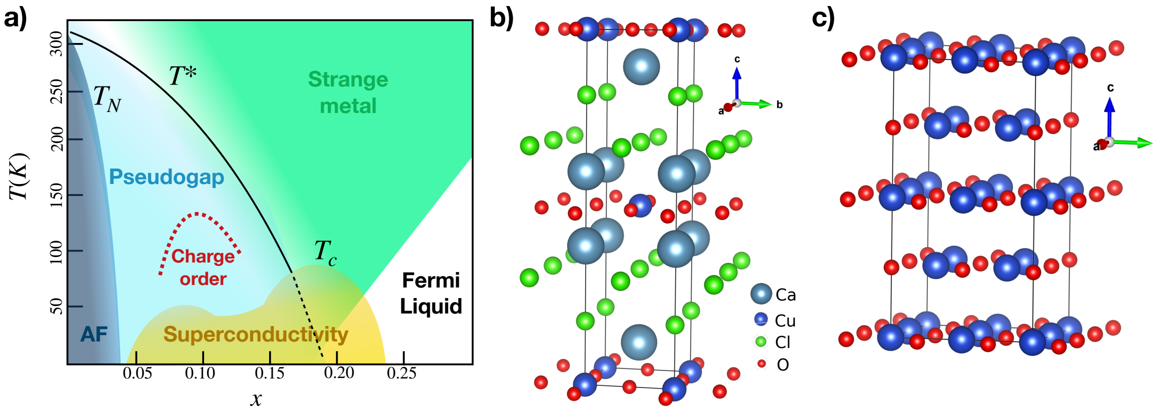

Figure 1: (a) Sketch of a typical cuprate's phase diagram as a function of hole doping x and temperature T. The acronym AF refers to an antiferromagnetic charge transfer insulator phase. (b)-(c) Crystal structures of the undoped ($x = 0$) NaCCOC and t-CuO respectively.

Copper oxide systems belong to the fascinating family of strongly correlated solids. These materials display extremely rich physics, providing a wide range of properties and applications. Some are good metals, other large-gap insulators, they can also be strong ferromagnets, or show antiferromagnetic ordering as for the undoped cuprates. All these different properties originate from a common ground: the electron-electron interactions are strong and can not be approximated as is usually the case for metals. Worse than that, the kinetic energy can neither be neglected since usually the Coulomb interaction is of the order of the bandwidth. In such a case, standard mean-field theories, or perturbative expansions either in kinetic or interaction energy fail to describe properly those materials. The strong competition between the two terms leads to the emergence of unique properties like giant magnetoresistance, ferroelectricity, and high temperature superconductivity to name a few, which are promising and even already used for practical applications.

Cuprates, discovered by Bednorz and Müller in 1986 [1], are best known for their high critical temperature under which superconductivity emerges, the highest at ambient pressure for Hg-based compounds [2], which sparked an immense scientific effort in the hope of finding the underlying mechanism. Indeed, the standard phonon-mediated Bardeen-Cooper-Schrieffer [3] pairing of the electrons is not compatible with the experimental evidences [4, 5]. It has been observed that the superconducting gap has a $d-$wave symmetry [4, 6], and although phonons can help the pairing caused by another mechanism [7], it can not alone account for this symmetry. Moreover, since in cuprates both the electron-phonon coupling and the phonon frequency responsible for the pairing are weak, the critical temperature derived from this theory could not reach the measured values in cuprates. While the coupling constant could be increased by enhancing the density of states at the Fermi level, this would ultimately lead to a renormalization of the phonons due to screening by the electronic cloud. The predominance of antiferromagnetic fluctuations, as we shall describe hereafter, point to a possible origin of superconductivity from antiferromagnetic correlations, but the mechanism remains mysterious [8–13]. The study is further complicated by the discovery of a complex phase diagram at low-temperature upon hole or electron doping. A typical example for the hole-doped compounds is sketched in Fig. 1(a) [9, 14].

While many different cuprates exist, they all have in common the 2D CuO_2 layers responsible for the low-energy properties, eventually sandwiched between the so-called charge reservoir layers (inert electronically), as shown in Fig. 1(b)-(c) where are displayed the crystal structures of $Ca_{2-x}Na_xCuO_2Cl_2$ (NaCCOC) and tetragonal CuO (t-CuO), the two materials on which we focus in this thesis. In the parent compounds, the Cu atoms are in a $3d^9$ configuration, i.e. with one partially filled orbital, while the oxygen atoms are in a $2p^6$ configuration. The half-filled orbital is usually of $d_{x^2-y^2}$ symmetry, but it can also be d_{xy} as is the case for t-CuO. Within a band structure picture, the presence of a half-filled band would mean that the system is metallic. However, due to the large effective Coulomb interaction on these narrow orbitals, it is energetically favorable for the electrons to localize [15, 16]: the parent compounds are charge transfer insulators. The half-filled band is splitted into a lower Hubbard band (LHB) and upper Hubbard band (UHB), and the splitting (Mott gap) is such that the lowest energy excitation is the transfer of an electron from an O site to a Cu site, hence the name charge transfer. The gap is large: usually of the order of 2eV or larger [9]. Even though the on-site Coulomb interaction is large, the hopping of an electron between different Cu sites, mediated by the O atoms, is non-zero, and lead to the coupling of the single electrons on each Cu site via an antiferromagnetic super-exchange term [17, 18]. Undoped cuprates are therefore antiferromagnetically ordered below the Néel temperature T_N [19, 20].

Upon hole doping of the CuO_2 layers, i.e. the insertion of holes, the electronic properties of the materials change drastically. Doping is usually achieved by chemical substitution in the charge reservoir layers that separate the 2D CuO_2 layers: for instance in NaCCOC, by the substitution of the Ca atoms by Na. At low temperatures, when increasing the hole doping one enters the $d-$wave [4, 6] superconductivity double dome, which vanishes at large dopings where the system becomes a Fermi liquid. Above the second dome, at temperature $T \geq T_c$ is observed the strange metal phase, characterized by a $T-$linear resistivity [14]. Finally, at moderate dopings and $T_c \leq T \leq T^*$ appears the pseudogap (PG) phase [21–23] characterized in the spectral function by the opening of an anisotropic gap in the Brillouin zone (BZ) [12, 24], as well as charge density wave (CDW) at lower temperatures [25–29].

The complex electronic properties of cuprates, highlighted by their phase diagram in which many different phases are interlaced, is extremely difficult to model theoretically. Indeed, even the undoped antiferromagnetic insulating phase can not be accounted for by the standard density functional theory (DFT), which within the local density approximation (LDA) would predict the system to be metallic since it has a half-filled band. Band structure calculations nevertheless provide a key first step in allowing to identify the partially occupied bands relevant for the description of the low-energy electronic properties [30, 31]. In cuprates, we usually expect a single band close to the Fermi level since only the Cu atoms have a partially filled shell. It is the result of the hybridization of the Cu $d_{x^2-y^2}$ and O $p_{x/y}$ orbitals which are coupled by the hopping amplitude t_{dp}. As mentioned above, a simplified view of this problem is that the Cu $d_{x^2-y^2}$ host a hole lying at an energy E_d, while the O $p_{x/y}$ is fully occupied and lies at the energy E_p, higher than E_d. The lowest energy excitation process is the hopping of the hole from the Cu to O with amplitude t_{dp}, but which has an extremely large cost $E_p - E_d$ since the energy of double occupancy is $E_d \sim U_d$, the Coulomb on-site repulsion. The latter being large compared to the hopping amplitude t_{dp}, the hole remains localized on the Cu site and the system has a large charge transfer gap [32].

From these considerations, the three-band model, called Emery model, taking into account the Cu $d_{x^2-y^2}$ and O $p_{x/y}$ orbitals seems to be the minimal model possible for cuprates [33, 34]. However, a further simplification can be done by considering a single-band Hubbard model [35–37] at half-filling, with the on-site Coulomb repulsion U being identified to $E_p - E_d$. Similarly to the three-band model, at large U the electrons are localized and a Mott gap opens [15, 16]. In fact, the simplification of the three-band model to a single-band one was first argued by Zhang and Rice, who proposed that upon doping the extra holes form a bound state between the Cu $d_{x^2-y^2}$ and the surrounding O $p_{x/y}$ orbitals, leading to the formation of the isolated Zhang-Rice singlets (ZRS) band at the Fermi level [38]. Hence, the low-energy properties of cuprates can be ultimately represented in a minimal 2D single-band Hubbard model, which we adopt in this thesis for the study of NaCCOC and t-CuO. The one-band Hubbard model captures most of the essential phases of the phase diagram sketched in Fig. 1 when parameterized for cuprates [39]. Still, a debate remains open on whether the one-band model can indeed capture the right physics [40, 41], and if the phenomena observed theoretically are indeed relevant for the real materials.

Although the minimal one-band Hubbard model drastically simplifies the problem, unless for specific cases like the non-interacting and atomic limit, or in 1D, it can not be solved exactly due to the competition between the kinetic and the electron-electron interaction terms. The Hamiltonian reads

$$H = \sum_{\langle i,j\rangle,\sigma} t_{ij} c^{\dagger}_{i\sigma} c_{j\sigma} + U \sum_{i} n_{i\uparrow} n_{i\downarrow}, \tag{0.1}$$

where t_{ij} are the hopping amplitudes between neighbors $\langle ij\rangle$, and U is the on-site Coulomb interaction. At parameters relevant for the cuprates, the bandwidth is roughly $W \simeq 8t$, with t the nearest-neighbor (NN) hopping term, and is of the order of the Coulomb repulsion $U \simeq 8-10t$ in general [31]. This prevents the use of perturbation theory, as well as weak- or strong-coupling approximations, such that even at half-filling the problem is not tractable analytically. In this context, the development of dynamical mean-field theory (DMFT) [42, 43], sparked by considerations on the properties of the Hubbard model at infinite dimension [44–47], was a huge step forward in the theoretical investigation of the Hubbard model, and hence of cuprates. Based on the mapping of the full interacting lattice problem onto an embedded impurity problem, which can be efficiently solved numerically, DMFT incorporates exactly the *local* correlations, and is able to capture the Mott transition [43].

Although extremely powerful, DMFT suffers from the approximation of purely local correlations for systems like cuprates, and in fact already at half-filling it overestimates the critical interaction strength U_c at which the Mott transition occurs [48]. A natural extension of DMFT is cluster dynamical mean-field theory (CDMFT), which we will use in this thesis. Within this framework, the single site impurity is replaced by a finite size cluster of sites [49–52], so that the non-local correlations up to the length scale of the cluster are treated exactly in the impurity problem. The latter is solved by the so-called impurity solvers, a large variety of which are nowadays available. Some examples are exact diagonalization methods [53, 54], renormalization group techniques [55], matrix-product state (MPS) [56, 57]-based methods [58, 59], and continuous-time quantum Monte Carlo (CTQMC) solvers [60–62]. CDMFT belongs to the family of quantum cluster methods [52], which are either used in a self-consistent DMFT scheme like CDMFT and dynamical cluster approximation (DCA) [63–65], or not, like the cluster perturbation theory [66, 67] and the variational cluster approximation (VCA) [68–70]. Similarly to CDMFT, although some conceptual differences, all these techniques aim at incorporating a part of the non-local fluctuations by considering a cluster defined in real or momentum space. Yet another route, not used in this thesis, is to go beyond the purely local correlations by incorporating the non-local fluctuations using diagrammatic expansions around the DMFT solution [71–76].

In addition to the theoretical difficulties in building and solving cuprates' effective models, the comparison to experiments is further complicated by possible effects from the charge reservoir layers, which may shed some ambiguity on the intrinsic properties of the CuO_2 planes. A typical example is the observation in n-layer Hg based cuprates of the coexistence of CDW and antiferromagnetic ordering in different CuO_2 layers [77, 78]. These materials are made up of groups of n CuO_2 planes, separated by charge reservoir layers. For $n \geq 3$ the CuO_2 planes can be separated into two groups: the outer planes directly connected to the charge reservoirs which can face large structural distortions, and the inner planes protected from such deformations. While in the former the antiferromagnetic order is quickly suppressed at low doping, the inner planes show a long-range ordering until a relatively large doping $x = 0.08$ [77]. Moreover, it was interpreted recently from quantum oscillations measurements that there could be a coexistence of CDW in the outer planes and antiferromagnetic ordering in inner planes, as signaled by the presence of three different frequencies in the oscillation spectrum [78]. This inner/outer plane differentiation also has strong consequences on the spectral function, as was shown by angle-resolved photoemission spectroscopy (ARPES) measurements on the same family of compounds, where was found a Fermi arc coexisting with a Fermi pocket at the nodal point in the PG phase [79]. Hence, in order to connect the theoretical models to the experiment, it is convenient to study cuprates with simple crystal structures, and even compounds free from charge reservoir layers.

In this thesis, we are particularly interested in NaCCOC and t-CuO, two compounds whose crystal structures are shown in Fig. 1(b)-(c). NaCCOC is composed of single CuO_2 planes separated by Cl and Ca atoms, with the particularity that the apical O atoms are replaced by Cl [80–83]. It sparked some attention when discovered since this was one of the first examples of superconducting samples without oxygen octahedra [80, 81]. Strictly speaking, NaCCOC is not a copper oxide, it is an oxychloride, but the similarity of its structure and its phase diagram [84] to those of usual cuprates makes it a promising candidate to confront the theoretical models to experiments. The parent compound [82] is a charge transfer insulator with a gap $0.5 \leq \Delta \leq 2.5$eV [85–89] , and long-range magnetic order [84]. A kink has been observed in the low-energy dispersion [86], reminiscent of the cuprates' *waterfall* feature [24], and which survives at low to intermediate dopings [90–92]. Upon hole doping, NaCCOC first enters the PG phase at arbitrarily low temperature [26, 90–94], and becomes superconducting for dopings $x \geq 0.1$ [84].

The waterfall feature appears at the nodal point due to the crossover between two different physical regimes at low and high energy. The low-energy part is well understood in terms of spin-polaron, that is to say carriers heavily dressed by the antiferromagnetic spin fluctuations [95–98]. However, the high-energy part has been attributed to different possible mechanisms like spin-charge separation [99, 100], weak-coupling spin-density wave, or to long-range hopping processes [101, 102] within a single magnetic sublattice [98]. The PG is characterized in the spectral function by the opening of an anisotropic gap in the BZ and the appearance of Fermi arcs (or pockets [79]) at the nodal points [12, 24]. It was in fact first discovered in Knight shifts [21] and spin-lattice relaxation time [22] measurements, and slightly later in transport experiments [23]. It has been shown with embedded quantum cluster methods like CDMFT [103–106], and DCA [65, 107–110], that the 2D one-band Hubbard model captures the PG upon hole-doping. Although it remained mysterious for quite some time, a theoretical consensus seems to be reached nowadays that the PG is intimately related to the antiferomagnetic correlations. First signs were obtained by quantum Monte Carlo (QMC) calculations [111], confirmed later on by quantum cluster methods [104, 107, 108] using relatively small clusters, as well as larger clusters [110]. The development of the fluctuation diagnostic reinforced the antiferromagnetic fluctuations scenario, by showing that the dominant channel contributing to the self-energy was the spin channel at $\mathbf{Q} = (\pi, \pi)$ [112–114], and was further confirmed by a dual boson expansion around the DMFT solution [75]. The similarities of the theoretical results to the experiments, for instance for the spectral function or the phase diagram, support this interpretation [115].

We will focus on the effects of the antiferromagnetic spin fluctuations on the spectral properties of NaCCOC by simultaneously studying the waterfall feature and the PG. CDMFT [49–52] calculations are performed with 2×2 and 8−site clusters, using the hybridization-expansion `CT-HYB` [116] and the interaction-expansion `CT-INT` [117] solvers based on the `ALPSCore` libraries [118], as well as the `CT-HYB` [119] solver from the `TRIQS` library [120]. Along with the theoretical calculations, ARPES measurements were carried out at the Photon Factory (Tsukuba, Japan) and SOLEIL (Saint-Aubin, France) synchrotrons to which the author actively participated. These measurements were performed in close collaboration with Matteo d'Astuto, Chafic Fawaz, and Hervé Cercellier from the Institut Néel (Grenoble, France), as well as Yukiko Obata from the Tokyo Tech World Research Hub Initiative (Tokyo, Japan).

We find that at all dopings considered, the one-band Hubbard model solved with a 2×2 and 8−site cluster is in astonishing agreement with the experimental measurements. The kink in the dispersion is particularly well reproduced, both in terms of momentum and energy position. Consistently with the existing literature, we identify the low-energy part of the waterfall as stemming from a spin-polaron by showing that the ARPES and CDMFT spectral functions are well accounted for by the propagation of a hole in an antiferromagnetic background, the dispersion of which is calculated within the self-consistent Born approximation (SCBA) [95]. Moreover, the high-energy part can be unambiguously described by assuming purely local correlations, i.e. within the Hubbard-I approximation, which is consistent with the vision of heavily dressed carriers in a background of localized moments. Furthermore, by studying the state histogram of the simple 2×2 cluster, it appears that the strong antiferromagnetic correlations are intimately linked with the opening of the PG, for it promotes as the leading term of the histogram a non-degenerate singlet state. We show, following Ref. 121, that such state leads to the suppression of the low-energy photoemission processes and thus to the opening of the PG at the antinodes, and argue that the picture is not limited to the specific 2×2 cluster. Finally, we calculate the dynamical spin structure factor (DSSF) for the 2×2 cluster, and find that it is maximum at $\mathbf{Q} = (\pi, \pi)$ for all dopings until $x = 0.1$, confirming the role of the antiferromagnetic fluctuations. We also identify a freezing of the inter-site spin-spin correlation function at large times $\tau \rightarrow \beta/2$ and at finite dopings, in agreement with recent findings [122, 123], and show that such freezing can be understood as a consequence of the emergence of low-energy spin excitations upon hole-doping. Most interestingly, we argue that such freezing may extend to arbitrarily large inter-site distances for larger systems, given a finite momentum broadening of the $\mathbf{Q} = (\pi, \pi)$ peak.

In contrast to NaCCOC, t-CuO has an even simpler crystal structure: it is composed of CuO planes (not CuO_2!), which are stacked along the c axis with a tetragonal distortion characterized by the ratio of basal and apical distances $c/a \simeq 1.37$ [124, 125]. In fact, t-CuO has to be synthesized as a thin film on a TiO_2-terminated $SrTiO_3$ (STO) substrate, and is stable until approximately 10 unit cells of CuO in the c direction [124, 126]. Above this critical thickness, CuO returns to its bulk low-symmetry monoclinic phase [127], in which well defined 2D CuO planes are missing. t-CuO has not been experimentally doped yet: the lack of charge reservoir layers prevents the use of the chemical substitution.

Ab initio studies including DFT with hybrid functionals [128–131] and DFT+U [132, 133] gave first insights into the electronic structure of t-CuO and were able to reproduce the experimentally observed tetragonal distortion [129], which is traced back to Jahn-Teller orbital ordering at the Cu d^9 ions [128, 131]. t-CuO is an insulator with a sizable gap $\Delta > 2.35\,\mathrm{eV}$ [126, 134], accompanied by an antiferromagnetic stripe ordering as found in resonant inelastic x-ray scattering (RIXS) and muon spin resonance (μ-SR) measurements [135, 136], as well as first principle calculations [128, 129, 131]. From heuristic extrapolations based on other binary transition metal oxides (TMO) [124, 137], and DFT calculations [128, 129, 131], the Néel temperature is estimated to be around $T_N \simeq 800K$, significantly higher than the critical temperature of its monoclinic counterpart ($T_N \sim 220\mathrm{K}$ [127]). Most interestingly, it was observed that the ARPES and RIXS spectra are consistent with an effective decoupling of the CuO planes into two weakly-correlated CuO_2 sublattices [134, 135]. However, within the simple one-band model derived from RIXS [135], the NN *inter*-sublattice hopping t_d is evaluated to be about one-fourth of the next-NN (NNN) *intra*-sublattice hopping t. A ratio of one-fourth is clearly too high to explain the sublattice decoupling seen experimentally, given the strong replica features observed in ARPES and the similitude of the magnon spectrum with that of conventional cuprates. Since the model is constructed from a Heisenberg-like Hamiltonian, and therefore lacks the dynamical effects from electron-electron interactions, this raises the question on the possible role of the dynamic correlations on the sublattice decoupling.

In close collaboration with Max Bramberger, Martin Grundner, Sebastian Paeckel and Ulrich Schollwöck from Ludwig-Maximilians-Universität München (Munich, Germany), we investigate the dynamical influence of the electronic correlations by means of CDMFT [49–52] calculations. Three different solvers were used: the CTQMC [60–62] hybridization-expansion `CT-HYB` [116] solver for which the author performed the calculations, and two MPS [56, 57]-based impurity solver working at effectively zero temperature and on the imaginary and the real axis [58, 59, 138–144] for which M. Bramberger and M. Grundner did the calculations. The inspection of the different self-energy components reveals a strong suppression of the inter-sublattice correlations, corresponding to the hopping t_d. This leads to an effective decrease of the non-interacting $\frac{t_d}{t} \sim \frac{1}{4}$ ratio, and therefore the enhancement of the sublattice decoupling which justifies the view of the CuO layers in t-CuO as two weakly coupled CuO_2 layers. Having revealed the underlying mechanism of the sublattice decoupling, we motivate the construction of a super-cluster allowing an improvement of the momentum resolution of our calculations without additional computational cost. This results in a spectral function in excellent agreement with the experimental one [134], whether using the `CT-HYB` sover or the MPS-based solver directly on the real axis. This *handshake* between finite and zero temperature techniques allows to study the influence of the antiferromagnetic spin fluctuations on the properties of t-CuO. Using the `CT-HYB` sover, we find two different insulating regimes: a paramagnetic insulator at high temperatures, characterized by a momentum selective divergence of the self-energy, and an antiferromagnetically ordered insulator at low temperature, for which the self-energy displays a spin dependent static shift of the order of U. This transition is accompanied by a drastic transformation of the spectral function, which agrees with the ARPES measurements and the zero temperature calculations only in the magnetically ordered regime, in which the low-energy dispersion is well accounted for by a SCBA calculation, thus further confirming the role the spin fluctuations. Finally, based on VCA [68–70] calculations performed by Benjamin Lenz, the sublattice decoupling is shown to survive upon hole doping and especially in the superconducting phase: it leads to a d_{xy} superconducting order parameter, which coexists with the antiferromagnetic stripes, although the two phases are in competition [50, 145–148].

Along with the existing literature, our findings would lead to a coherent and complete picture of the electronic properties of t-CuO, if it was not for the recent puzzling observation of paramagnetic spin and pinned orbital moments in x-ray magnetic circular dichroïsm (XMCD) measurements at the Cu $L_{2,3}$ edge [136]. Since t-CuO is an antiferromagnetic insulator with a sizable gap, one would rather expect the XMCD spectrum to be zero in the range of magnetic fields applied (from -6.5 to 6.5T). A minimal model was proposed in Ref. 136, which captures the essential features of the observations, but which is not line with the previous theoretical and experimental works. Indeed, according to their model, t-CuO would be composed of CuO layers with *in-plane* ferromagnetic ordering, which are antiferromagnetically stacked along the c axis. The last layer would follow the external field orientation and lead to the appearance of the paramagnetic spin moment, while the one-to-last layer would be pinned and uncompensated, hence giving rise to the pinned moment. Instead, the presence of a 2D electron gas (2DEG) at the t-CuO/STO interface would be a plausible scenario for the emergence of a paramagnetic spin moment, and that would especially be compatible with the antiferromagnetic stripe ordering observed both in experiments [135, 136] and *ab initio* calculations [128, 129, 131]. However, this possibility was argued against in Ref. 136 because of the absence of a XMCD Ti^{3+} signal at the Ti $L_{2,3}$ edge, which was previously seen in LaAlO_3/STO and γ-$\mathrm{Al}_2\mathrm{O}_23$/STO heterostructures in the presence of a 2DEG at the interface [149, 150], therefore leaving the question on the origin of these puzzling moments open.

By performing DFT+U [151–153] calculations on large unit cells, we show that a 2DEG emerges at the t-CuO/STO interface upon the formation of oxygen vacancies. Most importantly, the 2DEG is invisible at the Ti $L_{2,3}$ edge since the valence of the Ti atoms remains unchanged. We therefore show that the 2DEG scenario for the paramagnetic spin moments is in fact *not incompatible* with the XMCD measurements of Ref. 136. Moreover, the formation of oxygen vacancies leads to strong distortions, mainly located at the interface, which, in combination with the misfit of the monoxide CuO and the dioxide TiO_2 layers, leads to the breaking of both the local and the global C_4 rotational symmetries. This induces the pinning of the in-plane component of the orbital moment, while the out-of plane remains proportional and collinear with the spin moments, in excellent agreement with the XMCD measurements [136]. Our scenario therefore reconciles the appearance of the paramagnetic spin and orbital pinned moments with the current knowledge of t-CuO.

The remainder of the thesis is organized as follows. In Chap. 1, we first introduce DFT, and discuss to which extent it can be suited for the study of the strongly correlated systems' ground states properties. Then, in Chap. 2, we present how a low-energy effective model suitable for cuprates can be constructed starting from a DFT band structure, as well as a possible way of solving it: DMFT and CDMFT. The concept of analytic continuation is introduced, which is a necessary step to transform the Monte Carlo impurity solvers data from the imaginary to the real axis. We also present an effective spin model suited for lightly doped cuprates that can be solved within the SCBA, and which will prove to be useful for the interpretation of our CDMFT calculations. We proceed with the Chap. 3 dedicated to the study of NaCCOC, then Chap. 4 in which are discussed the bulk properties of t-CuO, and finally Chap. 5 focusing on the t-CuO/STO interface properties.

PART III

METHODS

1 ELECTRONIC STRUCTURE CALCULATIONS

1.1 DENSITY FUNCTIONAL THEORY

Density functional theory (DFT) has imposed itself as one of the most widely used numerical methods to study the ground state properties of solids and molecules. One of its main strengths lies in the fact that almost any solid can in principle be investigated *ab initio*, i.e. simply from the knowledge of its crystal structure, and with nowadays computational technologies large systems of $10^2 - 10^3$ atoms can be considered. Another advantage of DFT is that a large range of properties can be determined from the knowledge of the ground state: structural parameters, magnetism, optical properties, etc. In this chapter, we aim at giving an overview of the main equations and concepts of DFT, mainly following the review by Cottenier [154] and Kohn's Nobel lecture [155].

A solid is composed of many electrons moving in a network of positively charged ions. The Hamiltonian of this quantum many-body system reads:

$$\begin{aligned}\hat{H} &= \hat{T}_{ion} + \hat{T}_e + \hat{V}_{e-ion} + \hat{V}_{ion-ion} + \hat{V}_{e-e} \\ &= -\sum_i \frac{\nabla^2_{\mathbf{R_i}}}{2M_i} - \sum_i \frac{\nabla^2_{\mathbf{r_i}}}{2m_e} - \sum_{i,j} \frac{Z_i}{|\mathbf{R_i} - \mathbf{r_j}|} + \frac{1}{2}\sum_{i,j} \frac{Z_i Z_j}{|\mathbf{R_i} - \mathbf{R_j}|} + \frac{1}{2}\sum_{i,j} \frac{1}{|\mathbf{r_i} - \mathbf{r_j}|},\end{aligned} \tag{1.1}$$

where $\mathbf{R_i}$, M_i are respectively the ionic position and mass, $\mathbf{r_i}$, m_e the electronic ones, Z_i is the atomic number of the ions, and we used atomic units $e = \hbar = \frac{1}{4\pi\epsilon_0} = 1$. The two first terms of the Hamiltonian ($\hat{T}_{ion}$ and $\hat{T}_e$) are the kinetic energy of the ions and the electrons, they are single particle quantities. The last three terms are two-body operators ($\hat{V}_{e-ion}$, $\hat{V}_{ion-ion}$ and $\hat{V}_{e-e}$) which correspond to the Coulomb interaction between the particles. The Hamiltonian, in its exact form, is not solvable, so methods like DFT have been developed to obtain an approximate solution.

The first step is to notice that the mass of the ions is usually three orders of magnitude larger than that of the electrons $M_i \gg m_e$, such that their dynamic is much slower. The Born-Oppenheimer approximation, in its crudest form, consists in considering the ions as frozen at fixed positions and therefore neglecting their kinetic energy. They act as a positive charge background for the electrons: the ion-electron Coulomb interaction term $\hat{V}_{e-ion}$ can be considered as an external potential acting on the electrons, while $\hat{V}_{ion-ion}$ becomes a constant. Note that this assumption is justified for the compounds under considerations in this thesis which are composed of Cu, O atoms and eventually Ca, Cl and Na atoms, but it can break down for systems like H-based superconductors due to the small mass of the H atom [156]. This approximation results in a simpler Hamiltonian:

$$\hat{H} = \hat{T}_e + \hat{V}_{e-e} + \hat{V}_{ext}, \tag{1.2}$$

with $\hat{V}_{ext}$ the external potential created by the ionic network. A key aspect of this Hamiltonian is that the two first terms describe a system of interacting electrons independently from the particular solid they belong to, they are *universal*. The material's specificity is entirely encoded in the external potential $\hat{V}_{ext}$ and the electron filling.

Although the exact Hamiltonian has been drastically simplified, Eq. 1.2 remains not solvable because of the two-body term $\hat{V}_{e-e}$ that couples the electrons all together. Indeed, the eigenfunctions $|\phi(\mathbf{r})\rangle$ would be obtained by Slater determinants [157], i.e. linear combinations of anti-symmetric products of N-electron wave functions. In order to draw a rough estimate of the problem's complexity, the N-electron ground state wave function can be viewed as depending on the total number of parameters M [155]:

$$M \simeq p^{3N}, \tag{1.3}$$

where p is the number of parameters per variable for obtaining a desired accuracy, and at large N the number of variables for the N-body wave function is roughly $3N$ (in 3D space). Let us consider the simple case of $p = 3$. For a usual solid, $N \sim 10^{23}$ and obviously Eq. 1.2 can not be solved. A crystalline solid is periodic, so one could take into account only one unit-cell of the crystal, making the problem much easier. For instance, the parent compound NaCCOC ($x = 0$) that we study later in this thesis can be reduced to a unit cell containing a single atom of Ca, Cu, O and Cl atoms. This amounts to a system of 74 electrons, which would roughly require $M \simeq 3^{3\times 74} \simeq 10^{105}$ parameters ! This hand wavy argument is of course simplified, but it illustrates the need for tools to approximate the many-body problem.

One method to tackle this issue is DFT, which was formally proposed by Hohenberg and Kohn in 1964 [158]. They formulated two theorems:

1. The ground state density $n_0(\mathbf{r})$ of the many-body electronic system is uniquely determined by the external potential $\hat{V}_{ext}$. It follows that the ground state expectation value of any operator $\hat{O}$ is a unique functional of the ground state density

$$\langle\phi_0|\hat{O}|\phi_0\rangle = O[n_0] \tag{1.4}$$

2. Taking $\hat{O}$ to be the Hamiltonian $\hat{H}$, the ground state total energy functional reads

$$\begin{aligned} E[n] =& \langle\phi|\hat{T}_e + \hat{V_{e-e}}|\phi\rangle + \langle\phi|\hat{V_{ext}}|\phi\rangle \\ =& F_{HK}[n] + \int n(\mathbf{r})V_{ext}(\mathbf{r})d\mathbf{r}, \end{aligned} \tag{1.5}$$

   where $F_{HK}[n]$ is the *universal* Hohenberg-Kohn density functional that contains the kinetic and potential energy of the electrons. The ground state energy functional $E[n]$ is minimized at the ground state density $n(\mathbf{r}) = n_0(\mathbf{r})$.

These theorems tell us that the knowledge of the ground state density $n_0(\mathbf{r})$ provides the material's specific external potential $\hat{V_{ext}}$. Since the rest of the Hamiltonian 1.2 is universal, the ground state density determines the full $\hat{H}$, as well as the number of electrons N through its normalization. Therefore, the ground state density contains implicitly the same amount of information about *the energy* of the system than the ground state eigenfunction. This is a huge simplification since only a single function $n(\mathbf{r})$ has to be known. It is important to keep in mind that this is only true for the ground state: any other density will determine a different $\hat{V}_{ext}$ with no physical relevance for the system under investigation. Unfortunately, this step forward does not tell us how to obtain the ground state density $n_0(\mathbf{r})$. A way to its practical determination was given by Kohn and Sham [159] that we shall describe in the following section.

Before proceeding to the Kohn-Sham equations, it is useful to reformulate the second theorem following the framework of Levy [160]. The idea is to start from the variational principle on the wave functions, which gives the ground state energy as:

$$E_0 = \min_{\phi} \langle \phi | \hat{H} | \phi \rangle, \tag{1.6}$$

where the $|\phi\rangle$ are chosen in a set of normalized wave functions. This minimization procedure can be separated into two steps:

(i) given a density $n(\mathbf{r})$, minimize over all the wave functions that give the density $n(\mathbf{r})$,
(ii) minimize over the density functions $n(\mathbf{r})$.

The energy functional therefore reads:

$$\begin{aligned} E[n] &= \min_{\phi(n)} \langle \phi | \hat{H} | \phi \rangle \\ &= \min_{|\phi\rangle(n)} \langle \phi | \hat{T}_e + \hat{V}_{e-e} | \phi \rangle + \int n(\mathbf{r}) V_{ext}(\mathbf{r}) d\mathbf{r}, \end{aligned} \tag{1.7}$$

where the minimization is done over a set of wave functions $|\phi\rangle$ corresponding to the density n. Note that the second term involving an integration over the external potential does not need to be minimized with respect to the set of wave functions since they all correspond to the same density n. The ground state energy is minimal when n is the ground state density since:

$$E_0 = \min_n \left[\min_{|\phi\rangle(n)} \langle \phi | \hat{H} | \phi \rangle \right] = \min_n E[n]. \tag{1.8}$$

The minimization has to be done under the constraint $\int n(\mathbf{r}) d\mathbf{r} = N$. Introducing a Lagrange multiplier λ, we obtain the stationarity condition:

$$\frac{\partial T_e}{\partial n}(\mathbf{r}) + \frac{\partial V_{e-e}}{\partial n}(\mathbf{r}) + V_{ext}(\mathbf{r}) = \lambda, \tag{1.9}$$

which tells us that $\hat{V}_{ext}$ is uniquely determined by the density n.

1.2 MAPPING TO A SOLVABLE NON-INTERACTING PROBLEM: THE KOHN-SHAM EQUATIONS

The key concept of the Kohn-Sham equations is to map the many-body interacting system onto a fictitious *solvable non-interacting* system which mimics the ground state density n_0 [159]. Consider a non-interacting system, in which the electrons are moving inside an effective external field:

$$\hat{H}^0 = \hat{T}^0 + \hat{V}^0_{eff}, \tag{1.10}$$

where the superscript ^{0} denotes the non-interacting quantities. This fictitious system can follow the same minimization procedure as the ”true” system, and we can therefore write the following stationarity condition:

$$\frac{\partial T^0}{\partial n}(\mathbf{r}) + V^0_{eff}(\mathbf{r}) = \lambda', \tag{1.11}$$

where $\hat{V}^0_{eff}$ is the external potential for the given density n. If this stationarity condition was to be equivalent to that of the interacting system 1.9, we then get

$$\begin{aligned} V^0_{eff}(\mathbf{r}) =& \underbrace{\left[\frac{\partial T_e}{\partial n}(\mathbf{r}) - \frac{\partial T^0}{\partial n}(\mathbf{r})\right] + \left[\frac{\partial V_{e-e}}{\partial n}(\mathbf{r}) - \frac{\partial V_H}{\partial n}(\mathbf{r})\right]}_{\frac{\partial V_{xc}}{\partial n}(\mathbf{r})} + \frac{\partial V_H}{\partial n}(\mathbf{r}) + V_{ext}(\mathbf{r}) \\ =& \frac{\partial V_{xc}}{\partial n}(\mathbf{r}) + \frac{\partial V_H}{\partial n}(\mathbf{r}) + V_{ext}(\mathbf{r}) \end{aligned} \tag{1.12}$$

where the constant difference between λ and λ' can be absorbed in the external potential. $\frac{\partial V_{xc}}{\partial n}(\mathbf{r})$ is the so-called exchange-correlation potential, and V_H is the Hartree term defined by:

$$V_H[n] = \frac{1}{2}\int d\mathbf{r} \int d\mathbf{r}' \frac{n(\mathbf{r})n(\mathbf{r}')}{|\mathbf{r} - \mathbf{r}'|}. \tag{1.13}$$

Now, the non-interacting Hamiltonian, which shall be called the Kohn-Sham Hamiltonian hereafter, can be written:

$$\left(\hat{H}^0 =\right)\ \hat{H}_{KS} = -\sum_i \frac{\nabla_i^2}{2m_e} + \int d\mathbf{r}' \frac{n(\mathbf{r}')}{|\mathbf{r} - \mathbf{r}'|} + \hat{V}_{xc} + \hat{V}_{ext} \tag{1.14}$$

where the exchange correlation potential is given by:

$$\hat{V}_{xc} = \frac{\partial V_{xc}}{\partial n}. \tag{1.15}$$

Therefore, the many-body interacting problem can be mapped onto the non-interacting effective Kohn-Sham Hamiltonian, which consists of non-interacting electrons subject to two potentials: the material’s specific $\hat{V}_{ext}$, and the effective exchange-correlation potential $\hat{V}_{xc}$. $\hat{V}_{xc}$ contains all the involved contributions from the electron-electron interaction that are not included in the simple Hartree term. If in principle the mapping is exact, in general $\hat{V}_{xc}$ is unknown and needs to be approximated.

Assuming for a moment that $\hat{V}_{xc}$ is known, the initial variational problem of finding the ground state density of the fully interacting Hamiltonian is reformulated into solving the effective Kohn-Sham Hamiltonian for its ground state. Since it is a non-interacting Hamiltonian, its eigenfunctions can be obtained from:

$$\hat{H}_{KS}|\phi_i\rangle = \epsilon_i|\phi_i\rangle \tag{1.16}$$

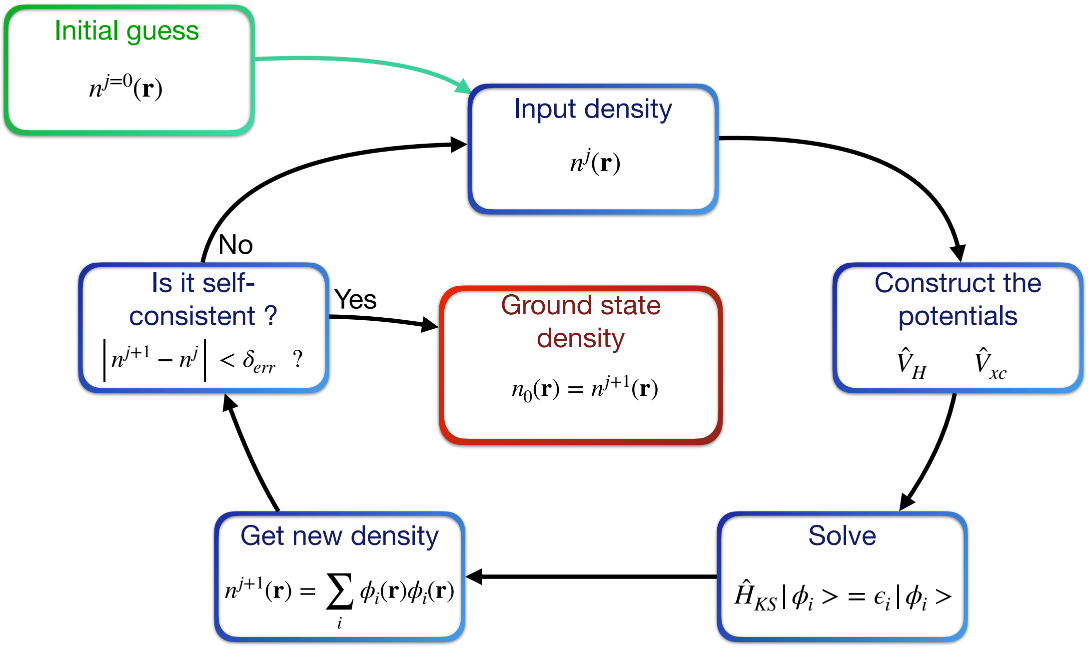

Figure 1.1: Sketch of the DFT self-consistent cycle at the iteration j. When the desired accuracy δ_{err} is reached, the procedure is stopped and the ground state density n_0 can be extracted.

where the $|\phi_i\rangle$ are the Kohn-Sham wave functions. The exact ground state density is then given by:

$$n_0(\mathbf{r}) = \sum_i^N \phi_i^*(\mathbf{r})\phi_i(\mathbf{r}). \tag{1.17}$$

This is a significant improvement, since instead of solving the interacting problem we can solve Eq. 1.16. However, one has to note that the Kohn-Sham wave functions are not the eigenfunctions of the original interacting problem. Only the density $n_0(\mathbf{r})$ calculated from these functions using Eq. 1.17 has a physical meaning. Similarly, the Kohn-Sham energies ϵ_i are not the one of the physical system, although some of them can approximately be identified to the ionization energies [161, 162].

One of the prices to pay for this construction, besides the determination of the exchange correlation that we still assume to be known for now, is that the latter $\hat{V}_{xc}$ and the Hartree potential $\hat{V}_H$ depend on the density $n(\mathbf{r})$. Hence, the Kohn-Sham Hamiltonian that we solve for its density $n(\mathbf{r})$, depends on this very density $n(\mathbf{r})$. We face here a self-consistent problem, that can be tackled by the following procedure (sketched in Fig. 1.1):

(i) Start from an initial guess $n^{j=0}(\mathbf{r})$ (not to be mistaken with the ground state density $n_0(\mathbf{r})$),
(ii) Determine the corresponding Hartree and exchange correlation terms $\hat{V}_H$ and $\hat{V}_{xc}$,
(iii) Solve the Kohn-Sham Hamiltonian 1.16 for its eigenfunctions $|\phi_i\rangle$
(iv) Compute the new density $n^{j+1}(\mathbf{r})$ using Eq. 1.17
(v) if $n^{j+1}(\mathbf{r}) \simeq n^j(\mathbf{r})$ up to the desired accuracy, stop the procedure and the ground state density is $n_0(\mathbf{r}) = n^{j+1}(\mathbf{r})$. If not, go back to (ii) and iterate.

Up to now, as mentioned above the procedure is exact (apart from the Born-Oppenheimer approximation). In fact, the interactions were hidden under the carpet since all the unknown terms were put into the exchange correlation potential. For practical calculations however, approximations of the exchange-correlation are needed.

1.3 LOCAL DENSITY APPROXIMATION

One of the most popular approximation to the exchange-correlation functional is the so-called local density approximation (LDA), which was already proposed by Kohn and Sham [159]. It is based on the observation that if the density of a system is sufficiently slowly varying, then the exchange correlation function can be written:

$$V_{xc}^{LDA}[n] = \int n(\mathbf{r})\epsilon_{xc}(n(\mathbf{r}))d\mathbf{r}, \tag{1.18}$$

where $\epsilon_{xc}(n(\mathbf{r}))$ is the exchange-correlation energy of the homogeneous electron gas at a particular density $n(\mathbf{r})$, which is known numerically. The main idea behind is the following: if the density $n(\mathbf{r})$ is slowly varying, then it can be divided into infinitesimal volumes where the density is locally constant. In each of these small volumes, at position $\mathbf{r}$, the electron gas can be considered as homogeneous, and therefore the exchange-correlation energy in each individual volume can be approximated by the well known exchange-correlation energy of an homogeneous gas of density equal to $n(\mathbf{r})$ (the local density of the true system). The total exchange-correlation functional is then obtained by integrating over all these infinitesimal volumes, yielding Eq. 1.18.

Within LDA, $V_{xc}[n]$ is purely local since the contribution to the functional at each point $\mathbf{r}$ is given by ϵ_{xc} evaluated at $n(\mathbf{r})$, and which is independent from the surrounding density. We expect this approximation to behave well for solids with delocalized electrons, like metals, for the wave functions in these systems extend over large distances thus leading to smoothly varying densities. In fact, it has proven to be efficient for many other systems beyond metals. It is for this reason that sometimes the Kohn-Sham energy bands are directly compared to ARPES measurements for instance, as will be done later in this thesis: for weakly correlated orbitals, the correction from the exchange-correlation potential is small and the electronic properties are rather lead by the crystalline potential which is accurately taken into account within DFT.

LDA can be extended to the spin polarized case with the local spin density approximation (LSDA), which can be written:

$$V_{xc}^{LSDA}[n] = \int n(\mathbf{r})\epsilon_{xc}(n^{\uparrow}(\mathbf{r}), n^{\downarrow}(\mathbf{r}))d\mathbf{r}, \tag{1.19}$$

where $n^{\downarrow/\uparrow}$ is the density for down/up spins, and ϵ_{xc} is now the exchange-correlation energy of the homogeneous spin polarized gas.

However, for materials like TMOs, such as NaCCOC or t-CuO that we study in this thesis, for which the valence electrons tend to be rather localized on atomic-like orbitals, the assumption of slowly varying density breaks down. While non-magnetic LDA predicts NaCCOC and t-CuO to be metallic (see Fig. 3.1(c) and Fig. 4.2), experiments show that they are insulators with a quite sizable gap [85, 124]. The electronic correlations are responsible for the localization of the electrons in such system: a more refined treatment is needed.

Many improvements to the local approximation have been formulated, a natural one being the generalised gradient approximation (GGA) in which the dependence to the gradient of the density is incorporated [163, 164], and which remains computationally cheap. Another possibility, more computationally demanding, is to include explicitly a part of the exact Hartree-Fock exchange

$$V_{HF} = -\frac{1}{2}\sum_{i,j} f_i f_j \int d\mathbf{r} \int d\mathbf{r}' \frac{\phi_j^*(\mathbf{r})\phi_i(\mathbf{r})\phi_i^*(\mathbf{r}')\phi_j(\mathbf{r}')}{|\mathbf{r}-\mathbf{r}'|} \tag{1.20}$$

which depends on the Kohn-Sham orbitals, i.e. is indirectly linked to the density. This class of approximation are called hybrid functionals [165], and they differ by the amount of mixing between the exact exchange and the LDA/GGA exchange correlation energy. We do not aim here at listing all the different approximations available which have been more or less successfully applied to real materials studies. We will instead focus on one of these many extensions of LDA in the next section, called LDA+U [151–153], that we have used in this thesis to study the interface properties of t-CuO.

1.4 LOCAL DENSITY APPROXIMATION + U

TMOs and rare-earth compounds showing the Mott-insulator transition usually contain partially filled d or f orbitals. The Comlomb interaction is effectively much stronger in these narrow orbitals as compared to the other shells since the electron-electron distance is shorter, and the inter-site overlaps smaller. Such materials can be insulating although they have a partially filled shell, in contrast to the usual band insulators. They are called Mott insulators [15, 16]. Not only LSDA usually predicts these materials to be metallic, but it also fails to capture the magnetic ground state. For instance for t-CuO, or NaCCOC ($x = 0$), the magnetic order vanishes in LSDA while there is experimental evidence for long-range magnetic order [136, 166]. The failing of LSDA for these system can be traced back to two main reasons [151, 167–170]:

1. the LSDA potential is orbital independent since it is built on the homogeneous gas exchange-correlation potential.
2. In LSDA, the splitting between two different spin states is governed by the homogeneous gas exchange parameter J, while in the Mott insulators it should be lead by the Coulomb interaction $U \gg J$ as will be shown in the following [151].

In 1991, Anisimov *et al.* proposed in Ref. 151 to overcome the LSDA shortcomings by adding an effective potential based on the mean-field solution of the Hubbard model [35–37], which is a simple model known to well account for strongly correlated systems [171]. Its simplest version consists of electrons moving on an effective single-orbital lattice:

$$H = \sum_{\langle i,j\rangle,\sigma} t_{ij} c^\dagger_{i\sigma} c_{j\sigma} + U \sum_i n_{i\uparrow} n_{i\downarrow}, \tag{1.21}$$

where $c_{i\sigma}^\dagger, c_{i\sigma}$ are the creation and annihilation operators of an electron on site i with spin σ, $n_{i\sigma}$ is the occupation operator, t_{ij} is the hopping amplitude from site j to i which is summed over the pairs of neighboring sites $\langle i, j\rangle$, and U is the effective on-site Coulomb interaction.

If $t_{ij} \gg U$, the electrons delocalize and the ground state energy dispersion is given by the Fourier transformation of the hoppings t_{ij}. In such a case, LSDA is a good approximation since the electronic wave functions are delocalized and the limit of the free electron gas is recovered. If $U \gg t_{ij}$ however (atomic limit), at half-filling, the electrons localize such that each orbital is singly occupied. The hopping processes are effectively suppressed because of the strong energy barrier U which makes the double occupation energetically too costly. This situation is similar to that of TMOs: the electronic wave functions are localized, they show strong local variations leading to the breakdown of the LSDA approximation.

The LDA+U approach [151–153] consists in treating the exchange-correlation potential with a mean-field solution of the Hubbard model in the atomic limit for the subset of d and/or f shells, while the remaining delocalized s, p electrons are still treated within LSDA. We represent the d or f shell by a N orbital-degenerate system, for which the Hamiltonian can be written down for one site only in the atomic limit $U \gg t_{ij}$:

$$H = \frac{U}{2} \sum_{\substack{\alpha,\alpha\prime \\ \alpha\neq\alpha\prime}} n_\alpha n_{\alpha\prime} \tag{1.22}$$

where $\alpha = \{m, \sigma\}$ combines the spin (σ) and orbital ($m = 1, \dots, N$) indices. Following Ref. 151, we show in the following that this simple Hamiltonian can overcome the two limitations of LSDA mentioned earlier in this section.

In the single orbital $N = 1$ case at half-filling, if the system is paramagnetic $n_\uparrow = n_\downarrow = 0.5$ then its energy at the mean-field level is $E_{PM} \simeq \frac{U}{4}$. This is not optimal compared to the spin-polarized case with $n_\uparrow = 1$ (or $n_\downarrow = 1$) which yields $E_{SP} \simeq 0$. The system favors the magnetic polarized solution and the energy splitting between the two spin states is $\simeq U$, i.e. is governed by the Coulomb interaction, in contrast to the LSDA approximation where it is lead by the homogeneous gas' exchange parameter. This exchange parameter is to be identified with the Hund's exchange, which is usually order order 1eV, much smaller than the effective Coulomb interaction $U \simeq 10$eV [151].

Now consider a N orbital degenerate system with n electrons. In the paramagnetic (both in terms of spin and orbital) limit, each of the $2N$ energy levels are filled by $\frac{n}{2N}$ electrons. Thus, the mean-field estimate for the energy is:

$$E_{PM} \simeq \frac{U}{2} 2N(2N-1)\Big(\frac{n}{2N}\Big)^2 = \frac{U}{2}(1 - \frac{1}{2N})n^2 \tag{1.23}$$

If spin polarization only is allowed, then the majority states will be on average occupied by $\frac{n}{N}$ (1) electrons if $n < N$ ($n > N$), and the minority states by $\frac{(n-N)}{N}$ if $N < n \leq 2N$, and 0 otherwise. This leads to:

$$\begin{aligned} E_{SP} &\simeq \frac{U}{2}N(N-1)\Big(\frac{n}{N}\Big)^2 = \frac{U}{2}(1-\frac{1}{N})n^2 && if \quad 0 < n \leq N \\ E_{SP} &\simeq \frac{U}{2}(1-\frac{1}{N})n^2 + U(n-N) && if \quad N < n \leq 2N. \end{aligned} \tag{1.24}$$

The spin polarized solution improves the energy compared to the paramagnetic case, but it is still not optimal. Most importantly, because of the orbital mixing the Slater gap is only between states of different spins. Therefore, there will be a gap only at half-filling, since for lower (higher) occupations states with the same spin flavor as the last occupied ones are available, providing gapless excitation channels. This underlines the necessity of including orbital polarization, since if we consider that the n electrons preferably occupy a certain set of orbitals, the ground state energy is approximately:

$$E_{SOP} \simeq \frac{U}{2}n(n-1). \tag{1.25}$$

Orbital and spin polarization therefore leads to the most optimal ground state energy, and the gap between the higher occupied state and the lower unoccupied is $\simeq U$, in contrast with standard LSDA in which the splitting is governed by Hund's exchange $J \ll U$ [151, 172]. Similarly to the spins, the orbital degree of freedom also polarizes due to the interactions, what can not be captured by the LSDA orbital-independent potential. To this effect can be added the crystal field splitting acting on the orbitals, which is usually weaker than the Coulomb interaction driven polarization.

LDA+U incorporates these effects in practice by defining a rotationally invariant potential for the correlated orbitals [153] (written for a single site for simplicity):

$$V^U[n] = \frac{1}{2}\sum_{m_1,m_2,\sigma} U_{m_1m_2}n_{m_1-\sigma}n_{m_2\sigma} + \sum_{m_1>m_2,\sigma}(U_{m_1m_2} - J_{m_1m_2})n_{m_1\sigma}n_{m_2\sigma} \tag{1.26}$$

where $U_{m_1m_2} = \langle m_1m_2|\hat{V}_{Coulomb}|m_1m_2\rangle$ and $J_{m_1m_2} = \langle m_1m_2|\hat{V}_{Coulomb}|m_2m_1\rangle$ are the screened Coulomb interaction matrix elements. The LSDA potential is corrected via:

$$V[n] = V^{LSDA}[n] + V^U[n] - V^{dc}[n] \tag{1.27}$$

where $V^{dc}[n]$ ensures that we recover the LSDA potential in absence of orbital polarization and is defined by:

$$V^{dc}[n] = \frac{1}{2}Un(n-1) - \frac{1}{2}J\big(n^{\uparrow}(n^{\uparrow}-1) + (n^{\downarrow}(n^{\downarrow}-1)\big) \tag{1.28}$$

with U and J the screened Coulomb and exchange parameters.

One of the main advantage of LDA+U is that it is computationally cheap. It will prove extremely useful in the study of the interface properties of the t-CuO/STO junction in Chap. 5 of this thesis.

For these kind of systems, DFT is the only computationally accessible technique due to the system size to be considered and LSDA alone would fail to give a correct description. Indeed t-CuO would be predicted to be a non-magnetic metal, preventing us to draw scenarios on the appearance of magnetic moments at the t-CuO/STO interface.

A clear limitation of LDA+U is that it requires spin and orbital polarization to open an electronic gap. This is related to the fact that this method amounts to add a constant and purely real correction term (the self-energy) to the non-interacting Hamiltonian. Such correction is non zero only if the system displays an orbital and/or spin polarization. The self-energy, that we discuss in more details in the next chapter, incorporates the modification of the non-interacting Hamiltonian from the presence of electronic interactions. Since it is fully real within LDA+U, the Kohn-Sham energies are purely real, which means that they have infinite lifetime. We remain in a band structure picture. LDA+U would not be able to capture a correlation-driven gap in the half-filled paramagnetic case as we will observe later in Chap. 4. In this situation, the metal-insulator transition is related to the divergence of the imaginary part of the self-energy at the Fermi level which suppresses the quasiparticle excitations [171] and decreases drastically their lifetime. All these effects showed to be essential to capture the spectral properties that can be probed for instance in photoemission measurements, and for which the knowledge of the excited states is essential but can not be obtained from a DFT calculation.

For all these reasons, one has to go beyond DFT(+U) and treat the interaction effects in the correlated subsystem: the *d* orbitals for the systems under investigation in this thesis. The Hubbard model has proven to be useful at the simple mean-field level within LDA+U, but a more involved treatment is needed to obtain the dynamic electronic properties. One powerful method is the so-called DMFT and its cluster extension CDMFT that we describe in the next chapter.

2 MANY-BODY METHODS

2.1 FROM THE BAND STRUCTURE TO A LOW-ENERGY EFFECTIVE MODEL

Despite the developments of new functionals, band-theory remains strongly limited for the description of correlated systems like the family of the TMOs [5], to which the copper oxides belong. The Coulomb interaction U being of the same order of magnitude than the bandwidth W, a mean-field treatment of the interaction fails and perturbation theory can not be applied neither in U, nor in W. Moreover, in order to interpret experimental probes like ARPES, the inclusion of the dynamic effects is essential (see App. A). Indeed, in a metal the quasi-free electrons have a long life-time which leads to sharp experimental bands close to the theoretical band picture. In contrast, strongly correlated systems can yield dramatic lifetime suppression, spectral weight redistributions, resulting in a much different spectral function as we shall see later in this thesis. Effective models, which focus on a restricted set of degrees of freedom, are needed to describe the relevant mechanisms in those materials.

In this section, we first motivate the use of the Hubbard model as an effective system that aims at describing the low-energy physics of copper oxides. We then present a way to parameterize the model such that it is suited to capture the essential low-energy physics of a specific material.

2.1.1 THE HUBBARD MODEL

The rich phase diagram of copper oxides at low temperature is related to the low-energy properties, i.e. to the electronic states close to the Fermi level. Since we have seen that the manifold of low-energy bands for such materials is rather related to localized orbitals, we can model it by a simple lattice of atomic-like orbitals. The overlaps between these orbitals allow the electrons to hop between neighboring sites, which can be represented by a tight-binding (TB) Hamiltonian. In the case of copper oxides, the d orbitals of the Cu atoms are in a d^9 configuration due to the hybridization with the surrounding O atoms: all d orbitals are filled but one, usually the $d_{x^2-y^2}$ which is half-filled. It has been proposed by Zhang and Rice that the low-energy properties of such system can be approximated by a single-orbital model due to the formation of ZRS between the Cu $d_{x^2-y^2}$ and O $p_{x/y}$ orbitals centered on the Cu sites [38], which then leads to a single-band TB Hamiltonian:

$$H_0 = \sum_{\langle i,j\rangle,\sigma} t_{ij} c^\dagger_{i\sigma} c_{j\sigma}, \tag{2.1}$$

where the indices i refer to the lattice sites, and t_{ij} is the hopping amplitude between two neighbors $\langle i,j\rangle$. H_0 gives rise to energy bands similarly to DFT. The ZRS form a 2D lattice of single orbitals, and for the sake of simplicity we assume that the hopping terms are limited to the NN term t. Using a Fourier transformation, one easily finds the following energy dispersion:

$$\epsilon(\mathbf{k}) = -2t\big[\cos(k_x) + \cos(k_y)\big], \tag{2.2}$$

where we set the lattice constant $a = 1$. This dispersion (Fig. 2.1(c)) can, for instance, be compared with the band structure of NaCCOC (Fig. 2.1(a)) calculated using the Wien2k package [173, 174] along the the $\Gamma - X - M - \Gamma$ **k**-path. As expected from the ZRS approximation, the low-energy part of NaCCOC is composed of an almost isolated single band crossing the Fermi energy. LDA predicts the system to be metallic since the ZRS band is half-filled, as discussed in the previous chapter. The simple TB results looks quite alike the DFT band that crosses the Fermi energy (see Fig. 2.1(c)), and in fact by including longer-range hoppings and choosing the right hopping parameters, one can adjust the TB dispersion so to fit as best a possible the DFT bands (see Fig. 2.1(c)). We show later in this section that this parameterization can be done rigorously by a transformation of the delocalized Bloch-like wavefunctions used in DFT (Fig. 2.1(d)) into a set of atomic-like localized Wannier functions (Fig. 2.1(e)). By providing the non-interacting part H_0 of the effective Hamiltonian, the band structure calculations with the LDA functional is a good starting point.

To our TB hamiltonian we can now add the Coulomb interaction, which in principle is a long-ranged interaction. The problem is simplified by considering that, due to electronic screening of the Coulomb potential, the effective on-site interaction U is much larger than the inter-site interaction V, which is then neglected in our modeling. This is verified in cuprates as shown by Hirayama *et al.* for different compounds: U is typically almost an order of magnitude larger than V [31]. Moreover, as is explained in Chap. II, 3 and 4, we will restrict our effective model to a single effective ZRS orbital on each site. With the addition of the on-site interaction U, we get to the well-known Hubbard model [35–37]:

$$H = \sum_{\langle i,j\rangle,\sigma} t_{ij} c^{\dagger}_{i\sigma} c_{j\sigma} + U \sum_i n_{i\uparrow} n_{i\downarrow}, \tag{2.3}$$

which we already mentioned in the context of LDA+U. This model can not be solved exactly because of the interplay between the one-body kinetic term and the two-body interaction one. To solve it beyond the mean-field solution, we use the powerful method called DMFT [42, 43] that is described later in this chapter. The combination of LDA to obtain the band structure and DMFT to treat the correlated subsystem is usually called single-shot LDA+DMFT, and was first apply shortly after DMFT was invented under the name of LDA++ [49, 152].

One might be puzzled here since in principle a part of the electronic interactions is taken into account at the DFT level, and which seems to be ignored in the TB Hamiltonian, such that if we add interactions to H_0 we shall face a double-counting problem. The interactions within DFT lead to a constant self-energy for each band, i.e. static band-dependent energy shifts which have to be corrected before adding correlations to the model [152]. In this thesis, the problem of double-counting is avoided since we consider only the single-band Hubbard model for which the

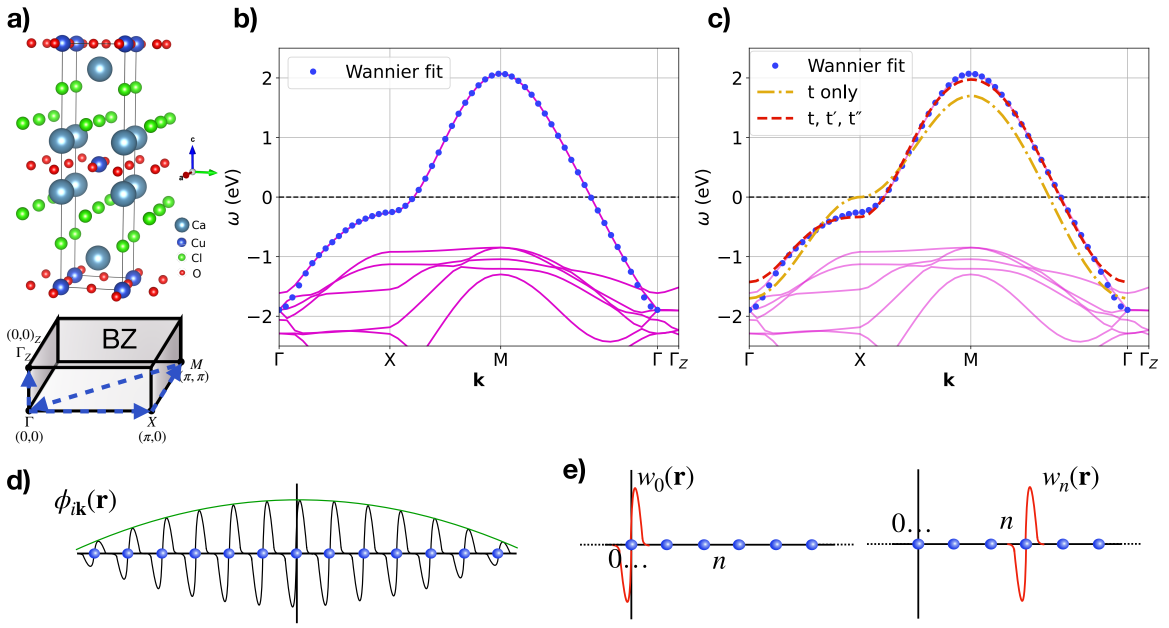

Figure 2.1: (a) Crystal structure of NaCCOC ($x = 0$) with a sketch of the $\mathbf{k}$ path in the first BZ. (b) Band structure obtained with a LDA calculation, along with the Wannier band obtained with the MLWF method (blue points). (c) Wannier band (blue points), and its approximated TB band obtained by neglecting the hoppings terms beyond the NNNN. The orange dashed-dotted line shows the 2D dispersion of Eq. 2.2 calculated with only t. (d) Sketch of a delocalized Bloch wavefunction $\phi_{n\mathbf{k}}(\mathbf{r})$: the black lines represent the periodic function $u_{n\mathbf{k}}$ weighted by the $e^{i\mathbf{k}\mathbf{r}}$ term (green). (e) Sketch of localized Wannier functions $w_n(\mathbf{r})$ centered around the atomic positions $\{n\}$.

constant shift can be absorbed in the chemical potential.

Now that we have motivated the use of the Hubbard model as an effective system for the correlated manifold, we are left with describing how to parameterize the hopping and interaction parameters to obtain a realistic description of the low-energy properties of the material of interest (the subject of the remainder of this section), and how efficiently solve this model (the remainder of this chapter).

2.1.2 PARAMETERIZATION

The DFT bands can be expressed with a set of delocalized Bloch wavefunctions (illustrated in Fig. 2.1(d))

$$\phi_{n\mathbf{k}}(\mathbf{r}) = u_{n\mathbf{k}}(\mathbf{r})e^{i\mathbf{k}\mathbf{r}}, \tag{2.4}$$

where $u_{n\mathbf{k}}(\mathbf{r})$ is a periodic function of $\mathbf{r}$, i.e. $u_{n\mathbf{k}}(\mathbf{r}+\mathbf{R}) = u_{n\mathbf{k}}(\mathbf{r})$ with $\mathbf{R}$ a lattice vector. To parameterize the non-interacting part of Eq. 2.3, we need to switch to a localized basis set $\{|w_i\rangle\}$ and compute the hopping terms as the overlaps between neighboring sites:

$$t_{ij} = \int d\mathbf{r}\langle w_i|H_{KS}|w_j\rangle. \tag{2.5}$$

There exist different methods to perform the transformation to a localized basis: one can use linear muffin-tin orbitals [49, 152, 175], N-th order muffin-tin orbitals [176], Wannier functions constructed by projection [177, 178], or projection of the full-potential linear augmented plane-wave onto a local basis [179, 180], just to name a few. In this thesis, we have use another method called the maximally localized Wannier functions (MLWF) [181, 182] that we present in the following.

From an isolated manifold of N occupied bloch bands $\phi_{n\mathbf{k}}(\mathbf{r})$, a set of N Wannier functions $w_{n\mathbf{R}}(\mathbf{r}-\mathbf{R})$, where $\mathbf{R}$ is a lattice vector, can be constructed:

$$|w_{n\mathbf{R}}\rangle = \frac{V}{(2\pi)^3}\int_{BZ}\left(\sum_{m=1}^{N} U^{\mathbf{k}}_{mn}|\phi_{m\mathbf{k}}\rangle\right)\mathrm{e}^{-i\mathbf{k}\mathbf{R}}d\mathbf{k}. \tag{2.6}$$

The integration is done over the BZ, and $U^{\mathbf{k}}$ is a unitary matrix mixing the bands at each $\mathbf{k}$ point. The Wannier functions are not unique since:

(i) the Bloch wave functions are defined up to a phase factor $\mathrm{e}^{i\theta(\mathbf{k})}$,
(ii) At each $\mathbf{k}$ point the set of occupied bands may be unitary transformed by some $U^{\mathbf{k}}$.

Instead of being an issue, this non-uniqueness of the Wannier functions can be exploited to construct MLWF as was first proposed by Marzari *et al.* [181]. The strategy consists in performing a variational search of the unitary matrix $U^{\mathbf{k}}$ that minimizes the spread function of the Wannier orbitals around their center:

$$\begin{aligned}\Omega &= \sum_{n=1}^{N}\left\langle(\mathbf{r}-\langle\mathbf{r}\rangle_n)^2\right\rangle_n = \sum_{n=1}^{N}\left(\left\langle\mathbf{r}^2\right\rangle_n - |\langle\mathbf{r}\rangle_n|^2\right)\\ \left\langle\hat{A}\right\rangle_n &= \langle w_{n\mathbf{0}}|\hat{A}|w_{n\mathbf{0}}\rangle.\end{aligned} \tag{2.7}$$

It is easily shown that the spread function Ω can be separated into two parts:

$$\begin{aligned}\Omega &= \sum_{n=1}^{N}\left(\left\langle\mathbf{r}^2\right\rangle_n - \sum_{m\mathbf{R}}|\langle w_{m\mathbf{R}}|\mathbf{r}|w_{n\mathbf{0}}\rangle|^2\right) + \sum_{n}\sum_{m\mathbf{R}\neq n\mathbf{0}}|\langle w_{m\mathbf{R}}|\mathbf{r}|w_{n\mathbf{0}}\rangle|^2\\ &=\Omega_I + \tilde{\Omega}.\end{aligned} \tag{2.8}$$

It turns out that Ω_I is gauge invariant [181], that is to say that it does not depend on the choice of the unitary matrix $U^{\mathbf{k}}$, such that the minimization procedure is only done on $\tilde{\Omega}$ by evolving $U^{\mathbf{k}}$ using a standard minimization algorithm. Note that the set of matrices $U^{\mathbf{k}}$ can be constrained if one expects a MLWF of a certain symmetry, for more details the interested reader can refer to the wannier90 package documentation [183, 184].

The main drawback of this method is that it is constructed on the assumption that there is an *isolated* set of N Bloch wavefunctions at our disposal. However, this is usually not the case, and especially when constructing simpler effective models like the single band Hubbard model we use in this thesis. Indeed, by inspecting Fig. 2.1(b), we notice that the band of interest is entangled with the manifold of bands lying around −1.5eV, preventing us from using the above method directly since it is designed to extract N Wannier functions from a set of N bands.

To overcome this issue, a *disentanglement* procedure was proposed by Souza *et al.* in Ref. 182, which amounts to perform an additional minimization of the gauge invariant function Ω_I. The first step is to select an energy window containing $N_k \leq N$ bands. At each $\mathbf{k}$ point, there exist multiple N-dimensional subspaces $\mathcal{S}^{(\mathbf{k})}$ which can be spanned by unitary transformation of the N_k states:

$$\left|u_{n\mathbf{k}}^{opt}\right\rangle = \sum_{m\in N_k} U_{mn}^{dis(\mathbf{k})} |u_{m\mathbf{k}}\rangle, \tag{2.9}$$

where $U^{dis(\mathbf{k})}$ is a rectangular $N_k \times N$ matrix, said to be unitary since $U^{dis(\mathbf{k})}(U^{dis(\mathbf{k})})^\dagger = \mathbb{1}$, and $|u_{n\mathbf{k}}\rangle$ refers to the periodic part of the Bloch functions. Since Ω_I is invariant within a given subspace $\mathcal{S}^{(\mathbf{k})}$, it can be considered as a functional of the subspace $\Omega_I\left[\mathcal{S}^{(\mathbf{k})}\right]$. For each $\mathbf{k}$ point, the latter is minimized by choosing the optimal subspace $\mathcal{S}_{opt}^{(\mathbf{k})}$, and then $\tilde{\Omega}$ is optimized within each $\mathcal{S}_{opt}^{(\mathbf{k})}$.

For a physical interpretation of this additional minimization, it is insightful to re-write Ω_I as follows [182]:

$$\begin{aligned} &\Omega_I \propto \sum_{\mathbf{k},\mathbf{k}'} w_{\mathbf{k}'} \sum_{m=1}^{N} \left(1 - \sum_{n=1}^{N} |M_{mn}^{(\mathbf{k},\mathbf{k}')}|^2\right), \\ &M_{mn}^{(\mathbf{k},\mathbf{k}')} = \langle u_{m\mathbf{k}} | u_{m\mathbf{k}+\mathbf{k}'}\rangle, \end{aligned} \tag{2.10}$$

where $w_{\mathbf{k}'}$ is a weight arising from the discretization linked with finite differences [181]. Intuitively, we notice that Ω_I is minimum when the overlaps $M_{mn}^{(\mathbf{k},\mathbf{k}')}$ are maximized, i.e. when $\mathcal{S}^{(\mathbf{k})}$ is the subspace with minimum mismatch as $\mathbf{k}$ is varied. For instance, in the attempt to apply such procedure to the case of NaCCOC, $\mathcal{S}^{(\mathbf{k})}$ is optimal when it keeps the single band crossing the Fermi energy and excludes the bands from the -1.5eV manifold.

MLWF can be routinely obtained from a band structure calculation with the `wannier90` package [183, 184]. Most importantly, hopping parameters can be extracted and an effective TB Hamiltonian is obtained. In Fig. 2.1(b)-(c), we show an example of an effective MLWF band obtained for NaCCOC by fitting the ZRS band that crosses the Fermi energy, and its approximated TB band for which the hopping terms were kept until the next-NNN (NNNN) neighbor. The Kohn-Sham band is extremely well reproduced by the Wannier band, as well as the simpler TB band: we now dispose of a low-energy non-interacting model with a set of hopping parameters t_{ij} obtained *ab initio*.

Having determined the non-interacting part of our effective model, we are left with the Coulomb interaction U. In principle, the Coulomb matrix (in the case of a multi-orbital system) can be determined *ab initio* [185] using method like the constrained random phase approximation [186, 187], or constrained DFT [188–190], but in this thesis we either determined it via a fit to an experimental measurement, or empirically. We therefore do not describe the procedure here, and rather go on with the description of a way to solve our realistic Hubbard model: the dynamical mean-field theory (DMFT).

2.2 SOLVING THE HUBBARD MODEL: DYNAMICAL MEAN-FIELD THEORY

There is no exact solution to the Hubbard model, except for limiting cases like the atomic limit ($t_{ij} = 0$), or the non-interacting limit ($U = 0$), or in 1D [191]. As we have seen in the previous chapter, static mean-field approaches can lead to constant and purely real corrections to the (almost) non-interacting solution, but it is insufficient for instance to capture the physics of the Mott insulating transition. In contrast, DMFT [42, 43] in its construction retains the full dynamics of the local quantum fluctuations. It is based on a mapping from the full lattice interacting problem onto an impurity model in which a site is dynamically embedded into a self-consistent electron bath. The impurity model can be seen as an Anderson's impurity model (AIM) [18] in which all the local fluctuations are treated exactly (while non-local correlations are discarded), and which can be efficiently solved numerically. In contrast to the well-known Weiss molecular-field theory for the Ising Model [192], in which the spin interactions are replaced by the action of a static mean-field, in DMFT the occupation of the effective impurity site is not kept constant since electrons can hop back and forth from the electron bath, i.e. it is a time-dependent problem. In principle, DMFT makes no further approximation and is valid for all ranges of temperatures, interaction strength, and similarly to the Weiss theory it becomes exact in the limit of infinite dimension $d \to \infty$, which amounts to $z \to \infty$ with z the coordination number.

In fact, DMFT was developed after the pioneering works of Metzner and Vollhardt [44–47] who studied the properties of the Hubbard model in infinite dimensions, that we present first in this section. Following these findings, Ohkawa [193] and Georges and Kotliar [42] showed that in the $d \to \infty$ limit there is an exact mapping between the Hubbard model and the AIM with an effective non-interacting electronic bath. We detail one of the possible derivations, the so-called cavity method [42, 43], and finally present the set of self-consistent equations at the heart of DMFT.

2.2.1 THE LIMIT OF INFINITE DIMENSION

Similarly to the Ising model, the Hubbard model in infinite dimension yields peculiar properties [44–46] that will lead to drastic simplifications of the problem. We first recall the Hamiltonian for the single-orbital case:

$$H = \sum_{\langle i,j\rangle,\sigma} t_{ij} c^{\dagger}_{i\sigma} c_{j\sigma} + U \sum_{i} n_{i\uparrow} n_{i\downarrow} - \mu \sum_{i} n_{i}, \tag{2.11}$$

where we keep, for the sake of simplicity, only the nearest-neighbor hopping term t, and we added the chemical potential (μ) term. Since the Hubbard U interaction is purely local, only the kinetic part of the Hamiltonian depends on the dimension d of the problem. Assuming that the system is a d-dimensional hypercubic lattice, i.e. the coordination number is $z = 2d$, the non-interacting dispersion can be written:

$$\epsilon_{\mathbf{k}} = -2t \sum_{i=1}^{d} \cos(k_i), \tag{2.12}$$

where we set the lattice constant $a = 1$. The density of states (DOS) associated to $\epsilon_{\mathbf{k}}$ is given by

$$D(\omega) = \sum_{\mathbf{k}} \delta(\omega - \epsilon_{\mathbf{k}}), \tag{2.13}$$

where δ is the delta Dirac function. The DOS can be interpreted as the probability density for $\omega = \epsilon_{\mathbf{k}}$ given a random choice of $\mathbf{k}$: the dispersion (Eq. 2.12) is simply a sum over random variables $-2t\cos(k_i)$ with $\mathbf{k} = (k_1, \dots, k_d)$. The summation being over the dimension d, in the limit of $d \to \infty$ one can apply the central limit theorem to the DOS $D(\omega)$ giving

$$D(\omega) \simeq \frac{1}{\sqrt{2\pi t\sqrt{2d}}} \mathrm{e}^{-\frac{1}{2}\left(\frac{\omega}{t\sqrt{2d}}\right)^2} = \frac{1}{\sqrt{2\pi t\sqrt{z}}} \mathrm{e}^{-\frac{1}{2}\left(\frac{\omega}{t\sqrt{z}}\right)^2}. \tag{2.14}$$

The variance $\sigma = t\sqrt{z}$ becomes infinite in the $d \to \infty$ limit if the hopping t is not rescaled. The DOS would therefore become flat and featureless, without any physical relevance. Rescaling the hopping t is necessary for having a well-defined DOS in infinite dimension, one of the possible choices is

$$t \to \frac{t}{\sqrt{z}}, \tag{2.15}$$

which results in [44]

$$D(\omega) = \frac{1}{\sqrt{2\pi t}} \mathrm{e}^{-\frac{1}{2}\left(\frac{\omega}{t}\right)^2}. \tag{2.16}$$

When $d \to \infty$, with this choice of rescaling, the DOS becomes a Gaussian. Interestingly, one observes that the DOS converges quickly to this limit as d is increased [47]: already at $d = 3$, i.e. $z = 6$, the shape is very similar to a Gaussian. Note that this choice of rescaling is not the only one possible [47], but it has the virtue of keeping the problem non-trivial at infinite dimension since the kinetic and Coulomb parts of the Hamiltonian remain in competition.

This scaling has important consequences on the many-body observables of the system like the Green's function or the self-energy. As a brief reminder, the Matsubara Green's function is defined as follows

$$G_{ij,\sigma}(\tau - \tau') = -\left\langle T_\tau c_{i\sigma}(\tau) c^\dagger_{j\sigma}(\tau') \right\rangle \tag{2.17}$$

where i, j denotes the site indices, τ is the imaginary time, T_τ is the time ordering operator, and $\langle . \rangle$ denotes the thermodynamic average. It measures the propagation of an electron through the correlated system from site j at time τ' to site i at time τ. In the case of a non-interacting system, say the Hubbard model restricted to its kinetic part, the non-interacting Green's function can be written as a function of Matsubara frequency and momentum $\mathbf{k}$ as:

$$G^0_{\mathbf{k},\sigma}(i\omega_n) = \frac{1}{i\omega_n + \mu - \epsilon_{\mathbf{k}}} \tag{2.18}$$

where $\omega_n = \frac{(2n+1)\pi}{\beta}$ are the fermionic Matsubara frequencies, β is the inverse temperature. When including interactions, the Hamiltonian can not be diagonalized anymore and the correlation effects can be conveniently encoded in the Self-energy $\Sigma_{\mathbf{k},\sigma}(i\omega_n)$, which is related to the interacting Green's function by:

$$\begin{aligned} G_{\mathbf{k},\sigma}(i\omega_n) &= \frac{1}{i\omega_n + \mu - \epsilon_{\mathbf{k}} - \Sigma_{\mathbf{k},\sigma}(i\omega_n)} \\ \Sigma_{\mathbf{k},\sigma}(i\omega_n) &= \left[G^0_{\mathbf{k},\sigma}(i\omega_n)\right]^{-1} - \left[G_{\mathbf{k},\sigma}(i\omega_n)\right]^{-1}. \end{aligned} \tag{2.19}$$

The second equation, that relates the Self-energy to the interacting and non-interacting Green's function, is the so-called Dyson equation.

To see the effects of the infinite dimension limit on the many-body observables, it is instructive to start from the following sum rule for a non-interacting system [45]:

$$\sum_i \left(\langle c^\dagger_{i\sigma} c_{j\sigma}\rangle^0\right)^2 = n^0_{j,\sigma} \tag{2.20}$$

where the superscript ^{0} denotes the observables evaluated for the non-interacting system. Now, the sum may be re-written by grouping the i indices with respect to their distance from the site j, that is to say we group them by groups of NN, NNN, etc. Taking care of the one term $i = j$, Eq. 2.20 may be written:

$$\begin{aligned} \sum_i \left(\langle c^\dagger_{i\sigma} c_{j\sigma}\rangle^0\right)^2 &= (n^0_{j,\sigma})^2 + \sum_{l=1}^{\infty} z_l \left(\langle c^\dagger_{l\sigma} c_{j\sigma}\rangle^0\right)^2 \\ \sum_{l=1}^{\infty} z_l \left(\langle c^\dagger_{l\sigma} c_{j\sigma}\rangle^0\right)^2 &= n^0_{j,\sigma} - (n^0_{j,\sigma})^2 \end{aligned} \tag{2.21}$$

where l denotes the neighbor rank (NN, NNN, etc), and z_l the number of neighbors of rank l. Therefore, we can obtain an upper bound for the non-interacting Green's function:

$$\left|\langle c^\dagger_{i\sigma} c_{j\sigma}\rangle^0\right| = \left|G^0_{ij,\sigma}(\tau \to 0)\right| \leq \left[\frac{n^0_{j,\sigma}(1 - n^0_{j,\sigma})}{z_l}\right]^{1/2}, \text{ for } \langle i, j\rangle \text{ of rank l.} \tag{2.22}$$

In an hypercubic lattice, each site has z NN, each of them having $z - 1$ neighbors (excluding the first site), and etc. This means that in the $d \to \infty$ limit, $z_l \propto z^l$, such that one may write

$$G^0_{ij,\sigma}(\tau \to 0) \propto \frac{1}{z^{\|\mathbf{R_i} - \mathbf{R_j}\|/2}} \tag{2.23}$$

where $\left\|\mathbf{R_i} - \mathbf{R_j}\right\|$ denotes the "Manhattan" distance between site i and j. Although this was demonstrated only for $\tau \to 0$, the Green's function $G^0_{ij,\sigma}$ must follow the same scaling at all times since it does not depend on the time evolution. We therefore have, for a general couple of sites (i, j):

$$G^0_{ij,\sigma} \propto \frac{1}{z^{\|\mathbf{R_i} - \mathbf{R_j}\|/2}} \tag{2.24}$$

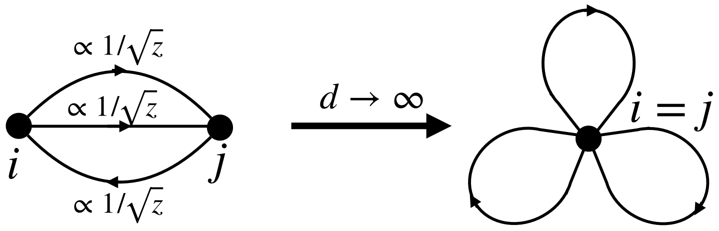

Figure 2.2: Sketch of a second order diagram in real space contributing to the fully irreducible self-energy Σ_{ij} (considering $\langle ij \rangle$ nearest-neighbor for simplicity). In the $d \to \infty$ limit all the diagrams become purely local due to the scaling discussed in the text.

Despite this scaling of the Green's function, one must not discard the inter-site elements since these terms still contribute to the kinetic energy:

$$E^0_{kin} = - \sum_{\langle i,j \rangle,\sigma} t_{ij} \Big\langle G^0_{ij,\sigma}(\tau \to 0^-) \Big\rangle^0 . \tag{2.25}$$

For a couple of neighbors $\langle ij \rangle$, the Green's function scales as $z^{-\left\|\mathbf{R_i}-\mathbf{R_j}\right\|/2}$, and the hopping as $t_{ij} \propto z^{-\left\|\mathbf{R_i}-\mathbf{R_j}\right\|/2}$, but the sum brings a factor $z^{\left\|\mathbf{R_i}-\mathbf{R_j}\right\|}$, the number of equivalent ways to consider two neighbors $\langle ij \rangle$ with the same distance $\left\|\mathbf{R_i} - \mathbf{R_j}\right\|$.

From the Green's function scaling one can show the most important simplification at $d \to \infty$: the self-energy becomes purely local [44, 45]. One suggestive way to show that is to consider the diagrammatic expansion of the self-energy. We can reduce the discussion to diagrams of order $n > 2$ since the Hartree term is just a constant and local correction, while the Fock term vanishes in the case of a Hubbard model with only the on-site U interaction. A typical second order diagram that contributes to the fully irreducible self-energy Σ_{ij} is shown in Fig. 2.2. Each line of the diagram, representing a non-interacting propagator between site i and j, will contribute to $z^{-\left\|\mathbf{R_i}-\mathbf{R_j}\right\|/2}$ in the $d \to \infty$ limit. In total, this amounts to a scaling of $z^{-3\left\|\mathbf{R_i}-\mathbf{R_j}\right\|/2}$, but the sum over all neighbors $\langle ij \rangle$ brings only a factor $z^{\left\|\mathbf{R_i}-\mathbf{R_j}\right\|}$, i.e. the overall contribution to Σ_{ij} scales as $z^{-\left\|\mathbf{R_i}-\mathbf{R_j}\right\|/2}$. The same can be shown for higher order diagrams, such that $\Sigma_{ij} \propto z^{-\left\|\mathbf{R_i}-\mathbf{R_j}\right\|/2}$ in the $d \to \infty$ limit. In other words, only the local component of the self-energy survives at infinite dimension, it is therefore purely local:

$$\lim_{d \to \infty} \Sigma_{ij,\sigma}(i\omega_n) = \delta_{ij} \Sigma_{ij,\sigma}(i\omega_n). \tag{2.26}$$

It follows that the self-energy becomes momentum independent:

$$\Sigma_{\mathbf{k},\sigma}(i\omega_n) = \Sigma(i\omega_n) \tag{2.27}$$

and the local Green's function is calculated via:

$$G_\sigma(i\omega_n) = \sum_{\mathbf{k}} \frac{1}{i\omega_n + \mu - \epsilon_{\mathbf{k}} - \Sigma_\sigma(i\omega_n)} \tag{2.28}$$

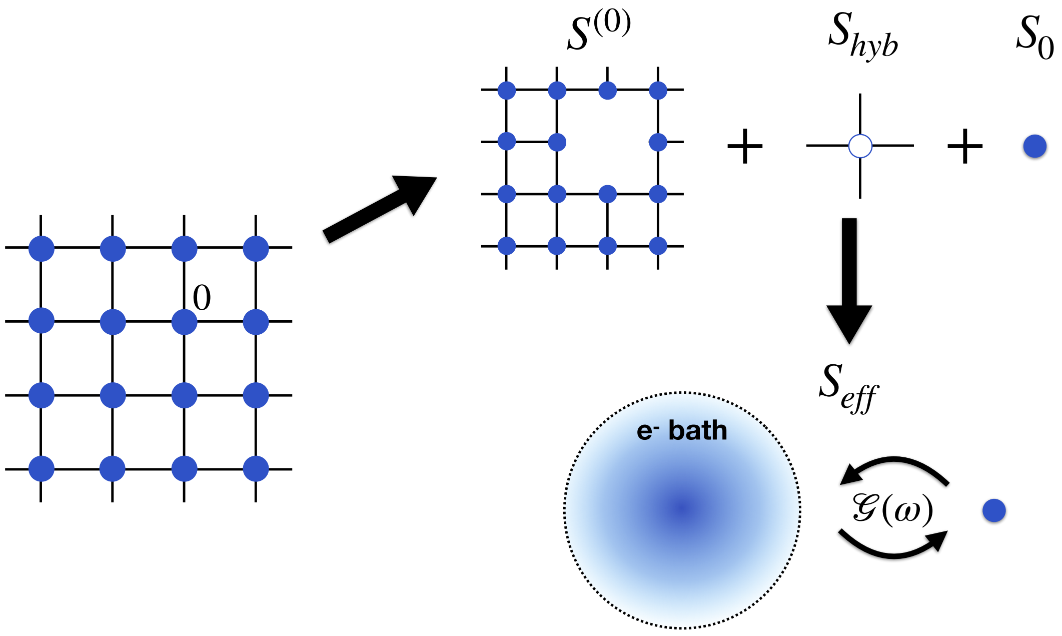

Figure 2.3: Illustration of the cavity method. The total action S is divided into three components $S^{(0)}$, S_{hyb}, S_0 by isolating the site 0 from the lattice. The lattice degrees of freedom are integrated out, leading to an effective Weiss field $\mathcal{G}$ coupling the site 0 to a bath of electrons.

It is important here note here that no approximation has been used to show that the self-energy becomes momentum independent in the $d \to \infty$ limit. Infinite dimension is of course an approximation for real materials with finite coordination number z, but in contrast to the standard Weiss mean-field theory the self-energy remains a function of frequency, i.e. the dynamics of the system is not suppressed.

2.2.2 THE CAVITY METHOD

Even though the correlations become local at infinite dimension, the Hubbard model remains intractable computationally. A huge step forward was the work of Ohkawa [193] and Georges and Kotliar [42], who showed that there exist an exact mapping between the Hubbard model and the AIM in the limit $d \to \infty$. The effective impurity model consists of a single site (the impurity) connected to a self-consistent bath of non-interacting electrons through an effective dynamic Weiss field. From a practical viewpoint, such a mapping is extremely useful since many numerical methods exist to solve the AIM: the Hirsch-Fye quantum Monte Carlo solver [194, 195], CTQMC [60–62], exact diagonalization [53, 54], renormalization group techniques [55], and MPS [56, 57]-based methods [58, 59].

DMFT equations can be derived by different methods, such as the generalized coherent potential approximation [196, 197], or via the Baym-Kardanoff functional [198, 199]. We present here the derivation based on the cavity method [42, 43], which consists in isolating a site (denoted 0) from the lattice, and integrating out all the remaining lattice degrees of freedom. This construction, illustrated in Fig. 2.3, leads to an effective representation of the many-body interacting problem by an isolated site embedded into a self-consistent non-interacting electron bath. By identifying the hybridization function of the AIM to the Weiss field of the cavity method, one observes that the solution of the Hubbard model in $d \to \infty$ can be obtained by solving an impurity problem. Similarly to DFT with the density, here the effective hybridization function is not known *a priori*, but can be found with a self-consistent procedure.

The cavity construction relies on the action formulation of the Hubbard model. We start from the partition function $\mathcal{Z}$ of the lattice system which is described by the action S:

$$\mathcal{Z} = \int \prod_{i,\sigma} \mathrm{D}c^{\dagger}_{i\sigma}\mathrm{D}c_{i\sigma}\mathrm{e}^{-S}, \tag{2.29}$$

where $c^{\dagger}_{i\sigma}, c_{i\sigma}$ are the Grassman variables [200], and the action S is given by:

$$S = \int_0^{\beta} d\tau\left[\sum_{i,\sigma} c^{\dagger}_{i\sigma}(\tau)\left(\frac{\partial}{\partial\tau} - \mu\right)c_{i\sigma}(\tau) - \sum_{i,j,\sigma} t_{ij}c^{\dagger}_{i\sigma}(\tau)c_{j\sigma}(\tau) + U\sum_{i} c^{\dagger}_{i\uparrow}(\tau)c_{i\uparrow}(\tau)c^{\dagger}_{i\downarrow}(\tau)c_{i\downarrow}(\tau)\right]. \tag{2.30}$$

We proceed by separating the action into three terms: S_0 which contains only the site 0, $S^{(0)}$ for the rest of the lattice, and S_{hyb} containing the hopping terms between the lattice and the site 0.

$$\begin{aligned}
S &= S_0 + S_{hyb} + S^{(0)}\\
S_0 &= \int_0^{\beta} d\tau\left[\sum_{\sigma} c^{\dagger}_{0\sigma}(\tau)\left(\frac{\partial}{\partial\tau} - \mu\right)c_{0\sigma}(\tau) + Uc^{\dagger}_{0\uparrow}(\tau)c_{0\uparrow}(\tau)c^{\dagger}_{0\downarrow}(\tau)c_{0\downarrow}(\tau)\right]\\
S_{hyb} &= -\int_0^{\beta} d\tau \sum_{i\neq 0,\sigma}\left[t_{i0}c^{\dagger}_{i\sigma}(\tau)c_{0\sigma}(\tau) + t_{0i}c^{\dagger}_{0\sigma}(\tau)c_{i\sigma}(\tau)\right] = -\int_0^{\beta} d\tau S_{hyb}(\tau)\\
S^{(0)} &= \int_0^{\beta} d\tau\left[\sum_{i\neq 0,\sigma} c^{\dagger}_{i\sigma}(\tau)\left(\frac{\partial}{\partial\tau} - \mu\right)c_{i\sigma}(\tau) - \sum_{i,j\neq 0,\sigma} t_{ij}c^{\dagger}_{i\sigma}(\tau)c_{j\sigma}(\tau) + U\sum_{i\neq 0} c^{\dagger}_{i\uparrow}(\tau)c_{i\uparrow}(\tau)c^{\dagger}_{i\downarrow}(\tau)c_{i\downarrow}(\tau)\right].
\end{aligned} \tag{2.31}$$

We can now insert Eq. 2.31 into Eq. 2.29, and explicitly separate the integration over the site 0 and the rest of the lattice:

$$\begin{aligned}
\mathcal{Z} = &\int \prod_{\sigma} \mathrm{D}c^{\dagger}_{0\sigma}\mathrm{D}c_{0\sigma}\mathrm{e}^{-S_0} \int \prod_{i\neq 0,\sigma} \mathrm{D}c^{\dagger}_{i\sigma}\mathrm{D}c_{i\sigma}\mathrm{e}^{-S_{hyb}-S^{(0)}}\\
=&\mathcal{Z}_{latt} \int \prod_{\sigma} \mathrm{D}c^{\dagger}_{0\sigma}\mathrm{D}c_{0\sigma}\mathrm{e}^{-S_0}\left\langle \mathrm{e}^{-S_{hyb}}\right\rangle_{latt}
\end{aligned} \tag{2.32}$$

where the second line is obtained by integrating out the rest of the lattice, yielding the thermodynamic average $\langle . \rangle_{latt}$ and the partial partition function $\mathcal{Z}_{latt}$. The exponential $\left\langle \mathrm{e}^{-S_{hyb}}\right\rangle_{latt}$ can be expanded in power series of S_{hyb}, and because it is averaged over the lattice without the 0 site, only the even terms in the expansion are non-zero (since odd terms do not conserve the number of particle in the lattice with site 0 excluded). The partition function is then written:

$$\begin{aligned}\mathcal{Z} = \int \prod_{\sigma} \mathrm{D}c^{\dagger}_{0\sigma}\mathrm{D}c_{0\sigma}\mathrm{e}^{-S_0}\Big[1 + \frac{1}{2!}\int_0^{\beta} d\tau_1 \int_0^{\beta} d\tau_2 \big\langle S_{hyb}(\tau_1)S_{hyb}(\tau_2)\big\rangle_{latt} \\ + \frac{1}{4!}\int_0^{\beta} d\tau_1 \int_0^{\beta} d\tau_2 \int_0^{\beta} d\tau_3 \int_0^{\beta} d\tau_4 \big\langle S_{hyb}(\tau_1)S_{hyb}(\tau_2)S_{hyb}(\tau_3)S_{hyb}(\tau_4)\big\rangle_{latt} + \ldots\Big].\end{aligned} \tag{2.33}$$

In the limit $d \rightarrow \infty$ the expansion of the exponential is drastically simplified thanks to the scaling of the propagators and the hopping terms. This is clearly seen by re-writing for instance the second order term of the expansion:

$$\frac{1}{2!}\int_0^{\beta} d\tau_1 \int_0^{\beta} d\tau_2 \big\langle S_{hyb}(\tau_1)S_{hyb}(\tau_2)\big\rangle_{latt} = -\frac{1}{2!}\sum_{ij\neq 0,\sigma} t_{i0}t_{0j}\int_0^{\beta} d\tau_1 \int_0^{\beta} d\tau_2 G^{(0)}_{ij,\sigma}(\tau_1-\tau_2)c^{\dagger}_{0\sigma}(\tau_1)c_{0\sigma}(\tau_2), \tag{2.34}$$

where $G^{(0)}_{ij,\sigma}$ is the Green's function of the lattice without the site 0, which is defined by:

$$G^{(0)}_{ij,\sigma}(\tau_1-\tau_2) = -\big\langle T_{\tau}c_{i\sigma}(\tau_1)c^{\dagger}_{j\sigma}(\tau_2)\big\rangle_{latt}. \tag{2.35}$$

Similarly to Eq. 2.34, the n^{th} (n even) term involves n hopping terms and a n-particle Green's function $G^{(0)}_{i_1,\ldots,i_n,\sigma}$. In the second order term, the two hopping terms contribute to the scaling as $\propto \frac{1}{d}$, the sums $\propto d^2$, while the Green's function scales as $\propto \frac{1}{d^{\|\mathbf{R_i}-\mathbf{R_j}\|/2}}$. Since $\big\|\mathbf{R_i}-\mathbf{R_j}\big\| \geq 2$ in the second order term, the scaling is overall $\mathcal{O}(1)$. This is different for the fourth order term, which involves four hopping terms $\propto \frac{1}{d^2}$, four sums $\propto d^4$, and a four-particle Green's function $G^{(0)}_{ijkl,\sigma}$ which scales as $\propto \frac{1}{d^{\|\mathbf{R_i}-\mathbf{R_j}\|/2}}\frac{1}{d^{\|\mathbf{R_j}-\mathbf{R_k}\|/2}}\frac{1}{d^{\|\mathbf{R_k}-\mathbf{R_l}\|/2}}$. Hence the scaling is at least $\propto \frac{1}{d}$, such that the fourth order and also all higher order terms are suppressed in infinite dimension. We end up with the effective local DMFT action:

$$\begin{aligned}S_{eff} = \int_0^{\beta} d\tau \sum_{\sigma} c^{\dagger}_{0\sigma}(\tau)\Big(\frac{\partial}{\partial\tau} - \mu\Big)c_{0\sigma}(\tau) + U\int_0^{\beta} d\tau c^{\dagger}_{0\uparrow}(\tau)c_{0\uparrow}(\tau)c^{\dagger}_{0\downarrow}(\tau)c_{0\downarrow}(\tau) \\ + \sum_{ij\neq 0,\sigma} t_{i0}t_{0j}\int_0^{\beta} d\tau_1 \int_0^{\beta} d\tau_2 G^{(0)}_{ij,\sigma}(\tau_1-\tau_2)c^{\dagger}_{0\sigma}(\tau_1)c_{0\sigma}(\tau_2),\end{aligned} \tag{2.36}$$

where all the hopping terms are implicitly rescaled using Eq. 2.15 since we are in the $d \rightarrow \infty$ limit. We now introduce the hybridization function Δ_{σ} and the Weiss field $\mathcal{G}_{\sigma}$ as:

$$\begin{aligned}\Delta_{\sigma}(\tau_1-\tau_2) &= \sum_{ij\neq 0} t_{i0}t_{0j}G^{(0)}_{ij,\sigma}(\tau_1-\tau_2) \\ \mathcal{G}^{-1}_{\sigma}(\tau_1-\tau_2) &= -\delta(\tau_1-\tau_2)\Big(\frac{\partial}{\partial\tau_1} - \mu\Big) - \Delta_{\sigma}(\tau_1-\tau_2). \\ \mathcal{G}^{-1}_{\sigma}(i\omega_n) &= i\omega_n + \mu - \Delta_{\sigma}(i\omega_n)\end{aligned} \tag{2.37}$$

The hybridization function $\Delta_{\sigma}(\tau_1-\tau_2)$ describes the coupling of the impurity electrons to the effective bath. It encodes the propagation of an electron that hops from the impurity to the bath at time τ_2, then propagates through the lattice without the impurity site via the lattice Green's function

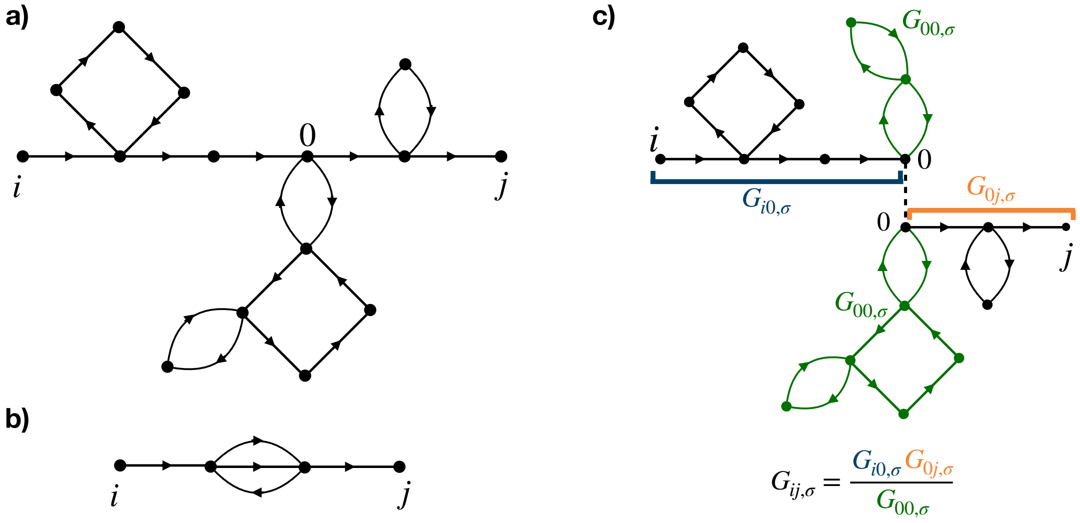

Figure 2.4: Each line of a diagram represents a hopping term, and each vertex a cumulant (which does not scale with dimension). Examples of diagrams that contribute to the Green's function $G_{ij,\sigma}$ at $d \to \infty$ (a), and that vanishes (b). (c) In infinite dimension, the diagrams contributing to $G_{ij,\sigma}$ and that pass by the specific site 0 can be separated into to contributions $G_{i0,\sigma}$ and $G_{0j,\sigma}$, such that $G_{ij,\sigma} \propto G_{i0,\sigma} G_{0j,\sigma}$. One observes that such decomposition induces a double counting of the decorations (in green) on site 0, evaluated to be $G_{00,\sigma}$, which is therefore corrected by writing $G_{ij,\sigma} = \frac{G_{i0,\sigma} G_{0j,\sigma}}{G_{00,\sigma}}$.

$G^{(0)}_{ij,\sigma}(\tau_1 - \tau_2)$, and hops back to the impurity at time τ_1. It therefore allows a time-dependent fluctuation of the electronic density on the impurity. When connected to a bath, the non-interacting Green's function of the impurity electrons, given by Eq. 2.18, is then corrected by the hybridization and yields the Weiss field $\mathcal{G}^{(}_{\sigma} i\omega_n)$, also called bath Green's function.

Using these definitions, the effective action may be written:

$$S_{eff} = -\int_0^{\beta} d\tau_1 \int_0^{\beta} d\tau_2 \sum_{\sigma} c^{\dagger}_{\sigma}(\tau_1) \mathcal{G}^{-1}_{\sigma}(\tau_1 - \tau_2) c_{\sigma}(\tau_2) + U \int_0^{\beta} d\tau c^{\dagger}_{\uparrow}(\tau) c_{\uparrow}(\tau) c^{\dagger}_{\downarrow}(\tau) c_{\downarrow}(\tau), \qquad (2.38)$$

where the subscript $_0$ was removed for readability. Therefore, as advertised above, in $d \to \infty$ the action of the Hubbard model can be exactly mapped onto that of an interacting impurity embedded into an effective bath of electrons. Eq. 2.37 provides the link between the Weiss field $\mathcal{G}_{\sigma}$ and the interacting Green's function $G^{(0)}_{ij,\sigma}$ of the full lattice with one site removed. The last missing element is the relation between $G^{(0)}_{ij,\sigma}$ and $G_{ij,\sigma}$, the Green's function of the original problem.

For this last step, it is convenient to follow the ideas of Metzner in Ref. 46: the Green's function is expanded in perturbation theory over the hopping terms, starting from the atomic limit $U \gg t$. The terms of the expansion can be written as diagrams, for which each line corresponds to a hopping term, and each vertex to a cumulant which does not scale with the dimension. At $d \to \infty$, the only diagrams that contribute to $G_{ij,\sigma}$ are fully two-particle reducible: they connect site i and j via a single line and may have local polygon decorations, as shown in Fig. 2.4(a).

Indeed, we will show that the diagrams which are not fully two-particle reducible, like the one shown in Fig. 2.4(b), give a vanishing contribution to the kinetic energy [46]

$$E_{kin} \propto -\sum_{\langle i,j\rangle,\sigma} t_{ij} G_{ij,\sigma}. \tag{2.39}$$

For simplicity, we consider only the nearest-neighbor hopping (the argument is easily generalized to longer-range hopping terms [46]). Because there are five lines, each corresponding to a hopping term, this diagram scales like $G_{ij,\sigma} \propto d^{-5/2}$. Since i and j are at a distance of 3 sites, $t_{ij} \propto d^{-3/2}$ and there are d^3 terms in the sum. In total, its contribution to the kinetic energy scales as $\propto d^{-1}$ and therefore vanishes at $d \to \infty$. Similarly, one can easily show that any polygon decoration as those shown in Fig. 2.4(a)-(c) contribute as $\mathcal{O}(1)$.

One immediately sees that for each contribution to $G_{ij,\sigma}$ which passes by the specific site 0, the diagram can be separated into two subdiagrams going from i to 0, and from 0 to j, as shown in Fig. 2.4(c). Since the Green's function $G_{ij,\sigma}$ of the full lattice can be obtained by the sum of all the paths avoiding the site 0 ($G^{(0)}_{ij,\sigma}$), and all the contributions explicitly passing by 0 ($\propto G_{i0,\sigma}G_{0j,\sigma}$), then we have [46]:

$$G_{ij,\sigma} = G^{(0)}_{ij,\sigma} + \frac{G_{i0,\sigma}G_{0j,\sigma}}{G_{00,\sigma}} \tag{2.40}$$

where we have divided by $G_{00,\sigma}$ to avoid the double counting of the diagram decorations on site 0 (see Fig. 2.4(c)). Such rescaling by $G_{00,\sigma}$ is necessary since in the decomposition into two subdiagrams the site 0 appears twice, hence all the processes starting and ending at site 0 ($G_{00,\sigma}$) are counted twice. Interestingly, this formula was already used by Hubbard [201]. $G_{00,\sigma}$ is nothing else but the local Green's function of the full lattice G_σ. Combining Eq. 2.40 with 2.37, one can show the relation between the local Green's function of the original problem and the Weiss field [43]:

$$G_\sigma^{-1}(i\omega_n) = \mathcal{G}_\sigma^{-1}(i\omega_n) - \Sigma_\sigma(i\omega_n), \tag{2.41}$$

where Σ_σ is the purely local ($d \to \infty$) self-energy of the full lattice. Using the momentum-dependent Green's function definition, the Weiss field and the self-energy can be directly related:

$$\mathcal{G}_\sigma^{-1}(i\omega_n) = \Sigma_\sigma(i\omega_n) + \sum_{\mathbf{k}} \frac{1}{i\omega_n + \mu - \epsilon_{\mathbf{k}} - \Sigma_\sigma(i\omega_n)}. \tag{2.42}$$

Therefore, with Eqs. 2.38, 2.41 and 2.42, we have a set of self-consistent equations where the only unknown observable is the self-energy Σ_σ. The DMFT self-consistency cycle, illustrated in Fig. 2.5, is as follows:

(i) Start from an initial guess for the self-energy Σ_σ,
(ii) From Eq. 2.42 compute the corresponding Weiss field,
(iii) Construct the effective action with Eq. 2.38,
(iv) Solve the impurity problem for its Green's function $G_{imp,\sigma}$, which is identified to the local Green's function $G_\sigma(i\omega_n)$, and obtain a new self-energy from the Dyson Eq. 2.41,

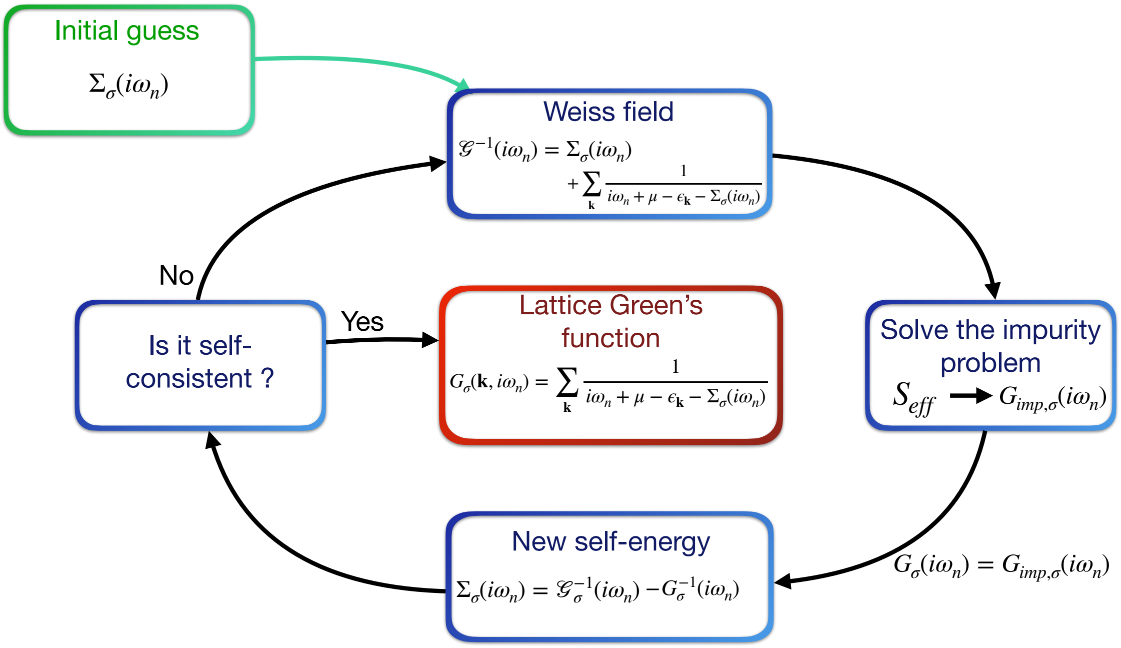

Figure 2.5: Sketch of the DMFT self-consistent equations.

(v) Check for self-consistency, and if needed, iterate again from (ii).

Therefore, until here we have shown how to parameterize the Hubbard model for the simple case of the single-band model. We derived the DMFT self-consistent equations, which provides a way to solve the Hubbard model at infinite dimension while keeping all the dynamic fluctuations. It is important to note that despite the local nature of the self-energy, the lattice Green's function remains momentum dependent via the dispersion relation $\epsilon_{\mathbf{k}}$. In practice, DMFT relies on the approximation that $1/z$ is small, which for 3D systems can be justified but becomes questionable for 2D systems like the CuO planes of cuprates. In fact, for the 2D Hubbard model the non-local fluctuations are essential: even though DMFT can resolve the Mott insulator transition at half-filling since the self-energy is frequency dependent, it overestimates the critical interaction strength U_c at which the transition occurs [48] compared to other methods partially including non-local fluctuations. In order to obtain a correct theoretical description of such systems, generalizations of DMFT to include a part of non-local interactions are therefore needed. One way is to start from the DMFT solution, which accounts well for the local correlations and perform a diagrammatic expansion around the DMFT result [71–73, 76]. In this thesis we rather rely on quantum cluster methods, which are based on generalizing the single-site impurity problem to a cluster impurity either containing multiple sites, or multiple patches in momentum space, and therefore allow to consider non-local self-energies on the length scale of the cluster [52].

2.3 BEYOND LOCAL CORRELATIONS: CLUSTER DYNAMICAL MEAN-FIELD THEORY

Remaining in the mindset of the cavity construction, a natural way to include non-local fluctuations would be to derive the effective action S_{eff} not only for a single-site impurity, but for a cluster of sites. A first step towards this successful method, called cluster dynamical mean-field theory (CDMFT) [49–52], was first proposed by Lichtenstein and Katsnelson [49] who performed a single-site two-orbital LDA+DMFT calculation. Although not being strictly speaking a finite size cluster, the two-orbital system can be thought of as a dimer in real-space in terms of bonding/anti-bonding states. Most importantly, considering a two-orbital system requires to formulate the DMFT equations with matrix-valued functions, just as the "true" CDMFT method whose first implementation was realized shortly afterwards by Lichtenstein and Katsnelson in the study of the interplay between superconductivity and antiferromagnetic fluctuations in the hole-doped 2D Hubbard model using a 2 × 2 plaquette cluster [50]. Soon after, Kotliar *et al.* formally expressed CDMFT in terms of the cavity construction [51].

Translational symmetry requires to construct a superlattice made of the individual clusters, as shown in Fig. 2.6(a). To be consistent, the cluster geometry and tiling has to be chosen such that it reproduces the original lattice. Following the notations of the lecture notes by Sénéchal [202], the position of a site may be written as:

$$\mathbf{r} = \mathbf{R} + \tilde{\mathbf{r}}, \tag{2.43}$$

where $\tilde{\mathbf{r}}$ is the cluster position, and $\mathbf{R}$ the site position inside the cluster (see Fig. 2.6(a)-(b)). The local (matrix-valued) Green's function is obtained by:

$$\mathbf{G}^{-1}_{\mathbf{RR}',\sigma}(i\omega_n) = \sum_{\tilde{\mathbf{k}}} \Big[\big(i\omega_n + \mu - \boldsymbol{\epsilon}_{\tilde{\mathbf{k}}} - \boldsymbol{\Sigma}_\sigma(i\omega_n) \big)^{-1} \Big]_{RR'} \tag{2.44}$$

where $\mathbf{G}_\sigma, \boldsymbol{\Sigma}_\sigma, \boldsymbol{\epsilon}$ are matrix-valued quantities, $\tilde{\mathbf{k}}$ is defined in the reduced BZ of the superlattice (see Fig. 2.6(b)) and corresponds to the Fourier transform with respect to $\tilde{\mathrm{r}}$. The self-energy is *local* on the length-scale of the cluster, i.e. some of the diagonal terms $\Sigma_{ij,\sigma}$ are kept and explicitly calculated within the Anderson impurity model. All the DMFT self-consistent equations remain valid, but should be expressed in terms of matrix-valued functions. Therefore the same self-consistent scheme as the one illustrated in Fig. 2.5 can be used.

However, the division of the original lattice into finite-size clusters leads to a breaking of the original lattice translational symmetry, which can be understood easily by thinking of a 1D chain. Assuming a decomposition of the 1D chain in terms of dimers, say made out of the couples $\langle 2i, 2i+1 \rangle$, then one immediately sees that $\Sigma_{2i,2i+1} \neq 0$ while $\Sigma_{2i+1,2i} = 0$ since the latter is not included in the cluster, as shown in Fig. 2.6(c). In other words, one bond is renormalized by the interactions, while the other is is left bare (i.e. at the non-interacting level). One could thus spark a Peierls gap not necessarily relevant for the system under investigation. For the 2D Hubbard model for instance, it has been shown that it can induce biased CDW [203]. There exist

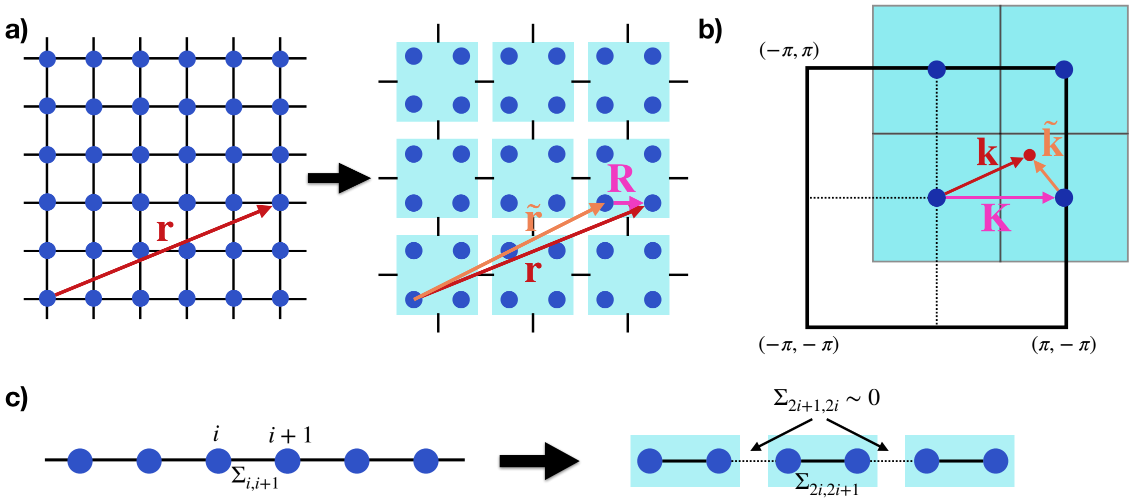

Figure 2.6: (a) Definition of the superlattice for the case of 2×2 plaquette clusters, the definition of the position vectors $\mathbf{r}$, $\mathbf{R}$, and $\tilde{\mathbf{r}}$ (see text) are illustrated. (b) Sketch of the reduced BZ (red squares) on top of the original BZ (black square), and illustration of the momentum vectors $\mathbf{k}$, $\mathbf{K}$, and $\tilde{\mathbf{k}}$. (c) Illustration of the translation symmetry breaking inherent from the clusterization of the lattice.

another successful extension of DMFT which was developed at the same time as CDMFT, called DCA [63–65], which we do not present here. In contrast to CDMFT, it preserves the translational symmetry by considering cluster defined directly in momentum space. However, this comes to the price of averaging the self-energy over patches in momentum space and is therefore a good approximation when the self-energy has a smooth momentum dependence. For phases like the PG in cuprates, which is studied in detail in Chap. 3, this can be a problem if too few patches are chosen since the self-energy has a strong momentum dependence. Moreover, in the study of the correlation effects on the sublattice decoupling in t-CuO, the real-space formulation of CDMFT allows to easily access to the inter- and intra-sublattice components of the self-energy. We therefore adopt the CDMFT framework in this thesis.

The direct consequence of the translational symmetry breaking is that the original lattice Green's function is no longer diagonal in momentum, i.e. $G \to G(\mathbf{k},\mathbf{k}')$. Since by construction the superlattice translation invariance is preserved, then the only off-diagonal elements allowed are the ones sharing the same momentum $\tilde{\mathbf{k}}$ in the superlattice BZ but which differ by the reciprocal superlattice momentum $\mathbf{K}$:

$$G(\mathbf{k},\mathbf{k}',i\omega_n) = G(\tilde{\mathbf{k}}+\mathbf{K},\tilde{\mathbf{k}}+\mathbf{K}',i\omega_n), \tag{2.45}$$

where G is the (scalar) Green's function of the original lattice. This can be directly seen by making the link between the latter $G(\tilde{\mathbf{k}}+\mathbf{K},\tilde{\mathbf{k}}+\mathbf{K}',i\omega_n)$ and the matrix-valued Green's function on the superlattice $\mathbf{G}_{\mathbf{R}\mathbf{R}'}(\tilde{\mathbf{k}},i\omega_n)$. To this aim, we can use the relation [202]:

$$c(\tilde{\mathbf{k}}+\mathbf{K}) = \frac{1}{L}\sum_{\mathbf{K}',\mathbf{R}} \mathrm{e}^{-i\mathbf{R}(\tilde{\mathbf{k}}+\mathbf{K}-\mathbf{K}')}\mathbf{c}_{\mathbf{K}'}(\tilde{\mathbf{k}}), \tag{2.46}$$

where L is the number of cluster sites, $c(\tilde{\mathbf{k}} + \mathbf{K})$ is the annihilation operator for an electron with momentum $\tilde{\mathbf{k}} + \mathbf{K}$, and $\mathbf{c}_{\mathbf{K}'}(\tilde{\mathbf{k}})$ the matrix element $\mathbf{K}'$ of the cluster annihilation operator $\mathbf{c}(\tilde{\mathbf{k}})$. It follows that the original lattice Green's function can be re-written:

$$\begin{aligned} G(\tilde{\mathbf{k}} + \mathbf{K}, \tilde{\mathbf{k}} + \mathbf{K}', i\omega_n) =& \frac{1}{L^2} \sum_{\mathbf{K}_1\mathbf{K}_2,\mathbf{R}\mathbf{R}'} \mathrm{e}^{-i\mathbf{R}(\tilde{\mathbf{k}}+\mathbf{K}-\mathbf{K}_1)} \mathrm{e}^{-i\mathbf{R}'(\tilde{\mathbf{k}}+\mathbf{K}'-\mathbf{K}_2)} \mathbf{G}_{\mathbf{K}_1\mathbf{K}_2}(\tilde{\mathbf{k}}, i\omega_n). \\ =& \frac{1}{L} \sum_{\mathbf{R}\mathbf{R}'} \mathrm{e}^{-i\mathbf{R}(\tilde{\mathbf{k}}+\mathbf{K})} \mathrm{e}^{-i\mathbf{R}'(\tilde{\mathbf{k}}+\mathbf{K}')} \mathbf{G}_{\mathbf{R}\mathbf{R}'}(\tilde{\mathbf{k}}, i\omega_n). \end{aligned} \tag{2.47}$$

Without translational symmetry the relation can not be further simplified. However, since the DOS and the spectral function that we compare to ARPES involves only the diagonal part of the Green's function (see App. A), the so-called periodization procedure [67, 202], in which only the diagonal elements of the lattice Green's function are kept, is justified although still being an approximation. In Eq. 2.47, this amounts to pick the terms with $\mathbf{K} = \mathbf{K}'$:

$$G(\mathbf{k}, i\omega_n) = G(\tilde{\mathbf{k}} + \mathbf{K}, i\omega_n) = \frac{1}{L} \sum_{\mathbf{R}\mathbf{R}'} \mathrm{e}^{-i(\mathbf{R}-\mathbf{R}')\tilde{\mathbf{k}}} \mathbf{G}_{\mathbf{R}\mathbf{R}'}(\tilde{\mathbf{k}}, i\omega_n). \tag{2.48}$$

This equation allows, at the price of neglecting the off-diagonal elements, to relate the translationally invariant lattice Green's function to the super-lattice matrix-valued one.

For a system without translation symmetry breaking this is an efficient way to overcome the CDMFT problem, however it can be questionable when there is, for instance, a long range magnetic ordering, or a CDW. Indeed, Eq. 2.48 restores the translational symmetry in the original lattice and would ignore the possible existence of, say, an antiferromagnetic order. Later in this thesis, we encounter such a situation when studying t-CuO, for which spin polarized CDMFT calculations are performed, and Eq. 2.48 is used to obtain the spectral function that is compared to ARPES. Although t-CuO has been shown to display a long-range antiferromagnetic stripe order [135, 136], the theoretical spectral function obtained with the above periodization procedure is in excellent agreement with the photoemission measurements [134]. The main reason behind is that in photoemission, if the incoming light spot size is larger than the characteristic magnetic correlation length, the measurement averages over the different magnetic configurations possible, similarly to the periodization procedure. This is true for the spectral function, but might be a limitation for other observables, and in such a case a refinement of the procedure to include the eventual symmetry breaking may be needed.

Finally, we presented here the periodization of the Green's function, but it is not the only possibility to restore the translational symmetry. Indeed, since the origin of the problem is that the inter-site self-energy is taken into account for the intra-cluster bonds only, one way would be to periodize the self-energy instead [51]. Yet another proposition is to periodize the cumulant [204]. The three different procedures can be summarized as follows [203]:

$$
\begin{aligned}
G_\sigma(\mathbf{k}, i\omega_n) &= \frac{1}{L}\sum_{\mathbf{R}\mathbf{R}'} \mathrm{e}^{-i(\mathbf{R}-\mathbf{R}')\tilde{\mathbf{k}}}\Big[\big(i\omega_n + \mu - \epsilon(\mathbf{k}) - \boldsymbol{\Sigma}_\sigma(i\omega_n)\big)^{-1}\Big]_{\mathbf{R}\mathbf{R}'}, \\
G^{\Sigma}_\sigma(\mathbf{k}, i\omega_n) &= \left(i\omega_n + \mu - \epsilon(\mathbf{k}) - \frac{1}{L}\sum_{\mathbf{R}\mathbf{R}'} \mathrm{e}^{-i(\mathbf{R}-\mathbf{R}')\tilde{\mathbf{k}}}\big[\boldsymbol{\Sigma}_\sigma(i\omega_n)\big]_{\mathbf{R}\mathbf{R}'}\right)^{-1}, \\
G^{M}_\sigma(\mathbf{k}, i\omega_n) &= \left(\left[\frac{1}{L}\sum_{\mathbf{R}\mathbf{R}'} \mathrm{e}^{-i(\mathbf{R}-\mathbf{R}')\tilde{\mathbf{k}}}\Big[\big(i\omega_n + \mu - \boldsymbol{\Sigma}_\sigma(i\omega_n)\big)^{-1}\Big]_{\mathbf{R}\mathbf{R}'}\right]^{-1} - \epsilon(\mathbf{k})\right)^{-1},
\end{aligned}
\tag{2.49}
$$

where G^{Σ} and G^{M} denote the reperiodized Green's function obtained respectively with the self-energy and the cumulant periodization. The periodized Green's function, self-energy, or cumulant preserve some features of the symmetry breaking in that they are all obtained by neglecting the off-diagonal momentum elements. The main difference comes from their connection to the real Green's function of the lattice $G(\tilde{\mathbf{k}}+\mathbf{K}, \tilde{\mathbf{k}}+\mathbf{K}', i\omega_n)$. When periodizing the Green's function, there is a direct link since the periodized Green's function at $\mathbf{k}$ is simply the diagonal elements of the lattice Green's function at $(\mathbf{k}, \mathbf{k})$. However, if instead the self-energy, or the cumulant are periodized, then the off-diagonal elements are neglected before performing the matrix inversion, leaving the relation between the periodized Green's function and the lattice Green's function unclear. Since in this thesis we mostly use the periodization procedure to study the momentum resolved spectral function, i.e. the imaginary part of the lattice Green's function, we will rather adopt the Green's function periodization (Eq. 2.48).

So far we have presented the theoretical framework of DMFT and CDMFT, as well as the main set of self-consistent equations. Although the self-consistent loop is simple and imply seemingly straightforward relations between the self-energy, Green's function, and Weiss field, in practice the implementation of CDMFT requires a few tricks necessary not to ruin the final result. In the next section, we briefly describe some tips that may be useful for readers interested in the implementation of the CDMFT self-consistent scheme.

2.4 CLUSTER DYNAMICAL MEAN FIELD THEORY: IMPLEMENTATION DETAILS

We review here some of the important details one faces when implementing a CDMFT code. Note that we do not consider here the impurity solver part, but only the set of self-consistent equation, given a solver that already works. We first present the problem of Fourier transforming functions from the Matsubara frequency axis to imaginary time, then we discuss the choice of the starting point for the CDMFT self-consistent calculations, as well as how to chose the chemical potential. Finally we present a simple way to switch to an advantageous basis, which is necessary for the hybridization-expansion [116, 119] CTQMC [60–62] solvers in order to reduce the sign problem.

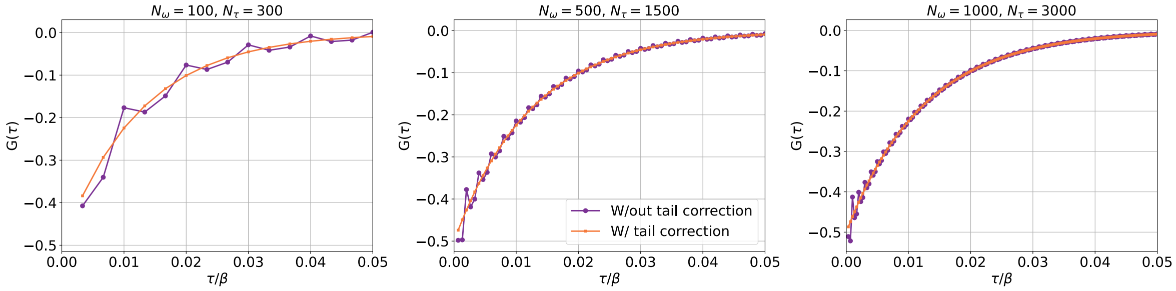

Figure 2.7: Fourier transform of the Green's function defined in Eq. 2.52 using different number of Matsubara frequencies, with and without the high-frequency expansion correction, calculated at $\beta = 40\text{eV}^{-1}$. The number of τ points is always $N_\tau = 3 \times N_\omega$.

2.4.1 FOURIER TRANSFORMATION

If the impurity solver used requires the hybridization function as a function of imaginary time, one faces the problem of Fourier transforming a function from the Matsubara to the imaginary time axis. More generally, the filling can also be obtained from the Green's function at the $\tau \to 0^-$ limit:

$$\begin{aligned} G_{ii}(\tau \to 0^-) &= \lim_{\tau \to 0^-} -\langle T_\tau c_i(\tau) c_i^\dagger(0) \rangle \\ &= \langle c_i^\dagger(0) c_i(0) \rangle \\ &= n_i, \end{aligned} \tag{2.50}$$

where n denotes the filling, which is necessarily checked during the self-consistent cycle.

The Fourier transformation reads

$$G_{ij}(\tau) = \frac{1}{\beta} \sum_{n=-\infty}^{+\infty} \mathrm{e}^{-i\tau\omega_n} G_{ij}(i\omega_n), \tag{2.51}$$

and implies a sum over an infinite number of Matsubara frequencies. The problem is that we have to chose a certain cutoff N for the number of Matsubara frequencies, but the diagonal components of the Green's function decay slowly $G_{ii}(i\omega_n) \propto \frac{1}{i\omega_n}$. A large number of frequency N would then be required to improve the precision, but at the same time one wants to limit as much as possible the number of frequency to keep the impurity solver computational complexity reasonable. In fact, as shown in Fig. 2.7 for the simple Green's function in the Hubbard-I approximation [35]

$$G(i\omega_n) = \frac{1}{i\omega_n - \frac{U^2}{4i\omega_n}}, \tag{2.52}$$

at $\beta = 40\text{eV}^{-1}$, even with a relatively large number of frequencies and τ points, a simple truncation of Eq. 2.51 leads to substantial errors especially around $\tau \simeq 0$, which is an important region in τ space since this is where the filling can be extracted for instance.

A relatively simple solution is to use the high-frequency tail expansion of the Green's function, that will allow to approximate the Green's function beyond the truncated frequencies. The expansion of a component of the Green's function is defined by

$$G_{ij}(i\omega_n) \simeq M_0 + \frac{M_1}{i\omega_n} + \frac{M_2}{(i\omega_n)^2} + \frac{M_3}{(i\omega_n)^3} + \frac{M_4}{(i\omega_n)^4}, \tag{2.53}$$

which we truncated at the fourth order and is valid at large ω_n. The coefficients $M_0, \dots, M_4$ are easily found using regular fitting methods on the last 20 to 30% Matsubara frequencies. The first coefficient M_0 has to be 0, and for a diagonal component the coefficient M_1 should be equal to 1. The later condition can be used to check the accuracy of the high-frequency expansion fit.

The Fourier transform may now be written

$$\begin{aligned} G_{ij}(\tau) =& \frac{1}{\beta} \sum_{n=-N}^{N} \mathrm{e}^{-i\tau\omega_n} G_{ij}(i\omega_n) + \sum_{n=[-\infty,-N[}^{]N,+\infty]} \mathrm{e}^{-i\tau\omega_n} G_{ij}(i\omega_n) \\ \simeq& \frac{1}{\beta} \sum_{n=-N}^{N} \mathrm{e}^{-i\tau\omega_n}\left(G_{ij}(i\omega_n) - \frac{M_1}{i\omega_n} - \frac{M_2}{(i\omega_n)^2} - \frac{M_3}{(i\omega_n)^3} - \frac{M_4}{(i\omega_n)^4}\right) \\ &+ \frac{1}{\beta} \sum_{n=-\infty}^{\infty} \mathrm{e}^{-i\tau\omega_n}\left(\frac{M_1}{i\omega_n} + \frac{M_2}{(i\omega_n)^2} + \frac{M_3}{(i\omega_n)^3} + \frac{M_4}{(i\omega_n)^4}\right). \end{aligned} \tag{2.54}$$

The great advantage of this reformulation is that the second term, which implies a sum over an infinite number of Matsubara frequencies, can be solve analytically (the detailed derivation can be found in the excellent Ref. [205]):

$$\begin{aligned} \frac{1}{\beta} \sum_{n=-\infty}^{\infty} \mathrm{e}^{-i\tau\omega_n} \frac{M_1}{i\omega_n} &= -\frac{M_1}{2} \mathrm{sign}(\tau) \\ \frac{1}{\beta} \sum_{n=-\infty}^{\infty} \mathrm{e}^{-i\tau\omega_n} \frac{M_2}{(i\omega_n)^2} &= \frac{M_2}{4}(2\tau-\beta) \\ \frac{1}{\beta} \sum_{n=-\infty}^{\infty} \mathrm{e}^{-i\tau\omega_n} \frac{M_3}{(i\omega_n)^3} &= \frac{M_3}{4}\tau(\beta-\tau)\mathrm{sign}(\tau) \\ \frac{1}{\beta} \sum_{n=-\infty}^{\infty} \mathrm{e}^{-i\tau\omega_n} \frac{M_4}{(i\omega_n)^4} &= \frac{M_4}{48}(2\tau-\beta)(2\tau^2-2\tau\beta-\beta^2). \end{aligned} \tag{2.55}$$

By inserting these relations in Eq. 2.54, and using the symmetry $G_{ii}(-i\omega_n) = G_{ii}^*(i\omega_n)$ which holds for the diagonal components of the Green's function, one obtains:

$$\begin{aligned} G_{ii}(\tau) =& \frac{2}{\beta} \sum_{n=0}^{N} \Big(\mathrm{Re}[G_{ii}(i\omega_n)] \cos(\omega_n\tau) + \mathrm{Im}[G_{ii}(i\omega_n)] \sin(\omega_n\tau) \\ &+ M_1 \frac{\sin(\omega_n\tau)}{\omega_n} + M_2 \frac{\cos(\omega_n\tau)}{\omega_n^2} - M_3 \frac{\sin(\omega_n\tau)}{\omega_n^3} - M_4 \frac{\cos(\omega_n\tau)}{\omega_n^4} \Big) \\ &- \frac{M_1}{2}\mathrm{sign}(\tau) + \frac{M_2}{4}(2\tau-\beta) + \frac{M_3}{4}\tau(\beta-\tau)\mathrm{sign}(\tau) + \frac{M_4}{48}(2\tau-\beta)(2\tau^2-2\tau\beta-\beta^2). \end{aligned} \tag{2.56}$$

This correction drastically improves the Fourier transform, as is shown in Fig. 2.7: already at $N_\omega = 100$ the result is smooth close to $\tau \simeq 0$ and not noisy as compared to the direct transformation. The high-frequency expansion is therefore a precious trick which allows to significantly reduce the number of Matsubara frequencies. Most importantly, if we showed here an example for the diagonal components of the Green's function, this formalism applies also to the hybridization function, and in fact to other Matsubara functions as long as the first coefficient M_0 is zero. Note that in general the off-diagonal components decay faster at high frequency than the diagonal ones, such that in practice for these elements we use the direct transformation (Eq. 2.51).

Similarly, the electron filling at some site/orbital can be determined from the corresponding diagonal component of the Green's function. Indeed, at $\tau \to 0^-$ Eq. 2.56 reduces to:

$$G_{ii}(\tau = 0^-) = n_i = \frac{M_1}{2} - \frac{M_2}{4}\beta + \frac{M_4}{48}\beta^3 + \frac{2}{\beta}\sum_{n=0}^{N}\left(\mathrm{Re}[G_{ii}(i\omega_n)] + \frac{M_2}{\omega_n^2} - \frac{M_4}{\omega_n^4}\right). \tag{2.57}$$

This relation is extremely useful in practice, especially when the chemical potential has to be adapted during the self-consistency to ensure that the system remains at the desired filling, as we discuss in the following.

2.4.2 INITIALIZATION AND CHOICE OF CHEMICAL POTENTIAL

At half-filling, the U-T phase diagram of the 2D one-band Hubbard model is characterized by a first order metal to insulator transition at low temperature, where a coexistence region is found in which both the metallic and insulating phases are possible solutions [206]. Therefore, in general one must be careful with the initialization of the CDMFT self-consistent loop. An example of possible consequences on the spectral function is discussed later in this thesis, in the study of NaCCOC in Chap. 3.

In our implementation, we find it convenient to initialize the calculation with the self-energy. There is an infinite number of possible choices, but we present here the three we used within this thesis. To start from a metallic solution, the most simple choice is to put all components of the self-energy to zero, such that the initial lattice Green's function is the non-interacting one. For an insulating starting point, the diagonal components for paramagnetic calculations are defined from the Hubbard-I approximation [35]

$$\Sigma_{ii,\sigma} = \frac{U^2}{4i\omega_n}, \tag{2.58}$$

and for spin polarized calculations a spin dependent constant self-energy is used

$$\begin{aligned} \Sigma_{ii,\sigma} &= U/2 \\ \Sigma_{ii,-\sigma} &= -U/2. \end{aligned} \tag{2.59}$$

In both cases, the off-diagonal components are initialized to zero.

Since the chemical potential μ determines the overall filling, to which the properties of the Hubbard model are extremely sensitive, it is crucial to precisely keep track of it during the calculations. In a metallic system, there is no ambiguity on the value of μ, and the latter has to be adapted during the self-consistent cycle to make sure that the system remains at the desired filling. To do so, it is convenient to use the impurity self-energy and calculate the local Green's function at a given μ via

$$\mathbf{G}_\sigma(i\omega_n) = \sum_{\mathbf{k}} \frac{1}{i\omega_n + \mu - \epsilon_{\mathbf{k}} - \mathbf{\Sigma}_\sigma(i\omega_n)} \tag{2.60}$$

and compute the filling using Eq. 2.57. The right μ can be found using a *regula-falsi* method: it is determined iteratively using

$$\mu^{i+1} = \frac{\mu^{i-1}(n^i - n) - \mu^i(n^{i-1} - n)}{n^i - n^{i+1}}, \tag{2.61}$$

until n^i corresponds to the desired filling n.

If the result is expected to be insulating, this method might lead to spurious jumps of μ since it can take any value inside the gap without changing the filling. It is therefore convenient to fix the chemical potential somewhere in the gap, for instance in the middle. As a practical example, when using the insulating spin-polarized initialization (Eq. 2.59), a natural choice for the chemical potential would be $\mu = 0$.

2.4.3 BASIS TRANSFORMATION

Having described general concepts of the implementation, we now turn to a solver specific aspect: the Monte-Carlo sign problem can be greatly reduced in the hybridization-expansion CTQMC solvers when transforming the cluster basis into an advantageous one in which the hybridization function is as diagonal as possible. For specific clusters like the dimer, or the 2 × 2 plaquette, a diagonal basis can be easily found, but for more general cluster such a basis can be difficult to find. Hence it is more convenient to find a suitable basis *on the fly*.

In order to determine it, we diagonalize a constant quantity, instead of the hybridization function at a given frequency. We chose the on-site energy matrix, which can be obtained from the first coefficient M_0 of the high-frequency expansion for each of the component of the inverse of the Weiss field $\mathcal{G}_\sigma^{-1}$, and may be understood in terms of orbital-dependent chemical potential. This quantity is then diagonalized and we obtain the transfer matrix $\mathbf{P}$, from which the hybridization function can be ”diagonalized” at each frequency

$$\tilde{\mathbf{\Delta}}(i\omega_n) = \mathbf{P}^{-1}\mathbf{\Delta}(i\omega_n)\mathbf{P}. \tag{2.62}$$

The interaction tensor $\mathbf{V}_{i,j,k,l}$ must be rotated accordingly. The transformation to the new basis set may be written:

$$\tilde{\mathbf{V}}_{a,b,c,d} = \sum_{i,j,k,l} \mathbf{P}^{-1}_{a,i}\mathbf{P}^{-1}_{b,j}\mathbf{V}_{i,j,k,l}\mathbf{P}_{k,c}\mathbf{P}_{l,d} \tag{2.63}$$

where a, b, c, d are the indices defined in the new diagonal basis. Defining the super-indices $X = (a, b)$, $Y = (c, d)$, $Z = (i, j)$ and $Z' = (k, l)$, the problem reduces to a simple matrix product:

$$\begin{aligned}
\tilde{\mathbf{V}}_{a,b,c,d} &= \sum_{i,j,k,l} \mathbf{P}^{-1}_{a,i}\mathbf{P}^{-1}_{b,j}\mathbf{V}_{i,j,k,l}\mathbf{P}_{k,c}\mathbf{P}_{l,d} \\
\tilde{\mathbf{V}}_{(a,b)(c,d)} &= \sum_{(i,j)(k,l)} \mathbf{T}^{-1}_{(a,b)(i,j)}\mathbf{V}_{(i,j)(k,l)}\mathbf{T}_{(k,l)(c,d)} \\
\tilde{\mathbf{V}}_{XY} &= \sum_{Z,Z'} \mathbf{T}^{-1}_{XZ}\mathbf{V}_{ZZ'}\mathbf{T}_{Z'Y} \\
\tilde{\mathbf{V}}_{XY} &= \left(\mathbf{T}^{-1}\mathbf{V}\mathbf{T}\right)_{XY}
\end{aligned} \tag{2.64}$$

Note that this derivation is general and does not imply any assumption on the form of the intraction tensor.

This concludes the presentation of DMFT and its cluster extension CDMFT. The latter allows to include the non-local fluctuations on short scales, and will prove extremely useful in the study of the undoped and doped phases of NaCCOC and t-CuO. All the formalism has been written in Matsubara imaginary time/frequency, but in principle all the CDMFT equations are valid on the real frequency axis. We chose the Matsubara formulation since the impurity solvers used during this thesis were based on CTQMC [60–62] techniques, which work at finite temperature on the imaginary frequency axis. We use the hybridization-expansion `CT-HYB` [116] solver, and the interaction-expansion `CT-INT` [117], based on the `ALPSCore` libraries [118]. We do not detail here how these solvers work, and instead refer the reader to the review by Gull *et al.* [62], except for the fact that they require the Matsubara imaginary time/frequency formalism. Therefore, in practice we face the problem of obtaining the real-frequency data (that can be compared with the experiments) only from the knowledge on the imaginary frequency axis. This is the subject of the next section.

2.5 ANALYTIC CONTINUATION

The purpose of the analytic continuation is to obtain the value of a function on the real axis given its value on the imaginary axis (frequency, or time), which amounts to:

$$G(i\omega_n) \to G(\omega \pm i\delta) \tag{2.65}$$

where ω denotes real frequencies, and δ is a small parameter used in practice to prevent the discontinuities of the function G on the real axis. As we first briefly show, such a transformation could be done directly by using the Kramers-Kroning relations [207, 208], but is extremely sensitive to noise and is in-fact ill defined. To illustrate that, for the sake of simplicity we consider only the diagonal component of the Green's function for which the spectral function is always positive:

$$A(\omega) = -\frac{1}{\pi}\mathrm{Im}[G(i\omega_n)] \geq 0. \tag{2.66}$$

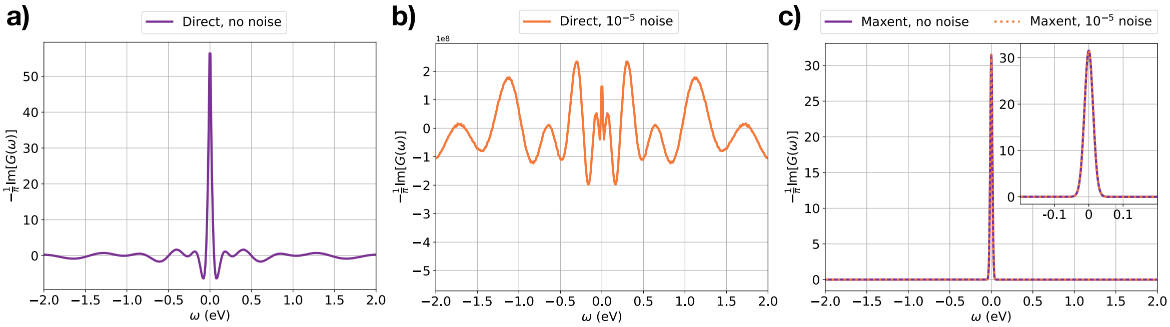

Figure 2.8: Analytic continuation of the Green's function $G(i\omega_n) = \frac{1}{i\omega_n}$ using (a) the direct inversion without noise, (b) the direct inversion with the addition of a random noise of 10^{-5} amplitude, (c) the MEM with and without noise. The *inset* in (c) is a zoom around $\omega = 0$.

In principle, one can formally relate the Green's function on the Matsubara axis to its real axis counterpart using Kramers-Kroning relations [207, 208]:

$$\begin{aligned} G(i\omega_n) =& \frac{1}{\pi}\int_{-\infty}^{+\infty} \frac{\mathrm{Im}[G_{real}(\omega)]}{\omega - i\omega_n} d\omega, \\ =& \frac{1}{\pi i}\int_{-\infty}^{+\infty} \frac{\mathrm{Re}[G_{real}(\omega)]}{\omega - i\omega_n} d\omega, \end{aligned} \tag{2.67}$$

where G_{real} denotes the Green's function on the real axis, and $G(i\omega_n)$ is restricted to $i\omega_n$ in the upper complex plane. However, usually we need to obtain $G_{real}(\omega)$ from $G(i\omega_n)$: Eq. 2.67 must be inverted. To this aim, the integral may be discretized on a frequency mesh $[\omega_1, \dots, \omega_N]$, with N the number of real frequencies:

$$\begin{aligned} G(i\omega_n) &= \lim_{N\to\infty} \sum_{l=1}^{N} \frac{1}{\pi} \frac{\omega_{l+1} - \omega_l}{\omega_l - i\omega_n} \mathrm{Im}[G_{real}(\omega_l)] \\ [\mathbf{G}]_n &= [\mathbf{M} \cdot \mathbf{G}_{real}]_n, \end{aligned} \tag{2.68}$$

where the Green's functions are considered as vectors and the matrix $\mathbf{M}$ is defined by $\mathbf{M}_{ln} = \frac{1}{\pi}\frac{\omega_{l+1}-\omega_l}{\omega_l - i\omega_n}$. Therefore, by inverting this matrix equality, one directly obtains the Green's function on the real axis with the pseudo-inverse of the matrix $\mathbf{M}_{ln}$.

In Fig. 2.8(a) is shown the result obtained from the direct inversion for a simple function $G(i\omega_n) = \frac{1}{i\omega_n}$, which should transform to a delta function on the real frequency axis. We notice many spurious features, although the main delta peak is reproduced. This is linked to the fact that the matrix elements $\mathbf{M}_{ln} = \frac{1}{\pi}\frac{\omega_{l+1}-\omega_l}{\omega_l - i\omega_n}$ vanish for n large, such that the inverse of the matrix $\mathbf{M}^{-1}$ is almost irregular and ill-conditioned. When inverted, it becomes extremely sensitive to small variations in the input $G(i\omega_n)$, which can induce large numerical errors as seen in Fig. 2.8(a). Moreover, in practice we need to perform an analytic continuation of Monte Carlo data, which is noisy and incomplete. The order of magnitude of the noise can be estimated from $\frac{1}{\sqrt{N_{sample}}}$. For a Green's function obtained with $N_{sample} = 10^7$, a quite high accuracy for impurity solvers, the sampling noise can be estimated to $\sim 3\cdot 10^{-4}$, and it would lead to an extremely noisy result using the direct inversion, as shown in Fig. 2.8(b) where a small noise of amplitude 10^{-5} was added to

$G(i\omega_n) = \frac{1}{i\omega_n}$.

Because of the vanishing elements $\mathbf{M}_{ln} = \frac{1}{\pi}\frac{\omega_{l+1}-\omega_l}{\omega_l - i\omega_n}$, the direct inversion is an ill-defined problem. Several methods have been proposed to overcome this issue, such as the Padé approximant [209, 210], the stochastic method [211], or the Nevanlina approach [212]. In this thesis we used methods based on the maximum entropy method (MEM) [213, 214], which we present in the following. This method was first developed for only the diagonal components of the Green's function since it is based on the positivity of the spectral function $A(\omega) = -\frac{1}{\pi}\mathrm{Im}[G_{real}(\omega)]$, such that it is not fully suited for the matrix-valued Green's function. Indeed, the off-diagonal elements are in general not fully positive, and they require a special treatment. Two different strategies to deal with the off-diagonal elements are presented. The first is the ”Poor Man's” matrix procedure, in which the off-diagonal elements are treated apart from the diagonal ones [215, 216]. The second, called maximum quantum entropy method (MQEM), consists in generalizing the MEM to treat directly the matrix-valued function as a whole [217].

2.5.1 MAXIMUM ENTROPY METHOD

A widely used method to perform analytic continuation is the maximum entropy method (MEM) [213, 214], which attempts to overcome the problem of fitting noisy functions on the imaginary axis by regularizing the trial spectral functions with a smooth *default model*. It is first convenient to re-write Eq. 2.67 in imaginary time:

$$\begin{aligned}
G(\tau) =& \frac{1}{\beta}\sum_{-\infty}^{+\infty} \mathrm{e}^{-i\omega_n\tau} G(i\omega_n) \\
=& \frac{1}{\pi}\int_{-\infty}^{+\infty} \mathrm{Im}[G_{real}(\omega)]\left[\frac{1}{\beta}\sum_{-\infty}^{+\infty}\frac{\mathrm{e}^{-i\omega_n\tau}}{\omega - i\omega_n}\right] d\omega \\
=& \frac{1}{\pi}\int_{-\infty}^{+\infty} \mathrm{Im}[G_{real}(\omega)]\frac{\mathrm{e}^{-\tau\omega}}{\mathrm{e}^{-\beta\omega}+1} d\omega \\
=& -\int_{-\infty}^{+\infty} A(\omega)\frac{\mathrm{e}^{-\tau\omega}}{\mathrm{e}^{-\beta\omega}+1} d\omega.
\end{aligned} \tag{2.69}$$

We restrict the discussion here to the diagonal components of the Green's function, for which $A(\omega)$ is purely real and positive. From the knowledge of a spectral function, the Green's function on the imaginary time axis can therefore be calculated by integrating the spectral function weighted by the kernel $K(\tau,\omega) = -\frac{\mathrm{e}^{-\tau\omega}}{\mathrm{e}^{-\beta\omega}+1}$. This is called the back-continuation, and is not ill-conditioned contrary to the direct inversion presented previously.

Assuming that we have a measured Green's function $\bar{G}(\tau)$ from a Monte-Carlo calculation, and a spectral function $A(\omega)$ supposed to reproduce the measured data, the goodness of the fit can be evaluated with the likelihood function

$$\begin{aligned}\chi^2 &= \int_0^\beta \frac{1}{\sigma^2(\tau)}\left|\bar{G}(\tau) - \int_{-\infty}^{+\infty} A(\omega)K(\tau,\omega)d\omega\right|^2 d\tau \\ &= \int_0^\beta \frac{1}{\sigma^2(\tau)}\left|\bar{G}(\tau) - G(\tau)d\omega\right|^2 d\tau,\end{aligned} \tag{2.70}$$

where $\sigma(\tau)$ is a measure of the noise, and $G(\tau)$ is the back-continued Green's function from $A(\omega)$. Using the likelihood function, an optimal spectral function can be searched via a least-square method, but the noise in the measured data will lead to nonphysical results and over-fitting.

In order to avoid that, the proposed spectral function can be simultaneously optimized and regularized by exploiting the Bayesian interference. As mentioned earlier, the spectral function is always positive and is normalized to 1, so that it can be thought of as a probability density. From Baye's theorem we have that for two events a, b, the probability of a given b $P[a|b]$ is:

$$P[a|b] = \frac{P[b|a]P[a]}{P[b]}. \tag{2.71}$$

For the analytic continuation, the event a corresponds to the spectral function $A(\omega)$, and b to the measured Green's function $\bar{G}(\tau)$. $P[A|\bar{G}]$ can therefore be interpreted as the probability that $A(\omega)$ is the true spectral function given the measured $\bar{G}(\tau)$. Similarly, $P[\bar{G}|A]$ is the probability that $\bar{G}(\tau)$ is the right measured function given the spectral function, i.e. it is related to the likelihood function χ^2. Taking $P[\bar{G}]$ as a constant that can not be improved within the continuation process, we have:

$$P[A|\bar{G}] \propto P[\bar{G}|A]P[A]. \tag{2.72}$$

The MEM consists in maximizing the probability $P[A|\bar{G}]$ by searching for a spectral function that maximized the product $P[\bar{G}|A]P[A]$.

$P[\bar{G}|A]$ is connected to the likelihood function, and it can be shown that [213, 214]

$$P[\bar{G}|A] \propto \mathrm{e}^{-\frac{\chi^2}{2}}, \tag{2.73}$$

so that $P[\bar{G}|A]$ is maximized by minimizing the likelihood function. As stated above, focusing only on this procedure would lead to nonphysical results due to the noise. In order to restrict the possible spectral functions, a *smooth* default model $D(\omega)$ can be defined and used as a reference for the spectral function by defining the following entropy:

$$S = -\int A(\omega)\ln\left(\frac{A(\omega)}{D(\omega)}\right)d\omega. \tag{2.74}$$

This is a useful quantity in the sense that it measures how ”far” is the spectral function from the noise-free default model which is constructed from the prior knowledge of the expected characteristics of the spectral function on the real axis. $P[A]$ is related to this entropy via [213, 214]

$$P[A] \propto \mathrm{e}^{\alpha S}, \tag{2.75}$$

where α is a constant introduced to weight $P[A]$ with respect to $P[\bar{G}|A]$, i.e. α controls how much the final spectral function should resemble the default model since the entropy is maximum when $A(\omega) = D(\omega)$. Finally, we have

$$P[A|\bar{G}] \propto \mathrm{e}^{-\frac{\chi^2}{2}+\alpha S}, \tag{2.76}$$

such that the search of the best $A(\omega)$ given the measured $\bar{G}(\tau)$ consists of a combined minimization of the likelihood function χ^2 and maximization of the entropy S.

It is clear from Eq. 2.76 that the final result of the probability maximization will depend on the value of α, with the two limiting cases being:

(i) $\alpha = 0$, the procedure only relies on the least-square fitting procedure and is noise sensitive,
(ii) $\alpha \to \infty$, the spectral function is equal to the default model.

Different methods have been proposed to chose the optimal α: the *classic* MEM selects the α which maximizes the probability $P[\alpha|\bar{G}]$ [214], or the *Bryan's* method which consists of a weighted average over different spectra calculated for a range of α [218]. Recently, another approach has been proposed in which the likelihood function $\chi^2[\alpha]$ is calculated for a range of α, and the optimal choice is determined at the maximum curvature of $\log\chi^2[\log\alpha]$ [219].

In Fig. 2.8(c) is shown the resulting spectral function for the Matsubara Green's function $G(i\omega_n) = \frac{1}{i\omega_n}$ obtained with MEM using the `MaxEnt` code [220] with the *Bryan's* method [218]. We use a default flat model, and the noise $\sigma(\tau)$ was set to 10^{-5}. A clear improvement is obtained compared to the direct inversion method, especially when inserting a random numerical noise in the ”measured” Matsubara Green's function. This is, of course, an extremely simple function and for more involved functions the result of the MEM can be (severely) parameter dependent: the choice of the α range, of how to chose the optimal α, which default model is used, etc. Nevertheless, the analytic continuation remains mandatory when using Quantum Monte Carlo methods, and in this context MEM brought a valuable improvement.

Note that the MEM can also be applied to the self-energy, which is convenient to directly obtain the momentum-resolved Green's function, or the periodized Green's function on the real frequency axis. To this aim, the self-energy has to be transformed into a Green's function-like quantity, and again here we restrict the discussion to the diagonal components. A simple approach can be to simply correct the high-frequency tail of the self-energy so that it has the correct $\frac{1}{i\omega_n}$ behavior:

$$\Sigma^{aux}(i\omega_n) = \frac{\Sigma(i\omega_n) - \Sigma(\infty)}{M_1}, \tag{2.77}$$

where $\Sigma(\infty)$ is the asymptotic value of the self-energy at $\omega_n \rightarrow \infty$, and M_1 is the first coefficient of the high frequency expansion:

$$\Sigma(i\omega_n) \simeq \Sigma(\infty) + \frac{M_1}{i\omega_n} + \frac{M_2}{(i\omega_n)^2} + \dots \tag{2.78}$$

$\Sigma^{aux}(i\omega_n)$ behaves like a Green's function and can therefore be continued using the MEM. The true self-energy is recovered by transforming back directly on the real frequency axis with the coefficients M_1 and $\Sigma(\infty)$. Another method that we have used for the spectral function of t-CuO is to construct an auxiliary Green's function from the self-energy:

$$G^{aux} = \frac{1}{i\omega_n - \Sigma(i\omega_n) + C}, \tag{2.79}$$

where C is a constant shift. The analytic continuation is performed for G^{aux} and the self-energy is recovered by inverting the previous equation directly on the real axis.

2.5.2 DEALING WITH MATRIX-VALUED FUNCTIONS: ELEMENT-WISE CONTINUATION

When using CDMFT we face the problem that not only the diagonal elements, but also the off-diagonal ones have to be analytically continued to the real axis. The MEM procedure described above can not straightforwardly be applied to the off-diagonal components since, contrary to their diagonal counterparts, they are not fully positive, preventing the use of the entropy in Eq. 2.74. One possible way is to transform the Green's function (or self-energy) to a favorable basis set in which it is almost diagonal and in which the off-diagonal elements can be neglected. The diagonal elements are continued separately, and the function can be rotated back. However, because of the systematic error of the MEM, the result becomes at least basis-dependent and it can even lead to causality problems when rotated back to the original basis (the rotation matrix is no longer suited for the continued quantity). Another strategy is based on the mixing of the off-diagonal elements with the diagonal ones already continued, so to create new fictitious positive spectral functions [221]. The limitation comes from the fact that already continued spectral functions enter the calculation for the off-diagonal components. In this thesis, we have used two different ways to go beyond these two procedures, a first in which each element of the matrix are treated separately with a modified entropy and specific default model for the off-diagonal elements, and a second one in which the entropy is redefined to perform the continuation on the whole matrix.

The "Poor Man's" matrix procedure [215, 216] is implemented within the TRIQS package [120]. The diagonal components are treated separately with the usual MEM described above. In order to treat the off-diagonal elements, the spectral function for each element A can be divided into two positive functions A^+ and A^-:

$$A(\omega) = A^+(\omega) - A^-(\omega). \tag{2.80}$$

The default model is accordingly separated into two parts $D^+(\omega)$, $D^-(\omega)$ and the modified entropy reads [215]:

$$S^{\pm} = \int \left[A^+(\omega) - D^+(\omega) - A^+(\omega) \ln \frac{A^+(\omega)}{D^+(\omega)} + A^-(\omega) - D^-(\omega) - A^-(\omega) \ln \frac{A^-(\omega)}{D^-(\omega)} \right] d\omega, \tag{2.81}$$

which is equivalent to Eq. 2.74. The MEM consists in maximizing the function

$$-\frac{\chi^2(A = A^+ - A^-)}{2} + \alpha S(A^+, A^-), \tag{2.82}$$

in which we note that the likelihood function depends only on the difference between $A^+(\omega)$ and $A^-(\omega)$. The maximization must therefore be done under the constraint $A(\omega) = A^+(\omega) - A^-(\omega)$, which is reached when [215]:

$$\begin{aligned} A^+(\omega) &= \frac{\sqrt{A(\omega)^2 + 4D^+(\omega)D^-(\omega)} + A(\omega)}{2} \\ A^-(\omega) &= \frac{\sqrt{A(\omega)^2 + 4D^+(\omega)D^-(\omega)} - A(\omega)}{2}. \end{aligned} \tag{2.83}$$

The entropy $S^{\pm}$ can then be transformed to [215]:

$$\begin{aligned} S^{\pm} = \int \Bigg[& \sqrt{A(\omega)^2 + 4D^+(\omega)D^-(\omega)} - D^+(\omega) - D^-(\omega) \\ & - A(\omega) \log \frac{\sqrt{A(\omega)^2 + 4D^+(\omega)D^-(\omega)} + A(\omega)}{2D^+(\omega)} \Bigg] d\omega. \end{aligned} \tag{2.84}$$

In practice, the diagonal elements are first continued so to obtain the set of $\{A_{ii}\}$, which are then used to construct the default models for the off-diagonal elements

$$\mathbf{D}_{ij}(\omega) = \sqrt{\mathbf{A}_{ii}(\omega)\mathbf{A}_{jj}(\omega)} + \delta, \tag{2.85}$$

where δ is a small non-zero constant to prevent the default model from being zero. This choice of default model, instead of a flat one, has shown to improve the results [215].

An example is shown in Fig. 2.9(a)-(b), where the analytic continuation of the self-energy of an isolated dimer cluster is performed with the Poor Man's method [215, 216], and compared to the exact result [222]. The two sites are connected with the hopping term $t = 0.4$eV, and the on-site Coulomb term is $U = 3.5$eV. The self-energy was transformed to an auxiliary Green's function following Eq. 2.79, and then continued element-wise. Note that the results depend on the choice of the constant C, which can sometimes drastically determine the final result. For this specific example, the two poles of the exact self-energy are well reproduced, although a spurious shoulder can be noticed in the occupied region in Fig. 2.9. Most interestingly, the off-diagonal part of the self-energy is well captured by the Poor Man's method, so that the resulting local Green's function is in fair agreement with the exact result.

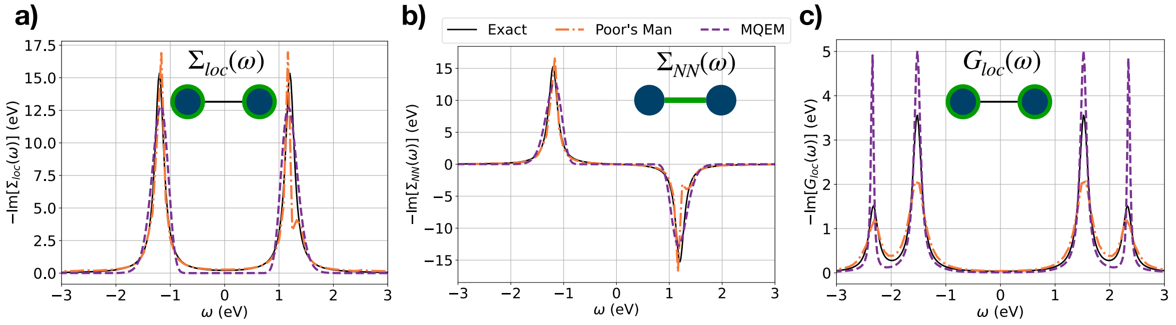

Figure 2.9: (a)-(b) Analytic continuation of the diagonal and the off-diagonal elements of the isolated dimer's self-energy, compared with the exact result [222]. The analytic continuation is performed with the MQEM and with the Poor Man's methods. For the latter the self-energy was transformed to an auxiliary Green's function following Eq. 2.79. (c) Corresponding local Green's function obtained from the self-energy on the real axis.

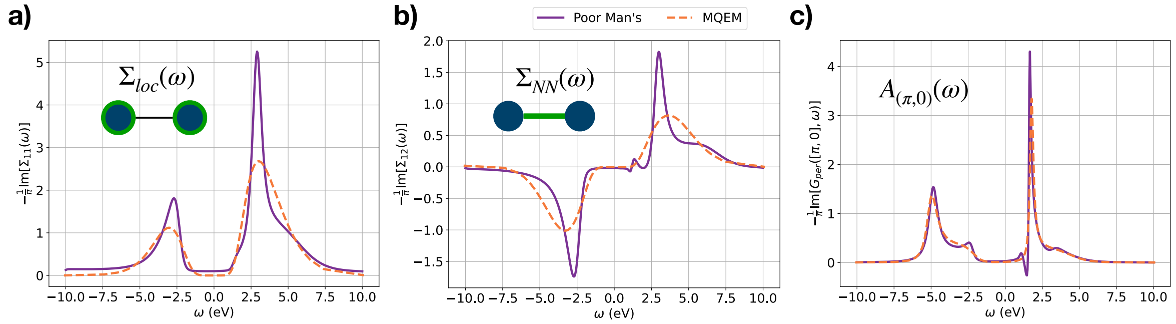

Figure 2.10: (a)-(b) Analytic continuation of the diagonal and the off-diagonal elements of a dimer cluster calculated within CDMFT and parameterized for t-CuO. The analytic continuation is performed with the MQEM and with the Poor Man's methods. For the latter the self-energy was transformed to an auxiliary Green's function following Eq. 2.79. (c) Corresponding spectral function at $\mathbf{k} = (\pi, 0)$ obtained by periodizing the Green's function directly in real frequency using the continued self-energy. Note the non-causality of the Poor's Man method in the positive frequency region.

In a more complicated situation however, treating the off-diagonal elements of the self-energy separately can lead to non-causality issues when applying the Dyson equation to obtain the Green's function, due to the systematic error of the MEM method. This is illustrated in Fig. 2.10, where is shown the analytic continuation for a dimer self-energy obtained with CDMFT for a single-band Hubbard model parameterized for t-CuO. Although there is no sign of non-causality in the local self-energy obtained with the Poor's Man method in Fig. 2.10(a), the spectral function at $\mathbf{k} = (\pi, 0)$ shows a negative weight in the occupied part, as shown in Fig. 2.10. In contrast, the MQEM method that we describe hereafter ensures the causality by a simultaneous treatment of the self-energy (Green's function) matrix.

2.5.3 DEALING WITH MATRIX-VALUED FUNCTIONS: MAXIMUM QUANTUM ENTROPY METHOD

The principle of maximum quantum entropy method (MQEM) [217] is still based on a probability maximization procedure, but a new definition for the entropy is introduced which is defined for matrix-valued functions. MQEM is therefore free of basis-dependence, as well as non-causality issues. The new entropy is defined by generalizing Eq. 2.74 to matrix-valued spectral function and default models [217]:

$$S = \int \mathrm{Tr}\mathbf{A}(\omega)[\ln \mathbf{A}(\omega) - \ln \mathbf{D}(\omega)]. \tag{2.86}$$

The likelihood function can also be extended to matrix-valued functions, and the rest of the procedure is similar to the MEM method.

The default model is matrix-valued, and is constructed from the coefficients of the high-frequency tail expansion of each element of the input Green's function:

$$\mathbf{G}(i\omega_n) = \frac{\mathbf{M}_0}{i\omega_n} + \frac{\mathbf{M}_1}{(i\omega_n)^2} + \ldots \tag{2.87}$$

where $\mathbf{M}_i = \int \omega^i \mathbf{A}(\omega) d\omega$ is the ith moment of the spectral function. In the case of a self-energy, one can easily transform it into a Green's function respecting such high-frequency expansion by using Eq. 2.78. Sim *et al.* proposed to find the default model which maximizes

$$S_D = \int \mathbf{D}(\omega) \ln \mathbf{D}(\omega) d\omega, \tag{2.88}$$

with the constraint

$$\mathbf{M}_i = \int \omega^i \mathbf{D}(\omega) d\omega. \tag{2.89}$$

Restricting the constraint to the first three moments leads to the stationarity condition:

$$\mathbf{D}(\omega) = \mathrm{e}^{\sum_{i=0}^{2} \lambda_i \omega^i} \tag{2.90}$$

where λ_i is a Lagrange multiplier introduced to enforce the constraint.

In Fig. 2.9 is shown the result for the isolated dimer self-energy which is good agreement with the Poor Man's method and the exact result. Both the local and NN components of the self-energy are well reproduced, and the local Green's function exhibits the expected four peak structure at the right frequencies. Note that the two methods seem to underestimate the difference in peak height between the outer and inner peaks.

In Fig. 2.10 is shown the analytic continuation using the MQEM method for the t-CuO dimer cluster. The results are in good agreement with the Poor's Man method, although some features seem washed out. Most importantly, the spectral function's causality is ensured in the whole frequency range by the simultaneous treatment of the matrix-valued functions, as can be seen in Fig. 2.10(c).

2.6 AN EFFECTIVE SPIN MODEL FOR LIGHTLY DOPED CUPRATES

DMFT and CDMFT are powerful techniques to treat exactly a part of the electron-electron interactions, either fully at the local level, or at some finite length scale. If they have been successful for studying various properties of the Hubbard model, like the Mott-insulator transition [43] or the *d*-wave superconductivity [50, 52], it remains extremely difficult to extract the underlying mechanisms. For instance, while *d*-wave superconductivity has been shown to exist in the 2D Hubbard model [50, 52, 145–148, 223], its origin remains elusive. Different strategies exist, which aim at interpreting the results by identifying the key ingredient(s) responsible for the studied feature. An example is the recently developed fluctuation-diagnostic, which allows to analyze the self-energy by a decomposition into different channels by using two-particle quantities [112, 113]. Although powerful and versatile, this method requires the computationally challenging calculation of two-particle quantities. Another strategy is to construct simpler effective models designed to capture only the relevant physics, and to be easier to solve as well as to interpret. We present here such an effective spin model, which is expected to capture at least partially the physics of undoped and lightly-doped cuprates.

Typical values of on-site interaction for cuprates are relatively large, of the order $U \sim 8-10t$. Although U is of the same order than the bandwitdth $W \simeq 8t$ (for a 2D square lattice), the ground state of the half-filled single-band Hubbard model can be approximated by a state consisting of singly-occupied sites. It is well described by an effective t-J model in which states with double-occupations are projected out [224–226]. The kinetic term is restricted to the hopping processes that do not create a double occupancy, and the Coulomb on-site interaction term is transformed into an Heisenberg exchange interaction between neighboring electrons mediated by the coupling $J \simeq 4t^2/U$. Considering for now the case with only NN hopping, the Hamiltonian reads

$$H_{t-J} = -t \sum_{\langle ij \rangle,\sigma} \tilde{c}^{\dagger}_{i\sigma}\tilde{c}_{j\sigma} + J \sum_{\langle ij \rangle} \Big(\mathbf{S}_i \mathbf{S}_j - \frac{1}{4} \mathrm{n}_i \mathrm{n}_j \Big), \tag{2.91}$$

where $\tilde{c}^{\dagger}_{i\sigma}, \tilde{c}_{i\sigma}$ are the restricted creation/annihilation operators to prevent from double occupancy $\tilde{c}^{\dagger}_{i\sigma} = c^{\dagger}_{i\sigma}(1 - n_{i-\sigma})$, and $\mathbf{S}_i$ is the spin operator on site i [224–226]. For simplicity, the spin exchange is assumed isotropic, but this does not restrict the generality of the method.

At half-filling, we can notice that the kinetic term vanishes since it is impossible for an electron to hop without generating a double occupancy. Therefore the ground state corresponds to the one of the Heisenberg model. The determination of the spectral function is however non trivial: initially a hole is created, and will propagate through the lattice since it can hop to neighboring sites without generating double occupancies. The hole is dressed by the antiferromagnetic spin fluctuations, and forms a spin polaron [95, 227–229], similarly to an electron/hole coupled to phonons [230, 231]. Interestingly, if there is a single spin polaron, the spectral function can be approximated by an analytical formula which allows to compute it directly on the real axis and at the thermodynamic limit [95]. To show that, the kinetic part of the Hamiltonian is rewritten as a coupling term between spinless holes and spin operators, and the spin fluctuations are treated as spin waves. This provides a Hamiltonian describing a hole coupled to magnons, whose self-energy can be approximated using the self-consistent Born approximation (SCBA) [232, 233]. Since we consider a single hole (we neglect the hole-hole coupling), the method is expected to hold for low doping values, and should quickly break down as more holes are introduced. A clear advantage of the SCBA is that it is computationally cheap, and allows to easily treat systems at the thermodynamic limit, thus free from finite size effects. Note that SCBA is not the only possibility to calculate the hole propagation in an antiferromagnetic background. For instance, a successful recent development is the parton theory [227–229] in which the spin polaron is regarded as the bound state of a spinon and a holon. We however restrict our work to the simple framework of SCBA which will show to be sufficient to interpret the theoretical and experimental spectral functions, and which can be thought of as an approximation to the more involved treatments as the parton theory.

The first step is to re-write the spin operators as bosonic operators using the Holstein-Primakoff transformation [234] (for half-integer spins):

$$\begin{aligned} S_i^+ &= \sqrt{1-\mathrm{a}_i^\dagger \mathrm{a}_i}\,\mathrm{a}_i \sim \mathrm{a}_i\,, \\ S_i^- &= \mathrm{a}_i^\dagger\sqrt{1-\mathrm{a}_i^\dagger \mathrm{a}_i} \sim \mathrm{a}_i^\dagger, \\ S_i^z &= \frac{1}{2} - \mathrm{a}_i^\dagger \mathrm{a}_i \end{aligned} \tag{2.92}$$

where $\mathrm{a}_i^\dagger, \mathrm{a}_i$ are Bose operators, and the linear approximation is used. Then, the fermionic operators $\mathrm{c}_{i\uparrow}, \mathrm{c}_{i\downarrow}$ are decomposed to define the spinless hole operator:

$$\begin{aligned} \mathrm{c}_{i\uparrow} &= \mathrm{h}_i^\dagger, \\ \mathrm{c}_{i\downarrow} &= \mathrm{h}_i^\dagger S_i^+. \end{aligned} \tag{2.93}$$

As defined, there is a discrepancy between the local fermion Hilbert space, composed of 3 states $|0\rangle$ $|\uparrow\rangle$, $|\downarrow\rangle$ and the local spin-hole Hilbert space which is composed of the four product states $|0,\uparrow\rangle$, $|1,\uparrow\rangle$, $|0,\downarrow\rangle$, $|1,\downarrow\rangle$. This can be cured by noting that there can not be on the same site a hole and a down spin state from the definition of $\mathrm{c}_{i\downarrow} = \mathrm{h}_i^\dagger S_i^+$, and may be directly taken into account in the SCBA. The constraint on the double occupation is automatically fulfilled:

$$\tilde{\mathrm{c}}_{i\uparrow}^\dagger|\downarrow\rangle = (1-\mathrm{n}_{i\downarrow})\mathrm{c}_{i\uparrow}^\dagger|\downarrow\rangle = 0 \tag{2.94}$$

since $\mathrm{h}_i\,|0,\downarrow\rangle = 0$.

From this definition, Eq. 2.91 may be written in terms of hole and bose operators:

$$H_{t-J} = -t\sum_{\langle ij\rangle}\left(\mathrm{h}_i\,\mathrm{h}_j^\dagger \mathrm{a}_j + h.c.\right) + \frac{J}{4}\sum_{\langle ij\rangle}\mathrm{h}_i\,\mathrm{h}_i^\dagger\left(\mathrm{a}_i\,\mathrm{a}_j + \mathrm{a}_i^\dagger \mathrm{a}_j^\dagger + \mathrm{a}_i^\dagger \mathrm{a}_i + \mathrm{a}_j^\dagger \mathrm{a}_j\right)\mathrm{h}_j\mathrm{h}_j^\dagger + \text{const.} \tag{2.95}$$

The first term describes the hopping of the hole which simultaneously couples with the spin degree of freedom. In the second term, the factors $\mathrm{h}_i\,\mathrm{h}_i^\dagger$ and $\mathrm{h}_j\mathrm{h}_j^\dagger$ ensure the loss of magnetic energy by the presence of holes inside the lattice. As it is, the second term is non-trivial and prevents from solving the model directly. It can approximated in a mean-field fashion: the hole operators are replaced by their mean-field average, thus transforming to a factor $(1-\delta)^2$ where δ is the concentration of holes. This amounts to take into account the hole doping as a simple damping of the magnon dispersion by a factor $(1-\delta)^2$. An additional difficulty arising from the second term, even within the mean-field approximation, is that it does not conserve the number of bosonic paricles. This may be solved by applying a Bogoliubov transformation, after having performed a Fourier transform [95]. The Hamiltonian transforms into:

$$H_{t-J} = \frac{zt}{\sqrt{N}} \sum_{\mathbf{k},\mathbf{q}} \left[\mathrm{h}_{\mathbf{k}} \mathrm{h}^{\dagger}_{\mathbf{k}-\mathbf{q}} \alpha_{\mathbf{q}} (u_{\mathbf{q}} \gamma_{\mathbf{k}-\mathbf{q}} + v_{\mathbf{q}} \gamma_{\mathbf{k}}) + h.c. \right] + \sum_{\mathbf{q}} \omega_{\mathbf{q}} \alpha_{\mathbf{q}} \alpha^{\dagger}_{\mathbf{q}}, \tag{2.96}$$

where $\gamma_{\mathbf{k}} = \frac{1}{2}(cos(k_x) + cos(k_y))$ is the usual dispersion of a square lattice, z is the coordination number, $\omega_{\mathbf{q}} = SzJ(1-\delta)^2 \nu_{\mathbf{q}}$ is the magnon dispersion with $\nu_{\mathbf{q}} = \sqrt{1-(\gamma_{\mathbf{q}})^2}$. $\alpha_{\mathbf{q}}, \alpha^{\dagger}_{\mathbf{q}}$ are defined via the Bogoliubov transformation as

$$\begin{aligned} \alpha_{\mathbf{q}} &= u_{\mathbf{q}} \mathrm{a}_{\mathbf{q}} - v_{\mathbf{q}} \mathrm{a}^{\dagger}_{-\mathbf{q}} \\ u_{\mathbf{q}} &= \left(\frac{1+\nu_{\mathbf{q}}}{2\nu_{\mathbf{q}}} \right)^{\frac{1}{2}} \\ v_{\mathbf{q}} &= -\mathrm{sign}(\gamma_{\mathbf{q}}) \left(\frac{1-\nu_{\mathbf{q}}}{2\nu_{\mathbf{q}}} \right)^{\frac{1}{2}}. \end{aligned} \tag{2.97}$$

Eq. 2.96 now has the simple form of a propagating hole which couples to the spin degree of freedom with the coupling $M_{\mathbf{k},\mathbf{q}} = (u_{\mathbf{q}} \gamma_{\mathbf{k}-\mathbf{q}} + v_{\mathbf{q}} \gamma_{\mathbf{k}})$. An important difference with the usual electron-phonon coupling has to be noted at this stage: in the case of a spin polaron, there is no bare kinetic term for the hole, its motion is entirely controlled by the coupling to the spins with a bandwidth on the scale of J. Therefore the usual picture of mass enhancement due to the coupling of "free" particles to phonons, i.e. in a weak-coupling regime, does not apply here. We face a strong-coupling problem since the hopping t is larger than the exchange coupling J, such that the dominating term in Eq. 2.96 is the coupling between the hole and the spin excitations.

The absolute value of the coupling $M_{\mathbf{k},\mathbf{q}}$ is shown in Fig. 2.11: at all k points it vanishes at $\mathbf{q} = (0,0)$ and $\mathbf{q} = (\pi,\pi)$, so it is the short-wavelength spin fluctuations that are important. While at $\mathbf{k} = (0,0)$ and $\mathbf{k} = (\pi,\pi)$ the coupling is relatively small at all $\mathbf{q}$, it shows a strong momentum dependence for $\mathbf{k} = (\pi,0)$ and $\mathbf{k} = (\frac{\pi}{2}, \frac{\pi}{2})$, i.e. in the region showing the largest spectral weight in the hole's spectral function which is discussed later in this section. Note that here $\mathbf{q}$ and $\mathbf{k}$ are both defined in the lattice BZ.

An analytic solution to this Hamiltonian can be obtained using the SCBA [95, 232, 233], from which the following self-energy can be derived:

$$\Sigma(\mathbf{k},\omega) = \frac{z^2 t^2}{N} \sum_{\mathbf{q}} \frac{|M_{\mathbf{k},\mathbf{q}}|^2}{\omega - \omega_{\mathbf{q}} - \Sigma(\mathbf{k}-\mathbf{q}, \omega - \omega_{\mathbf{q}}) + i\eta}, \tag{2.98}$$

where η is a small broadening number. The hole's Green's function is then given by:

$$G^h(\mathbf{k},\omega) = \frac{1}{\omega - \Sigma(\mathbf{k},\omega) + i\eta}. \tag{2.99}$$

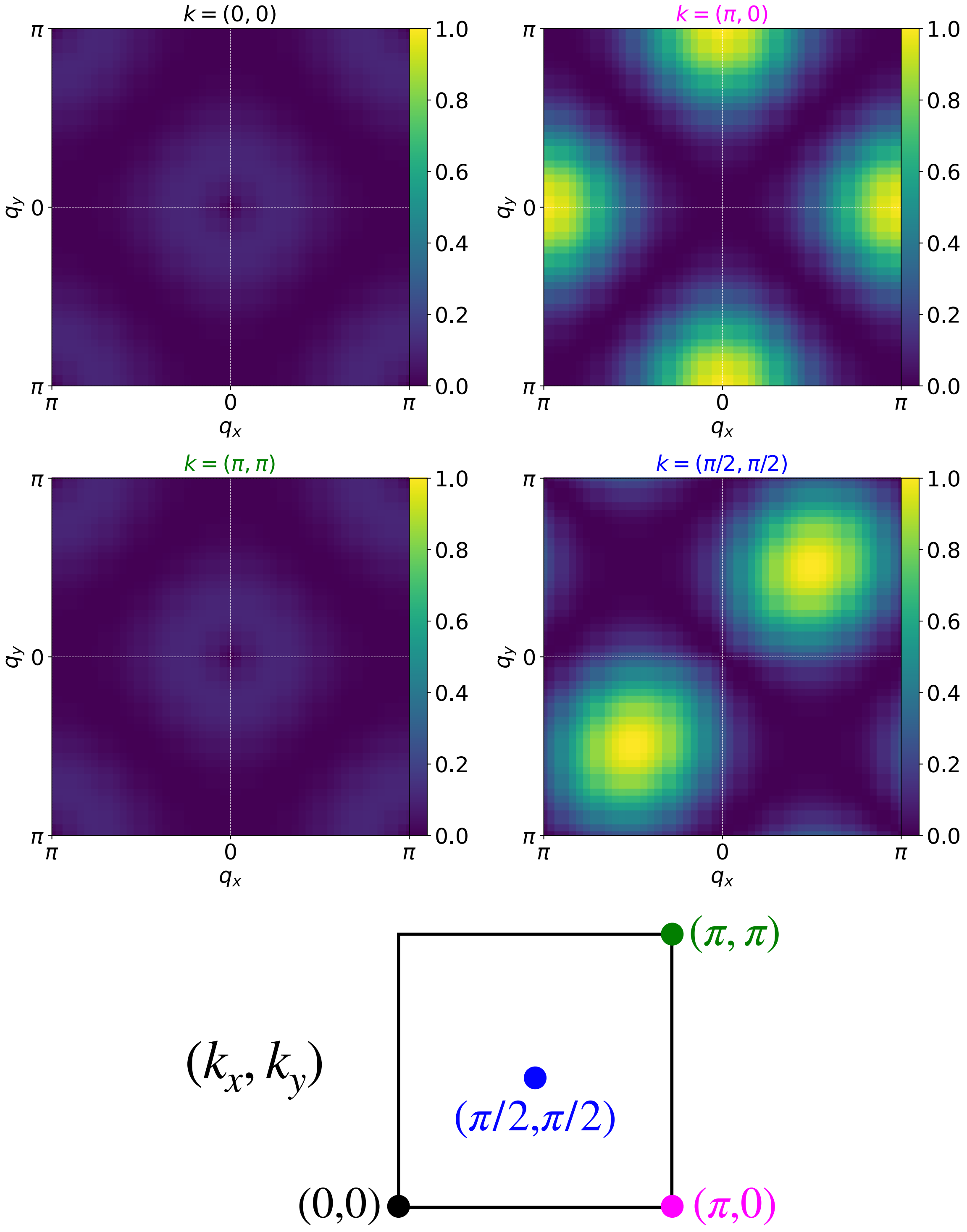

Figure 2.11: Absolute value of the coupling function $|M_{\mathbf{k},\mathbf{q}}|$ calculated as a function of $\mathbf{q}$ at different $\mathbf{k}$ points represented on the BZ sketch.

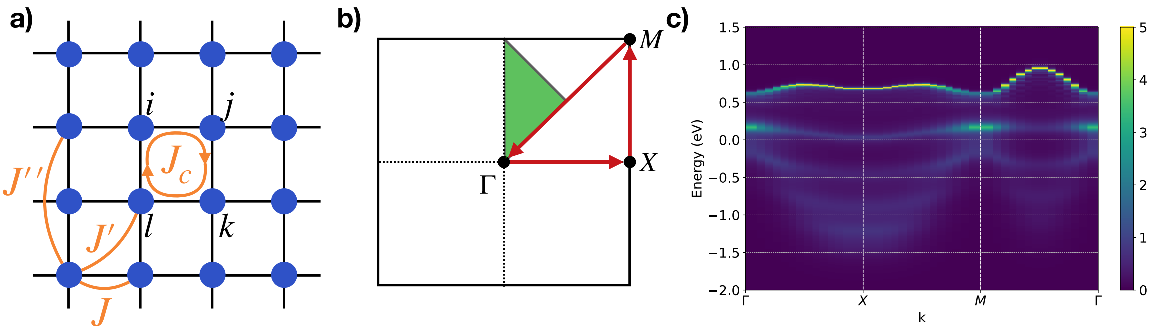

Figure 2.12: (a) Illustration of the different exchange couplings on a 2D square lattice. (b) Sketch of the BZ and the **k**-path along which is calculated the hole's spectral function shown in (c). The green wedge depicts the irreducible part of the BZ.

In practice the latter is obtained by first converging Eq. 2.98 in a self-consistent loop. Moreover, since in our Hubbard one-band effective models for NaCCOC and t-CuO we include the longer-ranged hopping amplitudes t' and t'', we use a modified magnon dispersion which incorporates the corrections from t' and t'' as well as higher order processes in t, following Ref. [235]. This leads to correct the NN exchange J as :

$$J = \frac{4t^2}{U} - \frac{24t^4}{U^3} \tag{2.100}$$

and to include the NNN $J' = \frac{4t'^2}{U} + \frac{4t^4}{U^3}$, NNNN $J'' = \frac{4t''^2}{U} + \frac{4t^4}{U^3}$, as well as the cyclic $J_c = \frac{80t^4}{U^3}$ exchange couplings. The latter is essential to capture the difference in energy in the magnon dispersion between $\mathbf{k} = (\pi, 0)$ and $\mathbf{k} = (\pi/2, \pi/2)$ which is seen in experiment [166]. These couplings are illustrated in Fig. 2.12(a) and correspond to the following Hamiltonian:

$$\begin{aligned} H_{J-J'-J''-J_c} =& J \sum_{\langle ij \rangle} \mathbf{S}_i \mathbf{S}_j + J' \sum_{\langle\langle ij \rangle\rangle} \mathbf{S}_i \mathbf{S}_j + J'' \sum_{\langle\langle\langle ij \rangle\rangle\rangle} \mathbf{S}_i \mathbf{S}_j \\ &+ J_c \sum_{\langle ijkl \rangle} \left[(\mathbf{S}_i \mathbf{S}_j)(\mathbf{S}_k \mathbf{S}_l) + (\mathbf{S}_i \mathbf{S}_l)(\mathbf{S}_k \mathbf{S}_j) - (\mathbf{S}_i \mathbf{S}_k)(\mathbf{S}_j \mathbf{S}_l) \right], \end{aligned} \tag{2.101}$$

where $\langle ijkl \rangle$ refer to a square plaquette of four neighboring sites i, j, k, l. With these corrected exchange parameters, the magnon dispersion is given by [236]:

$$\begin{aligned} \omega_{\mathbf{q}} &= Z_c(\mathbf{q})(1-\delta)^2 \sqrt{A_{\mathbf{q}}^2 - B_{\mathbf{q}}^2} \\ A_{\mathbf{q}} &= 4JS + 4J'S(\cos(q_x)\cos(q_y) - 1) + 2J''(\cos(2q_x) + \cos(2q_y) - 4J_c S^3(\cos(q_x)\cos(q_y) + 1) \\ B_{\mathbf{q}} &= 2JS(\cos(q_x) + \cos(q_y)) - 4J_c S^3(\cos(q_x) + \cos(q_y)) \end{aligned} \tag{2.102}$$

where the factor $Z_c(\mathbf{q})$ incorporates the effects of the quantum fluctuations [235, 236]. Moreover, since the t' and t'' hopping terms do not disturb the antiferromagnetic order, they simply result in a dispersion of the hole without coupling to the spin degree of freedom, leading to a modification of Eq. 2.98 as follows:

$$\Sigma(\mathbf{k},\omega)=\frac{z^2t^2}{N}\sum_{\mathbf{q}}\frac{\left|M_{\mathbf{k},\mathbf{q}}\right|^2}{\omega-\omega_{\mathbf{q}}-\epsilon_{\mathbf{k}-\mathbf{q}}-\Sigma(\mathbf{k}-\mathbf{q},\omega-\omega_{\mathbf{q}})+i\eta}, \tag{2.103}$$

where $\epsilon_{\mathrm{k}}=4t'\cos(k_x)\cos\left(k_y\right)+2t''\left(\cos(2k_x)+\cos\left(2k_y\right)\right)$ (note the positive sign since it is a hole dispersion).

In the practical implementation, the parameter η is first chosen relatively large and reduced as the self-consistent accuracy is reached. Moreover, one can make use of the high symmetry of the magnon dispersion of cuprates: the BZ can be reduced to the irreducible part as shown in green in Fig. 2.12(b). A typical SCBA spectrum obtained with parameters relevant for NaCCOC ($x=0$) is shown in Fig. 2.12(c): a coherent quasi-particle peak can be identified, with replica of the dispersion at lower energy which are increasingly incoherent. The system size is 30 × 30, way larger than what can be treated within CDMFT or other techniques treating explicitly the Hubbard interaction U, and which allows to eliminate finite size effects.

PART IV

STUDIES OF SELECTED COPPER OXIDES

3

STUDY OF THE ANTIFERROMAGNETIC FLUCTUATIONS IN $CA_{2-x}NA_xCUO_2CL_2$

3.1 INTRODUCTION

Although being a cuprate, strictly speaking $Ca_{2-x}Na_xCuO_2Cl_2$(NaCCOC) is not a copper oxide, but an oxychloride. It has a simple tetragonal crystal structure [80–83] illustrated in Fig. 3.1(a)). The main difference is the replacement of the apical O by Cl atoms, which confers a strong 2D character to the CuO_2 layers, making it an interesting candidate to connect to the ZRS picture [38]. In fact NaCCOC attracted the scientific attention since it was one of the first cuprates without oxygen octahedra to show superconductivity upon hole-doping [80, 81]. The introduction of hole carriers in the parent compound [82] can be performed by replacing the Ca by Na atoms [80, 81, 83], or by vacancies [237][1].

NaCCOC is antiferromagnetically ordered [84] (up to $x = 0.02$ doping) and shows a Mott gap $0.5 \leq \Delta \leq 2.5$eV [85–89]. Photoemission measurements identified a *kink* feature in the energy dispersion [86] at low energy, similar to the well-known *waterfall* feature of cuprates [24]. Upon hole-doping, NaCCOC becomes superconducting at $x \sim 0.10$ until $x = 0.20$ [80, 81, 84] with a superconducting gap of $d-$wave symmetry [240], and interestingly there is a region of the phase diagram around $x \sim 0.05$ where both the superconductivity and the long-range antiferromagnetic order are suppressed. In this low-doping region, a spin-glass like behavior has been identified [84], as well as a CDW [25–27] of period of 4 lattice constants, but without long-range order [241, 242]. The famous PG phase, present in all cuprate compounds [12, 14, 24], characterized in the spectral function by the opening of an anistropic gap in the BZ, is also observed at low to intermediate dopings [26, 90–94]. The maximum hole concentration experimentally available is $x = 0.20$, which is still in the superconducting phase, and hence prevents to infer on the existence of the Fermi liquid and the strange metal phases [14] in the overdoped regime. Though, the NaCCOC phase diagram until the optimal doping is in excellent agreement with the one of cuprates, with the peculiarity that the PG exists down to $T = 0$ around $x = 0.05$ since both the long-range antiferromagnetic order and the superconductivity are suppressed. Therefore, along with the fact that NaCCOC has a quite simple structure, it appears as a promising candidate to confront the cuprates' low-energy models to experiments.

In this chapter, we are particularly interested in the physical origin of the waterfall feature and the PG, which are both seen in ARPES measurements. The waterfall manifests itself as a kink

---

[1] Note that two other chemical substitutions are possible: replacing the Ca by K [238], and Cl by Br [239], but very few studies are dedicated to these options.

in the energy dispersion at low-energy [24, 86], and is induced by the cross-over between low- and high-energy sectors yielding different physics. It is observed in the parent NaCCOC compound ($x = 0$) and survives at low and intermediate dopings [90–92]. A similar kink is observed in the one-band Hubbard model which is often used as an effective model for cuprates, and the low-energy part has been theoretically identified as stemming from a spin-polaron [95–98], i.e. a hole propagating in an antiferromagnetic background. A consensus is however not reached for the high-energy part, which has been attributed to spin-charge separation [99, 100], to weak-coupling spin-density wave, or to long-range hopping processes [101, 102] within a single magnetic sublattice [98].

The PG is a universal feature of cuprates, and was first experimentally observed in the Knight shifts [21], spin-lattice relaxation time [22], transport measurements [23], photoemission [243–245], and others [12]. Its most well-known feature in hole-doped cuprates is the opening of a gap at the anti-nodes $(\pi, 0)$ while at the node $(\pi/2, \pi/2)$ a quasiparticle peak survives, leading to a discontinuous Fermi surface. Since the experimental discovery, it has been shown with embedded quantum cluster methods like CDMFT [103–106], and DCA [65, 107–110] that the 2D one-band Hubbard model display a PG upon hole-doping. It is linked to the Mott insulating transition since the PG occurs at finite doping for U values above the critical U_c for the insulating transition at half-filling. Though, it is a distinct phase: the value of the PG does not extrapolate to the Mott gap as the doping $x \to 0$ [106]. Early on, from QMC calculations it was proposed that the PG originates from short range antiferromagnetic fluctuations [111], which was corroborated later with the finding that quantum cluster methods with small cluster sizes (2-site and 2×2 plaquette) were also able to capture the right behavior [104, 107, 108]. Gull *et al.* showed that it was not an artifact from the finite size of the embedded cluster, and that considering larger systems does not significantly change the results [110]. More recently, a complementary analysis called *fluctuation diagnostic*, based on the decomposition of the contributions to the self-energy into different channels (spin, charge, and particle-particle), pointed out the dominance of the spin channel at the wavevector $\mathbf{Q} = (\pi, \pi)$ in the PG phase from the analysis of the self-energy obtained with DCA [112]. The same technique was also applied to self-energies obtained by diagrammatic Monte Carlo, whose recent developments allowed to perform calculation in a specific parameter regime relevant for the PG physics [113, 114]. In agreement to previous works, the anti-nodal self-energy is dominated by commensurate wavevector $\mathbf{Q} = (\pi, \pi)$ spin fluctuations while at the node the spin channel is also leading, but at an incommensurate wavevector $\mathbf{Q} = (\pi + \delta, \pi + \delta)$. Similar results were also obtained with the dual boson technique which includes long-range correlation effects by expanding around the DMFT solution [75]. Moreover, the correlation length was measured to be finite from DCA calculations [246]. Therefore, by the combination of many different techniques, a consensus seems to be reached that the PG in the hole-doped one-band Hubbard model, and by extension in cuprates, originates from short-range spin fluctuations [75, 104, 107, 111–114, 246].

Both the waterfall and the PG stem from the antiferromagnetic fluctuations, with the difference that the waterfall occurs already in the parent compound which hosts long-range antiferromagnetic order, whereas the PG is expected to emerge from short range fluctuations upon hole-doping. In this chapter, we study the emergence of both phenomena in NaCCOC using CDMFT on a 2×2 plaquette and 8-site cluster, confronting the results to the existent experimental literature and ARPES measurements performed in synchrotron facilities for $x \simeq 0.05$ and $x \simeq 0.10$ doped samples, to which we actively participated in collaboration with Matteo d'Astuto, Chafic Fawaz and Hervé Cercellier (Institut Néel, Grenoble France). We also compare our numerical results to RIXS measurements performed by Matteo d'Astuto, Blair Lebert *et al.* on undoped and doped NaCCOC [166].

Calculations for the parent compound provide a spectral function in excellent agreement with ARPES measurements [85–88], and show a clear waterfall feature. By performing SCBA calculations for an effective model as described in Sec. 2.6, we show that the low-energy part of the spectrum is well accounted for by a spin-polaron, in agreement with previous observations [95–98]. We find that the high-energy part is well captured at the atomic limit, i.e. by a self-energy calculated with the Hubbard-I [35] approximation, consistent with the picture of a hole propagating into a lattice of localized electrons (spins), which are antiferromagnetically ordered. Our analysis therefore provides a simple and unambiguous explanation for the high-energy part of the waterfall feature.

Upon hole-doping $x > 0$, we identify an emerging PG characterized by the opening of a gap at the anti-node $(\pi, 0)$ in the calculations, as well as the measured spectra, both being in good qualitative agreement. Similarly to observations of Shen *et al.* [92] at low doping, our ARPES measurements on $x \simeq 0.05$ and $x \simeq 0.1$ show a suppression of the coherent quasiparticle peak at the nodal point $(\pi/2, \pi/2)$, in sharp contrast to our calculations in which the peak is always present, challenging the simple picture of a perfect 2D lattice model for the underdoped region. However, we identify a double peak structure at the nodal point which is in excellent agreement, especially for the 8−site cluster, with previous experimental observations [91, 92].

We analyze the PG phase by dissecting the state histogram of the embedded 2×2 plaquette using a modified cluster basis in contrast to previous works [106, 121, 247]. We show that due to the presence of two degenerate orbitals in the 2×2 plaquette, which correspond to the cluster momenta $\mathbf{K} = (\pi, 0)$ and $\mathbf{K} = (0, \pi)$ and are weakly coupled to the self-consistent bath, the most probable state until $x = 0.12$ is a non-degenerate singlet state $S = 0$, in agreement with previous observations [106, 121, 247]. This singlet nature of the ground state leads to a cancellation of the zero-energy excitations for the two degenerate orbitals, that we explicitely show following Ref. 121 that we adapt to our new choice of basis, such that the lowest excitation channel carries a spin $S = 1$, momentum $\mathbf{Q} = (\pi, \pi)$ and a non-zero energy. This leads to the opening of the PG at the anti-nodes. The 2×2 plaquette is the minimum cluster containing this mechanism, and by comparison to the 8-site cluster we show that the picture remains valid for larger cluster.

Moreover, this observation is linked to the observation of a dominant $\mathbf{Q} = (\pi, \pi)$ peak in the DSSF, that we directly compare to RIXS measurements for both the undoped and doped systems.

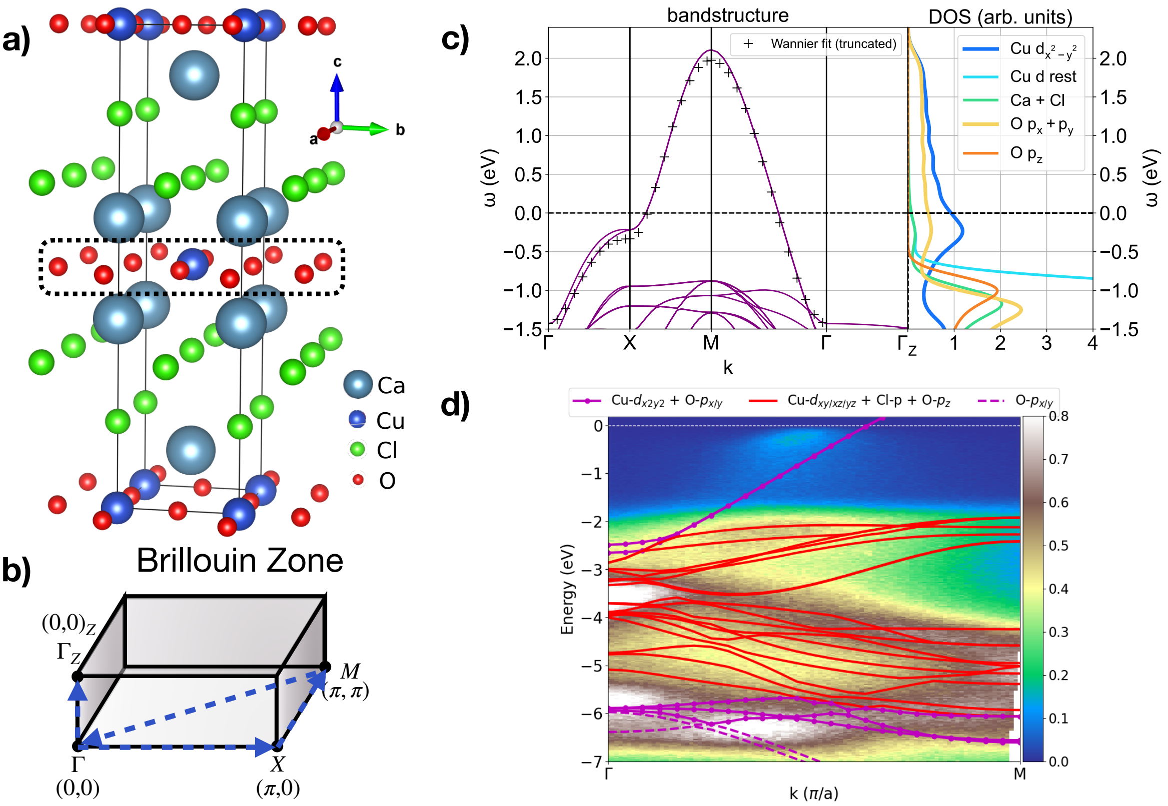

Figure 3.1: (a) Tetragonal crystal structure of the parent compound NaCCOC (x=0). (b) Sketch of the BZ and the **k**-path along which is plotted the band structure obtained from a LDA calculation shown in (c), along with the orbital projected DOS. (d) The LDA orbital projected band structure overlayed on the ARPES spectrum taken at SOLEIL synchrotron with a 10% doped sample. The LDA bands were all shifted by the same constant energy $\delta\epsilon$ to match the measurement.

Consistently with the experimental findings for NaCCOC [166] and other cuprates [248–250], we show that in the doped sample clear magnon excitations survive although having a shorter lifetime than in the parent compound. By inspecting the spin-spin correlation function, we find a similar behavior as Werner *et al.* [61, 123]: upon hole doping, at long imaginary times $\tau \to \beta/2$ the correlation function becomes larger than for the parent compound and does not decay with distance (on the scale of the 2×2 cluster). We show that this behavior, for which no clear explanation was found so far, is directly linked to the existence of low-energy spin excitations and that the "freezing" of the correlation function can extend to long-range distances as the temperature is lowered, what could be an interesting subject of further studies.

Overall, this chapter aims at depicting a unified description of the spectral and magnetic properties of NaCCOC by simultaneously focusing on the waterfall feature and PG phase with a combined theoretical and experimental approach. We emphasize the robustness of the 2×2 plaquette results by a systematic comparison to the 8−site cluster, and find a peculiar behavior of the long-range spin-spin correlation function at long times $\tau \to \beta/2$.

3.2 MODEL AND METHOD

Similarly to cuprates, NaCCOC is composed of CuO_2 planes, of 2D character [251], intercalated between charge reservoir layers made of Ca and Cl atoms, as shown in Fig. 3.1(a). The low energy window, relevant for the waterfall feature and the PG, is ruled by the physics of these 2D CuO_2 layers. In the following, we first describe the effective Hubbard model that we use to represent NaCCOC. We then present the clusters used for solving the model with CDMFT, and we give details about the ARPES measurements carried out at the Photon Factory (Tsukuba, Japan) and at SOLEIL (Saint-Aubin, France) synchrotrons.

3.2.1 BAND STRUCTURE OF $CA_2CUO_2CL_2$

Although DFT should not be used to study the spectral properties of this correlated material, it provides an interesting starting point for building an effective model of NaCCOC. Indeed, from electronic structure calculations with the LDA potential one can extract a TB Hamiltonian as explained in Sec. 2.1. In Fig. 3.1(c) is shown the band structure along the $\mathbf{k}$-path shown in Fig. 3.1(b) as obtained from a LDA calculation with Vienna *ab initio* simulation package (VASP) [252–255] for the parent compound ($x = 0$). As expected from a LDA calculation (see Sec. 1.4), a single band crosses the Fermi energy, consistent with the valence of the Cu atoms which are in d^9 electronic configuration, i.e. one of the d orbitals is half-filled. Note that actually two of these bands can be seen in the band structure, which is simply due to the fact that the unit cell contains two equivalent Cu atoms. A striking feature is that the single band is well isolated from the rest of the Cu d/ O p/ Cl p manifold which lies below (−1.5eV) and is in rather good agreement with the ARPES measurement done on a $x = 0.1$ hole-doped sample (see Fig. 3.1(d)). The isolated band, also seen in the experimental spectrum, can be traced back to be of Cu $d_{x^2-y^2}$ and O $p_{x/y}$ character as shown by the projected DOS in Fig. 3.1(c), consistent with a ZRS state [38].

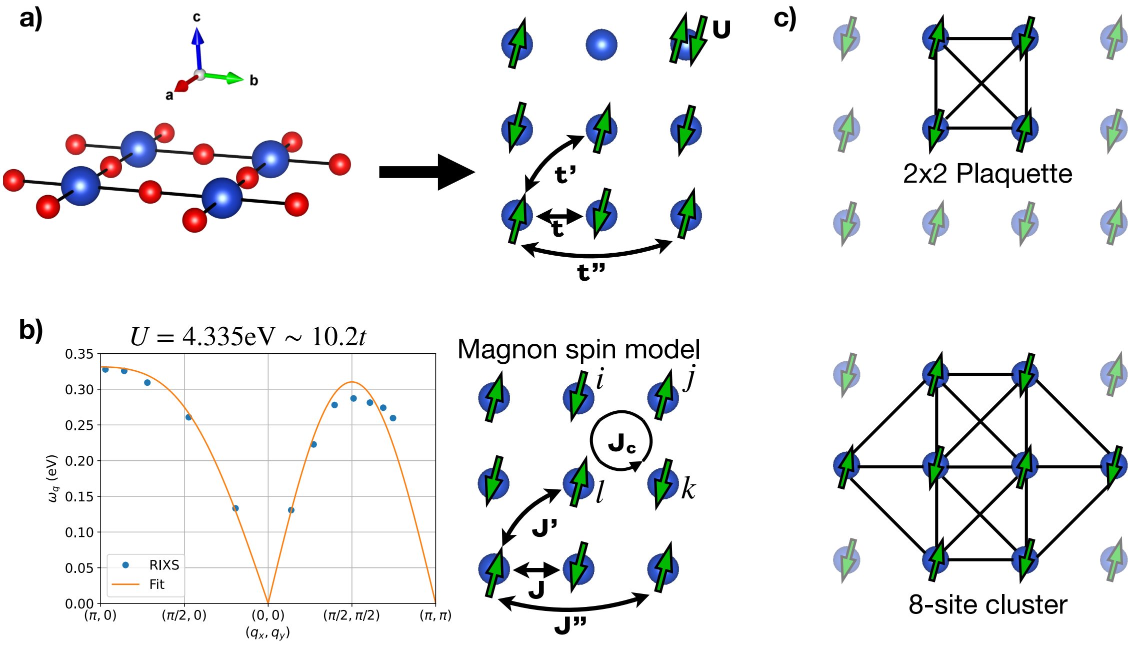

Figure 3.2: (a) The CuO_2 planes are modeled with an effective Hubbard model. The hopping parameters were obtained from the fit of the single band dispersion shown in Fig. 3.1(c), and the on-site U interaction is extracted from a fit of the experimental magnon dispersion (*left* panel of (b)) obtained from a RIXS measurement carried on an undoped sample by Lebert *et al.* [166]. The Heisenberg spin model used for the fit is shown in the *right* panel of (b). (c) The two different clusters considered for the CDMFT calculations: the 2×2 plaquette and the 8-site cluster.

The effective TB model can be restricted to a square lattice in two dimensions, for the single band shows a weak dispersion along the Γ-Γ_Z path, in agreement with transport measurements [251]. By performing a Wannier fit using the wannier90 [183, 184] package, we obtain the hopping parameters $t = 0.425\text{eV}$, $t' = -0.076\text{eV} \sim -0.2t$ and $t'' = 0.05\text{eV} \sim 0.1t$, which are close to the typical cuprates' hopping term $t'/t \simeq -0.2/0.3$. By restricting the 2D TB model to these three hopping terms only, we obtain the Wannier band shown in Fig. 3.1(c) which represents well the single DFT band. Note that a key feature of the dispersion is included in the 2D effective TB model: the dispersion becomes flat at the X point, i.e. at the antinode $(\pi, 0)$, yielding a van Hove singularity which is of importance in the PG physics [246, 256].

3.2.2 Low-energy effective Hubbard model

Based on these observations, we model NaCCOC by a single-band Hubbard model [35–37] which aims at capturing the low-energy physics of the CuO_2 planes. The model is illustrated in Fig. 3.2(a), the Hamiltonian reads:

$$H = U\sum_i n_{i\uparrow}n_{i\downarrow} - \mu\sum_i n_i - t\sum_{\langle ij\rangle,\sigma} c^\dagger_{i\sigma}c_{j\sigma} - t'\sum_{\langle\langle ij\rangle\rangle,\sigma} c^\dagger_{i\sigma}c_{j\sigma} - t''\sum_{\langle\langle\langle ij\rangle\rangle\rangle,\sigma} c^\dagger_{i\sigma}c_{j\sigma}, \tag{3.1}$$

where U is the Hubbard on-site interaction term, μ the chemical potential, $\langle.\rangle, \langle\langle.\rangle\rangle, \langle\langle\langle.\rangle\rangle\rangle$ denote respectively the NN, NNN and NNNN associated with the hopping terms $t = 0.425\text{eV}$, $t' = -0.076\text{eV} \sim -0.2t$ and $t'' = 0.05\text{eV} \sim 0.1t$. As described above, the latter are obtained by a fit of the LDA single band using MLWF [181, 182], and we are left with determining the U

value. Instead of calculating it *ab initio*, we rather rely on the magnon dispersion obtained by a RIXS measurement on the parent compound which was performed by our collaborators Lebert, d'Astuto *et al.* [166]. Since undoped NaCCOC is an antiferromagnetic insulator with long-range magnetic order [84], the magnon dispersion can approximately be represented by a spin-wave calculation based on the Heisenberg model shown in the *right* panel of Fig. 3.2(b). The spin model Hamiltonian is given by

$$\begin{aligned} H_{spin} =& J\sum_{\langle ij\rangle}\mathbf{S}_i\mathbf{S}_j + J'\sum_{\langle\langle ij\rangle\rangle}\mathbf{S}_i\mathbf{S}_j + J''\sum_{\langle\langle\langle ij\rangle\rangle\rangle}\mathbf{S}_i\mathbf{S}_j \\ &+ J_c\sum_{\langle ijkl\rangle}\left[(\mathbf{S}_i\mathbf{S}_j)(\mathbf{S}_k\mathbf{S}_l) + (\mathbf{S}_i\mathbf{S}_l)(\mathbf{S}_k\mathbf{S}_j) - (\mathbf{S}_i\mathbf{S}_k)(\mathbf{S}_j\mathbf{S}_l)\right] \end{aligned} \tag{3.2}$$

where $\langle ijkl\rangle$ refer to a square plaquette of four neighboring sites i, j, k, l (see Fig. 3.2(b)), and the exchange couplings are: $J = \frac{4t^2}{U} - \frac{24t^4}{U^3}$, $J' = \frac{4t'^2}{U} + \frac{4t^4}{U^3}$, $J'' = \frac{4t''^2}{U} + \frac{4t^4}{U^3}$ and $J_c = \frac{80t^4}{U^3}$ [235, 236]. Keeping the hopping parameters fixed to the value obtained *ab initio*, the on-site interaction U is treated as a fitting parameter. We stress the importance of the corrections of the exchange parameters from the t^4 processes, and especially the cyclic exchange J_c which allows to capture the difference in the magnon energy between $(\pi, 0)$ and $(\pi/2, \pi/2)$ [166]. This procedure results in the fitted magnon dispersion shown in Fig. 3.2(b), which is in excellent agreement with the experimental data, especially by considering only U as fitting parameter. We obtain $U \simeq 4.335\text{eV} = 10.2t$ which will be our default choice for the theoretical calculations (the only exception is for the state histogram discussed later in this chapter which were obtain with $U \simeq 4.25\text{eV} = 10t$).

The on-site Hubbard interaction U is of the same order of magnitude than the bandwidth $W \simeq 3.5\text{eV}$, preventing from the use of perturbation theory in either the kinetic or potential energy. To solve this many-body strongly correlated system, we perform CDMFT calculations with two different clusters presented in Fig. 3.2(c). Most of the calculations and results presented in this chapter are obtained with the 2×2 plaquette which contains the minimum ingredients to capture the PG in the hole-doped single band Hubbard model [121, 247]. The effective impurity model is solved using CTQMC [60–62]-based solvers working at finite temperature: the hybridization- CT-HYB [116] and the interaction-expansion CT-INT [117] solvers based on the ALPSCore libraries [118]. Additionally, we also used the hybridization-expansion solver of the TRIQS toolkit [119, 120] in order to obtain the state histograms. Thanks to the limited size of the plaquette cluster, it is possible to perform calculations at low temperature, deep in the PG phase. In order to check that the results we obtain are not an artifact from the specific properties of the plaquette cluster, we also perform calculations for the 8-site cluster shown in Fig. 3.2(c).

We ensured that all the theoretical CDMFT results presented in this chapter were well converged, and we performed extra self-consistent loops with a high Monte-Carlo sampling: the number of counts was always $\geq 2\cdot10^6$ for all temperatures and cluster sizes. To obtain the momentum-resolved spectral function, we first perform an analytic continuation of the cluster self-energy using the MQEM [217] presented in Sec. 2.5. From the self-energy, we compute the periodized Green's function using the Green's function periodization procedure (Eq. 2.48) [67]. For the

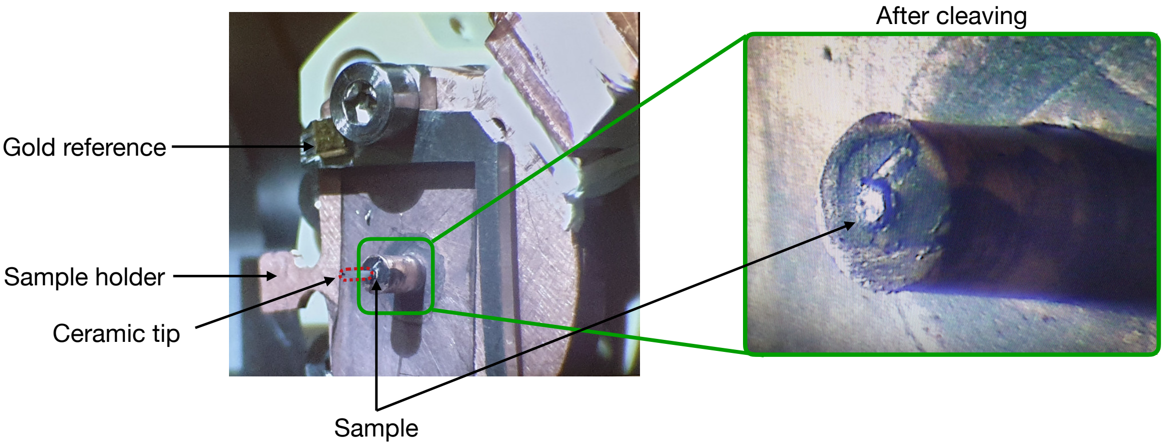

Figure 3.3: In-situ photography taken at SOLEIL synchrotron of the sample in the experiment chamber under UHV (*left*). A ceramic tip (highlighted by the red dotted frame) is glued on the sample surface to allow for cleaving under vacuum, resulting in a clean 2D surface as shown in the *right* panel. The sides of the samples are covered with a graphite spray (darker zone around the sample) to ensure the electrical contact with the copper sample holder. On the upper left side of the latter, one can notice the gold sample used for the Fermi energy reference.

DSSF, we use a different procedure: from the two-time two-particle imaginary time Green's function, the spin-structure factor is first calculated at the different **Q** points of interest, and then an analytic continuation with a bosonic kernel is performed using the `MaxEnt` package [220]. More details on the link between the DSSF and the two-time two-particle Green's function are given in the dedicated Sec. 3.5.

3.2.3 Angle-Resolved Photoemission Spectroscopy measurements

In addition to the theoretical calculations, we performed two ARPES measurements at synchrotron facilities: the Photon Factory (Tsukuba, Japan) in close collaboration with Matteo d'Astuto and Yukiko Obata, and SOLEIL (Saint-Aubin, France) along with Matteo d'Astuto, Chafic Fawaz and Hervé Cercellier. The samples measured were synthesized by Matteo d'Astuto, David Santos-Cottin, Hajime Yamamoto and Ikuya Yamada. The characterization and preparation of the samples for the experiments were done by Matteo d'Astuto, Yukiko Obata, and Chafic Fawaz. We do not detail the synthesis here, the interested reader can obtain more details in Ref. 83. The samples' characteristic size is about $2 \times 2 \times 0.2$mm (width×height×thickness). The doping is estimated by measuring the superconducting transition temperature T_c, a standard procedure for this material [90] but not that precise, and complemented by a measure of the lattice parameters. For the $x = 0.1$ samples, the T_c measurement leads to an estimation of the doping close to the expected value, but the error on the Na concentration is of the order of $1-2\%$, i.e. $x = 0.1 \pm 0.02$. This is even worse for the $x = 0.05$ sample since the sample is not superconducting and one can only rely on the lattice parameters measurements, from which it is estimated that the real doping is somewhere around $x \sim 0.05$.

The crystalline planes' orientation was characterized using x-ray diffraction, and the samples were then glued accordingly on the copper sample holder with a silver epoxy to ensure the electrical contact (see Fig. 3.3), always manipulating the material in a dry environment to prevent from surface pollution and oxidation. To further make sure that there is a good contact between the sample and the holder, to avoid surface charging during the measurement, graphite has been sprayed over. Finally, a ceramic tip is glued over the sample (see Fig. 3.3) and is only removed under ultra high vacuum (UHV) once in the experiment chamber at the synchrotron. The UHV was of the order of 10^{-11}mbar to avoid surface pollution as well as scattering of the emitted photoelectrons. The samples are cleaved in this environment, resulting in a clean 2D surface as shown in Fig. 3.3. At both synchrotrons the measurements were carried out at low temperature, $15\text{K} \leq T \leq 30\text{K}$. Unfortunately, at the Photon Factory the setup did not allow to control the temperature precisely, and at SOLEIL the temperature controller broke down during the beam time, so that a precise temperature dependent measurement could not be carried out.

Since the maximum momentum resolution is obtained along the slit of the analyzer, we first corrected the orientation of the sample with respect to the analyzer. In practice, the sample is rotated so that either the slit is parallel to the nodal direction $(1, 1, 0)$ or to the anti-nodal direction. Finally, the Fermi energy is determined using the gold sample attached to the sample holder. The author carried the data analysis of the experimental data and created all the experimental plots shown in the following chapter. We used the `pyARPES` package [257] which the author adapted to the beamlines where the measurements were performed. For more details about the ARPES formalism, its link to the Green's function calculated in CDMFT, and how the raw data is transformed back to momentum space, we refer the reader to App. A.

3.3 SPECTRAL FUNCTION

Both the PG and the waterfall feature can be observed in the momentum-resolved spectral function, which is directly calculated in CDMFT and obtained in ARPES (albeit the additional matrix-element effects [258]). In the following, we start by studying the parent compound NaCCOC ($x = 0$) and show that the waterfall feature seen by Ronning *et al.* [86] is well captured by CDMFT calculations. Using two different simpler effective models, we interpret the waterfall feature as a cross-over between low-energy spin polarons and higher-energy localized electrons. Then, we proceed with the hole-doped system for which the waterfall feature is still observed and a clear PG is captured by CDMFT, independently of the cluster size.

3.3.1 PARENT COMPOUND

In Fig. 3.4 is shown the spectral function calculated with the 2×2 plaquette cluster (see Fig. 3.2(c)) at $\beta = 60\text{eV}^{-1}$ with two different initializations, obtained by performing an analytic continuation of the self-energy using the MQEM method [217] presented in Sec. 2.5. All the one-particle spectra shown in this chapter were obtained using the same analytic continuation procedure. In both cases, either a metallic or insulating starting point, the final system is a Mott insulator with a gap $\Delta \simeq 2.5\text{eV}$, in good agreement with the scanning tunneling microscopy (STM) estimate [89]. In the occupied region, apart from the global shift of the chemical potential, the resulting spectra show drastic differences: in Fig. 3.4(a1)-(a3) we observe a low-energy dispersion around -0.5eV which is well separated from the LHB which lies around -2eV. In contrast, we see in Fig. 3.4(b1)-

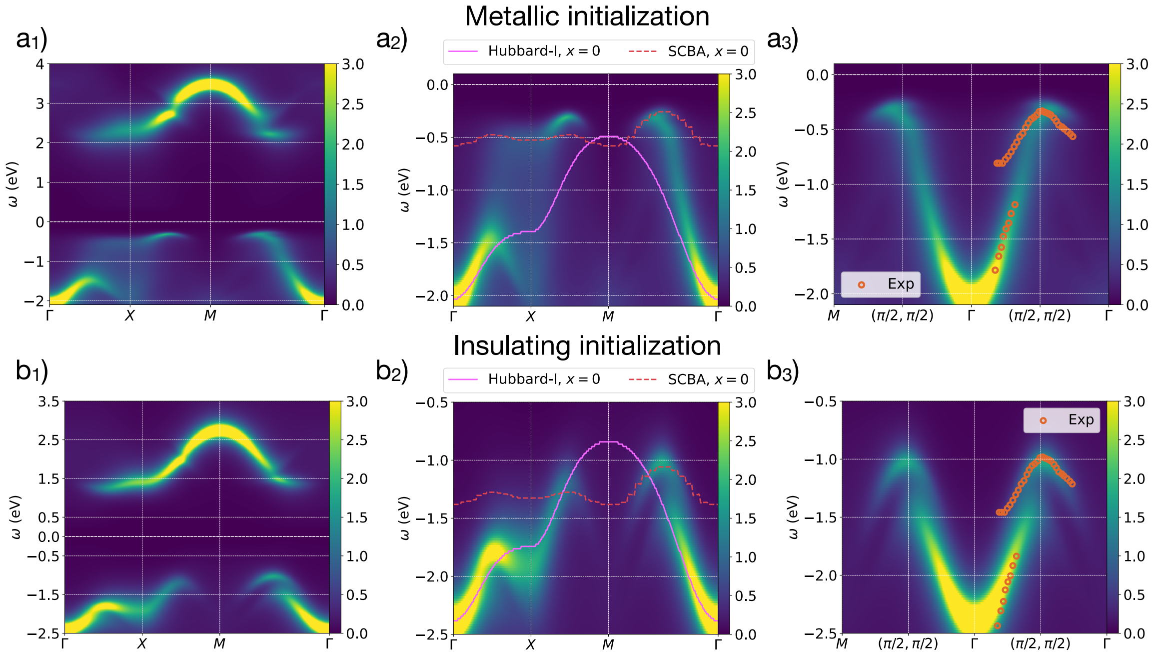

Figure 3.4: Spectral functions calculated with the plaquette cluster at $\beta = 60\text{eV}^{-1}$ with different initializations: starting (a1)-(a3) from a metallic state, (b1)-(b3) from an insulating state. Note that our set of parameters is close to the coexistence region were both the metallic and insulating phases are possible solutions. The final chemical potential is different, hence the static shift in energy of the two Hubbard bands depending on the starting point. The solid and dotted lines were extracted from the Hubbard-I and SCBA spectra and were shifted by a constant energy so to match the CDMFT dispersion. The orange circles depict the experimental dispersion measured by Ronning *et al.* on undoped NaCCOC ($x = 0$) and are extracted from Ref. 86. The circles have been shifted in energy for the panels (b3) to compensate for the difference in chemical potential.

(b3) that the insulating starting point leads to a rather continuous LHB dispersing from −2.5eV to −1.0eV, except at the nodal point between Γ and M where a low-energy dispersion distinct from the LHB appears.

Despite these differences, both calculations capture the waterfall feature at the nodal point which is signaled by a kink in the LHB dispersion: around −0.5eV and −1.25eV respectively for the metallic and insulating solution. As shown in Fig. 3.4(a2),(b2), it can be understood as a crossover between two different energy regimes. At high-energy, the LHB is well captured by a Hubbard-I approximation [35] in which the self-energy is approximated by the atomic limit result, given for a general filling and chemical potential by [259]:

$$\Sigma_\sigma = \frac{1}{2}nU + \frac{\frac{1}{2}n\left(1-\frac{1}{2}n\right)U^2}{\omega + \mu - \left(1-\frac{1}{2}n\right)U + i\delta} \tag{3.3}$$

where n is the electron filling. Within this approximation of purely local self-energy, the LHB is well reproduced around Γ where the energy is the lowest. Since this approximation is valid in the atomic limit, we observe in Fig. 3.4 that it works best for the insulating starting point.

At lower energy however this approximation of the self-energy is not valid: the effective mass of the electrons is increased leading to a kink in the dispersion. The purely local self-energy of the Hubbard-I approximation can not capture such a behavior since it is related to non-local antiferromagnetic fluctuations [95–98]. To illustrate that, we perform SCBA calculations following the formalism described in Sec. 2.6 using the specific parameters of NaCCOC. The low-energy dispersion of the SCBA spectrum is extracted and compared to the CDMFT calculations in Fig. 3.4(a2)-(b2). The spin-polaron dispersion is strongly renormalized due to the interaction with the surrounding spins and the dispersion becomes rather flat in comparison to the Hubbard-I approximation. The bandwidth of the spin-polaron feature is of the order of ∼ 0.4eV. The low-energy part of the spectrum around the nodal point $(\pi/2, \pi/2)$ is well captured by the spin-polaron physics, thus providing a clear explanation for the waterfall feature in terms of a crossover between a high-energy region where the correlations are purely local and a low-energy part governed by antiferromagnetic spin fluctuations. Note that while the SCBA calculation relies on long-range antiferromagnetic order, the CDMFT calculations here only incorporate short-range fluctuations, hence showing that the kink feature can survive in the hole-doped region in which the long-range spin correlations are suppressed. Note also that while in the SCBA spectrum as shown in Fig. 2.12 the spin-polaron has a large lifetime at the nodal point, in the CDMFT spectrum the feature is less coherent: the system is not a perfect antiferromagnet. Although we did not perform this analysis here, the comparison of the lifetime of the spin-polaron in theory and experiment could provide interesting information on the system.

Most interestingly, the CDMFT spectrum is in excellent agreement with the experimental measurements [85, 86, 91]. Both starting points very well reproduce the ARPES data of Ronning *et al.* [86] as shown in Fig. 3.4(a3)-(b3). While the high-energy part of the Γ-M dispersion seems to be better captured by the metallic starting point, the spin-polaron part is astonishingly agreeing for the in-

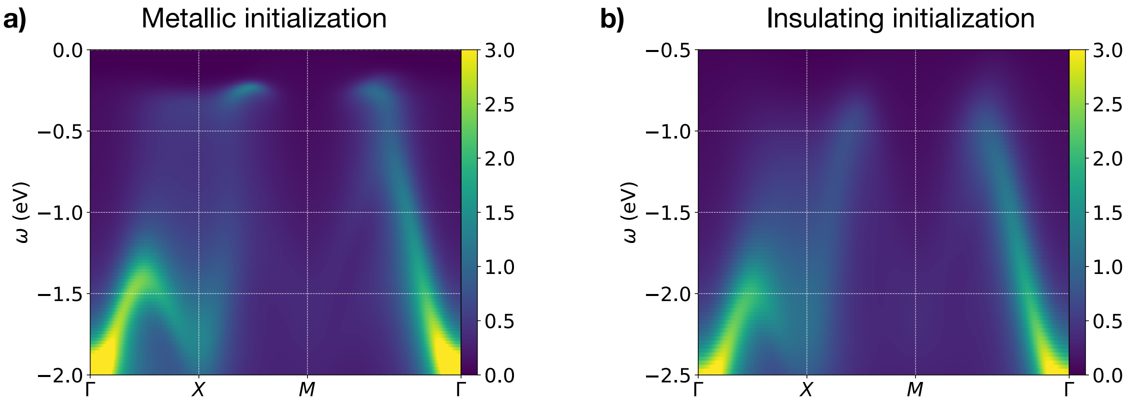

Figure 3.5: Spectral functions calculated with the plaquette cluster at $\beta = 20\mathrm{eV}^{-1}$ with different initializations: starting (a) from a metallic state, (b) from an insulating state. The final chemical potential is different, hence the static shift in energy of the two Hubbard bands depends on the starting point.

sulating initialization. Both in the theoretical and experimental spectra we observe a downturn of the low energy dispersion at the nodal point $(\pi/2, \pi/2)$, i.e. at the crossing with the antiferromagnetic BZ boundary, thus being another sign of the role of these fluctuations in the low-energy physics of undoped NaCCOC. The bandwidth of the spin-polaron is another argument for the identification of the experimental waterfall: The experimental and theoretical (both for CDMFT and SCBA) bandwidths ($\sim$ 0.4eV) are in excellent agreement. One of the main differences between the two theoretical spectra is seen around the anti-nodal point, where CDMFT predicts either a low-energy flat dispersion at the same-energy as the nodal point (metallic starting point), or a high-energy dispersion stemming from the atomic limit (insulating starting point). The second option seems to better account for the experimental data of Ref. [85] (most easily visualized in Fig. 2 of Ref. 91) since a clear difference in energy of roughly −0.5eV is observed between the nodal and anti-nodal point. Finally, one can note that the waterfall feature is similar to the spin-charge signature observed with ARPES in 1D spin chains [260]. Despite the fact that these two phenomena are related to the cross-over between two different energy regimes (atomic limit *vs* spin polaron, and spinon *vs* holon), the physics at play is different: in NaCCOC the motion of the hole is lead by the coupling to the spin degrees of freedom, while in the 1D spin chains the charge of the hole become entirely decoupled from the spin excitation.

Fig. 3.5 shows the spectral functions calculated with the two different initialization but for a higher temperature ($\beta = 20$) at which the spin fluctuations start to be suppressed. With the metallic initialization (Fig. 3.5(a)), we still observe a low-energy feature but there is a strong spectral weight transfer to the LHB as compared to the $\beta = 60\mathrm{eV}^{-1}$ calculation. It is even more striking for the insulating starting point (Fig. 3.5(b)) where the kink in the dispersion at the nodal point has completely disappeared. This is an additional sign that the waterfall feature observed in the parent compound originates from the spin fluctuations, and shows the utmost importance of performing the calculations at sufficiently low temperature to find an agreement with the low-temperature ARPES measurements.

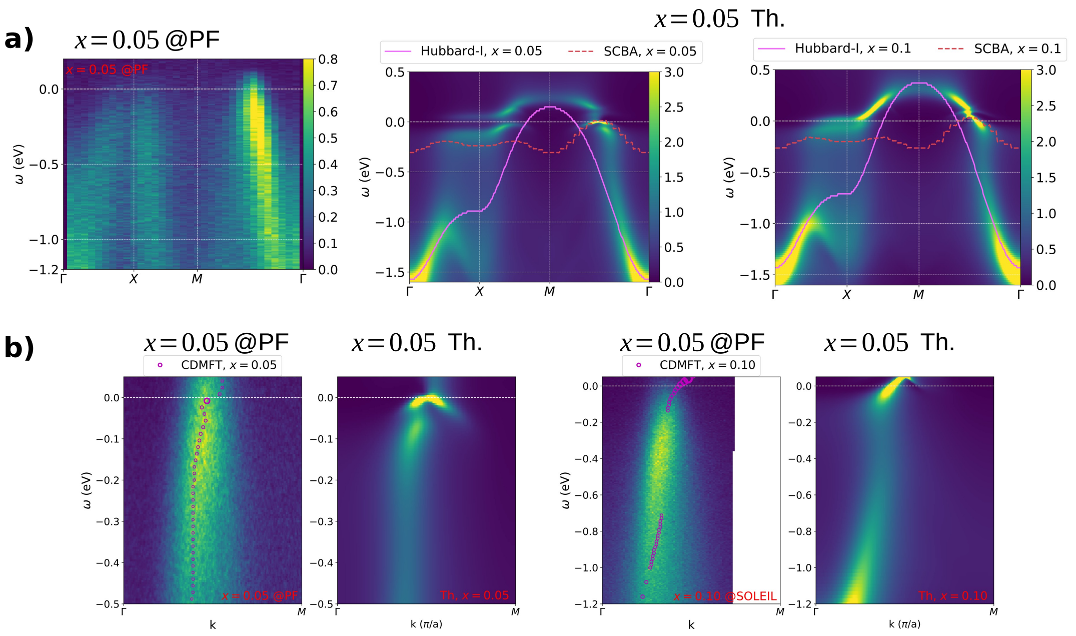

Figure 3.6: Experimental and theoretical momentum resolved spectral functions. (a) ARPES measurement on the $x = 0.05$ and calculated spectra for $x = 0.05$ and $x = 0.1$ at $\beta = 60$. The Hubbard-I approximation is no longer shifted in energy, but the SCBA dispersion still is. (b) Zoom at the nodal point to compare the experimental and theoretical results for both dopings. The purple circles denote the maximum of the theoretical spectral function at each k-point, and the relative spectral weight is depicted by the circle size.

3.3.2 HOLE DOPED SYSTEM

At finite hole doping, the chemical potential (and the spectral function) is no longer dependent on the starting point. Indeed, the coexistence region vanishes with doping: only the metallic solution survives. All the theoretical results presented in the following for the hole-doped NaCCOC are obtained with the insulating (at half-filling) starting point. The experimental data has been obtained with a $x = 0.05$ sample at the Photon Factory synchrotron, and a $x = 0.1$ sample measured at SOLEIL synchrotron. For the $x = 0.05$ sample, the experimental setup lacked of a gold sample for the Fermi energy reference, such that the later was obtained by a fit of the occupied bands of NaCCOC. To be consistent, the Fermi energy for the $x = 0.1$ sample was corrected according to the method used for the $x = 0.05$.

The momentum-resolved spectral functions along $\Gamma - X - M - \Gamma$ are shown in Fig. 3.6(a) for the $x = 0.05$ sample and calculations at $\beta = 60\text{eV}^{-1}$ for $x = 0.05, 0.1$ with the plaquette cluster. We observe a clear coherent dispersion at the nodal point for the $x = 0.05$ sample, along with a gapped weaker spectral weight around the anti-nodal point. This is in good agreement with the calculated spectrum for $x = 0.05$: a coherent quasiparticle peak is seen at the nodal point and two split flat dispersions appear at the anti-nodal point below and above the Fermi level. This is a clear sign of the opening of a PG, which starts to close at higher doping concentrations $x = 0.1$ in the calculations. Interestingly, the waterfall feature survives in the $\Gamma - M$ dispersion since the spectrum is still well described by a cross-over between a Hubbard-I approximation and a SCBA dispersion. Note that the Hubbard-I dispersion needs no longer to be shifted to adapt to the right

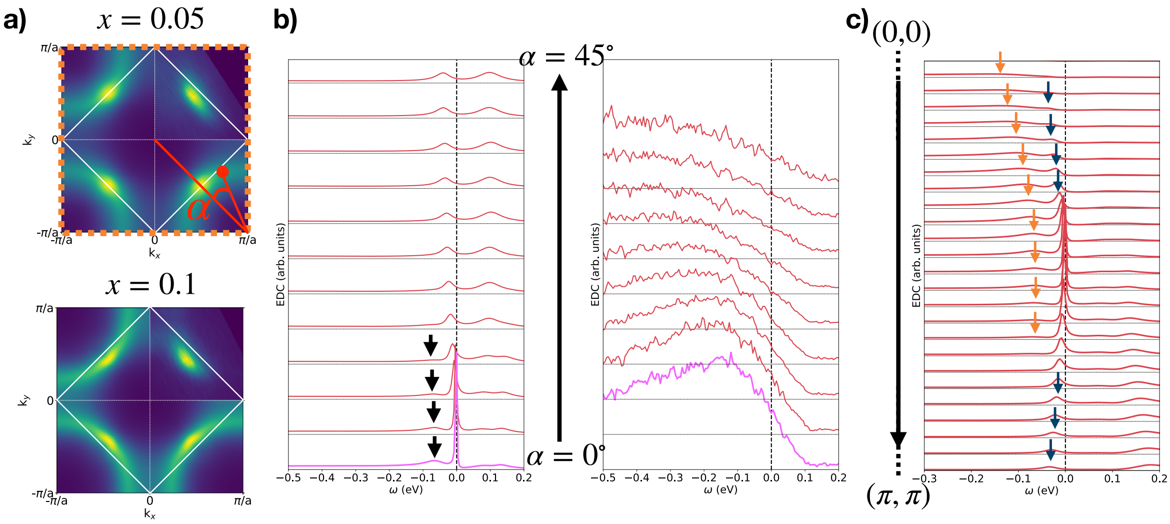

Figure 3.7: (a) Theoretical and experimental Fermi surface for the $x = 0.05$ and $x = 0.1$ samples, the ARPES measurement is shown in the top right corner of the BZ. The white rotated square illustrates the antiferromagnetic BZ. (b) EDC around the Fermi arc (the definition of the angle α is shown in (a)) for the $x = 0.05$ sample. (c) EDC around the nodal point on the path $\Gamma - M$. The orange (blue) arrows highlight the high- (low-) energy peaks.

chemical potential, hence showing the robustness of this qualitative picture. At the anti-nodal point where we observe a PG, neither the Hubbard-I nor the SCBA give a good agreement with the CDMFT spectrum since yet another physical mechanism is at play and which is the subject of the next section.

To further compare the experimental and theoretical spectra, we show in Fig. 3.6(b) a zoom on the $\Gamma - M$ dispersion. Similarly to the undoped case, we oberve an excellent agreement in the position of the dispersion and the kink which appears around 0.3eV, showing that the antiferromagnetic fluctuations survive at those values of doping. The increase of spectral weight as $\mathbf{k}$ gets closer to the nodal point $(\pi/2, \pi/2)$ is seen in all the spectra. Note that these data show an excellent agreement with the previous ARPES measurements [26, 90–93]. However, one can notice that in the experimental spectrum, the coherent and intense quasiparticle at $\omega = 0$ captured by CDMFT is not seen, which was also observed by Shen *et al.* for dopings below $x = 0.10$ [26, 92]. This is best seen by inspecting the energy distribution curve (EDC) around the nodal point, as shown in Fig. 3.7.

We show in panel (a) the Fermi surfaces for the two dopings for which we observe the famous Fermi arc, hallmark of the PG in photoemission data [24], both in the experimental and the theoretical data. The opening of the PG can be directly observed in the EDC around the nodal point, which are presented in Fig. 3.7(b) for the $x = 0.05$ sample. It is clear that in contrast to the CDMFT calculation, no coherent peak is observed for the $x = 0.05$ sample at the nodal point, although a PG is obtained due to a shift and broadening of the spectral function at low energy as going towards the anti-nodal point. Similarly, the quasiparticle peak in the ARPES measurements of the $x = 0.1$ sample is also absent (not shown here), which is a sign that the doping could be overestimated, based on the observations of Shen *et al.* in Ref. 92. The missing quasi-

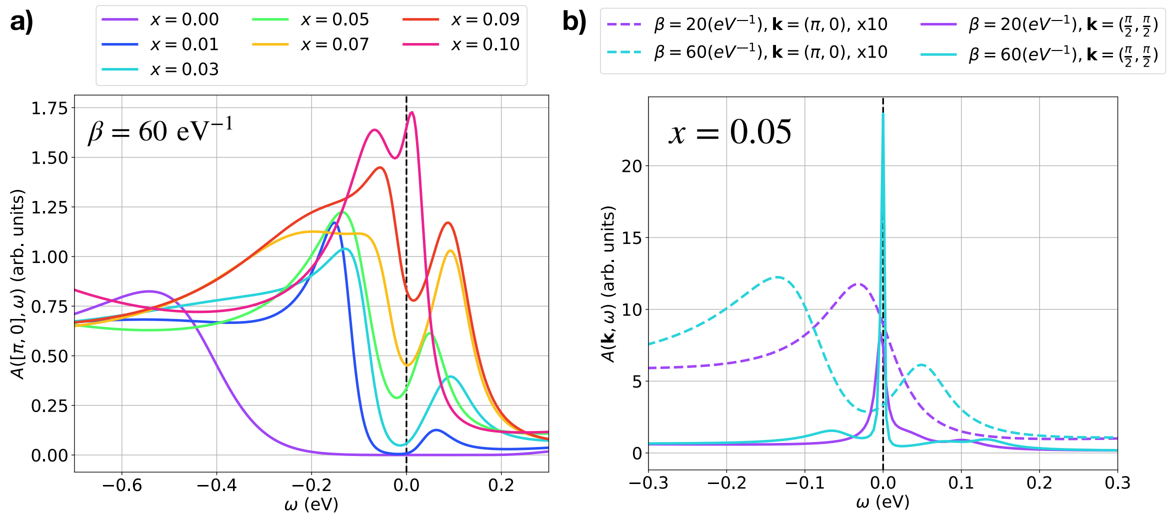

Figure 3.8: (a) Spectral function at the anti-nodal point $(\pi, 0)$ for different dopings $(0.0 \leq x \leq 0.1)$ at $\beta = 60\text{eV}^{-1}$. (b) Spectral function at the nodal $(\pi/2, \pi/2)$ and anti-nodal point $(\pi, 0)$ (multiplied by a factor 10) at two temperatures below and above the PG transition for $x = 0.05$.

particle was attributed to a coupling to phonons which are not included within our theoretical framework. We do not infer on the validity of this proposition since this would require a better characterization of many samples and a comparison between a larger number of them, as well as the modification of our simple effective model to allow for the coupling of the electrons to additional degrees of freedom.

When a quasiparticle peak is present in the photoemission data, a double peak structure at the nodal point is observed [91, 92]. As shown in Fig. 3.7(c), the double peak structure is reproduced, although the peak separation is much sharper than in experiment. The quasiparticle peak forms at low-energy as the dispersion goes from Γ to M, like in the measured data, and it is backfolded when crossing the nodal point. The latter is not clearly seen in experiment, which may come from the quasi-particle suppression, or an overestimation of the strength of the antiferromagnetic spin fluctuations in the 2×2 plaquette.

Though, overall the CDMFT calculations yield an excellent agreement with the ARPES measurements, and capture the essential ingredients of the hole-doped NaCCOC spectral function: the opening of a PG at low doping and a waterfall feature at the nodal point at low-energy. It is furthermore insightful to study the doping and temperature dependence of the PG and the quasiparticle peak at the nodal point. In Fig. 3.8(a) is shown the doping dependence of the spectral function at the anti-nodal point $(\pi, 0)$ at $\beta = 60\text{eV}^{-1}$. The undoped system shows a broad peak around -0.5eV as we have seen previously. As the doping is increased, and even for the lowest doping $(x = 0.01)$, we see an asymmetric double peak structure appearing with two peaks located away from the Fermi level, roughly at $\omega = \pm 0.15$eV. The difference between the occupied and

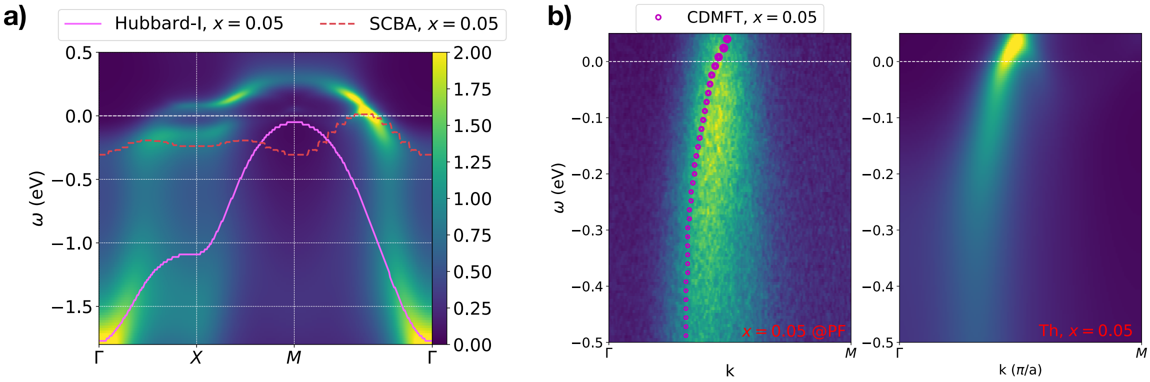

Figure 3.9: (a) calculated spectral function for $x = 0.05$ at $\beta = 40\text{eV}^{-1}$. The Hubbard-I approximation is slightly shifted for the sake of comparison in energy, as well as the SCBA dispersion. (b) Comparison between the experimental and theoretical spectrum for the $x = 0.05$ sample around the nodal point. The purple circles denote the maximum of the theoretical spectral function at each k-point, and the relative spectral weight is depicted by the circle size.

empty regions comes from the particle-hole asymmetry, and is therefore reduced as the doping is increased. Upon increasing the hole concentration, the gap fills up until an almost closing of the PG, but the two peaks below and above the Fermi level do not collapse, consistently with previous observations [261]. Note that the peaks position may vary between the different dopings due to systematic errors from the analytic continuation.

The temperature dependence of the spectral function provides useful information about the possible origin of the PG. In Fig. 3.8(b) is shown the spectral function both at the nodal and anti-nodal point for $x = 0.05$ at two different temperatures: $\beta = 20, 60\text{eV}^{-1}$. Similarly to the undoped case, we observe that for high temperature the anti-nodal PG disappears, as well as the double peak structure at the nodal point. This may indicate an influence of the spin fluctuations on the PG [75, 104, 107, 111–114, 246] since the double peak structure at the nodal point is related to the spin-polaron physics as shown in Fig 3.6(a) where we observe that the coherent quasiparticle peak dispersion corresponds well to that of a spin-polaron. It is the subject of the next section, in which we dissect the CDMFT result to search for the physical origin of the PG in the 2D Hubbard model, and thus, by extension, in cuprates.

Before proceeding to such an analysis, it is important to note that the waterfall feature and the PG are not a peculiar consequence of the 2×2 cluster. In Fig. 3.9 is shown the CDMFT spectral function obtained with an 8-site cluster (see Fig. 3.2(c)) at $\beta = 40\text{eV}^{-1}$ for $x = 0.05$, and its comparison to the experimental spectrum. Because the 8-site cluster is breaking the x/y symmetry since it is elongated along one or the other direction (see Fig. 3.2(c)), we restore the symmetry when performing the Green's function reperiodization by averaging between the $x-$ and $y-$ oriented clusters. We first notice that both the waterfall feature and the PG are captured by this larger cluster, in agreement with the findings by Gull *et al.* that the cluster size (though in DCA) does not influence much the main characteristics of the spectrum [110]. The Hubbard-I approximation accounts well for the high-energy part of the dispersion, although a small constant shift of 0.15eV has been applied. Similarly, the spin-polaron captures rather well the low-energy part

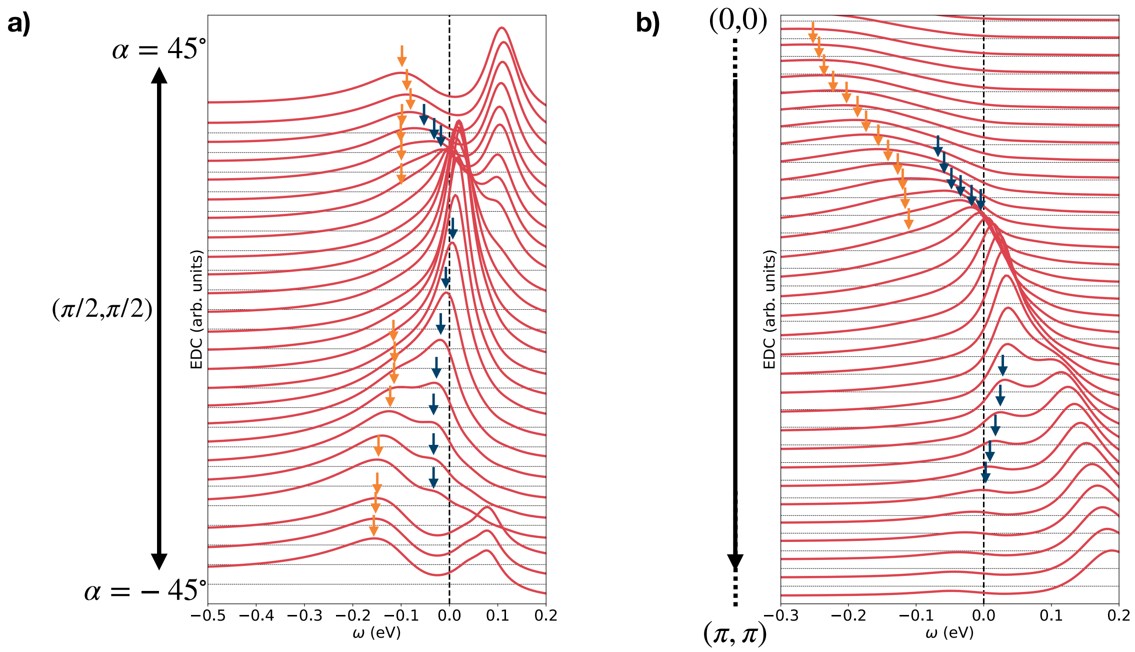

Figure 3.10: (a) EDC along the Fermi arc following the convention of Fig. 3.7(b) obtained with the 8−site cluster at $\beta = 40\text{eV}^{-1}$ for $x = 0.05$. (b) EDC around the nodal point along the path $\Gamma - M$. The orange (blue) arrows highlight the high- (low-) energy peaks.

of the spectrum, although it seems to overestimate slightly the effective mass of the electrons, which is to be expected since in the doped system the antiferromagnetic fluctuations are weaker than at half-filling. The $\Gamma - M$ dispersion is again in excellent agreement with the experimental measurements with a clear kink in the dispersion around 0.3eV.

In Fig. 3.10 we show the EDC calculated with the 8−site cluster at $\beta = 40\text{eV}^{-1}$ for $x = 0.05$. Interestingly the EDC along the Fermi arc show a different qualitative behavior than that of the plaquette cluster: for the latter a secondary peak appears at the nodal point around −0.1eV while the low-energy peak is already formed, whereas for the 8−site cluster the low-energy peak arises at the nodal point from the higher-energy feature which disperses between −0.2, −0.1eV. We come back on this difference later in the chapter. The 8−site cluster is in better agreeement with the measured spectrum of Ref. 91,92 along the path $\Gamma - M$, as shown in Fig. 3.10(b). Indeed, there is no longer a clear separation between the two peaks at the nodal point, and the absence in experiment of backfolding of the low-energy peak when crossing the nodal point can be explained by the fact that it happens in the occupied part of the spectrum, as shown in Fig. 3.10(b). This is a clear improvement of the 8−site cluster as compared to the plaquette, since with the latter the backfolded quasiparticle peak always lies below the Fermi level.

3.4 CLUSTER ANALYSIS

The analysis of the waterfall feature in terms of a crossover between a localized limit at high energy and a spin-polaron at low-energy, as well as the correspondence between the closing of the PG and the disappearance of the waterfall feature at high temperature point to the importance of the short-range spin fluctuations in describing the low-energy physics of the 2D Hubbard model, and by extension to that of the cuprates. These observations are in line with the existing literature finding hallmarks of dominating short-range spin fluctuations [75, 104, 107, 111–114, 246]. In the following, we aim at deepening further the analysis of the CDMFT calculations by investigating the cluster state histogram which can be extracted from the impurity solver. The histogram provides the probability for the plaquette connected to a self-consistent electron bath to be in specific states. We dissect the results for the 2×2 plaquette which is simple enough to provide insightful information at a low cost, and we show, following the argument of Merino and Gunnarsson [121], that its simple state histogram can provide a scenario for the opening of a PG and that it is not limited to the peculiar 2×2 plaquette cluster. We emphasize the importance of this analysis: it is essential to understand the mechanisms leading to the opening of the PG in the CDMFT calculations since it will allow to extract precious information about the PG phase in the 2D Hubbard model, and therefore in cuprates.

3.4.1 STATE HISTOGRAM

In order to obtain the state histogram, we performed calculations using the `CT-HYB` solver from `TRIQS` [119, 120]. Note that the state histograms were obtained with $U = 10t$, in contrast to the usual $U = 10.2t$ in this chapter. This small difference in U has no consequence on the validity of the analysis. All the other quantities discussed in the following were obtained for $U = 10.2t$ as found from the fit of the RIXS data.

Instead of using the site basis, it is more convenient to switch to the cluster momenta basis in which the observables are diagonal in the 2×2 cluster. It is defined as follow:

$$\begin{aligned}
c^{\dagger}_{(0,0),\sigma} &= \frac{1}{2}\left(c^{\dagger}_{1,\sigma} + c^{\dagger}_{2,\sigma} + c^{\dagger}_{3,\sigma} + c^{\dagger}_{4,\sigma}\right) \\
c^{\dagger}_{(\pi,\pi),\sigma} &= \frac{1}{2}\left(c^{\dagger}_{1,\sigma} - c^{\dagger}_{2,\sigma} + c^{\dagger}_{3,\sigma} - c^{\dagger}_{4,\sigma}\right) \\
c^{\dagger}_{(\pi,0),\sigma} &= \frac{1}{2}\left(c^{\dagger}_{1,\sigma} + c^{\dagger}_{2,\sigma} - c^{\dagger}_{3,\sigma} - c^{\dagger}_{4,\sigma}\right) \\
c^{\dagger}_{(0,\pi),\sigma} &= \frac{1}{2}\left(c^{\dagger}_{1,\sigma} - c^{\dagger}_{2,\sigma} - c^{\dagger}_{3,\sigma} + c^{\dagger}_{4,\sigma}\right),
\end{aligned} \tag{3.4}$$

where $1, 2, 3, 4$ denotes the plaquette sites labeled clockwise, see Fig. 3.11(a). Although this basis is convenient, in this chapter we prefer to replace the usual two $c^{\dagger}_{(\pi,0),\sigma}, c^{\dagger}_{(0,\pi),\sigma}$ by their bonding/anti-bonding combination which are defined by:

$$\begin{aligned}
c^{\dagger}_{D13,\sigma} &= \frac{1}{\sqrt{2}}\left(c^{\dagger}_{(\pi,0),\sigma} + c^{\dagger}_{(0,\pi),\sigma}\right) = \frac{1}{\sqrt{2}}\left(c^{\dagger}_{1,\sigma} - c^{\dagger}_{3,\sigma}\right) \\
c^{\dagger}_{D42,\sigma} &= \frac{1}{\sqrt{2}}\left(-c^{\dagger}_{(\pi,0),\sigma} + c^{\dagger}_{(0,\pi),\sigma}\right) = \frac{1}{\sqrt{2}}\left(c^{\dagger}_{4,\sigma} - c^{\dagger}_{2,\sigma}\right)
\end{aligned} \tag{3.5}$$

where the $D13, D42$ orbitals are diagonal bonding orbitals between sites $1, 3$ and $4, 2$. We therefore analyze the plaquette state histogram with the basis set $\{(0,0), (\pi,\pi), D13, D42\}$.

For the isolated cluster, these four orbitals have different on-site energies illustrated in Fig. 3.11(a):

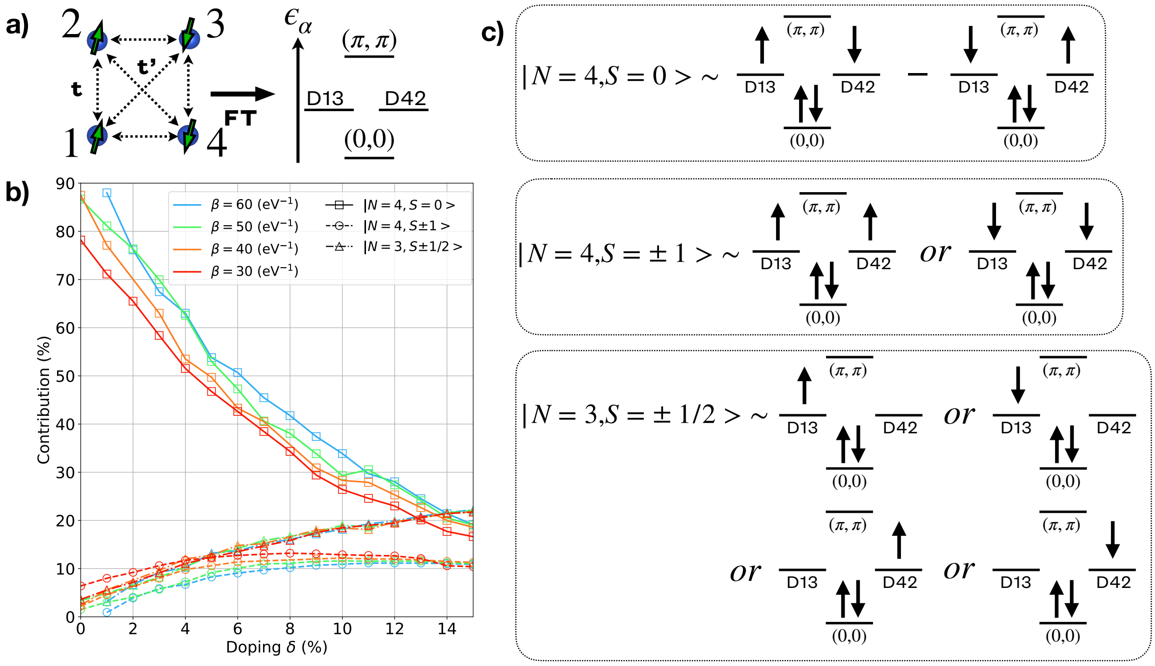

Figure 3.11: (a) Sketch of the on-site energies of the isolated plaquette cluster. (b) Doping and temperature dependent state histogram calculated with $U = 10t$. (c) Sketch of the three leading groups of states.

at half-filling the $(0,0)$ orbital is expected to be doubly occupied, while the orbitals $D13$ and $D42$ will share the two electrons left since they are degenerate, and the orbital (π,π) is empty. In agreement with this simple picture, and with previous works [48, 247, 262], we find that the state histogram is dominated by only a few states which can be grouped into three categories, as shown in Fig. 3.11(b)-(c). These states, reduced to their most important components, can be approximately written

$$\begin{aligned}
|N = 4, S = 0\rangle &\simeq |\uparrow\downarrow, 0\rangle \otimes (|\uparrow,\downarrow\rangle - |\downarrow,\uparrow\rangle) \\
|N = 4, S = 1\rangle &\simeq |\uparrow\downarrow, 0\rangle \otimes |\uparrow,\uparrow\rangle \qquad (3.6)\\
|N = 3, S = 1/2\rangle &\simeq |\uparrow\downarrow, 0\rangle \otimes |\uparrow, 0\rangle
\end{aligned}$$

where we adopt the convention $|\phi\rangle = |(0,0),(\pi,\pi)\rangle \otimes |D13, D42\rangle$, i.e. we separate $(0,0),(\pi,\pi)$ and $D13, D42$ orbitals for convenience, and we show only one of the two (four) possible configurations for the states $|N = 4, S = 1\rangle$ ($|N = 3, S = 1/2\rangle$) (see Fig. 3.11(c)).

The most likely state is $|N = 4, S = 0\rangle$, which corresponds to a superposition of resonating valence bond (RVB) singlets [263] between NN [121, 247]. Interestingly, within our new choice of basis, this state involves a singlet between the $D13$ and $D42$ orbitals. As expected from the isolated plaquette limit, this state dominates the histogram at low doping, and its contribution increases with decreasing temperature, showing that the short range antiferromagnetic fluctuations play a crucial role in the physics of the PG. At high temperature ($\beta = 30\text{eV}^{-1}$), the second group of states is $|N = 4, S = 1\rangle$ which corresponds to a spin flip excitation: going from $|N = 4, S = 0\rangle$ to $|N = 4, S = 1\rangle$ involves for instance the spin flip term $c^{\dagger}_{D13,\sigma}c_{D42,-\sigma}$, which carries a spin $S = 1$ and a momentum $\mathbf{Q} = (\pi,\pi)$. As the doping is increased, i.e. as electrons are removed from the lattice, this group's contribution shows an increase until $x \sim 0.1$ where it saturates and slowly drops as the doping is further increased. Therefore, at intermediate dopings the $N = 4$ configurations are increasingly populated by these $S = 1$ excitations, showing that the singlet state breaks into $S = 1$ triplet states. At large dopings, the dominating group of states is $|N = 3, S = 1/2\rangle$, which simply corresponds to the removal of an electron in the $D13$, $D42$ orbitals.

Since the $D13$, $D42$ are directly related to the $(\pi, 0)$, $(0, \pi)$ orbitals, and since they are half-filled, we can expect that the low-energy physics close to the anti-nodal point is related to the physics of these orbitals which forms a singlet in the state $|N = 4, S = 0\rangle$. Similarly, from this simple picture we expect the $(0, 0)$ orbital to account for the LHB dispersion around the Γ point, and from the (π, π) orbital to capture the unoccupied part of the spectrum close to M. In fact, this can be directly visualized in the spectral function by decomposing it into different contributions from the $(0, 0), (\pi, \pi), D13, D42$ orbitals. To this aim, the site-basis component of the Green's function $\tilde{G}_\sigma$ can be expressed with the diagonal components of the Green's function $\tilde{\mathbf{G}}_\sigma$ in the rotated basis:

$$\mathbf{G}_\sigma = \mathbf{P}\begin{pmatrix} \tilde{\mathbf{G}}_{(0,0),\sigma} & 0 & 0 & 0 \\ 0 & \tilde{\mathbf{G}}_{D13,\sigma} & 0 & 0 \\ 0 & 0 & \tilde{\mathbf{G}}_{D42,\sigma} & 0 \\ 0 & 0 & 0 & \tilde{\mathbf{G}}_{(\pi,\pi),\sigma} \end{pmatrix}\mathbf{P}^{-1} \quad \mathbf{P} = \frac{1}{2}\begin{pmatrix} 1 & \sqrt{2} & 0 & -1 \\ 1 & 0 & -\sqrt{2} & 1 \\ 1 & -\sqrt{2} & 0 & -1 \\ 1 & 0 & \sqrt{2} & 1 \end{pmatrix}. \tag{3.7}$$

The Green's function reperiodization (Eq. 2.48) can then be re-written in terms of the diagonal $\tilde{\mathbf{G}}_{(0,0),\sigma}, \tilde{\mathbf{G}}_{D13,\sigma}, \tilde{\mathbf{G}}_{D42,\sigma}, \tilde{\mathbf{G}}_{(\pi,\pi),\sigma}$ components as:

$$G^{per}_\sigma(\mathbf{k}, i\omega_n) = \sum_m a_m(\mathbf{k})\tilde{\mathbf{G}}_{m,\sigma}, \tag{3.8}$$

where m denote the orbitals $\{(0, 0), (\pi, \pi), D13, D42\}$ and $a_m(\mathbf{k})$ are momentum-dependent weights for each of the components.

The result of such decomposition is shown in Fig. 3.12 for the $x = 0.05$ and $x = 0.10$ that we have already discussed previously, i.e. calculated at $\beta = 60\text{eV}^{-1}$ with the plaquette cluster. As expected, the (π, π) contribution is almost limited to the occupied region around the M point, some incoherent spectral weight can be noticed in the occupied part due to the small but non-zero filling of this orbital. The $(0, 0)$ contribution is substantial around Γ and is therefore responsible for the atomic limit behavior. Interestingly, it also accounts for most of the spectral weight at the nodal point $(\pi/2, \pi/2)$ and a clear waterfall feature is seen, i.e. the $(0, 0)$ also hosts the coherent spin-polaron at low-energy. Most importantly, its contribution at the anti-nodal point $(\pi, 0)$ vanishes, leaving the $D13$ and $D42$ as the only non-zero terms in this region. This provides a hint for why the SCBA dispersion is in good agreement at the nodal point, but always seems to be shifted in energy at the anti-nodal point: these two regions are in fact determined by electrons living on different orbitals. The $D13$, $D42$ orbitals are responsible for the PG physics: they display two rather flat dispersions around the anti-nodal point. Note that they also have a non-zero contribution at the nodal point, such that the double peak feature observed in the 2×2 plaquette results is a consequence of the periodization procedure, which at the nodal point superposes the

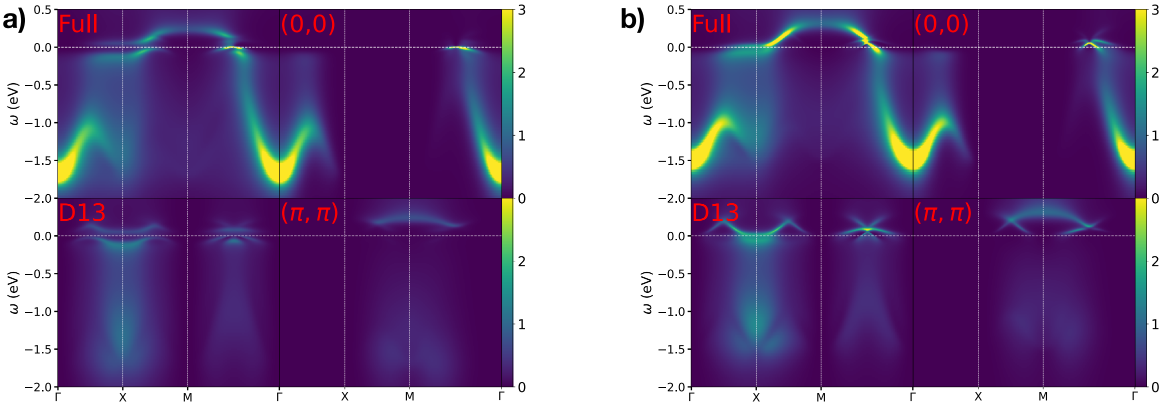

Figure 3.12: Momentum-resolved spectral function and its decomposition into the different diagonal $\tilde{\mathbf{G}}_{(0,0),\sigma}$, $\tilde{\mathbf{G}}_{D13,\sigma}$, $\tilde{\mathbf{G}}_{D42,\sigma}$, $\tilde{\mathbf{G}}_{(\pi,\pi),\sigma}$ components for (a) $x = 0.05$ and (b) $x = 0.1$, both calculated at $\beta = 60\text{eV}^{-1}$ with the plaquette cluster.

contribution from $(0, 0)$ and the $D13$, $D42$ orbitals. We shall get back to this point later with the 8-site cluster.

This simple analysis allows us to make a difference between the key features of the spectral function. Most importantly, it shows that the PG is related to the behavior of the $D13$, $D42$ orbitals which have the tendency to form a singlet state at low doping. If the cluster is isolated, this singlet state naturally leads to an opening of a gap at the anti-nodal point (one can think of it as a dimer). However, when it is connected to a bath of non-interacting electrons, it is not clear why the gap would remain open: this is the case of the $(0, 0)$ orbital for instance, which in the isolated cluster is supposed to be doubly occupied but shows a large quasiparticle peak at the Fermi energy in the CDMFT spectral function! In the following, based on the derivation of Merino *et al.* [121] that we adapt to our specific choice of basis, we show that the gap remains open due to the very nature of the non-degenerate singlet state using a simple effective model. Moreover, we also discuss why this mechanism should hold for the 8-site cluster, and therefore for larger systems.

3.4.2 Origin of the pseudogap

Despite the fact that the isolated $D13$, $D42$ orbitals would show a gap since they form a singlet state, it is not straightforward that the gap remains open when coupling to a continuous bath of electrons. Indeed, the latter allows photoemission processes from a state with N electrons on the cluster to the same state with N electrons on the cluster and one missing bath electrons, thus giving a zero energy contribution. Following the derivation of Ref. 121 that we specialize for the singlet state $|N = 4, S = 0\rangle$, we show in this section that in the limit of large U, the non-degenerate singlet ground state leads to a destructive interference of such processes, so that the gap remains non-zero even if the system is coupled to a continuous bath of electrons.

To derive a simple effective model, we will approximate the $D13$, $D42$ orbitals as disconnected from the $(0, 0)$, (π, π) orbitals such that they form a two-level system connected to a continuous bath of non-interacting electrons. This is a reasonable approximation given that the Green's func-

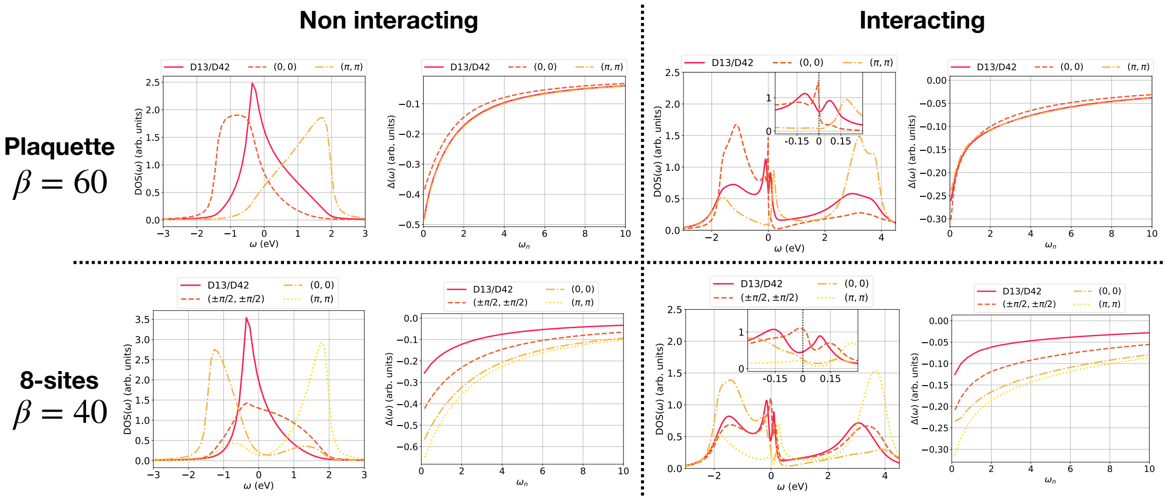

Figure 3.13: Non-interacting and interacting (obtained from the last CDMFT calculation) imaginary part of the hybridization function on the Matsubara axis $\Delta(i\omega_n)$ and DOS on the real axis, for both the plaquette and 8−site cluster.

tion in this basis is purely diagonal. The details of the Hamiltonian governing the isolated $D13$, $D42$ orbitals are not important, as long as they lead to a ground state of the form (for the isolated orbitals):

$$|GS\rangle = \frac{1}{\sqrt{2}}(|\uparrow,\downarrow\rangle - |\downarrow,\uparrow\rangle), \tag{3.9}$$

consistently with the state $|N = 4, S = 0\rangle$. In the 2×2 cluster, it is the short range antiferromagnetic fluctuations that causes the emergence of the RVB-like singlet state.

The coupling to the continuous bath of non-interacting electrons can be written:

$$H_{hyb} = \sum_{m\sigma,\epsilon} V_\epsilon\left(d^\dagger_{m\sigma,\epsilon} c_{m\sigma} + h.c.\right) \tag{3.10}$$

where $d^\dagger_{m\sigma,\epsilon}, d_{m\sigma,\epsilon}$ are the creation and annihilation operators of a bath electron of orbital m, spin σ and energy ϵ, $c^\dagger_{m\sigma}, c_{m\sigma}$ the ones of the cluster electrons, and V_ϵ the coupling between the bath and the cluster, taken to be orbital independent since they are equivalent. The orbital index m refers either to $D13$ or $D42$. Since we are in the limit $U \gg t$, we can also consider that $U \gg V_\epsilon$, such that the hybridization to the bath may be treated in perturbation theory. This is justified by inspecting the hybridization function of the different orbitals of the plaquette both for the non-interacting case, and for the interacting case obtained after the CDMFT self-consistent cycle (i.e. with correlated effects already incorporated), as shown in Fig. 3.13. The hybridization function has a maximum of −0.5 for the $D13$, $D42$ orbitals in the non-interacting case, which is further reduced after the CDMFT self-consistent calculations, and is in both cases much lower than U. While the non-interacting DOS shows a van Hove sigularity for the $D13$, $D42$ orbital [247], after the CDMFT cycle it shows a PG, while the $(0, 0)$ orbital shows a coherent peak a the Fermi energy.

In the ground state (Eq. 3.9), the two orbitals are half-filled and there are two cluster electrons. When connecting the cluster to the bath, the number of electrons on the cluster is not fixed, but that of the full system is conserved. At first order, the correction to the ground state originates from states formed by the hopping of a cluster electron to the bath, or the reverse, i.e. states of the form:

$$\begin{aligned} &d^\dagger_{m\sigma,\epsilon}c_{m\sigma}|GS\rangle \\ &c^\dagger_{m\sigma}d_{m\sigma,\epsilon}|GS\rangle, \end{aligned} \tag{3.11}$$

which are states with $N-1$ and $N+1$ electrons on the cluster, and where we take the convention that the $|GS\rangle$ is a product between the cluster and the bath states (not explicitly written for the sake of simplicity). The corrections to the ground state will involve matrix elements of the type:

$$\begin{aligned} \langle GS|d^\dagger_{m\sigma,\epsilon}c_{m\sigma}V_\epsilon c^\dagger_{m'\sigma'}d_{m'\sigma',\epsilon}|GS\rangle =&\delta_{mm',\sigma\sigma',\epsilon\epsilon'}\langle GS|d^\dagger_{m\sigma,\epsilon}c_{m\sigma}V_\epsilon c^\dagger_{m'\sigma'}d_{m'\sigma',\epsilon}|GS\rangle \\ =&V_\epsilon\langle GS|n^d_{m\sigma,\epsilon}(1-n^c_{m\sigma})|GS\rangle, \end{aligned} \tag{3.12}$$

for the $N-1$ contribution, and for the $N+1$:

$$V_\epsilon\langle GS|n^c_{m\sigma}(1-n^d_{m\sigma,\epsilon})|GS\rangle. \tag{3.13}$$

We consider in the following

$$V_\epsilon\langle GS|n^d_{m\sigma,\epsilon}(1-n^c_{m\sigma})|GS\rangle \simeq V_\epsilon\langle GS|n^c_{m\sigma}(1-n^d_{m\sigma,\epsilon})|GS\rangle = \tilde{V}_\epsilon, \tag{3.14}$$

such that both $N+1$ and $N-1$ correction terms have the same amplitude, which is justified since the self-consistent electron bath is supposed to be at the same relative filling as the cluster.

We can now write the corrected ground state as

$$\begin{aligned} |\psi\rangle &= |GS\rangle + \sum_{m\sigma,\epsilon}\frac{\tilde{V}_\epsilon}{\Delta_+ - \epsilon}c^\dagger_{m\sigma}d_{m\sigma,\epsilon}|GS\rangle + \sum_{m\sigma,\epsilon}\frac{\tilde{V}_\epsilon}{\Delta_- + \epsilon}d^\dagger_{m\sigma,\epsilon}c_{m\sigma}|GS\rangle \\ &= |GS\rangle - \sum_{m\sigma,\epsilon}\frac{\tilde{V}_\epsilon}{\Delta_+ - \epsilon}d_{m\sigma,\epsilon}c^\dagger_{m\sigma}|GS\rangle + \sum_{m\sigma,\epsilon}\frac{\tilde{V}_\epsilon}{\Delta_- + \epsilon}d^\dagger_{m\sigma,\epsilon}c_{m\sigma}|GS\rangle, \end{aligned} \tag{3.15}$$

where $\Delta_\pm$ corresponds to the difference in cluster energy between the ground state and the $N+1/N-1$ states, and we ordered the operators in the second term such that the cluster creation/annihilation operators always appear to the right with respect to the bath operators. In principle, as mentioned above, the coupling to the bath authorizes photoemission processes between the ground state $|GS\rangle$, and a final state like $\sim d_{m\sigma,\epsilon}|GS\rangle$ which, if it is a bath electron at the Fermi level, leads to a non-zero spectral weight at zero energy since $|GS\rangle$ and $\sim d_{m\sigma,\epsilon_F}|GS\rangle$ would have the same energy. To show that such process is in fact canceled when the ground state is of the nature of Eq. 3.9, we take the example (not restrictive) of a photoemission process that involves the removal of an electron $c_{D13\uparrow}$ on the cluster. We need to calculate a matrix element of the type

$$\langle\phi_f|c_{D13\uparrow}|\psi\rangle, \tag{3.16}$$

where we consider the final state $|\phi_f\rangle$ composed of the cluster in its ground state and a removed bath electron at the Fermi energy:

$$|\phi_f\rangle = d_{m\sigma,\epsilon_F}|GS\rangle - \sum_{m\sigma,\epsilon} \frac{\tilde{V}_\epsilon}{\Delta_+ - \epsilon} d_{m\sigma,\epsilon} c^\dagger_{m\sigma} d_{m\sigma,\epsilon_F}|GS\rangle + \sum_{m\sigma,\epsilon} \frac{\tilde{V}_\epsilon}{\Delta_- + \epsilon} d^\dagger_{m\sigma,\epsilon} c_{m\sigma} d_{m\sigma,\epsilon_F}|GS\rangle. \tag{3.17}$$

In order to calculate this matrix element, it is useful to re-write the corrected ground state using the explicit expression of $|GS\rangle$:

$$\begin{aligned}|\psi\rangle =& \frac{1}{\sqrt{2}}(|\uparrow,\downarrow\rangle - |\downarrow,\uparrow\rangle) \\ &+ \frac{1}{\sqrt{2}}\sum_\epsilon \frac{\tilde{V}_\epsilon}{\Delta_+ - \epsilon}\Big[d_{D13\uparrow,\epsilon}|\uparrow\downarrow,\uparrow\rangle + d_{D13\downarrow,\epsilon}|\uparrow\downarrow,\downarrow\rangle + d_{D42\uparrow,\epsilon}|\uparrow,\uparrow\downarrow\rangle + d_{D42\downarrow,\epsilon}|\downarrow,\uparrow\downarrow\rangle\Big] \\ &+ \frac{1}{\sqrt{2}}\sum_\epsilon \frac{\tilde{V}_\epsilon}{\Delta_- + \epsilon}\Big[d^\dagger_{D13\uparrow,\epsilon}|0,\downarrow\rangle - d^\dagger_{D13\downarrow,\epsilon}|0,\uparrow\rangle - d^\dagger_{D42\uparrow,\epsilon}|\downarrow,0\rangle + d^\dagger_{D42\downarrow,\epsilon}|\uparrow,0\rangle\Big].\end{aligned} \tag{3.18}$$

The action of the annihilation operator $c_{D13\uparrow}$ on the corrected ground state gives

$$c_{D13\uparrow}|\psi\rangle = \frac{1}{\sqrt{2}}|0,\downarrow\rangle + \frac{1}{\sqrt{2}}\sum_\epsilon \frac{\tilde{V}_\epsilon}{\Delta_+ - \epsilon}\Big[-d_{D13\uparrow,\epsilon}|\downarrow,\uparrow\rangle + \dots\Big] + \dots \tag{3.19}$$

where we kept only the terms that will contribute to the matrix element. Similarly, keeping only the relevant elements, the final state can be written

$$|\phi_f\rangle = d_{D13\uparrow,\epsilon_F}\frac{1}{\sqrt{2}}(|\uparrow,\downarrow\rangle - |\downarrow,\uparrow\rangle) - \sum_\epsilon \frac{\tilde{V}_\epsilon}{\Delta_- + \epsilon}\Big[d^\dagger_{D13\uparrow,\epsilon} d_{D13\uparrow,\epsilon_F}|0,\downarrow\rangle + \dots\Big] + \dots \tag{3.20}$$

Combining Eq. 3.19 and 3.20, we obtain the following approximated expression for the matrix element [121]

$$\langle\phi_f|c_{D13\uparrow}|\psi\rangle = \frac{1}{2}\sum_\epsilon \frac{\tilde{V}_\epsilon}{\Delta_+ - \epsilon}\langle\downarrow,\uparrow|d^\dagger_{D13\uparrow,\epsilon_F} d_{D13\uparrow,\epsilon}|\downarrow,\uparrow\rangle - \frac{1}{2}\sum_\epsilon \frac{\tilde{V}_\epsilon}{\Delta_- + \epsilon}\langle 0,\downarrow|d^\dagger_{D13\uparrow,\epsilon_F} d_{D13\uparrow,\epsilon}|0,\downarrow\rangle. \tag{3.21}$$

Since $\langle\downarrow,\uparrow|d^\dagger_{D13\uparrow,\epsilon_F} d_{D13\uparrow,\epsilon}|\downarrow,\uparrow\rangle = \langle 0,\downarrow|d^\dagger_{D13\uparrow,\epsilon_F} d_{D13\uparrow,\epsilon}|0,\downarrow\rangle = \delta_{\epsilon,\epsilon_F}$, in the symmetric case ($\Delta_+ = \Delta_-$) the two terms cancel each other. The very same derivation can be done for $c_{D13\downarrow}, c_{D42\uparrow}, c_{D42\downarrow}$, hence the zero-energy spectral weight is entirely suppressed. This mechanism is at the origin of the PG observed at the anti-nodal point for the 2 × 2 plaquette.

The first non-zero excitation channel will be the one relating the singlet ground state $|N = 4, S = 0\rangle$ to the lowest excited state, which is the triplet $|N = 4, S = 1\rangle$. The PG is therefore related to the breaking of the RVB-like singlets by excitations carrying a spin $S = 1$ and momentum $\mathbf{Q} = (\pi,\pi)$. This is in agreement with the observations made via the fluctuation diagnostic technique [112–114], as well as dual boson calculations [75]. At relatively high doping, this picture breaks down since the state histogram shows substantial contributions from the degenerate set of states $|N = 3, S = 1/2\rangle$ which do not lead to a cancellation of the zero-energy excitation [121].

An important point is whether this mechanism is an artifact of the plaquette cluster, or if this holds for larger systems. In particular, for the 8−site cluster there are not only the $(\pi,0)/(0,\pi)$ (i.e. $D13/D42$) orbitals which are degenerate and related by $\mathbf{Q}=(\pi,\pi)$, but also the $(\pm\pi/2,\pm\pi/2)$ so that one may expect that the same mechanism occurs also for these orbitals thus inducing a gap at the nodal point. As shown previously, we observe a clear quasi-particle peak at the nodal point, so that the scenario described above for the $D13$, $D42$ orbitals seems not to apply to the $(\pm\pi/2,\pm\pi/2)$ orbitals. The reason behind this is illustrated in Fig. 3.13: the hybridization of the $(\pm\pi/2,\pm\pi/2)$ orbitals to the bath is twice larger than the one of the $D13$, $D42$ orbitals. The isolated ground state on the cluster is no longer a good approximation for these orbitals. Instead, the $(\pm\pi/2,\pm\pi/2)$ orbitals hybridize with the bath leading to a clear quasi-particle peak in the interacting DOS obtained after the CDMFT cycle. Interestingly, the difference between the $D13$, $D42$ and $(\pm\pi/2,\pm\pi/2)$ orbitals is already present at the non-interacting level (see Fig. 3.13), due to the difference in the energy dispersion [121].

From these considerations we can understand the qualitative differences in the EDC shown in Fig. 3.7 and Fig. 3.10, respectively for the plaquette and the 8−site cluster. At the nodal point, it is shown in Fig. 3.12 that the spectral function calculated with the plaquette is the superposition of the contributions from the $(0,0)$ and $D13/D42$ orbitals. These two sets of orbitals are almost independent from each other, and their superposition at the nodal point is the product of the periodization procedure, such that the two-peak structure observed in Fig. 3.7(c) is ”artificial” and overestimates the peak splitting. It also has a large influence on the dispersion along the Fermi arc: in Fig. 3.7(b), the low-energy peak at the Fermi level is already present at the anti-nodal point (although shifted in energy) and smoothly evolves into the sharp quasiparticle peak at the nodal point, along with the appearance of a sub feature around −0.1eV. This can be linked with a smooth evolution from a $D13/D42$ to a $(0,0)$ contribution as getting closer to the nodal point, along with the appearance of a well separated satellite at the nodal point due to the $D13/D42$ orbitals, as can be seen in Fig. 3.12.

For the 8−site cluster the scenario is different: at the nodal point the periodization procedure ensure that the cluster momenta orbitals $(\pm\pi/2,\pm\pi/2)$ are the only contributors. Towards the nodal point, the spectral function smoothly evolves from a $(0,0)$ to a $(\pm\pi/2,\pm\pi/2)$ contribution along the path $\Gamma-M$, and from $D13/D42$ to $(\pm\pi/2,\pm\pi/2)$ along the Fermi arc (by varying α). Since the $(\pm\pi/2,\pm\pi/2)$ orbitals are also subject to the $\mathbf{Q}=(\pi,\pi)$ fluctuations and are more sensitive than the $(0,0)$ orbital (the hybridization to the bath is weaker, see Fig. 3.13), the resulting quasi-particle peak at the nodal point is broader and the double peak are less distinct, in agreement with the experiment. Especially along the Fermi arc, the behavior of the EDC as a function of α is different from the plaquette cluster: the low-energy peak emerges close to the nodal point but does not come from a smooth evolution of the PG peak at the anti-nodal point. This is linked to the explicit existence of the $(\pm\pi/2,\pm\pi/2)$ orbitals which becomes the main contribution around the nodal point, in contrast with the plaquette cluster where it is a combination of $D13/D42$ and

(0, 0) orbitals. The PG peak at the anti-nodal point seems to be smoothly absorbed into a shoulder of the quasiparticle peak at the nodal point.

3.5 DYNAMICAL SPIN STRUCTURE FACTOR: A DIRECT PROBE OF THE SPIN FLUCTUATIONS

The results we have shown and analyzed so far point to an understanding of the waterfall and PG physics in a unified framework of antiferromagnetic spin fluctuations. It is therefore interesting to probe directly the collective spin fluctuations: in experiment this can be done with RIXS measurements which have proven useful to extract information about the magnon excitations in cuprates [166, 248–250]. Contrary to ARPES, calculating a RIXS spectrum is extremely challenging [264], and it is easier to use indirect comparison between theory and experiments. RIXS is sensitive to the DSSF [264], which is at the origin of the low-energy peaks usually identified as (para)-magnons.

The DSSF can be determined within CDMFT via the two-time two-particle Green's function which is accessible through some impurity solvers. In this thesis, we used the `CT-HYB` [116] solver to obtain the two-time two-particle Green's function. After a the self-consistent CDMFT loop is converged using the `CT-INT` [117] solver, an extra loop is done with `CT-HYB`. In order to improve the sampling of the two-particle quantity, the eigen states of the isolated cluster having an energy larger than 5eV with respect to the ground state were projected out [116]. We ensured that the projection did not change significantly the results, but simply improved the statistics of the two-particle quantity sampling. Unfortunately, the `CT-HYB` was not able to manage the 8−site cluster for it was impossible to perform the calculation in a reasonable amount of time, and since the two-time two-particle Green's function can not be obtained with the `CT-INT` (not implemented yet), we are limited to the 2 × 2 plaquette.

In order to relate the two-time two-particle Green's function to the DSSF, we start from the definition of the latter in imaginary time (since the impurity solver works in Matsubara space):

$$\mathcal{S}(\mathbf{k},\tau) = \frac{1}{L}\sum_{\mathbf{R}_i\mathbf{R}_j} \mathrm{e}^{i\mathbf{k}(\mathbf{R}_j-\mathbf{R}_i)}\langle \mathbf{S}_i(\tau)\mathbf{S}_j(0)\rangle, \tag{3.22}$$

where L is the number of cluster sites, $\mathbf{R}_i$ denotes the position of the site i, and $\mathbf{S}_i(\tau)$ the spin operator acting on site i at time τ. The correlation functions in the sum can be expanded in terms of fermionic creation/annihilation operators.

$$\begin{aligned}
\langle \mathbf{S}_i(\tau)\mathbf{S}_j(0)\rangle =& \left\langle \mathbf{S}^z_i(\tau)\mathbf{S}^z_j(0)\right\rangle + \frac{1}{2}\left[\left\langle \mathbf{S}^+_i(\tau)\mathbf{S}^-_j(0)\right\rangle + \left\langle \mathbf{S}^-_i(\tau)\mathbf{S}^+_j(0)\right\rangle\right] \\
=& \frac{1}{4}\langle (n_{i\uparrow}(\tau) - n_{i\downarrow}(\tau))(n_{j\uparrow}(0) - n_{j\downarrow}(0))\rangle \\
&+ \frac{1}{2}\left[\left\langle c^\dagger_{i\uparrow}(\tau)c_{i\downarrow}(\tau)c^\dagger_{j\downarrow}(0)c_{j\uparrow}(0)\right\rangle + \left\langle c^\dagger_{i\downarrow}(\tau)c_{i\uparrow}(\tau)c^\dagger_{j\uparrow}(0)c_{j\downarrow}(0)\right\rangle\right] \\
=& \frac{1}{4}\left(G_{i\uparrow,i\uparrow,j\uparrow,j\uparrow}(\tau) + G_{i\downarrow,i\downarrow,j\downarrow,j\downarrow}(\tau) - G_{i\uparrow,i\uparrow,j\downarrow,j\downarrow}(\tau) - G_{i\downarrow,i\downarrow,j\uparrow,j\uparrow}(\tau)\right) \\
&+ \frac{1}{2}\left(G_{i\uparrow,i\downarrow,j\downarrow,j\uparrow}(\tau) + G_{i\downarrow,i\uparrow,j\uparrow,j\downarrow}(\tau)\right),
\end{aligned} \tag{3.23}$$

where $G_{i\sigma_i,j\sigma_j,k\sigma_k,l\sigma_l} = \left\langle c^\dagger_{i\sigma_i}(\tau)c_{j\sigma_j}(\tau)c^\dagger_{k\sigma_k}(0)c_{l\sigma_l}(0)\right\rangle$ is the two-time two-particle Green's function which can be directly obtained from the `CT-HYB` solver [116]. Because of the limited size of the 2×2 cluster, we have only access to $\langle \mathbf{S}_i(\tau)\mathbf{S}_j(0)\rangle$ up to the NNN, which is a quite drastic approximation to the Eq. 3.22. In fact, this equation corresponds to the periodization procedure applied to the momentum independent spin-spin correlation functions. For the cluster momenta $(0,0), (\pi,0), (0,\pi), (\pi,\pi)$, it amounts to a basis transformation from the site basis. To compare to the RIXS measurements, we again need to perform an analytic continuation of the DSSF. In practice, due to the noise in the data even with a large sampling number (for $\beta = 60\text{eV}^{-1}$, the lowest number of counts obtained for $x = 0.1$ was $\sim 50 \cdot 10^6$), it is not possible to first perform an analytic continuation of each $\langle \mathbf{S}_i(\tau)\mathbf{S}_j(0)\rangle$ individually, and then apply Eq. 3.22. Instead, the DSSF is calculated at each desired $\mathbf{k}$ point in imaginary time, and then we apply the MEM method with a bosonic kernel using the `MaxEnt` package [220].

The results are shown in Fig. 3.14(a) at a few specific $\mathbf{k}$ points as a function of doping, calculated at $\beta = 60\text{eV}^{-1}$. In agreement with our analysis above and with the literature [75, 111–113], the DSSF is maximum at $\mathbf{Q} = (\pi,\pi)$, hence directly showing the importance of the antiferromagnetic spin fluctuations. Interestingly, the $\mathbf{Q} = (\pi,\pi)$ sector is dominant for all the doping considered (up to $x = 0.1$), and it is stronger in the undoped system as expected. The DSSF's peak at $\mathbf{Q} = (\pi/2,\pi/2)$ is located at lower energy than at $\mathbf{Q} = (\pi,0)/(0,\pi)$, consistently with the experimental observation of Ref. 166 for the parent NaCCOC compound ($x = 0$). However, the difference in energy is overestimated: it is roughly about 100meV for $x = 0$, while in experiment it is measured to be of the order of 40meV [166]. Given that the experimental resolution was 130meV, and that the $\mathbf{Q} = (\pi/2,\pi/2)$ point is not explicitly a cluster momentum, the overall qualitative agreement is satisfying. Most importantly, the CDMFT calculations are able to account for the asymmetric line shape of the peaks which is even more visible at larger dopings as the spectrum broadens, in agreement with the RIXS measurements. As we will show later with the DSSF calculated for a spin-only model, this asymmetric line shape originates from the coupling of the spin excitations to the charge degrees of freedom.

A problem can nevertheless be identified in the doping dependence of the DSSF. Indeed, for

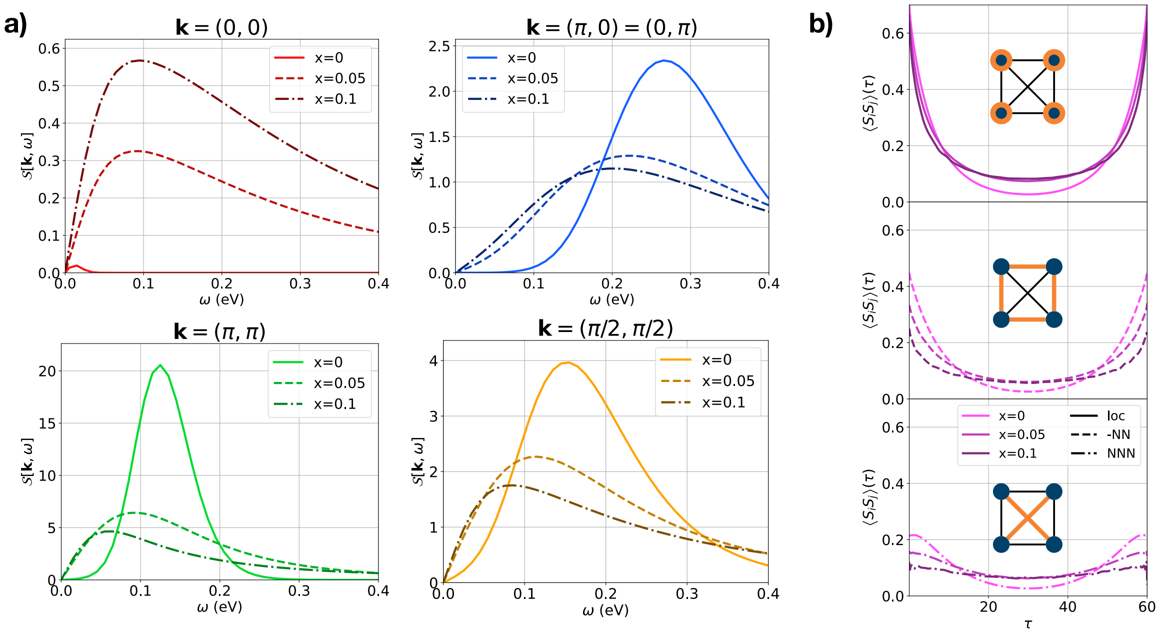

Figure 3.14: (a) DSSF at different **k** points as a function of doping ($x = 0, x = 0.05, x = 0.1$), all calculated at $\beta = 60\text{eV}^{-1}$. The same error estimate (10^{-2}) was used for all spectra to perform the analytic continuation. (b) Local, NN, and NNN cluster spin-spin correlation functions as a function of imaginary time, for different dopings and calculated at $\beta = 60\text{eV}^{-1}$. Note that the NN component has been multiplied by -1.

all the $\mathbf{Q}$ showed here but $\mathbf{Q} = (0,0)$, we observe a softening of the DSSF peak as the doping is increased. It is roughly of the order of 50meV, whereas it was observed experimentally and theoretically with different methods that the peak position should almost not move as a function of doping, or even increase [75, 248–250]. Given that some of these results were obtained after an analytic continuation procedure, the culprit is most probably the finite size of our plaquette cluster. Indeed, the $\mathbf{Q} = (\pi, \pi)$ excitation can only connect the $D13, D42$ orbitals, or the $(0,0), (\pi,\pi)$ orbitals, and therefore lacks the important $(\pm\pi/2, \pm\pi/2)$ channel, which would be included in the 8−site cluster. This is of importance, since the $D13, D42$ orbitals are gapped, while the $(\pm\pi/2, \pm\pi/2)$ orbitals show a coherent quasiparticle peak at the Fermi energy (see Fig. 3.13). Also, one can notice in Fig. 3.14(b) that as the doping is increased, the spin-spin correlation functions saturate at $\tau = \beta/2$ and even exceed the value obtained for the undoped compound. The NNN correlation function at $\tau = \beta/2$ is even slightly larger than the NN component. This phenomenon has already been observed previously [122, 123], and shows that the longer ranged spin-spin correlation functions should be incorporated since they do not show a fast decay with distance at long times $\tau \sim \beta/2$.

The non-zero value of the spin-spin correlation functions at large time $\tau \to \beta/2$ is directly linked to the existence of low-energy spectral weight in the DSSF, i.e. to low-energy excitation modes. Indeed, similarly to the Eq. 2.69 linking the fermionic imaginary time Green's function to its real frequency counterpart, we can relate the imaginary time spin-spin correlation function to its spectral function on the real axis. For the sake of simplicity, we write the imaginary time correlation function as $\mathcal{S}_{ij}(\tau) = \langle \mathbf{S}_i(\tau)\mathbf{S}_j(0)\rangle$, and its relation to the real frequency axis $\mathcal{S}_{ij}(\omega)$ reads

$$
\begin{aligned}
\mathcal{S}_{ij}(\tau) =& \frac{1}{2}\int_{-\infty}^{+\infty} \mathcal{S}_{ij}(\omega)\frac{\mathrm{e}^{-\omega(\beta-\tau)}+\mathrm{e}^{-\omega\tau}}{1-\mathrm{e}^{-\omega\beta}}d\omega \\
=& \int_{0}^{+\infty} \frac{\mathcal{S}_{ij}(\omega)}{\omega}\omega\frac{\mathrm{e}^{-\omega(\beta-\tau)}+\mathrm{e}^{-\omega\tau}}{1-\mathrm{e}^{-\omega\beta}}d\omega,
\end{aligned}
\tag{3.24}
$$

where we use the asymmetry of the function $\mathcal{S}_{ij}(\omega)$ to obtain the second line, in which we artificially divided and multiplied by ω for convenience. At $\tau = \beta/2$, the above expression can be drastically simplified:

$$
\begin{aligned}
\mathcal{S}_{ij}(\beta/2) =& \int_{0}^{+\infty} \frac{\mathcal{S}_{ij}(\omega)}{\omega}\omega\frac{\mathrm{e}^{-\omega(\beta/2)}+\mathrm{e}^{-\omega\beta/2}}{1-\mathrm{e}^{-\omega\beta}}d\omega \\
=& \frac{1}{2}\int_{0}^{+\infty} \frac{\mathcal{S}_{ij}(\omega)}{\omega}\frac{\omega}{\sinh(\omega\beta/2)}d\omega \\
=& \frac{2}{\beta^2}\int_{0}^{+\infty} \left(\frac{\mathcal{S}_{ij}(2\omega/\beta)}{2\omega/\beta}\right)\frac{\omega}{\sinh(\omega)}d\omega.
\end{aligned}
\tag{3.25}
$$

Therefore, at $\tau = \beta/2$ there is a weighting function in the integral of the form $\frac{\omega}{\sinh(\omega)}$, which very quickly goes to zero as ω is increased, whereas its low frequency limit is given by:

$$
\lim_{\omega\to 0}\frac{\omega}{\sinh(\omega)} = \frac{1}{1+\frac{\omega^2}{3!}}.
\tag{3.26}
$$

This means that $\mathcal{S}_{ij}(\beta/2)$ is finite only if $\frac{\mathcal{S}_{ij}(\omega)}{\omega}$ is non-zero at $\omega \to 0$, i.e. if there are low-energy spin excitations.

The plateau observed at long imaginary times in Fig. 3.14 for the doped system is easily explained by these considerations. In the undoped case, the system has a large gap which prevents the low-energy spin excitations, such that at all cluster momenta the DSSF is either suppressed or gapped. However, for both $x = 0.05$ and $x = 0.1$ hole concentration, at all cluster momenta the DSSF is non-zero at low energies, therefore leading to an increase of the spin-spin correlation function at $\tau = \beta/2$. At $\beta = 20$, we can notice that at $\mathbf{Q} = (\pi, \pi)$ and $\mathbf{Q} = (\pi/2, \pi/2)$ the DSSF is not gapped even at $x = 0$, which leads to a much stronger value at $\tau = \beta/2$ for the undoped system, resulting in the absence of the spin freezing phenomena. Note that despite this kind of changes in the DSSF, the temperature also has direct implications on the value of the spin-spin correlation function at $\tau = \beta/2$: as can be seen in Eq. 3.25, a lower temperature results in a lower $\frac{1}{\beta}$ constant, as well as a narrowing of the energy window which effectively contributes to the integral since the frequency dependence of $\mathcal{S}_{ij}$ is scaled by a $\frac{1}{\beta}$ factor. Therefore, in general we can expect the value at $\tau = \beta/2$ to decrease with the temperature. It is indeed what is observed if we compare for instance the spin-spin correlation function calculated at $\beta = 40\text{eV}^{-1}$ and $\beta = 60\text{eV}^{-1}$, two inverse temperatures at which we observe the PG. The results are shown in Fig. 3.15: as expected, the value of the correlation function at long times decreases with decreasing temperature. In-

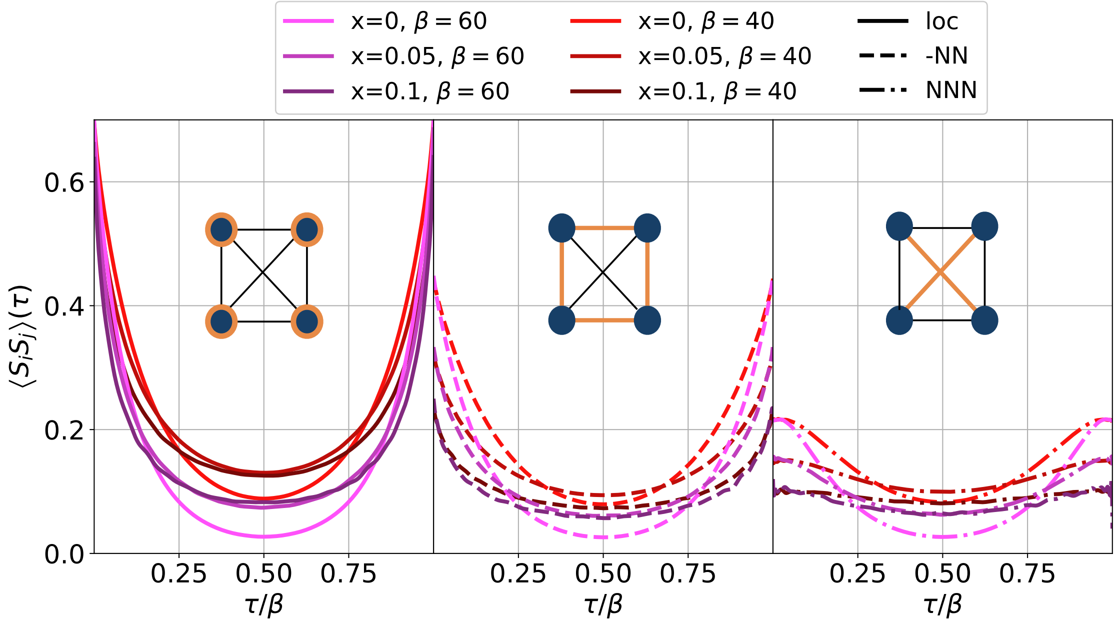

Figure 3.15: Local, NN, and NNN cluster spin-spin correlation functions as a function of imaginary time, for different dopings and calculated at $\beta = 60\text{eV}^{-1}$ and $\beta = 40\text{eV}^{-1}$. Note that the NN component has been multiplied by -1.

terestingly, one can notice that for the doping $x = 0.1$, although its absolute value is lower at $\beta = 60\text{eV}^{-1}$ than at $\beta = 40\text{eV}^{-1}$, it is closer to that of $x = 0$ and $x = 0.05$ at lower temperature, hence being a sign that the freezing propagates to larger dopings with decreasing temperature, which is in agreement with the results of Ref. 123.

If we can explain the increase of the correlation function at $\tau = \beta/2$ from the undoped to the doped system, it is still not clear why it freezes to almost the same value independently of the distance between the sites i and j. It is of utmost importance to understand this point, since it is a clear sign that at long times the correlation function is distance-independent, i.e. is long-ranged. A hint can be found by reversing the Fourier transform of Eq. 3.22:

$$\mathcal{S}_{ij}(\omega) = \frac{1}{L}\sum_{\mathbf{k}} \mathcal{S}(\mathbf{k},\omega). \tag{3.27}$$

With the **k** sum restricted to the cluster momenta, we can obtain the local, NN and NNN correlation function for the 2×2 plaquette:

$$\begin{aligned}\mathcal{S}_{loc}(\omega) =& \frac{1}{4}(\mathcal{S}((0,0),\omega) + \mathcal{S}((\pi,0),\omega) + \mathcal{S}((0,\pi),\omega) + \mathcal{S}((\pi,\pi),\omega))\\ \mathcal{S}_{NN}(\omega) =& \frac{1}{4}(\mathcal{S}((0,0),\omega) - \mathcal{S}((\pi,0),\omega) + \mathcal{S}((0,\pi),\omega) - \mathcal{S}((\pi,\pi),\omega))\\ \mathcal{S}_{NNN}(\omega) =& \frac{1}{4}(\mathcal{S}((0,0),\omega) - \mathcal{S}((\pi,0),\omega) - \mathcal{S}((0,\pi),\omega) + \mathcal{S}((\pi,\pi),\omega)).\end{aligned} \tag{3.28}$$

The key point is to notice that the $\mathbf{Q} = (\pi,\pi)$ term clearly dominates all the others at low-frequency, for small ω all the spin-spin correlation functions in absolute value $|\mathcal{S}_{loc}|$, $|\mathcal{S}_{NN}|$, $|\mathcal{S}_{NNN}|$ are roughly of the same order: $\frac{1}{4}|\mathcal{S}((\pi,\pi),\omega)|$. Combining this observation with the previous argument, it is clear that the spin-spin correlation functions at $\tau = \beta/2$ are equal because they all share the same contribution from $\mathcal{S}((\pi,\pi),\omega)$, such that we have identified the origin of the spin freezing observed by Werner *et al.* [122, 123]. Upon further increasing the hole doping, the $\mathbf{Q} = (\pi,\pi)$ becomes less dominant because the spin-spin fluctuations strongly weaken so that the freezing mechanism disappears, coherent with the temperature dependence observed in Fig. 3.15 and the findings of Werner *et al.* [123]. This result is even more general than the ferromagnetic fluctuations between NNN [123]: all longer ranged spin-spin fluctuations will have the same contribution from $\mathbf{Q} = (\pi,\pi)$ such that the freezing extends to long-range correlation functions. We emphasize that such a mechanism can occur only if there are low-energy spin excitations, and it is even enhanced when there are zero-frequency spin excitations. In this regard, the freezing mechanism can be expected to be even larger in the 8−site cluster! Interestingly, it is at least confirmed in the 8-site cluster for the NN and NNN components in Ref. 123 using DCA.

One may wonder at this stage if this freezing might be an effect of the finite size of the cluster. Indeed, the $\mathcal{S}((\pi,\pi),\omega)$ is in fact weighted by $\frac{1}{L}$, with L the number of cluster sites, such that its contribution at low energy is suppressed for a larger number of sites, hence canceling the freezing mechanism. This is true only if the large spin excitations have no momentum broadening, i.e. if only the $\mathbf{Q} = (\pi,\pi)$ response is strong, yielding a scaling factor $\mathcal{S}((\pi,\pi),\omega)/L$ going to zero for large systems. However, in reality a relatively large momentum broadening is observed, as can be seen for instance in the diagrammatic Monte Carlo calculations of Wu *et al.* [113]. Therefore, in a certain length scale δ_k the DSSF can be considered as large as at $\mathbf{Q} = (\pi,\pi)$. For a square cluster made of $\sqrt{L} \times \sqrt{L}$ sites, this implies that each spin-spin correlation function $\mathcal{S}_{ij}(\omega)$ has $(\delta_k)^2 L$ contributions of the order of $\mathcal{S}((\pi,\pi),\omega)/L$, such that the overall contribution is

$$\mathcal{S}_{ij}(\omega) \propto (\delta_k)^2 \mathcal{S}((\pi,\pi),\omega). \tag{3.29}$$

If the broadening is sufficiently large, and if the $\mathbf{Q} = (\pi,\pi)$ strongly dominates, there is a freezing of the spin-spin correlation function at large distances in the doped system. This is an intriguing result that asks for further investigations. It is important to point here that we do *not* claim here that this observation is linked with the spin-glass-like phase observed experimentally [84] which occurs at lower temperature ($T \sim 6$K). Calculations at lower temperature, or even zero-temperature, would be necessary to further explore a possible link.

Another sign that this spin-freezing is related to the PG can be seen in Fig. 3.16, where we show essentially the same plots as in Fig. 3.14 but calculated at $\beta = 20\text{eV}^{-1}$ where we do not observe a PG. The DSSF spectra are quite similar to those calculated at $\beta = 60\text{eV}^{-1}$, although the peaks at higher dopings are shifted to higher energies. The softening of the DSSF peak maximum seems to be slightly reduced. Most importantly, the spin-spin correlation functions show a drastically different behavior: they continuously decrease with increasing doping, without any sign of freezing, in sharp contrast to the $\beta = 60\text{eV}^{-1}$ results. This can be understood from the fact that in the undoped system the DSSF at $\mathbf{Q} = (\pi,\pi)$ is already non-gapped thus leading to a different behavior than at lower temperature.

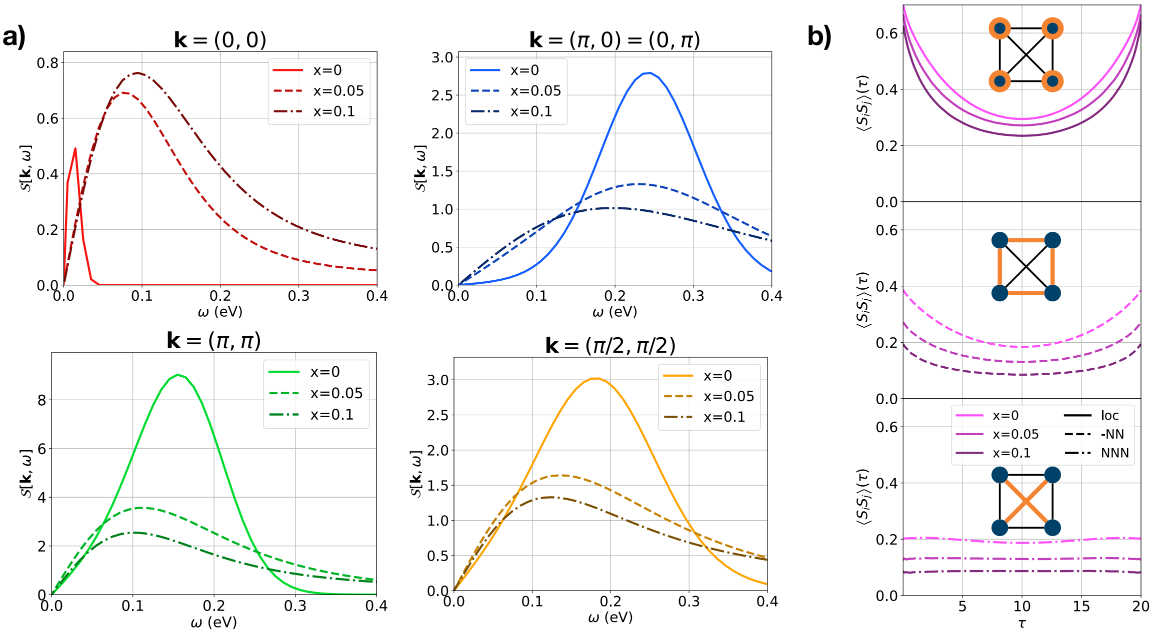

Figure 3.16: (a) DSSF at different $\mathbf{k}$ points as a function of doping ($x = 0, x = 0.05, x = 0.1$), all calculated at $\beta = 20\text{eV}^{-1}$. The same error estimate (10^{-2}) was used for all spectra to perform the analytic continuation. (b) Local, NN, and NNN cluster spin-spin correlation functions as a function of imaginary time, for different dopings and calculated at $\beta = 60\text{eV}^{-1}$. Note that the NN component has been multiplied by -1.

The usual antiferromagnetic magnon dispersion goes to zero at $\mathbf{Q} = (\pi, \pi)$, while in our calculations the peak rather appears around $\omega \sim 0.1\text{eV}$ even for the undoped system. Since the finite size of our cluster induces strong limitations as we have discussed above, it is legitimate to wonder if the non-zero frequency of the peak at $\mathbf{Q} = (\pi, \pi)$ is another spurious finite size effect. In order to check that, we performed exact diagonalization (ED) calculations for a simple Heisenberg spin model with only NN echange interactions, at half filling:

$$H = J \sum_{\langle ij \rangle} \mathbf{S}_i \mathbf{S}_j + h \sum_i (-1)^{x_i + y_i} S_i^z \tag{3.30}$$

with $J = \frac{4t^2}{U} - \frac{24t^4}{U^3}$ [235], and where h is a staggered field giving the possibility to lift the degeneracy between the two antiferromagnetic configuration possible. We solve the model for a 2×2 and a 4×4 plaquette with ED using the QuSpin package [265, 266] with periodic boundary conditions. Once the system solved for its eigen states and energies, the DSSF at zero temperature can be calculated by a modified Lehmann representation:

$$\mathcal{S}(\mathbf{k}, \omega) = \sum_{\mathbf{R}_i \mathbf{R}_j} \mathrm{e}^{i\mathbf{k}(\mathbf{R}_j - \mathbf{R}_i)} \sum_m \frac{\langle GS|\mathbf{S}_i|m\rangle\langle m|\mathbf{S}_j|GS\rangle}{\omega + i\delta + E_{GS} - E_m}, \tag{3.31}$$

where m runs over the excited states. In practice, the vector product of the two spin operators is expanded before introducing the closure relation.

The results are presented in Fig. 3.17(a) for the 2×2 and 4×4 system with and without staggered

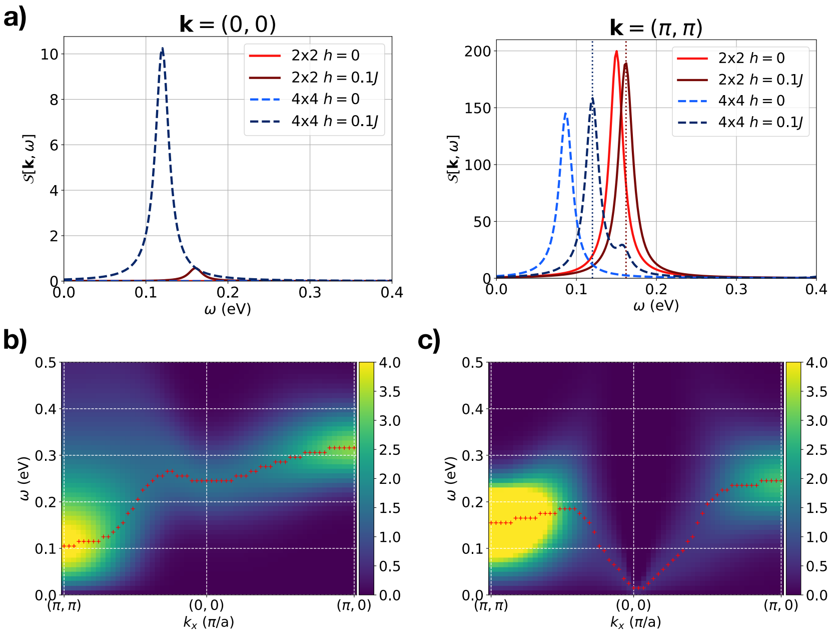

Figure 3.17: (a) DSSF of the spin-only model calculated for a 2×2 and 4×4 system with eventually a non-zero staggered field. The vertical dotted lines in the *right* panel highlight the position of the peak at $\mathbf{k} = (0, 0)$ (*right* panel) for a non-zero staggered field. (b) Momentum resolved DSSF obtained from an antiferromagnetic (*left*) and paramagnetic (*right*) CDMFT calculation at $\beta = 20\text{eV}^{-1}$. The red line is a guide to the eye following the peak maximum at each momentum, we emphasize that it should be be thought as a dispersion.

field. Without the staggered field, the degeneracy of the two possible antiferromagnetic configurations lead to a suppression of the peak at $(0, 0)$. At (π, π), we observe that the peak is shifted to lower energy as the system size is increased, in agreement with the expectations mentioned earlier. When turning on the staggered field, we observe a non-zero peak at $(0, 0)$ since the two antiferromagnetic configurations are not equivalent anymore. As highlighted by the dotted vertical lines in the *right* panel of Fig. 3.17(a), the peak at $(0, 0)$ appears at the exact same energy as the peak at (π, π). Again, although a small shift of the peak energy due to the non-zero staggered field, increasing the cluster size also leads to a decrease in the energy at which the maxima appears when the antiferromagnetic configuration degeneracy is lifted.

The fact that the peaks at (π, π) and $(0, 0)$ in the spin-only model appear at the exact same energy, and that the peak line shape is perfectly symmetric in the spin-only model, are direct evidences of the role of the charge degrees of freedom. To show that, we performed an antiferromagnetic CDMFT calculation at $\beta = 20\text{eV}^{-1}$, that we compare to the usual paramagnetic calculations, as shown in Fig. 3.17(b). As for the spin-only model, in the antiferromagnetic calculations a sizable peak at $(0, 0)$ at finite frequency appears, in sharp contrast to the paramagnetic case which shows a suppression of the DSSF at $(0, 0)$, in agreement with the spin-only model. However, the peak at (π, π) is significantly shifted as compared to the one at $(0, 0)$. Hence the peak position at (π, π) is not only influenced by finite size effects: it is also governed by the interplay between charge and spin fluctuations, even though the latter dominate the former [112, 113].

Therefore, despite the fact that the PG is well described by limited short-range interactions, the DSSF seems to require the incorporation of longer range correlation functions, as well as the excitation channel between the nodal points $\mathbf{Q} = (\pm\pi/2, \pm\pi/2)$, to be in good agreement with the experiment. If the line shape and the increasing broadening as a function of doping is consistent with the experimental and theoretical findings [75, 166, 248–250], the softening of the DSSF peak is not well captured within our method. A future step is to use the 8−site cluster, which we expect to significantly change the results.

3.6 CONCLUSION

By combining state-of-the-art theoretical and experimental techniques, as well as simpler effective models that capture the essential mechanisms, we show in this chapter that the spectral properties of NaCCOC from zero to intermediate doping, and by extension that of the cuprates, can be well understood in a unified framework in which the short range antiferromagnetic fluctuations play a key role. The waterfall feature, seen both in the undoped and the doped system can be described as a crossover between a spin-polaron physics at low-energy [95–98], and an atomic-like behavior with purely local correlations at higher energy. We obtain an excellent agreement between the CDMFT calculations and the ARPES measurements, which further confirms that the kink observed in photoemission is the consequence of the dressing of electrons by the spin fluctuations. Interestingly, at low-doping the waterfall feature is also well described by the SCBA, showing that strong antiferromagnetic fluctuations are still present. The CDMFT calculations performed on the small plaquette cluster display a kink position and spectral weight dispersion that matches the experimental ones. This demonstrates that the waterfall feature at all dopings can be caused by short range antiferromagnetic fluctuations. We moreover argue that this is not a consequence of the specific shape and size of the plaquette cluster by performing calculations for a 8−site cluster which confirm the results.

Our analysis, in agreement with previous findings [75, 104, 107, 111–114, 246], show that the short-range antiferromagnetic fluctuations are also responsible for the opening of the PG. By exploiting the simple state histogram of the plaquette cluster, it is possible to draw a scenario for the opening of the PG: the non-degenerate singlet nature of the most probable state $|N = 4, S = 0\rangle$ leads to a suppression of the zero-energy excitation channel for the $D13, D42$ orbitals which are solely responsible for the spectral weight at the anti-node. The first excitation channel available is the transition to $|N = 4, S = 1\rangle$ state in which the $D13, D42$ are in a triplet state. The PG is therefore linked to the destruction of the RVB-like singlets into triplets for the electrons with $(\pi, 0), (0, \pi)$ momentum. This scenario holds for the 8−site cluster: even though the $(\pm\pi/2, \pm\pi/2)$ are susceptible to form similar singlet states as the $D13, D42$ orbitals, they rather couple to the non-interacting electron bath since they show a larger hybridization function either the interactions are included or not.

Finally, to directly probe the spin fluctuations we calculate the DSSF for the 2×2 plaquette. The doping dependence of the peak position is not in line with the experimental and theoretical previous findings [75, 248–250], and we argue that this is probably due to a finite size effect. As the doping is increased we observe in the PG phase a freezing of the spin-spin correlation functions at $\tau \rightarrow \beta/2$ which prevents from a fast decay of the correlators with distance. We found an explanation for the spin freezing phenomenon, which is induced by the dominance of the $\mathbf{Q} = (\pi, \pi)$ sector at low energy in the DSSF. The mechanism can be generalized to large cluster sizes given a certain momentum broadening of the strong DSSF peak around $\mathbf{Q} = (\pi, \pi)$, such that at long imaginary times $\tau \rightarrow \beta/2$ the spin freezing extends to long distances. We believe that this may have important consequences on the electronic properties and that it would be interesting to deepen the analysis in further studies. It will be also crucial to calculate the DSSF for the $8-$site (and larger) cluster which contains expliticely the non-gapped $(\pm\pi/2, \pm\pi/2)$ orbitals, and which could be a first test case with CDMFT for the generalization of the spin-freezing mechanism.

4

BULK PROPERTIES OF TETRAGONAL *CuO*

The following chapter is based on Ref. 267, which was carried out in close collaboration with Max Bramberger, Martin Grundner, Sebastian Paeckel and Ulrich Schollwöck (Arnold Sommerfeld Center of Theoretical Physics, Department of Physics, University of Munich). The figures extracted from the publication are signaled explicitly in the caption. The results shown here that were not calculated by the present author are also clearly indicated.

4.1 INTRODUCTION

As we have seen for NaCCOC, the two-dimensional CuO_2 layers are mainly responsible for the cuprates' low-energy physics. Sometimes, however, an emergent phenomenon appearing in the CuO_2 planes can be the consequence of distortions or disorder effects due to the surrounding ligand atoms. For instance, it was shown in Hg-based n-layer cuprates, in which n CuO_2 layers are sandwiched between charge reservoir layers, that long-range antiferromagnetic order coexists with CDW order in the different CuO_2 layers [77–79]. The CDW is attributed to the CuO_2 outer planes which are closer to the charge reservoir layers and which undergo larger distortions due to chemical substitution, while the antiferromagnetic order exists in the cleaner inner planes which are protected from the structural distortions [77, 78]. This can result in significantly different outcomes in the spectral function, as was observed in Ref. 79 where Fermi arcs and pockets were observed and attributed again to inner and outer CuO_2 planes, as well as for the Fermi surface topology [78]. There is therefore some ambiguity on the properties of the pure CuO_2 layers, which motivates for the search of an *ideal* cuprate without ligand atoms to better connect the theoretical effective models with experiments.

In this context, polymorphs of pure CuO planes were considered [268], but it turns out that bulk CuO has a low-symmetry monoclinic crystal structure [269], far from the ideal 2D planes. Fortunately, when thin films of CuO are grown on a STO substrate, they stack along the c axis in a tetragonal crystal structure [124–126], as shown in Fig. 4.1(a). Above a critical thickness, of approximately 10 unit cells [124, 126], the crystal returns in its monoclinic phase. In this distorted rocksalt structure the Cu-O distances for basal and apical oxygens differ by a factor 1.37 [124, 125], which amounts to well separated 2D layers. First principles studies including DFT with hybrid functionals [128–131] and DFT+U [132, 133] gave first insights into the electronic structure of tetragonal CuO (t-CuO) and were able to reproduce the experimentally observed tetragonal distortion [129], which could be traced back to Jahn-Teller orbital ordering at the Cu d^9 ions [128, 131].

Ab initio calculations also proposed an antiferromagnetic stripe order [128, 129, 131], which is in agreement with the experimental findings from RIXS [135]. Extrapolation from other binary TMOs [124, 137] and estimates from first principles calculations [128, 129, 131] place the Néel temperature around $\sim$ 800K, which is much higher than the critical temperature of its monoclinic bulk phase ($T_N \sim$ 220K [127]). Such a high estimate of the Néel temperature is promising regarding superconductivity since it signals a high exchange coupling J, which was recently claimed to be correlated with the superconducting order parameter in cuprates [223, 270–272]. However, hole- or electron-doping of t-CuO has not been experimentally achieved yet, and some questions remain open for the undoped compound.

t-CuO is an insulator with quite sizeable gap, $\Delta > 2.35\,\mathrm{eV}$, of which the electronic structure was measured via ARPES [134] and used to construct effective three- and one-band $t-J$ models [134, 273, 274]. Although t-CuO does not escape from the long-standing debate [40, 41] on whether or not ZRS [38] can describe the low-energy spectral features of cuprates, the one-band model derived from RIXS in Ref. 135 is in qualitative agreement with the ZRS one [274]. We do not aim at contributing to this discussion, but we rather study the signature of sublattice decoupling which was observed in ARPES and RIXS [134, 135], and illustrated in Fig. 4.1(b). Strong replica features were found outside of the single sublattice BZ, corroborating with the fact that the t-CuO RIXS spectrum is reminiscent of $Sr_2CuCl_2O_2$ (SCOC), a standard cuprate made of CuO_2 layers. These observations suggest that each of the CuO planes constituting t-CuO can be seen as two weakly coupled CuO_2 sublattices, but the question about the physical origin remains open.

From the simple one-band model derived from RIXS [135], the NN *inter*-sublattice hopping t_d is evaluated to be about one-fourth of the NNN *intra*-sublattice hopping t, a surprisingly high value considering the strong replica features observed in ARPES and the similitude of the magnon spectrum with conventional cuprates. Such model is constructed from a Heisenberg-like Hamiltonian [135], and therefore lacks the dynamical effects from electron-electron interactions. In this chapter, we investigate the dynamical influence of the inter-sublattice hopping t_d and the electronic correlations by the means of CDMFT [49–52], which has been successful in studying the Hubbard model and especially cuprates [50, 103–106]. Our key finding is that the inter-sublattice correlations are heavily suppressed as compared to local and short-range intra-sublattice correlations, which formally justifies to regard t-CuO as weakly-coupled interlaced CuO_2 lattices. While t hopping is renormalized by the intra-sublattice correlations, t_d is let bare since the inter-sublattice correlations are vanishing, such that the effective t_d/t is decreased by a factor $\simeq 2$. With the sublattices being weakly connected to each other, we can motivate an efficient block-construction scheme for our cluster calculations, allowing to increase *for free* the momentum resolution of the calculated spectral functions. In Sec. 4.4, using a MPS [56, 57]-based impurity solver working directly on the real axis [58, 141–144] and at effectively zero temperature, the equal energy maps and momentum resolved spectral functions are reproduced, in remarkable agreement with ARPES measurements without the need for analytic continuation. These calculations, performed by M. Bramberger and M. Grundner, are also in excellent agreement with results obtained at finite temperature by the author using the hybridization-expansion CTQMC [60, 62] solver `CT-HYB` [116] based on the `ALPSCore` libraries [118]. Then in Sec. 4.5.1, the magnetic

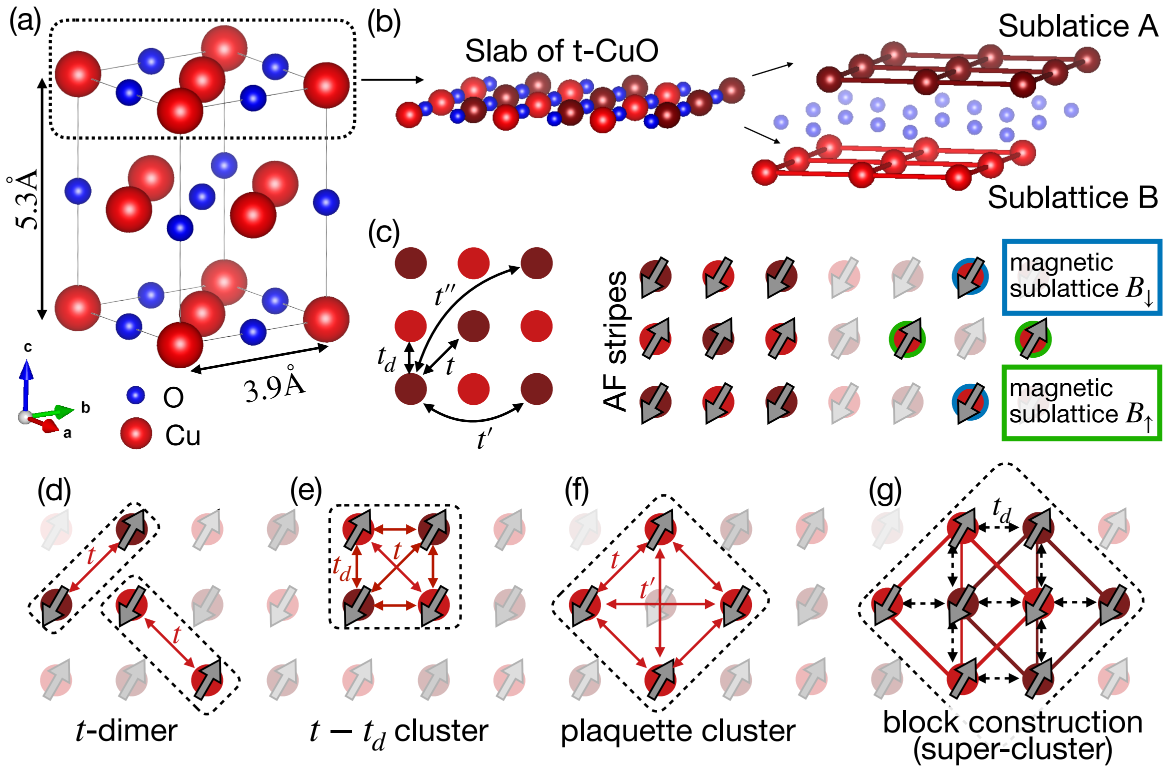

Figure 4.1: *Figure taken from Ref. 267.* (a) Rock salt crystal structure of tetragonal CuO. (b) slab of CuO within the a-b plane. Bright (dark) red atoms indicate the sublattice A and B of our model. (c) Two identical Cu-sublattices and indication of the hoppings t_d, t, t' and t'' included in the model. The arrows sketch the stripe order considered throughout the chapter. Highlighted in blue and green are the magnetic sublattices that correspond to the stripe order. (d-g) Clusters including different hopping terms as discussed in the text.

ordering in t-CuO is analyzed as a function of temperature and two driving mechanisms for the insulating phase are identified. We also find an increase of the local correlations close to the critical temperature T_c at which the clusters antiferromagnetically order, and show with a minimal model derived by the author that it is a pure effect of thermal and spin fluctuations. Finally in Sec. 4.6, despite that t-CuO has not been experimentally doped, i.e. that superconductivity has not been observed yet, the emergence and symmetry of the superconducting order parameter upon hole-doping is studied using VCA [68], a complementary cluster technique, for which the calculations were carried out by B. Lenz. The sublattice decoupling has direct consequences even in the hole-doped regime: a coexistence of magnetic stripe order and superconductivity of d_{xy} symmetry is found, whereas the usual cuprate $d_{x^2-y^2}$ symmetry is strongly suppressed.

4.2 MODEL AND METHOD

We start by presenting the band structure of t-CuO, from which we can motivate the construction of an effective one-band Hubbard model, similarly to NaCCOC. We then detail how the model is solved using CDMFT and VCA calculations.

4.2.1 ONE-BAND EFFECTIVE MODEL

To construct a minimal model for t-CuO, it is instructive to analyze its band structure obtained from a simple DFT calculation done within LDA using the Wien2k package [173, 174], shown in Fig. 4.2. As expected, the system is predicted to be metallic since the Cu atoms are in a d^9 configuration (and no symmetry is broken). The d_{xy} orbital is half-filled, in contrast to usual cuprates like NaCCOC for which it would be the $d_{x^2-y^2}$. In t-CuO, the $d_{x^2-y^2}$ orbital is favored against d_{xy} by the crystal field due to the O atoms' position. Regardless of these differences, there are strong similarities between t-CuO and the previously studied NaCCOC:

(i) we find a single band crossing the Fermi energy (actually two here because there are two Cu atoms in the unit cell),
(ii) this band is only of Cu d_{xy} (equivalently $d_{x^2-y^2}$ for NaCCOC) and O $p_{x/y}$ character,
(iii) it has a weak dispersion along k_z.

We observe another set of bands close to X and $(\pi/2, \pi/2)$, which are reminiscent of the spectral weight seen in ARPES and labeled β by Moser *et al.* [134]. They are of Cu d and O p_z character, and they have no contribution from the d_{xy} nor the $p_{x/y}$ orbitals.

Close to the Fermi level, t-CuO's electronic structure is composed of a quasi 2D single half-filled band of mixed Cu d_{xy}/O $p_{x/y}$ character, which we identify to the single band observed in ARPES. It is moreover the only partially filled band, i.e. the one contributing mostly to the magnon part of the RIXS spectrum. One can notice signs of the sublattice decoupling at the DFT level: the single band dispersion between M and Γ is almost symmetric with respect to the red zone boundary which represents the single sublattice BZ, and the band energy at those two points only differs slightly. However, this observation can not be put on equal footing to the experimental observations, since ARPES is sensitive to spectral properties and RIXS to collective fluctuations, whereas DFT provides the ground state properties. Therefore, an explicit treatment of the electronic correlations is needed: both to obtain the expected insulating behavior, as well as to incorporate the collective dynamic correlations.

To this aim, we consider a single CuO layer as shown in Fig. 4.1(a)-(b), and model it by a single-band Hubbard model [35–37]:

$$H = U\sum_i n_{i\uparrow}n_{i\downarrow} + \sum_{\substack{i,j,\sigma \\ |\mathbf{i}-\mathbf{j}|=a}} t_d c^\dagger_{i\sigma}c_{j\sigma} + \sum_{\substack{i,j,\sigma \\ |\mathbf{i}-\mathbf{j}|=\sqrt{2}a}} t c^\dagger_{i\sigma}c_{j\sigma} + \sum_{\substack{i,j,\sigma \\ |\mathbf{i}-\mathbf{j}|=2a}} t' c^\dagger_{i\sigma}c_{j\sigma} + \sum_{\substack{i,j,\sigma \\ |\mathbf{i}-\mathbf{j}|=2\sqrt{2}a}} t'' c^\dagger_{i\sigma}c_{j\sigma}. \tag{4.1}$$

Since we are not interested in the fine tuning of the model, we chose to take the hopping parameters $t_d = -0.1$eV, $t = 0.44$eV, $t' = -0.2$eV, $t'' = 0.075$eV (see Fig. 4.1(c)) from the fit of the RIXS magnon spectrum of Ref. 135. As mentioned above, the O atoms favor the NNN hopping t rather than the NN t_d, in contrast to the usual CuO_2 layers. We set the on-site Hubbard interaction $U = 7$eV, significantly higher than the one obtained from the magnon fitting of Ref. 135, but necessary for obtaining a gap that is larger than the ARPES lower bound [134], but still lower than the STM upper bound [126], and consistent with hybrid DFT [129] (2.7eV).

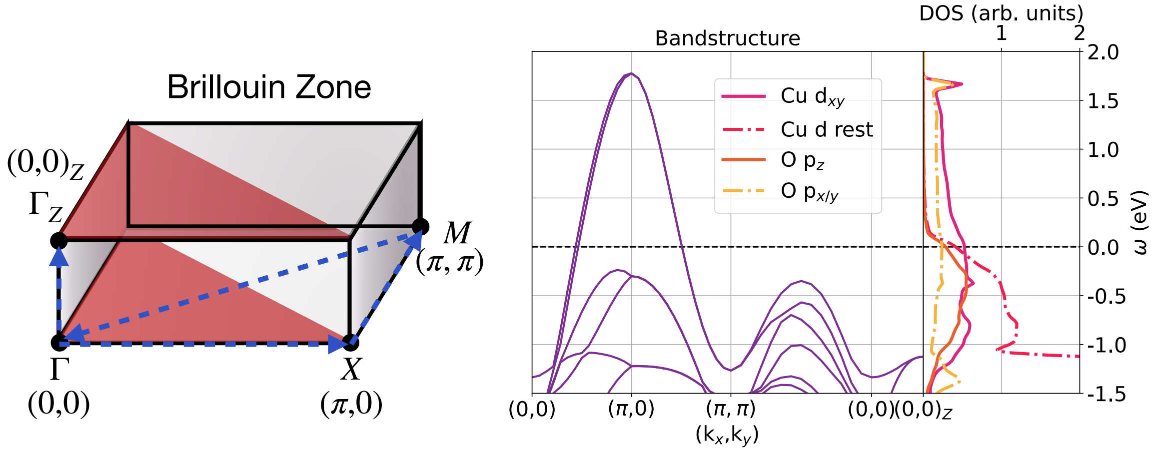

Figure 4.2: t-CuO band structure on a k-point illustrated on the BZ (*left*) obtained with a non spin polarized DFT calculation, along with the projected DOS. The red shaded area highlights the BZ of a single CuO_2 sublattice.

4.2.2 METHODOLOGY

To solve this effective interacting many-body problem, we use CDMFT [50–52], which was introduced in Sec. 2.2. We perform antiferromagnetic calculations and chose the cluster tilings such that they are in line with the antiferromagnetic stripes. The calculations are initialized using a spin-polarized (constant) self-energy as presented in Sec. 2.4, and the chemical potential is kept fixed in the middle of the gap. In Sec. 4.3, we first study the sublattice decoupling using the t-dimer and $t - t_d$ clusters of Fig. 4.1(d)-(e). The t-dimer is composed of two sites belonging to the same sublattice, i.e. connected via the NNN hopping t. The $t - t_d$ cluster is composed of two of those dimers explicitly connected through the t_d hopping, thus allowing to directly study the effect of including t_d on the correlations. Following our results of Sec. 4.3, we then motivate the use of the block construction (Fig. 4.1(g)) in Sec. 4.4 to compute the spectral function of t-CuO with an increased momentum accuracy. Similarly to the $t - t_d$ cluster, the super-cluster is composed of two 2×2 plaquette clusters on each sublattice, but this time the inter-sublattice hopping t_d is treated at the non-interacting level and is not included in the effective impurity. In other words, based on our observations in Sec. 4.3, the inter-sublattice correlations are neglected such that we solve the CDMFT impurity problem for only one of the two plaquette clusters. All the details of this construction are given in Sec. 4.4.

Having defined our impurity clusters, we are left with choosing the solver. As mentioned in the introduction of this chapter, three different complementary techniques were used: two MPS-based solvers working both on the imaginary [59, 138–140] and real [58, 141–144] frequency axis for which M. Bramberger and M. Grundner performed the calculations, and the hybridization-expansion CTQMC [60–62] solver CT-HYB [116] based on the ALPSCore libraries [118] for which the author performed the calculations. The combination of these techniques allows us to combine zero and finite temperature analysis on the imaginary axis, as well as to obtain a direct information on the real axis (without the need for analytic continuation) that can be directly compared to experiments.

Finally, in Sec. 4.6, VCA [68–70] calculations, performed by B. Lenz, are used to investigate the possible superconducting solutions. This variational quantum cluster technique is well-suited to check for different symmetry-breaking orders of the interacting lattice system [145, 275]. Here, the self-energy functional which is to be minimized has several variational parameters. It includes the chemical potential of the cluster [276], and the one of the lattice [277], which are first determined. Then, the different symmetry-breaking Weiss fields are sequentially added with an adiabatic switching to allow for long-range order [145, 275, 276]. The antiferromagnetic stripe order with ordering wavevector $\mathbf{Q} = (0, \pi)$ is triggered by a suitable field on the cluster:

$$\mathcal{H}_{\mathrm{AFS}}^{\mathrm{Weiss}} = M \sum_{\mathbf{R}} (-1)^{R_y \cdot \pi} \big(n_{\mathbf{R}\uparrow} - n_{\mathbf{R}\downarrow} \big),$$

where we denote the cluster sites with $\mathbf{R}$, M is the field strength determined via the variational principle. Likewise, superconducting pairing fields are added via

$$\mathcal{H}_{\mathrm{SC}}^{\mathrm{Weiss}} = D \sum_{i,j} \Delta_{i,j} \big(c_{i\uparrow} c_{j\downarrow} + \mathrm{h.c.} \big),$$

where D denotes the variational parameter and $\Delta_{i,j}$ is chosen such that it amounts to pairing with d_{xy} or $d_{x^2-y^2}$ symmetry. The cluster self-energy is calculated using exact diagonalization with a band Lanczos algorithm [278]. Moreover, a Nambu transformation is employed to include the superconductivity fields [145].

4.3 SUBLATTICE DECOUPLING

At the single particle level it is hard to argue for the decoupling of the two sublattices since the nearest-neighbor hopping t_d is of the same order of magnitude as the next-nearest neighbor hopping ($t_d \sim -\frac{t}{4}$). Therefore it is important to also take into account the self-energy which captures the modification of the non-interacting Hamiltonian due to the presence of electronic interactions in the correlated material.

As we have seen in Chap. 2, within the framework of CDMFT the local interactions, hopping terms on the given cluster and dynamical fluctuations to an electronic reservoir are taken into account exactly, while longer-ranged exchange with the rest of the lattice is included on the single-particle level and enters via the self-consistency loop [279]. The cluster self-energy $\mathbf{\Sigma}(\omega)$ is a matrix-valued quantity in terms of combined cluster-spin indices. It links the non-interacting and interacting cluster Green's functions, $\mathbf{G}_0(\mathbf{k}, \omega)$ and $\mathbf{G}(\mathbf{k}, \omega)$, via the Dyson equation

$$\mathbf{\Sigma}(\omega) = \mathbf{G}_0(\mathbf{k}, \omega)^{-1} - \mathbf{G}(\mathbf{k}, \omega)^{-1}.$$

Besides the local component, $\Sigma_{\mathrm{loc}}(\omega)$, non-local self-energies within the cluster are accessible, which we denote with respect to the hopping term connecting the corresponding sites, e.g. $\Sigma_t(\omega)$, $\Sigma_{t_d}(\omega)$. By choosing different impurity cluster geometries, namely the t-dimer (Fig. 4.1 (d)) and the $t - t_d$ (Fig. 4.1 (e)) clusters, we are able to probe the influence of the inter-sublattice com-

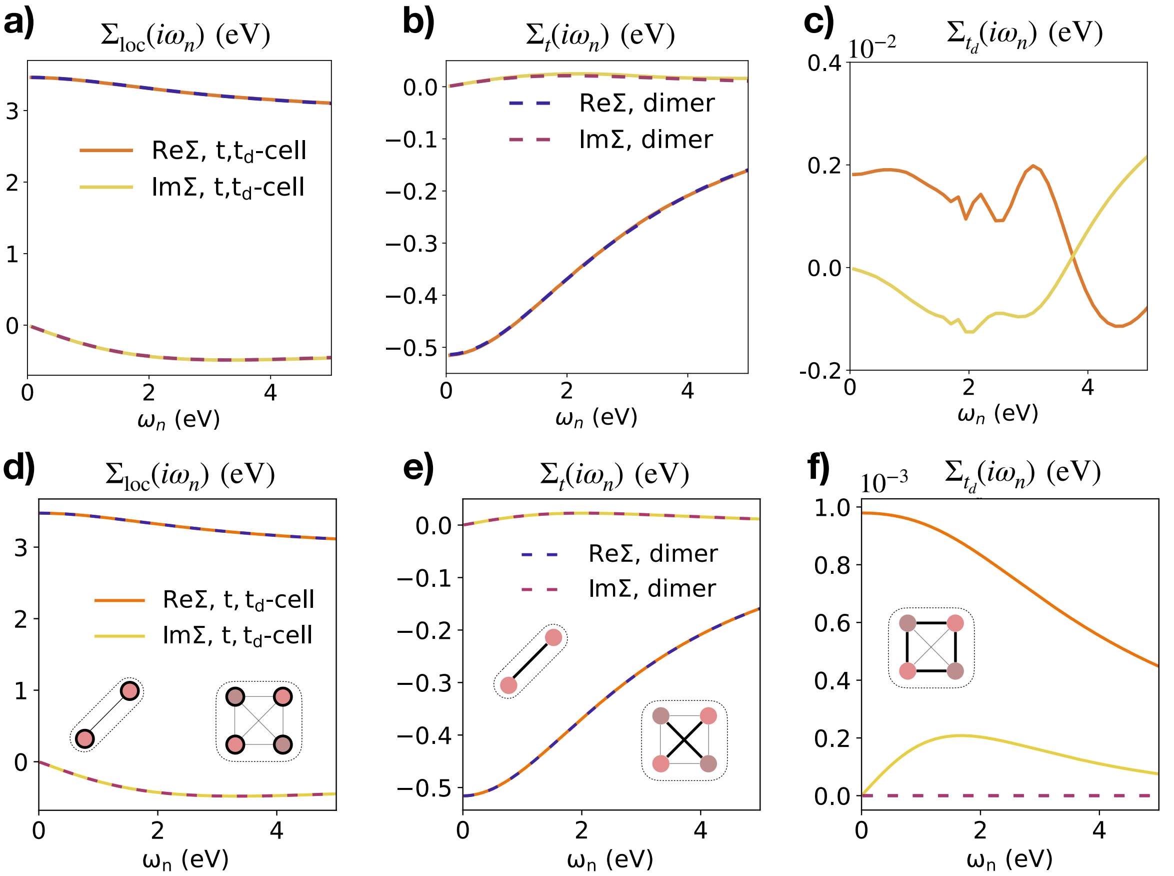

Figure 4.3: *Panels (d)-(f) were extracted from Ref. 267.* Comparison between selected elements of the self-energy computed on two different clusters using (a)-(c) the CT-HYB solver at $\beta = 50\text{eV}^{-1}$, and (d)-(f) the MPS-based solver on the imaginary axis. Note the difference in scales between the panels (c),(f) and (a)-(b),(d)-(e). The components shown belong to the up-spin block of the self-energy.

ponent $\Sigma_{t_d}(\omega)$ on the other components $\Sigma_{\text{loc}}(\omega)$ and $\Sigma_t(\omega)$, i.e. on the coupling between the two sublattices. The following results have been obtained by a MPS-based impurity solver [59, 138, 140] working on the imaginary axis at effectively zero temperature ($T = 0\,\text{K}$), and by the CT-HYB [116, 118] solver at low temperature $\beta = 50\text{eV}^{-1}$.

We show in Fig. 4.3(a)-(b),(d)-(e) the elements of the self-energy already included in the dimer cluster both calculated with the MPS-based and the CT-HYB solver, which do essentially not change by incorporating explicitly the t_d hopping in the impurity cluster. Both the real and imaginary part of $\Sigma_{\text{loc}}(\omega)$ and $\Sigma_t(\omega)$ computed with the dimer are equal to the ones computed with the $t - t_d$ cluster. This is related to the inter-sublattice component $\Sigma_{t_d}(\omega)$ being strongly suppressed, as shown in Fig. 4.3(c),(f). It is two to three orders of magnitude smaller than the intra-sublattice element $\Sigma_t(\omega)$ (Fig. 4.3(b),(e)) depending on which solver is used. Since the inter-sublattice hopping t_d is roughly about one fourth of the leading order hopping ($|t_d| \approx |\frac{t}{4}|$), this strong suppression is far from trivial and indicates that electronic correlations effects favor intra-sublattice hopping t. Indeed, from a hand-wavy view of the self-energy as a static correction to the Hamiltonian, $Re[\Sigma_t(\omega = 0)] \simeq -0.5\text{eV}$ would roughly double t, while $Re\big[\Sigma_{t_d}(\omega = 0)\big] \simeq 0$ lets t_d bare, so that the t_d/t ratio is effectively decreased by the correlations. Note that the CT-HYB $\Sigma_{t_d}(\omega)$ is noisy since its value is close to the sampling error, estimated to be roughly about $0.1 \cdot 10^{-3}$. Apart from this statistical noise in $\Sigma_{t_d}(\omega)$, the result of the self-energy components are in excellent agreement with the results at zero temperature and confirms that the sublattice decoupling survives at finite temperature.

The driving mechanism behind the formation of sublattices is linked to the fact that the hopping elements t_d, t, t', t'' are not decreasing monotonically with distance. Independent of whether it is the NN, NNN or any longer ranged hopping, it is the leading order one that is favored by the electronic correlations. Indeed, from a simple bonding viewpoint, it is energetically favorable for the electrons to form bonding states between sites connected via the larger hopping term. Moreover, if the NN hopping would be the largest, then all the sites of the lattice would be connected via processes including only the favored hopping (see Fig. 4.4(a)), leading to a smoothly decaying self-energy with distance. However, in t-CuO the NNN is the leading order hopping due to the position of the oxygen atoms which are located between NNN Cu sites and hence favor t against t_d. Since the t hopping term connects sites belonging to the same sublattice, as shown in Fig. 4.4(b), the NN sites are not connected by higher-order hopping processes t^n, leading to a strong suppression of the inter-sublattice self-energy $\Sigma_{t_d}(\omega)$.

These results are of importance, since they prove that thinking of t-CuO as two weakly coupled sublattices is correct, and it reveals the physical origin of this behavior. Since hallmarks of the decoupling had been seen in the ARPES spectra of Ref. 134, we calculate in the following the momentum-resolved spectral function of t-CuO. As we have pointed out in Sec. 2.2, CDMFT provides a Green's function of limited momentum resolution due to the finite cluster size, and the only way to improve it is to consider a larger cluster. In order to enlarge our cluster while keeping the impurity problem numerically tractable, we show in the following that the sublattice

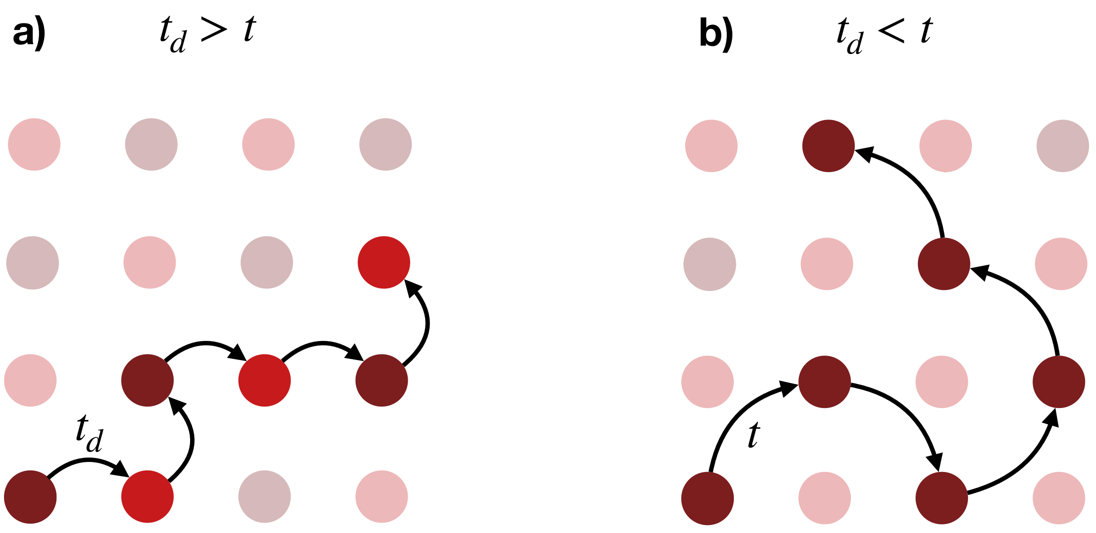

Figure 4.4: Sketch of higher order hopping processes. In (a), the leading order hopping can connect to every site, thus leading to a smoothly decaying self-energy, contrary to (b) where t is the largest hopping, hence leading to a suppression of Σ_{t_d} since it only connects sites of the same sublattice.

decoupling can be used for constructing an 8-site super-cluster (Fig. 4.1(g)) that requires solving a 4-site impurity problem only. This technique, that we call hereafter the *block construction*, allows us to increase *for free* the momentum resolution of our calculations.

4.4 SPECTRAL FUNCTION

In this section, we first describe the block-construction framework, and then present the resulting spectral functions.

4.4.1 THE BLOCK CONSTRUCTION

An illustration of the block construction principle is given in Fig. 4.5. As mentioned in the previous section, our goal is to solve the CDMFT equations for the 8-site cluster of Fig. 4.5(a) for its self-energy Σ_{8site}, which would be computationally very expensive. Grouping the indices that belong to the same sublattices, Σ_{8site} can be written as a block matrix:

$$\Sigma_{8site} = \begin{pmatrix} \Sigma_A & \Sigma_{AB} \\ \Sigma_{AB} & \Sigma_B \end{pmatrix}, \tag{4.2}$$

where the diagonal blocks Σ_A (Σ_B) correspond to the self-energy of the 4-site plaquette on the sublattice A (B), and the off-diagonal Σ_{AB} is the inter-sublattice self-energy. We have seen that the inter-sublattice self-energy between NN sites is suppressed, so that we can expect any longer ranged inter-sublattice self-energy to also vanish, i.e. $\Sigma_{AB} \sim 0$. The latter will therefore be neglected, and Σ_{8site} is approximated by the block construction self-energy:

$$\Sigma_{8site} \simeq \Sigma_{block-constr.} = \begin{pmatrix} \Sigma_A & 0 \\ 0 & \Sigma_B \end{pmatrix}. \tag{4.3}$$

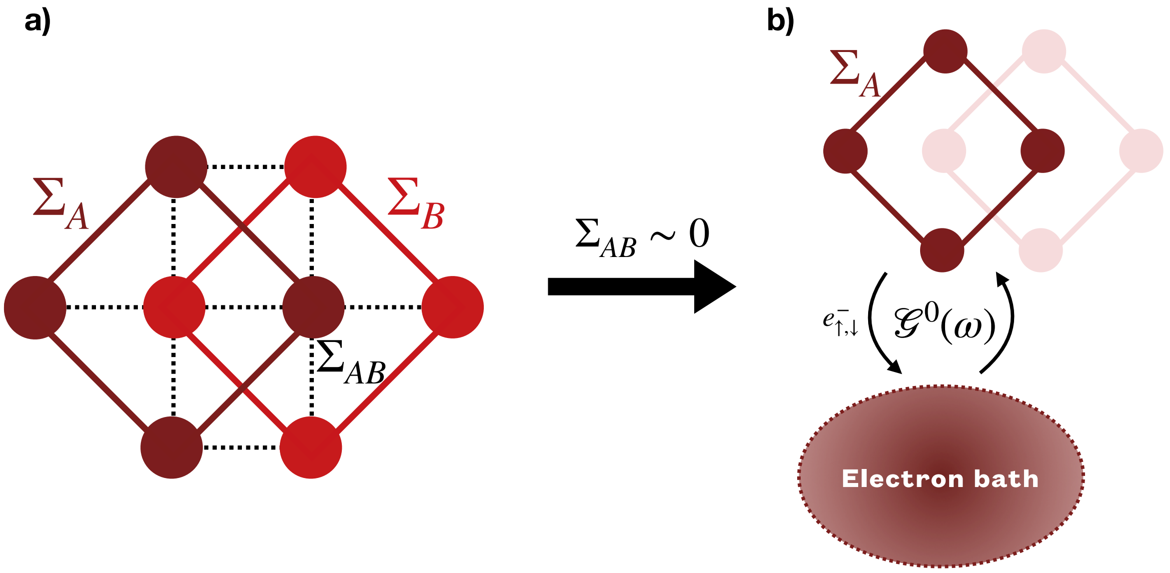

Figure 4.5: Sketch of the block construction: we start from the full 8-site cluster in (a), made of two 4-site plaquettes on each sublattice A and B. Based on the observations of Sec. 4.3, the inter-sublattice self-energy $\Sigma_{AB} \simeq 0.0$ is neglected and accordingly the cluster impurity problem in (b) is solved only for one of the two 4-site plaquettes.

We are left with only solving the impurity problem for one of the two sublattices so to obtain $\Sigma_{A/B}$, and use Eq. 4.3 to get the 8-site cluster impurity self-energy. After closing the self-consistency loop, we project down onto one of those blocks and obtain the hybridization function for one of the two sublattices only.

Within this approximation, we treat the two largest hopping terms $t = 0.440$eV and $t' = -0.2$eV explicitly in the correlated effective impurity, while the two lowest ones, $t_d = 0.1$eV and $t'' = 0.075$eV, are treated at the non-interacting level. Similar block construction techniques have been already used successfully within CDMFT [280, 281].

4.4.2 RESULTS

Having introduced the block construction scheme, we now compare the calculated spectral functions using the block-construction to the ARPES data of Ref. 134. They were obtained using the MPS-based impurity solver on the real axis [58, 141–144] at zero temperature and the CT-HYB [116, 118] solver at $\beta = 40\text{eV}^{-1}$ for which an additional analytic continuation was performed on the cluster self-energy using the Poor's Man method [215, 216].

In Fig. 4.6(a),(c) are shown equal energy cuts on the top of the valence band ($E = -2.2$eV) which are in good agreement with the experimental energy map (Ref. 134, Fig. 1(a)): the strong maxima are recovered in the middle of the BZ (which are rotated by 90° with respect to the experimental data). The replica features outside the single-sublattice BZ (dashed black line), which experimentally justified the assumption of sublattice decoupling, are also reproduced by our calculations. It is interesting to emphasize here that in the case of entirely decoupled sublattices ($t_d = 0$), the spectral features inside the first BZ of a single sublattice would be exactly replicated outside this

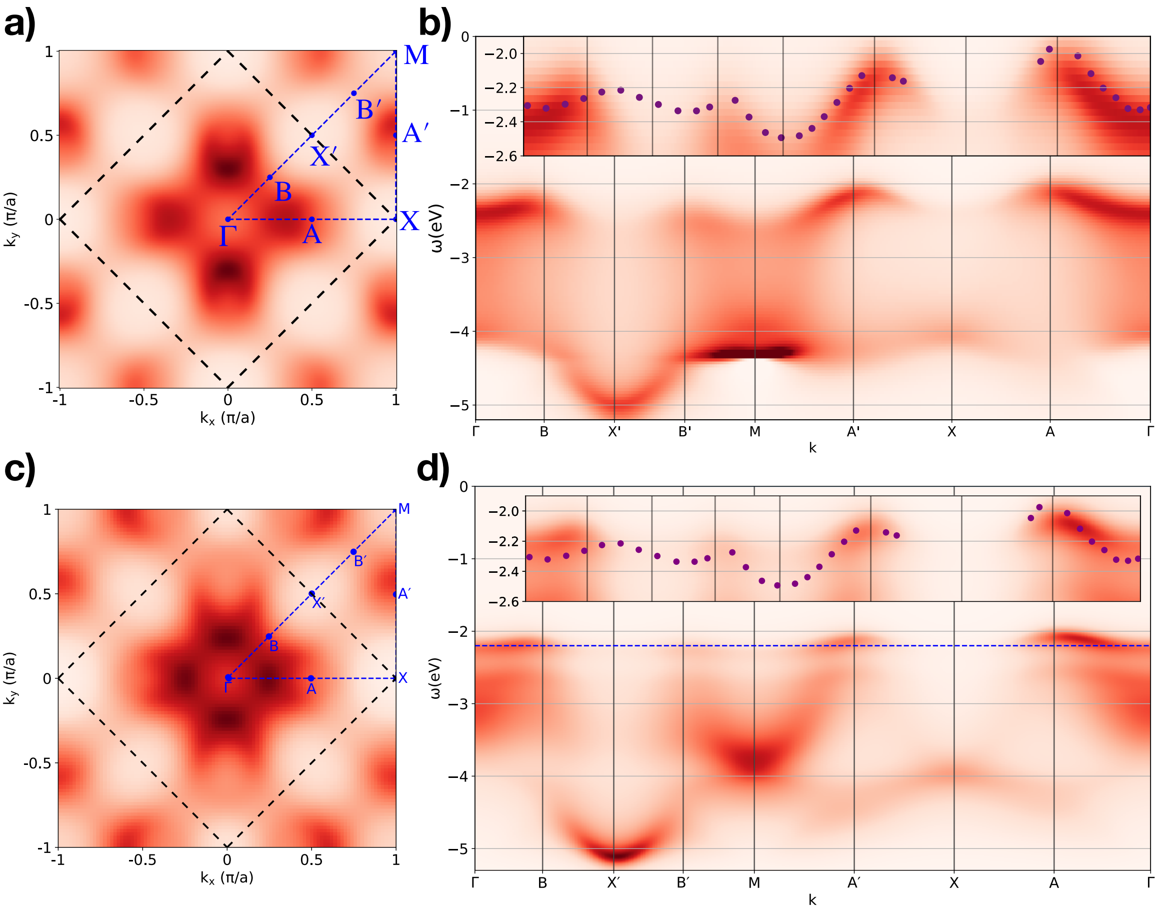

Figure 4.6: *Panels (c)-(d) were extracted from Ref. 267* Spectral function $A(\mathbf{k},\omega)$ obtained with the (a)-(b) CT-HYB and the (c)-(d) MPS-based solver. (a),(c) Equal energy maps at $E = -2.2$ eV where the dashed black line depicts the first BZ of a single sublattice. (b),(d) $A(\mathbf{k},\omega)$ along high-symmetry $\mathbf{k}$-path as computed with the block-construction scheme and compared to the experimentally measured dispersion (purple circles in inset) extracted from Ref. 134 and shifted by 0.4 eV in order to align the chemical potentials. All heat maps are normalized to the maximal value displayed and averaged over the possible orientations in the block-construction (see Fig. 4.7).

BZ (i.e. outside the dashed black line in Fig. 4.6(a)-(c)). Here, since $t_d \neq 0$ the outside replica features are slightly different from the ones inside. However, we find a close resemblance since the self-energy decreases the t_d/t ratio by a factor ~ 2 such that t is effectively 10 times stronger than t_d. Unlike in ARPES there are no matrix-element effects [258] in our calculations, i.e. no additional intensity modulation, contrary to the ones seen in the experimental energy map of Ref. 134 across the different BZ. Still, one can notice an asymmetry between x and y axis, which is not due to the asymmetry of the cluster itself since we average over the cluster orientations (Fig. 4.7), but rather to the antiferromagnetic stripes' orientation (Fig. 4.8). We come back in more details on this point later in this section. As in the previous section, we find a striking resemblance of the CT-HYB and the MPS-based solver, even though an additional analytic continuation step is needed for the former.

The agreement between the two solvers is confirmed in the momentum resolved spectral function of the valence band using the block construction, as shown in Fig. 4.6(b),(d). Comparing our results to ARPES (cf. Fig. 2(a) in Ref. 134) we find an overall good agreement. In particular, we observe a Zhang-Rice-like band separated from the lower Hubbard band at higher binding energy, which coincides with the experimental low-energy spectrum, as shown in the inset of Fig. 4.6(b),(d). A clear separation is seen for the MPS solver which works directly on the real axis, but is blurred out by the analytic continuation for the finite temperature results. As we shall justify in the next section with finite temperature calculations (Fig. 4.10), we identify this band to stem from a spin-polaron, i.e. a hole propagating in an antiferromagnetic background. We find that around the M and Γ high-symmetry points, there is an incoherent and dispersive spectrum without well-defined structures captured by both solvers, consistently with ARPES. Moreover we reproduce the experimentally observed missing spectral weight at the X point, a feature which was not obtained within a SCBA calculation based on a ZRS spin-model [38, 274]. Hence, the overall agreement between our model and the experiment is striking.

An obvious feature that the calculations presented in this work can not reproduce are the contributions from a lower lying band marked with β in the experimental data [134], which is not included in our low-energy one-band model as we have seen in Sec. 4.2. Although in the undoped system it is justified to neglect the β band since they do not directly participate to the magnetic order, nor the sublattice decoupling, one may wonder if this is still a good approximation when hole-doping the material. It is argued by Moser. *et al.* that the β band originates from a Cu d orbital manifold of different symmetry than the low-energy Zhang-Rice-like band of d_{xy} character, which is corroborated by the LDA band structure as discussed previously. Upon hole-doping in cuprates, it is experimentally observed that the hole is located on the O sites [282–284], and from a theoretical standpoint the doped holes are expected to form ZRS states between the Cu d_{xy} and O $p_{x/y}$ orbitals. Therefore, it is unlikely that these holes will populate manifolds of different symmetry such as the one at the origin of the β band, so that the one-band model should remain a good approximation upon hole-doping.

As mentioned above, the equal energy maps and momentum-resolved spectral functions shown

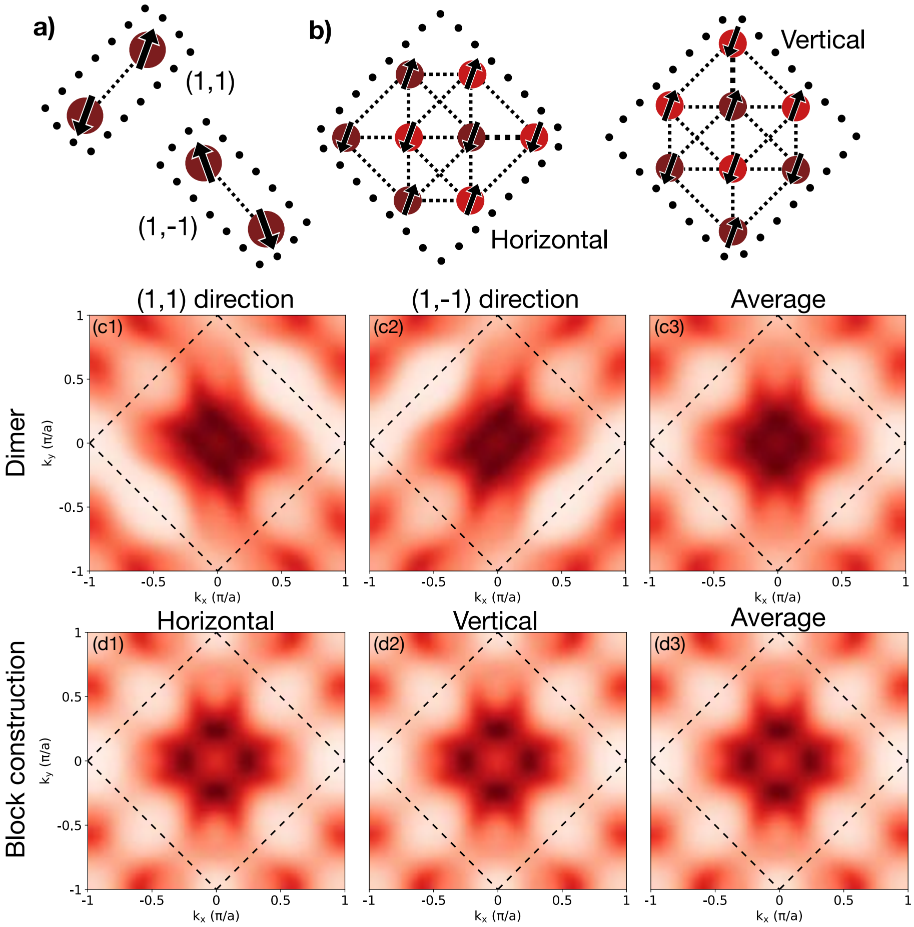

Figure 4.7: *Figure taken from Ref. 267, the results were obtained with the MPS-based solver on the real frequency axis.* Sketch of the two possible orientations within a given magnetic stripe order for (a) the dimer and (b) the block construction. In panels (c) and (d) are shown the corresponding equal energy maps obtained at $E = -2.2\text{eV}$ using these cluster orientations as well as their average. The dashed black line indicates the BZ of a single sublattice.

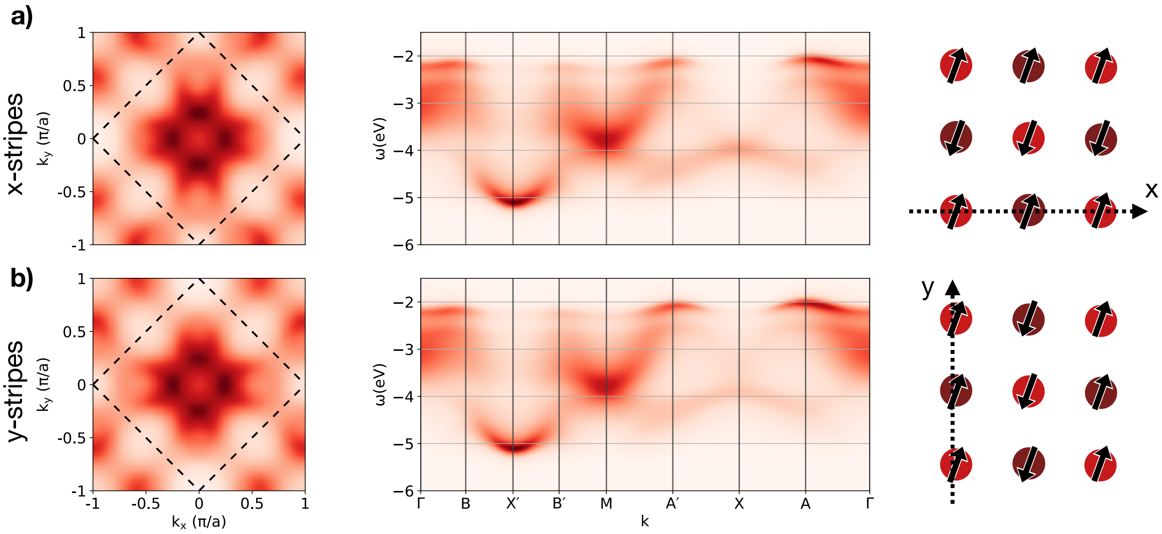

Figure 4.8: *Figure taken from Ref. 267, the results were obtained with the MPS-based solver on the real frequency axis.* Comparison of equal energy maps and momentum resolved spectral functions for the two different directions of the stripe order: (a) along x, (b) along y.

in Fig. 4.6 were obtained by averaging over the cluster orientations. Similarly, all the results shown in this chapter which were obtained using a dimer cluster were always averaged over the different cluster orientations, following the Oriented-Cluster DMFT scheme [285]. Averaging over the two different orientations is an important step, as illustrated in Fig. 4.7. The bias comes from the fact that hopping terms along (1,1) and (1,-1) (x and y) for the dimer (block construction) are no longer equivalent when solving the impurity problem since they are not treated equally in the cluster. The most dramatic effect is observed for the dimer cluster as is shown in Fig. 4.7(c), but the bias is removed by considering an averaging between (1,1) and (1,-1) oriented dimers. In comparison, the block construction suffers less from the bias, especially since in the block construction scheme, only one of the two the 4-site plaquettes, which are perfectly symmetric (if the coupling to the other sublattice is discarded), is solved in the impurity model, such that the asymmetry is incorporated at the non-interacting level only (though having some consequences on the self-energy via the self-consistency).

The remaining asymmetry originates from the antiferromagnetic stripes, as can be seen in Fig. 4.8. By changing the stripe orientation, we can perfectly switch the role of x and y. The most visible consequence is on the energy maps, while in the momentum resolved spectral functions only slight differences can be noticed at the A and A' high-symmetry points (in terms of spectral weight and energy position), which would probably be washed out by the experimental resolution. Unfortunately, even for the equal energy maps the extra modulation from matrix elements and the high probability that the incoming light spot covers zones with different stripes orientations prevent from the observation of this asymmetry in the experimental data.

4.5 TEMPERATURE DEPENDENCE

In this section, we first present the finite temperature results obtained with the `CT-HYB` [116, 118] solver, and show that two different insulating regimes can be identified: paramagnetic and antiferromagnetically ordered. At the magnetic ordering temperature, we observe an intriguing enhancement of the real part of the self-energy at $\omega_n \to 0$, that is explained with a simple effective model in the second part.

4.5.1 RESULTS

All the results we have presented so far were computed at $T = 0$K. However, there have been multiple predictions about the Néel temperature T_N for the antiferromagnetic ordering of t-CuO in the literature [124, 128, 129, 137]. From an heuristic extrapolation, Siemons *et al.* predicted that the tetragonal phase of CuO would exhibit a high $T_N \simeq 800K$ (see Fig. 1(a) of Ref. 124). In CuO-Cu_2O heterostructures, an antiferromagnetic alignment was observed at $T_N = 600$K by Rabinovich *et al.* and attributed to the formation of cubic crystals of CuO. From *ab initio*, Peralta *et al.* predicted $T_N = 300 - 410$K with the self-interaction-corrected local density-function method [286], while Chen *et al.* estimated the ordering temperature to be $T_N = 865 - 1000$K with hybrid DFT [165] based on the Heyd-Scuseria-Ernzerhof method [287]. These theoretical predictions were obtained by estimating the exchange couplings, and evalutating T_N within molecular-field theory [288, 289], to which an Anderson rescaling [17] is applied. Although these estimates cover a wide range of temperatures, they are all well above the monoclinic transition temperature $T_N \simeq 200K$. This motivates for further investigation of the finite-temperature behavior of t-CuO. Our simple 2D model prevent from inferring on the value of the Néel temperature itself, however using CTQMC solvers working at finite temperature within antiferromagnetic CDMFT calculations, we can study the properties of the system at temperatures above and below the ordering temperature of the clusters T_c.

In Fig. 4.9(a) we show the staggered magnetization as a function of the inverse temperature β as obtained with the dimer and the block construction clusters (Fig. 4.1(d),(g)). First, we note the asymptotic convergence of the staggered magnetization towards the $T = 0$ K value obtained with the MPS-based solver for $\beta \to \infty$. We identify an inverse temperature at which the order melts, namely $\beta_c \approx 18.5\,\mathrm{eV}^{-1}$ ($14.5\,\mathrm{eV}^{-1}$), corresponding to a critical temperature of $T_c \approx 627$ K (800 K) obtained with the block-construction (dimer) cluster. T_c is determined using a fit function of the type:

$$M(T) = \theta(T_c - T)\gamma\left(1 - \frac{T}{T_c}\right)^{\alpha},$$

where T_c, γ, α are fitting parameters and $\theta(T)$ is the Heaviside step function. By inspection of the self-energies close to the transition region, lower and upper critical tempatures are determined: the lower boundary is set by the temparature at which the spin splitting of the real-part of the self-energy vanishes, while the upper boundary is set such that the imaginary part of the diagonal components of the self-energy tends to 0 as $w_n \to 0$. By varying the fit boundaries within these two limits, we obtain a collection of fit from which the average critical value is extracted, as well

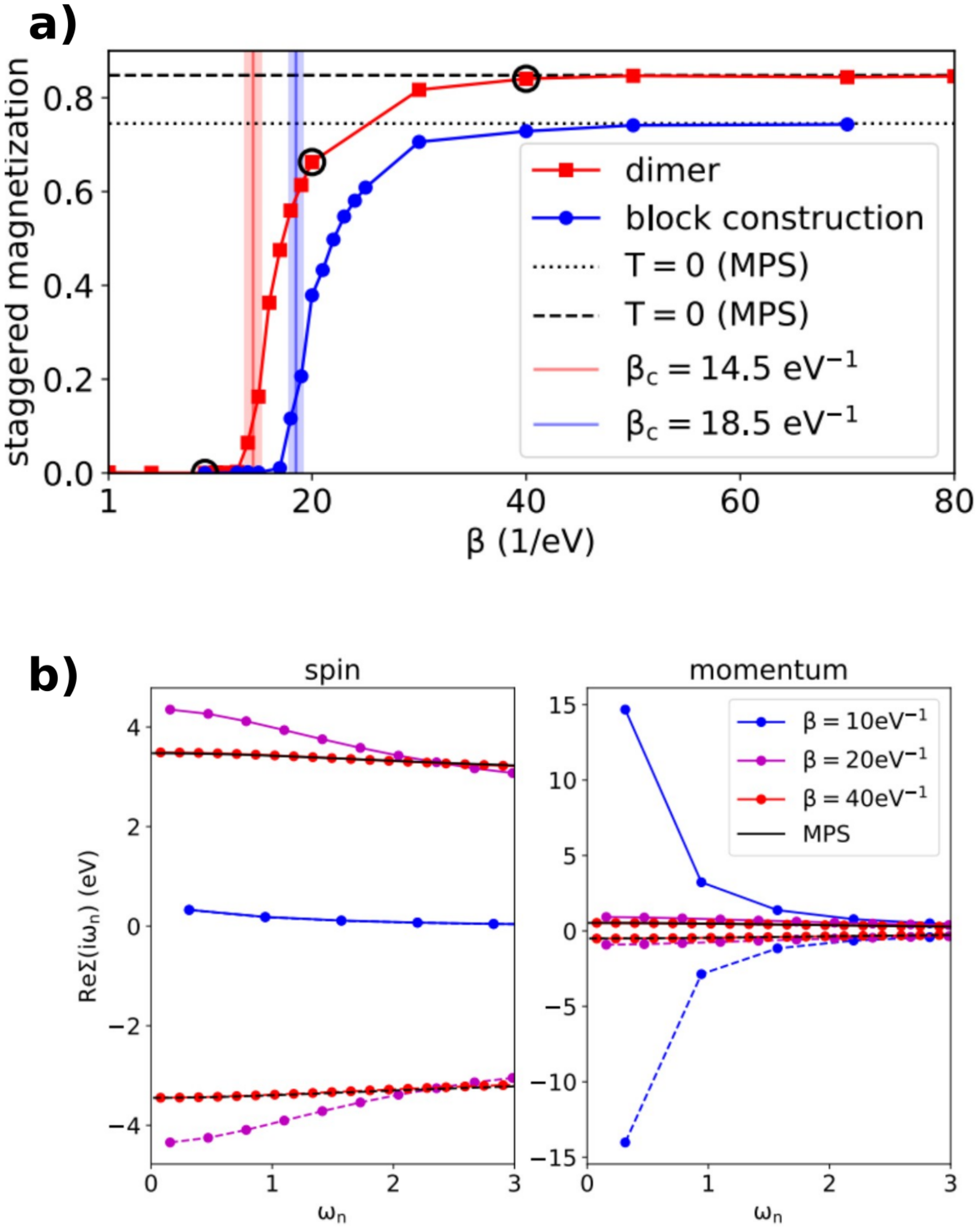

Figure 4.9: *Figure taken from Ref. 267.* (a) Staggered magnetization calculated using the dimer cluster and the block-construction. The dashed black lines indicate the $\beta = \infty$ result computed with the MPS-based impurity solver on the imaginary axis. The vertical lines depict the inverse critical temperature $\beta_c = (18.5{\pm}0.7)\,\mathrm{eV}^{-1}$ ($(14.5{\pm}0.8)\,\mathrm{eV}^{-1}$) for the block-construction (dimer) cluster. The shaded area depicts the error bar for β_c. (b) Real part of the diagonal components of the self-energy for different inverse temperatures β indicated in (a). The curves shown on the *left* correspond to the spin up (solid) and down (dashed) components on a cluster site. On the *right*, we show the self-energy at the two cluster momenta $K_1 = (0,0)$ (solid) and $K_2 = \left(0, \frac{\pi}{a}\right)$ (dashed) respectively.

as the error bars in Fig. 4.9(a) from the standard deviation of β_c in the fit collection.

While the dimer cluster overestimates the magnetic order, the block-construction, which includes slightly longer-ranged magnetic fluctuations, leads to a smaller value of T_c. As mentioned above, here we study a simplified 2D model which does not include the inter-layer magnetic exchange coupling, and therefore for which the long-range antiferromagnetic order should not be stable at finite temperature [290]. The non-zero staggered magnetization of our CDMFT calculations is rather a consequence of choosing one of the two possible stripe directions within the mean-field scheme, than an actual hallmark of the long-range magnetic order. Despite prohibiting a direct determination of T_N, the reduction of T_c upon extending the cluster size and its relatively high value nevertheless show the importance of including in-plane spin fluctuations.

At all temperatures, although there can be different magnetic orders, the system remains insulating. In order to understand the different mechanisms at play as a function of temperature, it is instructive to inspect the real part of the Matsubara self-energies, as shown in Fig. 4.9(b). For the sake of clarity, we discuss here the self-energies of the dimer cluster, but none of the conclusions change in the block-construction cluster. We compare the self-energies at three characteristic temperatures: in the paramagnetic regime ($\beta = 10\text{eV}^{-1}$), within the transition region ($\beta = 20\text{eV}^{-1}$), and in the ordered regime ($\beta = 40\text{eV}^{-1}$). First, as the system enters the insulating ordered phase, we observe the asymptotic convergence towards the MPS results (see Fig. 4.9(b)). The frequency dependence of the self-energy gets strongly suppressed. This is well described in the atomic limit as derived in Ref. 291, or by the asymptotic development of the self-energy which becomes static in the antiferromagnetic ordered limit [292].

In the paramagnetic phase the insulating behavior can not be attributed to a freezing of dynamics due to large spin polarization, but rather to a momentum-selective level splitting (*right* panel of Fig. 4.9(b)). Close to the real axis, the $K_1 = (0, 0)$ orbital is very strongly favored with respect to the $K_2 = (0, \frac{\pi}{a})$ orbital. This is consistent with previous quantum cluster calculations performed for the dimer and larger cluster, and can be interpreted as a freezing of electron movement that is not generated by spin polarization but rather by penalizing electrons with non-zero momentum [48, 103, 108].

These different mechanisms have a drastic effect on the spectral function depending on the temperature. In Fig. 4.10 we show the momentum resolved spectral function obtained with the dimer cluster obtained at the three characteristic inverse temperature $\beta = 10,\ 20,\ 40\text{eV}^{-1}$. These spectra were obtained by performing an analytic continuation with the Poor man's method from TRIQS [120, 215, 216]. We find good agreement with the experimental data only when the system is antiferromagnetic, thus showing the importance to take into account spin fluctuations in the model. At high temperature ($\beta = 10\text{eV}^{-1}$), the spectral function is divided into a LHB and UHB, of which we show only the lower in Fig. 4.9, while at low-temperature ($\beta = 40\text{eV}^{-1}$) the LHB shows a secondary splitting. It is the low-energy part of the LHB that agrees well with the experimental data. Moreover, we can reproduce with very good agreement this part of the spectrum

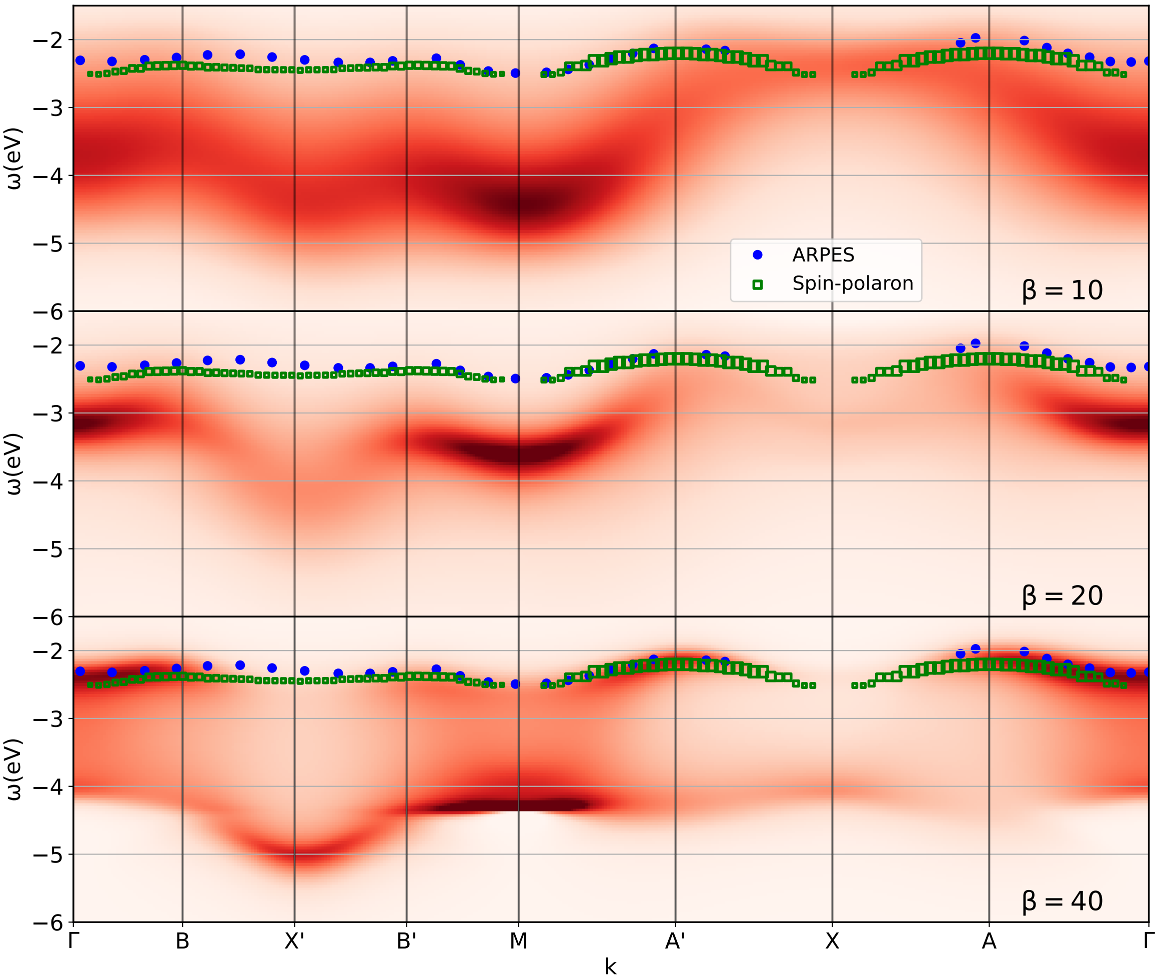

Figure 4.10: Momentum resolved spectral function obtained with the block construction. The k-path is the same as the one used in Fig. 4.6. The experimental dispersion was shifted by 0.4eV consistently with Fig. 4.6(b). The SCBA dispersion has also been shifted by $U/2$ to match the CDMFT one, and was extracted by taking the largest value in the low energy part of the SCBA spectrum. The size of the green markers represent the relative spectral weight intensity of the SCBA dispersion.

by considering a hole propagating in an antiferromagnetic background. The author performed a SCBA calculation as described in Sec. 2.6 on one sublattice only, which accounts well for the low-energy part of the spectrum below the magnetic ordering temperature T_c. The agreement with ARPES and CDMFT is excellent, even if the SCBA dispersion is symmetric at the B and B', A and A' points since we considered only one sublattice. The consequence is therefore twofold: first it means that the low-energy band observed in ARPES and CDMFT physically corresponds to a hole propagating in an antiferromagnetic background. This is consistent with the necessity of including spin fluctuations in our effective model and of lowering the temperature so to obtain a good agreement with the experiments. Then, it is a further proof that thinking of t-CuO as two weakly connected sublattices is justified, since a hole propagating inside only one of the two sublattices is enough to get a very good agreeement with experiments.

Overall, this underlines that there is a correlation-driven static level splitting present in the ordered phase whereas the paramagnetic phase is driven by dynamic splitting of momentum orbitals. One can note that despite the freezing of the dynamics of the self-energy as decreasing the temperature, at $\beta = 20\text{eV}^{-1}$ (i.e. at the magnetic transition), the spin-resolved self-energy shows an extra dynamic splitting at $w_n \to 0$, see the *left* panel of Fig. 4.9. The static part given by the high-frequency tail of the self-energy however is constantly increasing as decreasing the temperature. It is surprising to observe a splitting larger than U (the value that should be reached at 0K) at such high temperature, since from a simple screening picture we would expect the splitting to gradually decrease when increasing the temperature. In fact, we show in the following that with an effective single-site model incorporating non-local spin fluctuations in a mean-field fashion, such behavior can be recovered at the magnetic transition temperature.

4.5.2 EFFECTIVE SINGLE SITE MODEL

To identify the leading mechanism behind this extra dynamic splitting at the critical temperature, we derive here a simple single-site model including thermal fluctuations as well as antiferromagnetic fluctuations at the mean-field level. We take inspiration from the work of Stepanov *et al.* in Ref. 291 and consider a single Hubbard site subject to an external magnetic field representing the spin-exchange with the neighboring sites in a mean field fashion:

$$H = -\mu \sum_{\sigma} n_{\sigma} - h(n_{\uparrow} - n_{\downarrow}) + U n_{\uparrow} n_{\downarrow}, \tag{4.4}$$

where $\sigma = \{\uparrow, \downarrow\}$ is the spin index, $\mu = U/2$ is the chemical potential set for half-filling, h is the effective field, and U the on-site Coulomb interaction. The model is illustrated in Fig. 4.11: being close to the $U \gg t$ limit, and knowing that the system remains insulating at all temperatures, we can consider our system as a collection localized spin-1/2 which interact via an antiferromagnetic exchange coupling (Fig. 4.11(a)). For simplicity, we restrain our model to a single CuO_2 sublattice, i.e. an antiferromagnetic square lattice. We then approximate these two-body interaction by a simple staggered magnetic field on each site (Fig. 4.11(b)), which originates from the spin environment, and which in principle could be determined self-consistently. Here, we do not aim at solving exactly this problem, but rather to extract asymptotic behaviors that could explain the

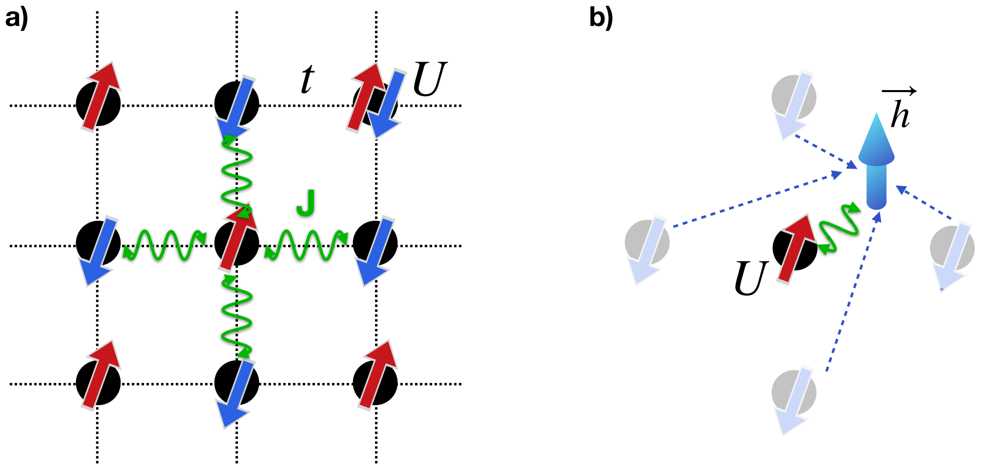

Figure 4.11: Sketch of the effective single site model restricted to one sublattice for simplicity. Since $U \gg t$ we can consider that the electrons are rather localized and antiferromagnetically aligned and interacting via the exchange term J. This many-body interacting system is approximated by the mean-field model shown in (b) in which the antiferromagnetic fluctuations with nearest-neighbors are integrated out as an effective magnetic field acting on each individual site.

Eigenstate	Energy (interacting)	Energy (non-interacting)
$\lvert 0\rangle$	0	0
$\lvert\uparrow\rangle$	$-U/2-h$	$-U/2-h$
$\lvert\downarrow\rangle$	$-U/2+h$	$-U/2+h$
$\lvert\uparrow\downarrow\rangle$	0	$-U$

Table 4.1: Eigenvectors and eigenvalues of the Hamiltonian 4.4 for the interacting and non-interacting case ($U = 0$). Note that the chemical potential is $\mu = -U/2$.

extra dynamic splitting in the self-energy.

In order to have access to the self-energy as a function of field h and inverse temperature β, we determine the non-interacting and interacting Green's functions using the finite-temperature Lehmann's representation for a single site:

$$G_\sigma(i\omega_n) = \frac{1}{\mathcal{Z}}\sum_{i,j} |\langle i|c_\sigma|j\rangle|^2 \frac{e^{-\beta E_i} + e^{-\beta E_j}}{i\omega_n + E_i - E_j},$$

and then use the Dyson equation:

$$\Sigma_\sigma(i\omega_n) = \left[G^0_\sigma(i\omega_n)\right]^{-1} - \left[G_\sigma(i\omega_n)\right]^{-1}. \tag{4.5}$$

Since the on-site Coulomb interaction is the largest characteristic energy of the system, we assume $\beta U \gg 1$ and $\beta U \gg \beta h$. Using the eigenvectors and eigenvalues of Table 4.1, one can obtain the partition functions:

$$\begin{aligned}\mathcal{Z}_0 &= 2e^{\beta(\frac{U}{2})}(\cosh\left(\beta\frac{U}{2}\right) + \cosh(\beta h))\\ \mathcal{Z} &= 2(1 + e^{\beta\frac{U}{2}}\cosh(\beta h))\end{aligned}$$

where the subscript $_0$ refers to the non-interacting system. The interacting and non-interacting Green's functions can then be written (using $\beta U \gg 1$ and $\beta U \gg \beta h$ for the interacting case):

$$\begin{aligned}G^0_\uparrow(i\omega_n) =& \frac{1}{i\omega_n + h + \frac{U}{2}}\\ G^0_\downarrow(i\omega_n) =& \frac{1}{i\omega_n - h + \frac{U}{2}}\\ G_\uparrow(i\omega_n) \approx& \frac{1}{(i\omega_n + h)^2 - \frac{U^2}{4}}\left(i\omega_n + h - \frac{U}{2}\tanh(\beta h)\right)\\ G_\downarrow(i\omega_n) \approx& \frac{1}{(i\omega_n - h)^2 - \frac{U^2}{4}}\left(i\omega_n - h + \frac{U}{2}\tanh(\beta h)\right).\end{aligned}$$

Now, using the Dyson equation 4.5, we obtain the self-energy:

$$\begin{aligned}\Sigma_\uparrow(i\omega_n) =& i\omega_n + h + \frac{U}{2} - \frac{(i\omega_n + h)^2 - \frac{U^2}{4}}{i\omega_n + h - \frac{U}{2}\tanh(\beta h)}\\ \Sigma_\downarrow(i\omega_n) =& i\omega_n - h + \frac{U}{2} - \frac{(i\omega_n - h)^2 - \frac{U^2}{4}}{i\omega_n - h + \frac{U}{2}\tanh(\beta h)}.\end{aligned}$$

We first need to check that this expression for the self-energy behaves correctly deep in the paramagnetic and in the antiferromagnetic regime. In the paramagnetic limit, i.e. $\beta h \to 0$, one gets:

$$\begin{aligned}\lim_{\beta h\to 0}\Sigma_\uparrow(i\omega_n) =& \frac{U}{2} + \frac{U^2}{4(i\omega_n + h)}\\ \lim_{\beta h\to 0}\Sigma_\downarrow(i\omega_n) =& \frac{U}{2} + \frac{U^2}{4(i\omega_n - h)}.\end{aligned}$$

The Hubbard-I [35, 201] limit is recovered up to a constant $U/2$ shift, which is consistent with the $\beta = 10\text{eV}^{-1}$ data of Fig. 4.9(a): the two spin flavors become degenerate and the high frequency tail goes to zero ($U/2$ in our expression here due to the chemical potential shift). This is in good agreement with Fig. 4.12 where is shown the splitting in the real part of the self-energy between the two spin flavors as a function of inverse temperature. At high temperature, i.e. $\beta h \to 0$ in our effective model, the splitting vanishes. We also find a good agreement in the antiferromagnetic

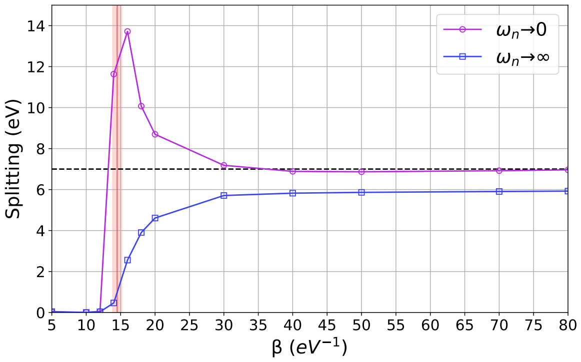

Figure 4.12: Splitting in the real part of the local component of the Self-energy between the two spin flavors obtained with the dimer cluster as a function of the inverse temperature β. The shaded vertical region depicts the critical inverse temperature $\beta_c = 14.5 \pm 0.8\mathrm{eV}^{-1}$. The horizontal black dotted line indicates the value of the Coulomb on-site interaction $U = 7\mathrm{eV}$.

limit $\beta h \to \infty$ (h finite), since we recover the real static splitting U between the two different spin flavors:

$$\begin{aligned}\lim_{\beta h \to \infty} \Sigma_{\uparrow}(i\omega_n) =& 0 \\ \lim_{\beta h \to \infty} \Sigma_{\downarrow}(i\omega_n) =& U.\end{aligned}$$

This is in very good agreement with the CDMFT calculations at $\beta > 40\mathrm{eV}^{-1}$ shown in Fig. 4.12.

Now that we have shown that the correct limits are recovered as a function of temperature, we place ourselves below the critical temperature T_c, so that βh is finite, and compute the low- and high-frequency limits:

$$\begin{aligned}\Sigma_{\uparrow}(i\omega_n \to \infty) =& \frac{U}{2} - \frac{U}{2}\tanh(\beta h) \\ \Sigma_{\downarrow}(i\omega_n \to \infty) =& \frac{U}{2} + \frac{U}{2}\tanh(\beta h) \\ \Sigma_{\uparrow}(i\omega_n \to 0) =& \frac{U}{2} - \frac{U}{2}\frac{1}{\tanh(\beta h)} \\ \Sigma_{\downarrow}(i\omega_n \to 0) =& \frac{U}{2} + \frac{U}{2}\frac{1}{\tanh(\beta h)}.\end{aligned}$$

One can immediately see that as the temperature increases, i.e. as βh decreases, the splitting of the high-frequency tail for the two spin species decreases. The same trend is observed in the CDMFT calculations close to the transition, as can be seen in Fig. 4.12. Moreover, since in the low-frequency limit the $\tanh(\beta h)$ appears in the denominator, the splitting becomes larger than U as the temperature increases until h remains finite. This is again perfectly consistent with the trend observed in Fig. 4.12, where we find that at the magnetic transition the splitting at the $w_n \to 0$ limit diverges at the transition temperature T_c.

Therefore, this simple single-site effective mean-field model can capture the surprising enhancement of the spin splitting in the self-energy at low-frequency. This behavior in the ordered phase

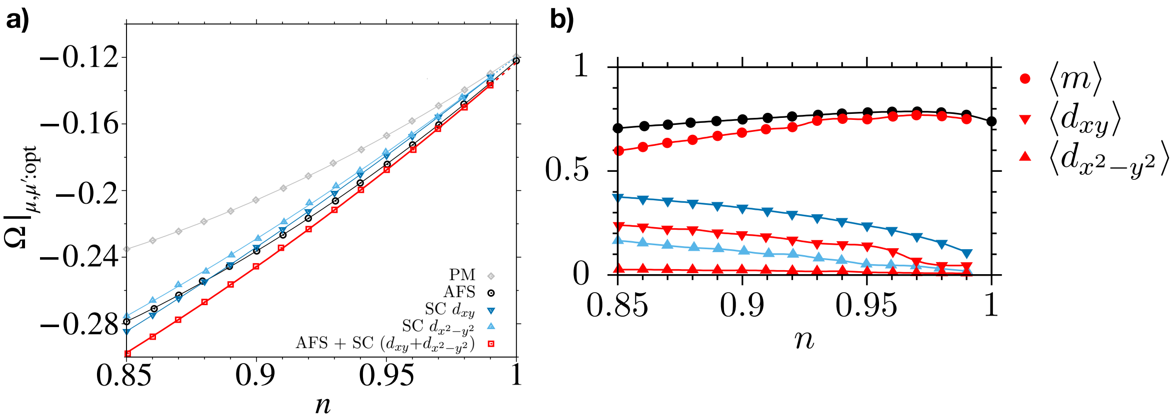

Figure 4.13: *Figure taken from Ref. 267*. (a) Internal energy Ω as a function of filling n for different solutions within VCA: Antiferromagnetic stripe order (AFS), superconductivity (SC) of d_{xy} or $d_{x^2-y^2}$ symmetry as well as coexistence of all three. In (b) are shown the corresponding order parameters; the colors correspond to the solutions of (a). For all calculations we used the full 8-site diamond cluster of Fig. 4.1(g), i.e. *without* block-construction and optimized the functional in addition with respect to the (cluster) chemical potential μ (μ').

can in large parts be traced back to an interplay between thermal and magnetic fluctuations at the magnetic transition.

4.6 SUPERCONDUCTIVITY

So far in this chapter we have studied the correlations effects in undoped t-CuO. Although the parent compound already shows remarkable behavior such as the sublattice decoupling, a much richer physics may occur upon hole-doping. Experimentally achieving the chemical doping of t-CuO is extremely difficult, and has not been realized yet, since the standard chemical substitution used for cuprates is impossible due to the lack of charge reservoir layers. Theoretical doping is much simpler since we can tune at will the chemical potential in the effective 2D one-band model. In this section, we study the emergence of superconductivity upon hole-doping: its symmetry and possible interplay with the antiferromagnetic fluctuations. To this aim, B. Lenz performed VCA [68–70] calculations, a method particularly well suited to study the energetics of different symmetry breaking solutions of the model and their competition.

In usual cuprates, superconductivity occurs upon hole-doping and has an order parameter of $d_{x^2-y^2}$ symmetry due to the geometry of the CuO$_2$ layers. In t-CuO however, we expect that the sublattice decoupling survives as doping the material, such that the order parameter would rather be of d_{xy} symmetry (since the two CuO$_2$ sublattice are rotated by 45° with respect to the usual cuprates). To check for these different symmetry channels, a paramagnetic calculation is performed first, using the full 8-site cluster of Fig. 4.1(g) *without* block construction, and the internal energy Ω is calculated as a function of doping (ranging from $\delta = 0.0$ to $\delta = 0.15$). The result is shown as the gray curve in Fig. 4.13(a). Then, calculations were performed for different ordering fields separately: antiferromagnetic stripes, $d_{x^2-y^2}$ and d_{xy} superconductivity. All channels, separately, provide energetically favorable solutions for fillings $n < 1$ compared to the paramagnetic solution, with the antiferromagnetic stripes being the most favorable at almost all doping until $n \simeq 0.9$. Interestingly, the magnetization is slightly enhanced at very low dopings ($0.95 < n < 1$) with respect to the undoped solution, see Fig. 4.13(b). While both pairing channels also lower the internal energy compared to the paramagnetic case, the d_{xy} superconductivity shows a significantly larger order parameter than $d_{x^2-y^2}$, consistently with our expectations based on the sublattice decoupling scenario.

When allowing for competition, we find that the coexistence of superconductivity and antiferromagnetic stripes leads to the overall lowest energy solution at zero temperature, see red curve in Fig. 4.13(a). This is consistent with previous studies finding coexistence of the two phases [50, 145–148]. In Fig. 4.13(b) we observe that the corresponding order parameters are reduced in the coexistence solution as compared to the pure solutions mentioned above. This indicates a competition between magnetic and superconducting orders upon doping [145, 146]. Most interestingly, the $d_{x^2-y^2}$ superconducting order parameter is strongly suppressed by the presence of the antiferromagnetic stripe order such that the Cooper pairing is mainly of d_{xy}-symmetry. Finally, we note that superconductivity of d_{xy} symmetry actually corresponds to $d_{x^2-y^2}$ symmetry within each of the two sublattices (by placing ourselves in the 45° rotated reference frame). Therefore, in the context of sublattice decoupling, the energetically most favorable solution could be interpreted as the emergence of a $d_{x^2-y^2}$ superconducting state coexisting with an (Néel) antiferromagnetic order on each sublattice.

4.7 CONCLUSION

In this chapter, we give a first formal justification of the description of t-CuO as two weakly interacting CuO_2 sublattices [135] which explains the weak symmetry breaking found in ARPES [134]. Indeed, by inspecting selected moments of Matsubara self-energies, we show that the dynamic correlations effectively weakens the sublattice coupling. Making use of this mechanism, we motivate the construction of a super-cluster which improves the momentum-resolved spectral functions and equal energy maps computed with CDMFT on the real axis [58, 141–144], and is in excellent agreement with experiments [134]. We perform calculations at finite temperatures from which we identify the driving mechanism for the insulating behavior found in the ordered as well as the PM phases. We find an enhancement of the spin splitting in the Matsubara self-energy at the magnetic transition temperature, which we trace back to be of intertwined magnetic and thermal origin by constructing an effective single-site mean-field model.

Given the good agreement of our results with experiment, we believe that a minimal one-band Hubbard model is sufficient to capture most electronic and magnetic properties of t-CuO as long as dynamical local and short-range fluctuations are treated properly. Further, using VCA we are able to make predictions about the presence and symmetry of superconductivity upon hole doping. We find that the decoupling of the sublattices carries through to the superconducting state, in coexistence with antiferromagnetic stripe order. The d_{xy} symmetry of the superconducting order parameter can be interpreted as a superconducting state of $d_{x^2-y^2}$-type within each sublattice.

Due to its tetragonal symmetry, the lack of interstitial atoms between the well separated 2D CuO layers, and the fact that the electronic properties are mainly governed by its interlaced CuO_2 sublattices, we believe that t-CuO may be the ideal material to gain a more complete understanding of the physics behind cuprate superconductivity. Although doping of t-CuO by chemical substitution is probably not feasible experimentally, the study of doped t-CuO by other experimental techniques like space charge doping [293], which has been successfully applied to other cuprates [294], could be an option. Another interesting route to pursue experimentally consists in growing CuO layers on top of a different substrate. Recently, copper-oxide films have been grown on $Bi_2Sr_2CaCu_2O_{8+\delta}$, which resulted in nodeless pairing in the superconducting state [295]. Whereas the monolayer was most likely of CuO_2 structure, the possibility of CuO could not be ruled out and is supported by *ab initio* calculations [296].

5 INTERFACE PROPERTIES OF TETRAGONAL CuO

5.1 PUZZLING SPIN AND ORBITAL MOMENTS

As shown in the previous chapter, using CDMFT, we are able to explain the experimentally observed sublattice decoupling [126, 134, 135], reproduce the ARPES spectrum of Ref. 134, and predict the nature of the superconducting order parameter [267]. We moreover confirm the antiferromagnetic stripe order observed in RIXS [135] and μ-SR [136] as stemming from the superposition of two usual antiferromagnetic square sublattices, in agreement with hybrid DFT calculations [128, 129, 131]. Along with the experimental and theoretical knowledge on the structure of t-CuO [124, 125, 128–131], we would now dispose of a coherent understanding of the bulk properties of t-CuO, if it was not for the recent finding of an anisotropic paramagnetic spin moment and a pinned orbital moment in C/t-CuO/STO samples using XMCD at the Cu $L_{2,3}$ edge [136].

The existence of such moments is puzzling since t-CuO is antiferromagnetically ordered and does not contain any element with strong spin-orbit coupling (SOC). Hernandez *et al.* proposed a simple model [136] (see Fig. 5.1), in which t-CuO would be composed of ferromagnetically ordered CuO layers (in-plane), which are antiferromagnetically stacked along the *c* axis (out-of-plane). The last CuO layer would be paramagnetic hence would follow the magnetic field, while another layer would be uncompensated and therefore would yield the pinned moments. Although this minimal model qualitatively accounts for the experimental observations, it is not satisfactory since:

(i) the ferromagnetic ordering inside each layer is in contradiction with all previous experimental [135] and theoretical [128, 129, 131] findings which support antiferromagnetic stripe ordering of the Cu spins inside the layers,
(ii) the uncompensated layer is composed of spin moments and not orbital ones, whereas the pinned moment is mainly of orbital character,
(iii) there is no reason why one layer should have a paramagnetic behavior, especially if all the Cu spins inside such layer are ferromagnetically ordered.

None of the experimental and theoretical work already published can provide a clear explanation. Our minimal model for bulk t-CuO in the previous chapter does not account for the presence of a paramagnetic moment, neither for an orbital one. More generally, the bulk properties of t-CuO seem incompatible with the XMCD measurements, what calls for a careful analysis of its interface with STO. Indeed, oxide heterostructures are known to display a large range of emergent phenomena [297, 298], and more especially STO-based junctions which can yield a

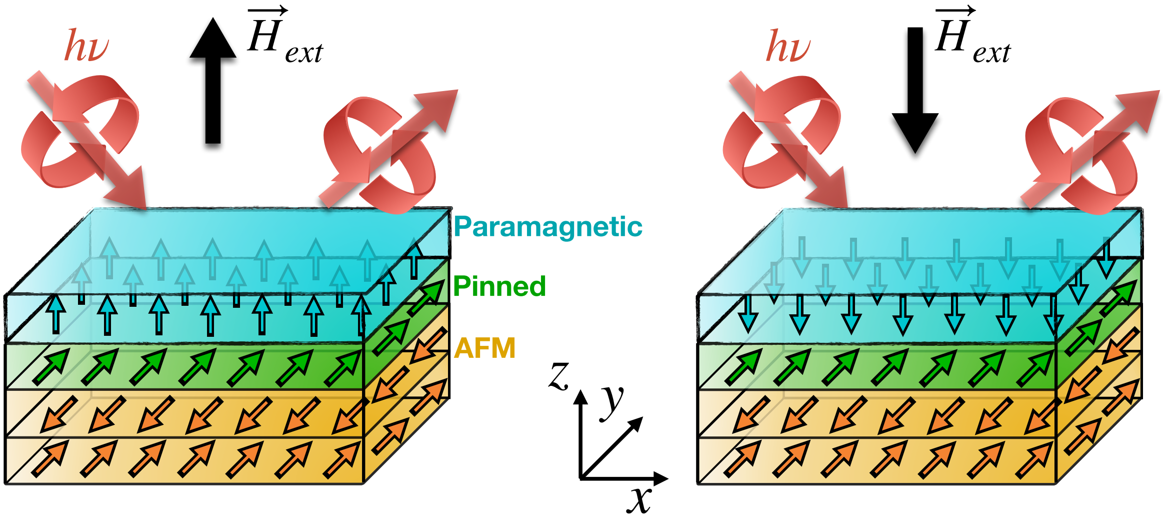

Figure 5.1: Sketch of the model proposed in Ref. 136. The paramagnetic top layer aligns with the external magnetic field, while the pinned and antiferromagnetic layers below are insensitive. The incoming x-ray circularly polarized is shown with the pink arrows (only one of the two circular polarization is illustrated).

2DEG at their interface. The latter is observed in $BiMnO_3$/STO, $LaAlO_3$/STO, γ-Al_2O_3/STO and $LaVO_3$/STO [149, 150, 299, 300] for instance. The existence of a 2DEG at the t-CuO/STO interface is a promising prospect, for it was observed by Mardegan *et al.* that γ-Al_2O_3/STO samples display a paramagnetic spin moment [150], knowing that high electron mobility has been observed at the interface [301–303]. This scenario however does not provide a clear insight for the presence of a pinned orbital moment.

The pinned moment being an order of magnitude smaller than the spin one [136], and its origin being even more unclear, we will focus our modeling on the search of a 2DEG at the t-CuO/STO interface. In the case of $BiMnO_3$/STO, $LaAlO_3$/STO, and $LaVO_3$/STO, the metallic behavior is due to the polar discontinuity at the interface [149, 150, 299, 300]. However, the CuO layers are not polar, and we have seen in the previous chapter that it is a Mott insulator with a gap $\Delta > 2.35$eV. Since STO is a band insulator, the presence of a 2DEG at the bare interface does not seem straightforward. Though, it is known for other heterostructures or bulk materials that the formation of O vacancies, to which STO is higly susceptible, can spark a 2DEG [304–308]. Considering that the STO substrate is fixed at 600K during the epitaxial growth, even if the pressure in oxygen is high and if the sample is annihilated, vacancies are very likely to be formed.

Although the 2DEG scenario is promising, Hernandez *et al.* argued against it since they did not observe any sign of Ti^{3+} in the XMCD signal at the Ti $L_{2,3}$ edge [136], contrary to $LaAlO_3$/STO and γ-Al_2O_3/STO in which a spin moment is carried on the Ti atoms [149, 150, 299]. In this chapter, using first principle DFT+U calculations, we show that a 2DEG at the t-CuO/STO interface is in fact *not incompatible* with the XMCD measurements. More precisely, the formation of vacancies at the interface can lead to the appearance of a polarized 2DEG hosted in the CuO layer. Most importantly, even if the defect is located in the TiO_2 interface layer, the overall valence of the Ti atoms is unchanged with respect to the bulk, such that the 2DEG is invisible at the Ti $L_{2,3}$ edge. In our calculations, the interface metallic states have a non-zero spin polarization, although there is no external magnetic field, due to the finite size of the unit cells and the specific arrangement of the stripes and vacancies. Since the latter are randomly distributed in the real material, without external magnetic field the 2DEG would be non-polarized, as expected for a paramagnetic spin moment. We find that both the *local* and *global* C_4 symmetries are broken in the CuO layer above the vacancy, which leads to the pinning of the in-plane component of the orbital moment, while its out-of-plane counterpart remains collinear and proportional to the out-of-plane spin moment. Our scenario therefore provides a mechanism for the paramagnetic spin moments, being a consequence of a 2DEG, as well as for the pinned in-plane orbital moment, which results from the breaking of the local and global C_4 symmetries when forming vacancies in the interface TiO_2 layer.

5.2 MODEL AND METHOD

We describe in the following how we model the t-CuO/STO heterostructure, with and without vacancies, and how the calculations are carried out.

5.2.1 MODEL

To model the t-CuO/STO junction we use unit cells of the type shown in Fig. 5.2(a): the CuO layers are stacked onto a 2 unit cell-thick TiO_2-terminated STO substrate [125, 130, 133]. Cu atoms in t-CuO have a half-filled d_{xy} orbital which would lead within LDA to a metallic ground state. We therefore apply DFT+U [151–153], as presented in Sec 1.4, using the semilocal Perdew–Burke–Ernzerhof (PBE) functional [163, 164], with a local $U = 6$eV on the Cu d orbitals. Since XMCD measurements are highly sensitive to the magnetic properties of the sample, we make sure that our unit cells enable the stripe ordering. We moreover double the unit cell in the (x,y) plane (see Fig. 5.4) when inserting an oxygen vacancy and, to keep the computations tractable, we restrict our model to a 4 CuO layer coverage. We refer to the different layers following the nomenclature of Fig. 5.2(a): CuO-$\{1, 2, 3, 4\}$, SrO-$\{1, 2\}$ and TiO_2-$\{1, 2\}$. Note that the large unit cells considered also prevent the use of hybrid functionals, which have shown to yield excellent results for t-CuO [128–131]. In particular, Franchini *et al.* studied the thickness dependence of the t-CuO film on the crystal structure and the DOS, and found that the experimental results were best reproduced with a 8 CuO layer coverage [130]. To be consistent with such results, we decided to use as a starting point the inter-layer distances from Ref. 130. The STO lateral lattice parameter is set to $a = 3.9$Å, as obtained with hybrid DFT [165, 309] in excellent agreement with experiments [310].

5.2.2 METHODOLOGY

First an ionic relaxation is performed using the VASP [252–255] with a $6 \times 6 \times 1$ Monkhorst-Pack **k**-grid, until the maximum force on each atom is smaller than 10meV. We use projector augmented wave-PBE pseudopotentials [311] with a cut-off energy of 400eV for the bare interface, which is increased up to 600eV for the larger unit cells with vacancies. The CuO layers are

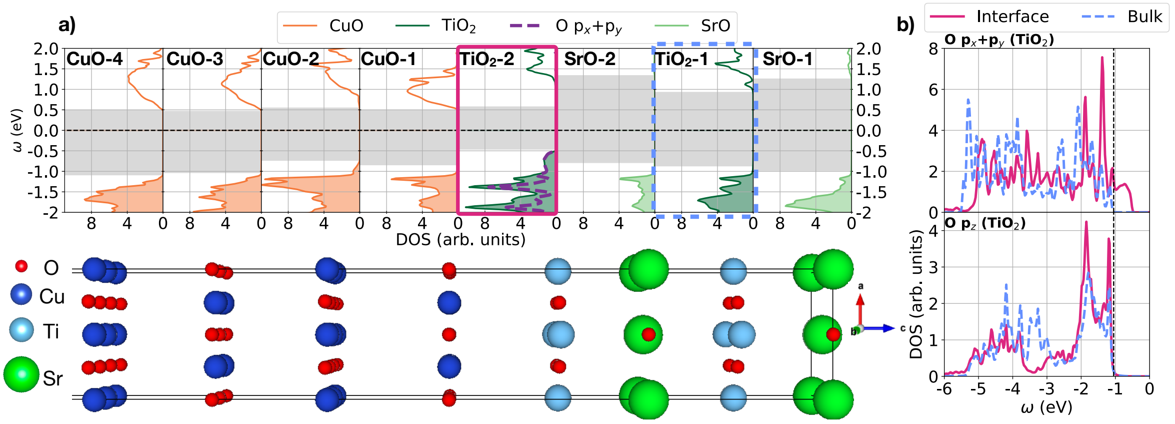

Figure 5.2: (a) Layer-resolved DOS calculated for the t-CuO/STO junction without defect. The colored shaded area depicts the occupied states, and the grey shaded patches highlight the gap in each layer. We also illustrate the crystal structure of the t-CuO/STO junction (before ionic relaxation). (b) Projected DOS on the $p_{x,y,z}$ orbitals of the O atoms in the two TiO_2 layers corresponding to the two framed panels in (a).

relaxed while the STO atoms are kept fixed except when considering an oxygen vacancy in the TiO_2-2 interface layer, in which case the whole structure is optimized. We did check that keeping the STO structure fixed did not change any conclusion. In fact, in the absence of vacancies in the STO layers the relaxation is small, in contrast to t-CuO which always shows a large buckling (see Fig. 5.11). We illustrate it for instance in the case of the bare interface in Fig. 5.3. Observing larger distortions in t-CuO seems quite natural since its crystal structure is sparser than that of its substrate, and we will show in the following that those distortions have a direct impact on the electronic structure and the magnetic moments.

In order to check the consistency of the VASP calculations, we also performed PBE+U calculations using Wien2k package [173, 174]. The results are qualitatively the same for all the cases considered, however we notice that despite using the same PBE functional and U value, the gap obtained in Wien2k is always larger (of about 0.5eV for the CuO layers) than in VASP (for $U = 0$ the two codes agree), as shown in Fig. 5.3 for the bare interface. Changing the smearing factor and type in VASP does not change this discrepancy, as well as the wavefunction cut-off energy. We then perform a Wien2k calculation on the relaxed structured resulting from VASP for each of the cases considered, and from which all analysis and conclusions will be drawn. A $6 \times 6 \times 1$ Monkhorst-Pack **k**-grid is used, and due to computational limitations we managed the size of the planewave basis set by reducing the RKmax value when necessary (the smallest value being 5.14). We did check for the bare interface that lowering the RKmax value did not change significantly the DOS. To have access to the value of the orbital moment we also performed calculations with SOC on the Sr, Ti and Cu atoms.

5.3 BARE INTERFACE

From previous studies on the t-CuO/STO junction we know that the bare (i.e. defect-free) interface should not yield a 2DEG [130, 133]. This is consistent with our results, see Fig. 5.2(a), in

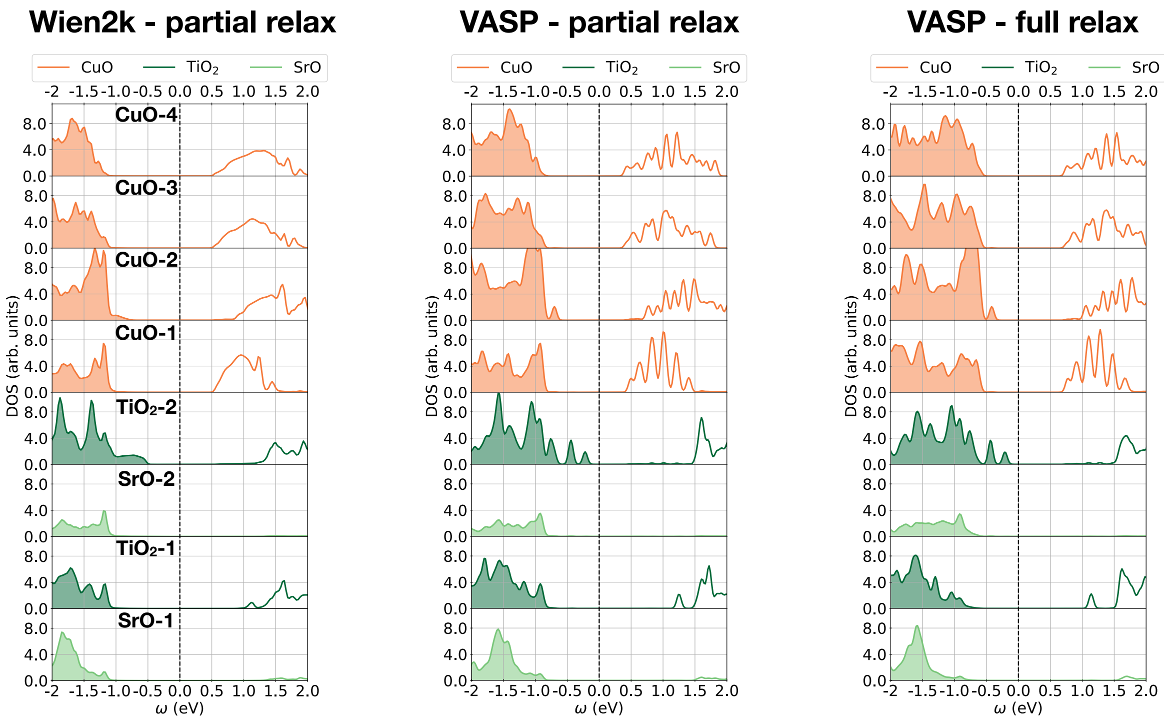

Figure 5.3: Layered resolved DOS for the bare junction using Wien2k (*left*) and VASP (*center*) with relaxation of the CuO layers only, and VASP with relaxation of the whole structure (*right*). For the VASP calculations we used a Gaussian smearing $\gamma = 0.05\text{eV}$.

which we plot the layer-projected DOS. The gap $\Delta_{DFT+U} \simeq 1.5\text{eV}$ in t-CuO is layer independent and in good agreement with previous DFT+U calculations [133], although smaller than the photoemission lower bound $\Delta \geq 2.4\text{eV}$ [134]. The situation is different in the STO substrate where a clear difference can be seen between the interface and *bulk* TiO_2 layers: the gap is reduced from 2eV in the *bulk* (TiO_2-1) to 1.5eV at the interface (TiO_2-2). The states reducing the gap are traced back to be of O p_x/p_y origin. Fig. 5.2(b) shows that the p_x/p_y orbital states are pushed towards the Fermi level at the interface, whereas the p_z orbital states are stable in energy and even slightly de-populated at the interface as evidenced by the loss of density around -3.5eV. This is consistent with previous first principles calculations performed for TiO_2-terminated STO and $BaTiO_3$, and is the consequence of the emergence of pure O p_x/p_y states not hybridized with the Ti orbitals at the surface [312, 313]. Interestingly, adding a thin film of t-CuO above STO does not change this behavior. Due to the large original band gap of STO the system remains insulating since no 2DEG is observed at the bare interface, and the t-CuO antiferromagnetic stripe order is not disturbed.

As expected, from the bare interface we can not draw an explanation of the XMCD results since the system remains insulating and perfectly antiferromagnetic, ruling out any possibility of a paramagnetic spin moment. In the following we explore the effects of inserting O vacancies at the interface layers. Among the many possibilities to do so, we focus on five of them which should already give an clear trend of the effects on the electronic properties. We first study the case of a vacancy in the CuO-1 layer (Fig. 5.4(a)) in Sec. 5.4. Then, in Sec. 5.5 we focus on the most promising case in which a vacancy is considered in the TiO_2-2 layer (Fig. 5.4(b)). Since a 2DEG

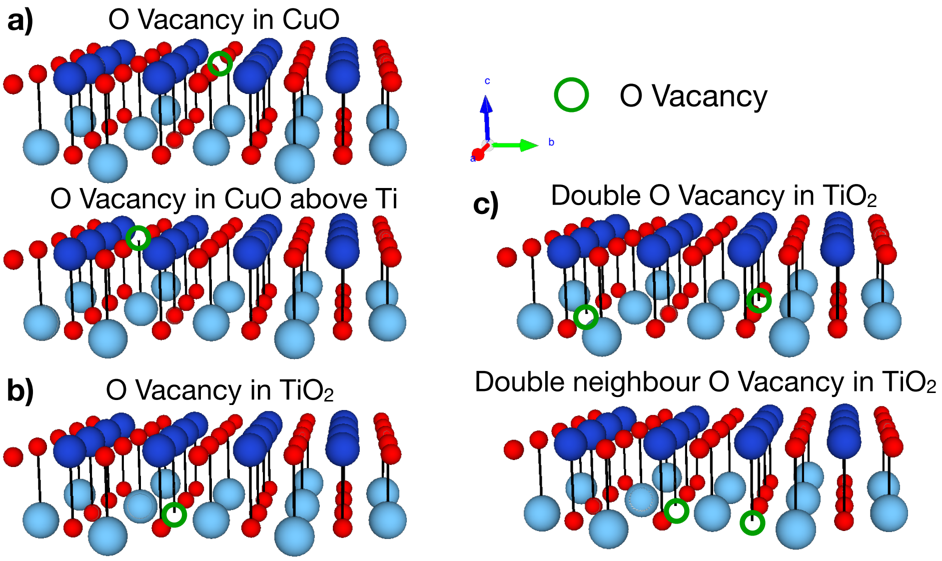

Figure 5.4: (a)-(c) Zoom on the two interface CuO-1 and TiO_2-2 layers presenting the 5 vacancy configurations considered in this work. The black lines between the O and Cu/Ti atoms show that half of the O in the CuO-1 layer do not have a Ti neighbor.

appears in the latter case, we increase the vacancy concentration further (Fig. 5.4(c)) trying two different configurations.

5.4 VACANCY IN THE CuO INTERFACE LAYER

There are two geometrically different ways of creating an O vacancy in the interface CuO-1 layer (see Fig 5.4(a)): either by removing an O having a neighboring Ti in the layer below, or an O having no such neighbor. It is important to note that these two cases preserve the global C_4 rotational symmetry both in the CuO-1 and the TiO_2-2 layers. For the two configurations interestingly give the same results, we mostly focus here, in Fig. 5.5, on the ones obtained considering the vacancy without neighboring Ti atom. STO behaves similarly to the bare interface configuration, see Fig. 5.5(a). The gap is again reduced by 0.5eV at the interface, but with the addition of small extra contributions around ±0.4eV sparked by the large in-gap states appearing in the interface CuO-1 layer. The latter shows a drastic change compared to the bare interface case since a new set of in-gap states of mostly Cu d orbital character appears. Contrary to the usual effect of chemical doping in cuprates, where a ZRS [38] is formed between the Cu d and O p, here the O does not significantly contribute. Those states are localized around the vacancy, as can be seen in Fig. 5.5(b) where we show the projected DOS on the NN Cu atoms with respect to the vacancy, NNN and NNNN. The fact that only the four NN have a sizable contribution, that the oxygen contribution is weak, and that the surrounding layers DOS display a vanishing density at ±0.4eV show the localized nature of these states, both in- and out-of-plane. As expected, it is the d_{xy} orbital of the NN Cu atoms surrounding the vacancy that mostly contributes to these in-gap states, see Fig. 5.5(c), although we notice a sizable contribution from the d_{z^2} orbital in the occupied region.

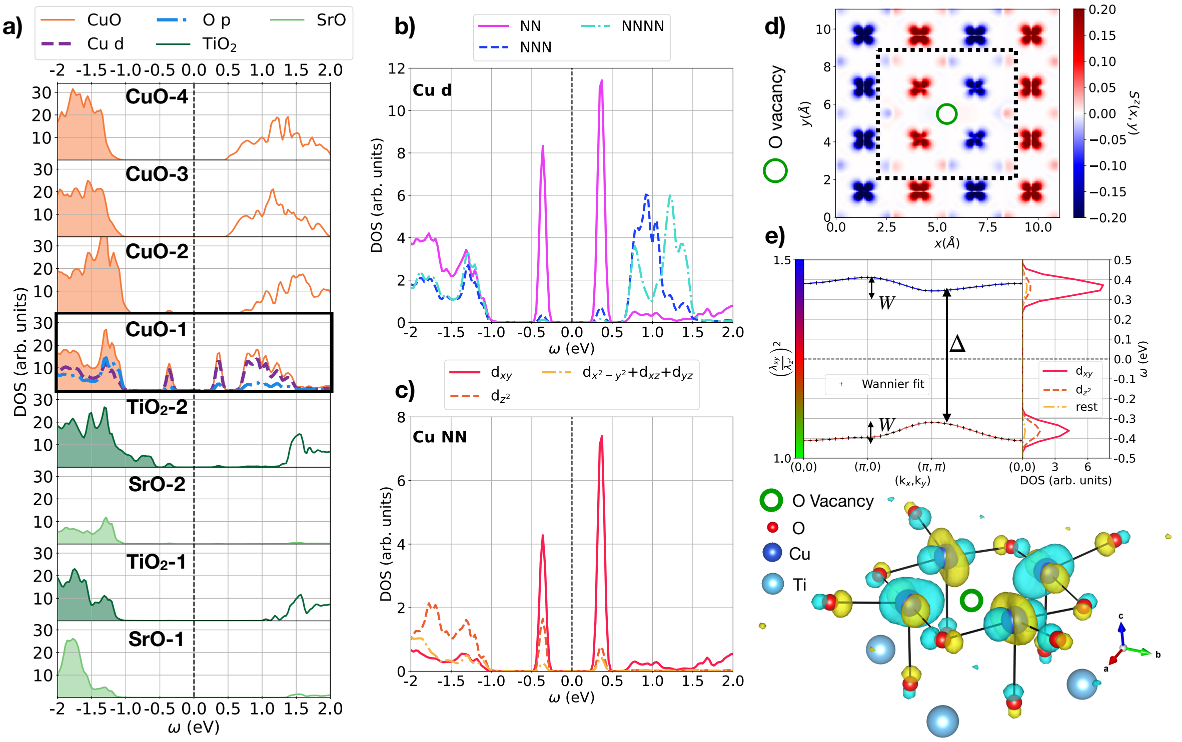

Figure 5.5: (a) Layer-resolved DOS calculated for the case of an O vacancy in the CuO-1 layer. (b)-(c) Site and orbital projected DOS for the Cu atoms at the CuO-1 interface layer corresponding to the framed panel in (a). (d) Spin density map of the interface CuO-1 layer. (e) Band structure and projected DOS zoomed on the in-gap states along with the fitted Wannier bands (*top*) resulting in the wannier orbitals showed in the *bottom* around the vacancy, which are centered on the four NN Cu sites highlighted with the dotted frame in (d). The band color depicts the ratio $\left(\frac{\lambda_{xy}}{\lambda_{z^2}}\right)^2$ between the contributions from d_{xy} and d_{z^2}.

Unit-Cell translation	$t_{1,1}$ (eV)	$t_{1,2}$ (eV)	$t_{2,1}$ (eV)	$t_{2,2}$ (eV)
$(0,0,0)$	-0.002	0.364	0.364	-0.002
$(1,0,0)$	-0.006	-0.001	-0.001	-0.006
$(-1,0,0)$	-0.006	-0.001	-0.001	-0.006
$(0,1,0)$	-0.001	0.038	-0.003	-0.001
$(0,-1,0)$	-0.001	-0.003	0.038	-0.001

Table 5.1: Hopping parameters extracted from the Wannier fit showed in Fig. 5.5(e) for only two of the four NN Cu atoms (labeled 1, 2). The unit-cell translation indicates if the hopping is inside the first unit-cell $(0,0,0)$, or outside $(x,y,0)$.

The missing O leads to an increase of the electronic density on the surrounding NN Cu sites, which results, in combination with the d_{z^2}/d_{xy} orbital mixing, in a peculiar effective orbital carrying the in-gap states on the NN sites. It is shown in the spin density plot of Fig. 5.5(d): the local C_4 symmetry on each NN Cu site is broken, but the global symmetry around the vacancy is conserved. The symmetry of the in-gap states around the Fermi level and the position of the Cu atoms around the vacancy advocate for the formation of bonding/anti-bonding localized states around the vacancy, thus preventing the formation of an electron gas. This can be seen by performing a fit of the in-gap bands with Wannier functions using `wannier90` [183, 184], as shown in Fig 5.5(e). The two bands are degenerate in spin, hence we present the fit performed only for the up spin part (the down spin giving the exact same results). We performed the fit starting from the two d_{xy} orbitals of two of the NN Cu atoms, i.e. two Cu for the up spin flavor, and obtained a perfect matching with the two PBE+U bands. Consistently with the spin density, the Wannier orbitals break the local C_4 symmetry, and they expand towards the vacancy position in the middle of the four NN Cu. They interestingly have a d_{z^2}-like shape but rotated in-plane with the main lobe pointing towards the vacancy. This translates in the tight-binding Hamiltonian obtained from the Wannierization to a large hopping amplitude between the NN Cu sites inside the unit-cell $t_{in} \simeq 0.364$eV, and small hopping outside $t_{out} \simeq t_{in}/10$, with on-site energy $\epsilon \simeq 0$. Hence, the splitting between the two bands $\Delta \simeq 2t_{in}$ is consistent with a dimerization picture, and large comparatively to the small bandwidth W since t_{out} is one order of magnitude smaller than t_{in}, see Table 5.1.

Alike the previous case, the system remains insulating (although the gap is reduced at the interface CuO-1 layer) and antiferromagnetic, i.e. no paramagnetic spin moments would be observed. Still, it is interesting to study the orbital moments obtained from the calculations including SOC. Indeed, as advocated in Ref. 314, a crystalline defect could be at the origin of an orbital momentum pinning. If the magnetization axis is set out-of plane (0,0,1), the orbital moment is parallel and proportional to the local spin, such that on the NN Cu sites the absolute value of the orbital moment is reduced (see Fig. 5.6(a)). On every other site the magnetization is $m_{spin} \simeq \pm 0.70\mu_B$ and $m_{orb} \simeq \pm 0.14\mu_B$, while on the four NN sites it is weaker: $m_{spin} \simeq \pm 0.45\mu_B$ and $m_{orb} \simeq \pm 0.09\mu_B$. Moreover, as the four NN sites are equally dispatched on the up and down spin stripes the total orbital moment is zero. Most importantly, the out-of plane part of the orbital moment is collinear with the spin.

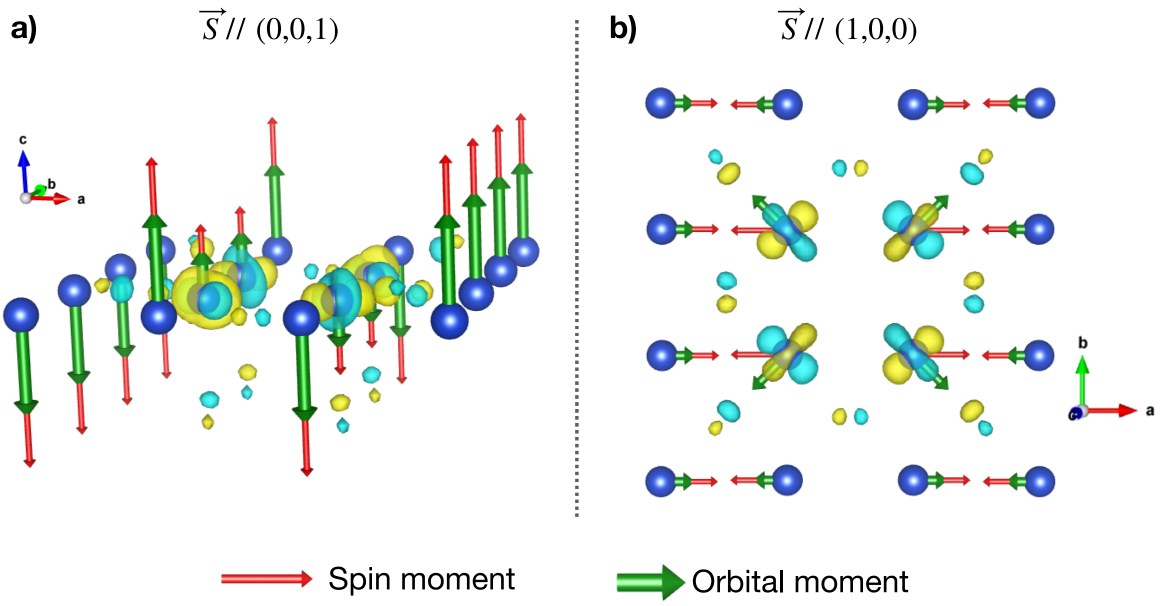

Figure 5.6: Schematic representation of the orbital momentum orientation for two different magnetization axis: (a) (0,0,1), (b) (1,0,0). The length of the vectors illustrates the variation of the absolute value of the moments.

The situation is different when setting the magnetization axis in-plane. If it is along (1,0,0), or (0,1,0), the orbital moment is collinear with the spin on all the Cu sites but the four NN ones, on which it is pinned along (±1,±1,0), as illustrated in Fig. 5.6(b). Moreover, its value is not proportional anymore to the spin moment, it is even inversely proportional if the magnetization axis is set along (1,1,0) for the two NN atoms aligned along (1,1,0) around the vacancy. Indeed, in the case of (1,1,0), most of the sites display a spin moment $m_{spin} \simeq \pm 0.70\mu_B$ and $m_{orb} \simeq \pm 0.05\mu_B$ (along the magnetization direction), unless for the two aforementioned sites which carry $m_{spin} \simeq \pm 0.45\mu_B$ and $m_{orb} \simeq \pm 0.07\mu_B$. Therefore, although the total orbital moment averages out to zero because the global C_4 symmetry is not broken, we identify here a pinning mechanism which is intimately linked with the breaking of the on-site C_4 symmetry. On the four NN sites, the in-plane part of the orbital moment can be non-collinear and its absolute value even inversely proportional to that of the spin moment.

None of these conclusions change when considering an O vacancy lying above a Ti site instead of vacuum. We do not extensively describe this case here, as it is very similar, but for completeness we show the layered-DOS in Fig. 5.7. The same in-gap states appear, again confined in the CuO-1 layer only, and since this type of vacancy also preserves the global C_4 symmetry of the unit cell, the very same arguments and conclusions apply.

Hence, while this scenario is not suited for explaining the paramagnetic spin moment feature, it provides precious insights on the orbital moment behavior close to a vacancy. A key argument in favor of this pinning mechanism is that it would be consistent with the XMCD measurements in which only the in-plane component of the orbital moment is pinned [136]. What is missing in

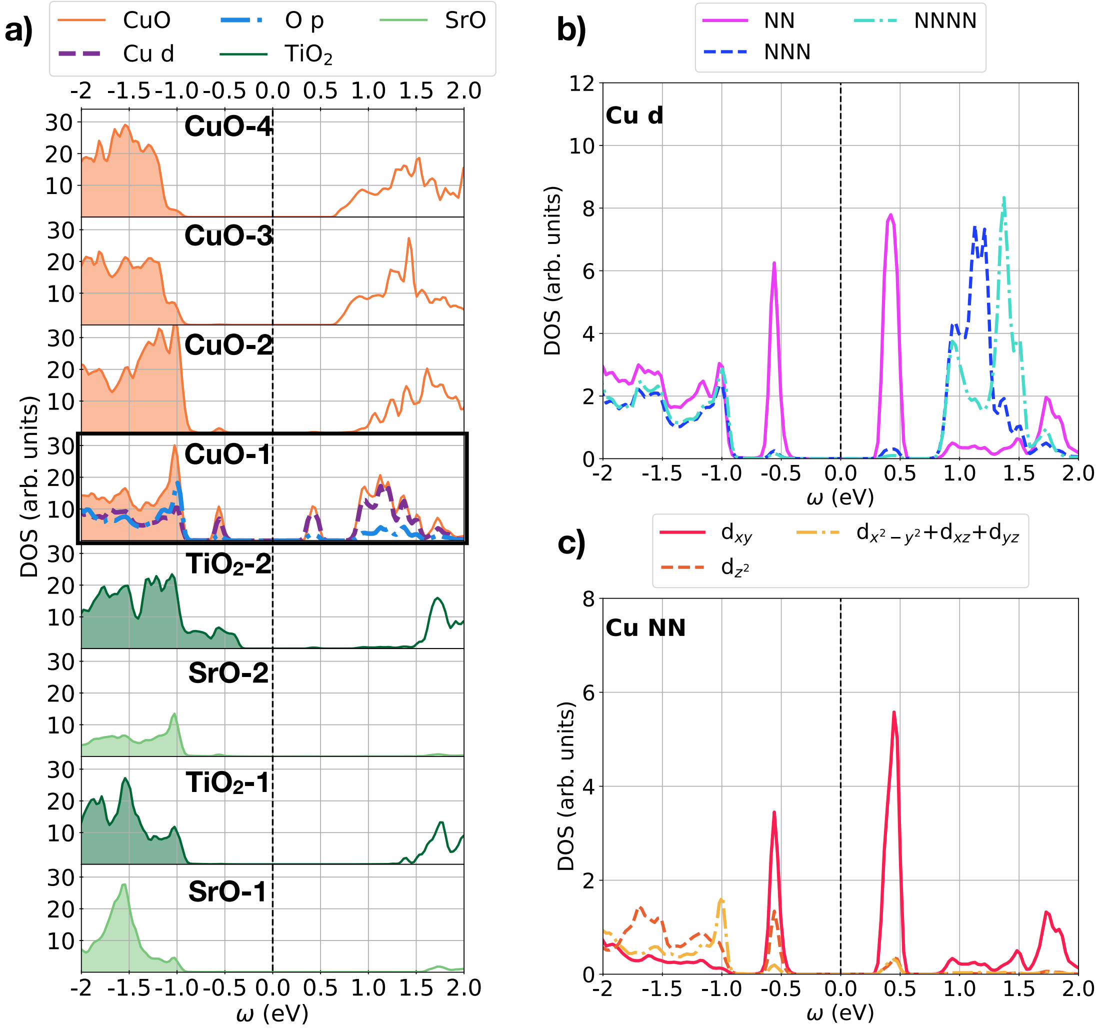

Figure 5.7: (a) Layer-resolved DOS calculated for the case of an O vacancy in the CuO-1 layer above a Ti site. (b)-(c) Site and orbital projected DOS for the Cu atoms at the CuO-1 interface layer corresponding to the framed panel in (a).

these two configurations is the breaking of the *global* C_4 symmetry to allow the emergence of a non-zero in-plane pinned orbital moment in the unit cell.

5.5 VACANCY IN THE TiO_2 INTERFACE LAYER

The physics is different if the O vacancy is created in the TiO_2-2 layer instead (Fig. 5.4(b)). The layer- and spin-resolved DOS are presented in Fig. 5.8(a): the CuO layer at the interface is metallic and spin polarized. Despite the global shift of the chemical potential, the system is only metallic at the interface since sizable DOS at the Fermi level only appears there. Similarly to the previous cases, those states are mostly of Cu *d* orbital character with almost no contribution from the O *p* orbitals. A striking result is that the DOS of the interface TiO_2-2 layer, where the O vacancy is located, is not affected by the defect: the valence of the Ti atoms is unchanged and they remain non-magnetic. This is an important result, since it shows that it is possible to generate a polarized 2DEG at the interface CuO-1 layer which is invisible at the Ti $L_{2,3}$ edge, since their *d* orbitals remain empty and non polarized. Moreover, note that the O vacancy does not intrinsically favor

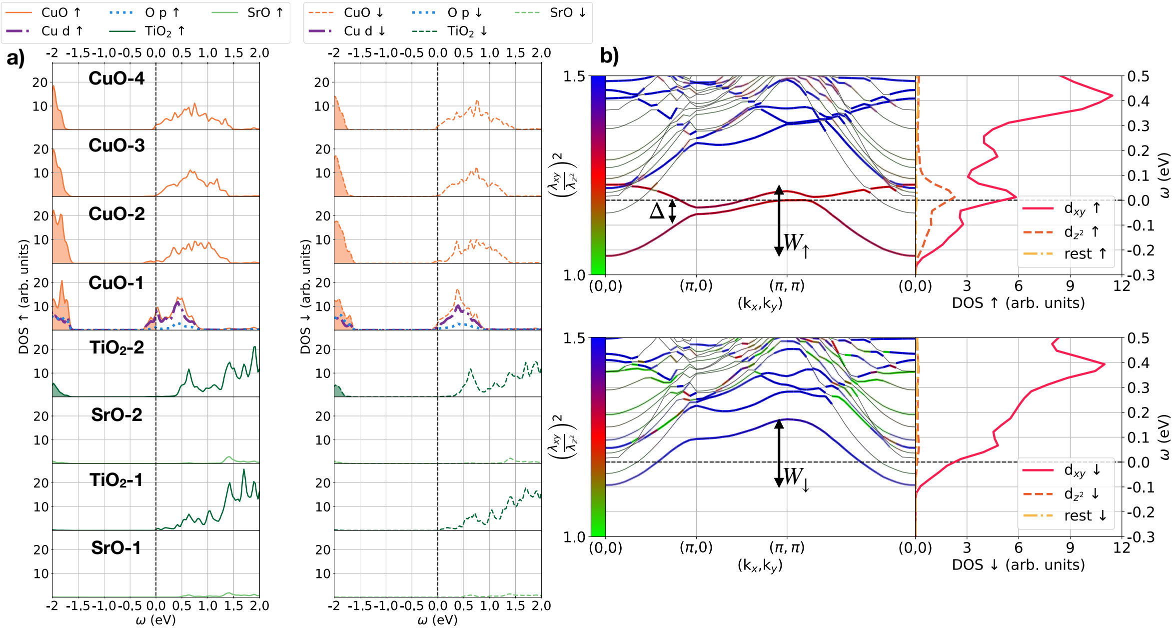

Figure 5.8: (a) Layer-resolved DOS for up (*left*) and down (*right*) spins in the case of a vacancy in the TiO_2-2 layer. (b) Projected band structure and DOS on the Cu d_{xy} and d_{z^2} orbitals of the interface CuO-1 layer. The band color depicts the ratio between the contributions from d_{xy} and d_{z^2}, while the opacity indicates their overall contribution to the bands. The black arrows indicate the bandwidth $W_{\uparrow/\downarrow}$.

positive spin moments. The sign of the resulting moment depends on the defect and the stripes position so that if we shift the vacancy, or if we swap the up and down spin stripes we obtain a down-spin polarized electron gas as shown in Fig. 5.9, obtained by keeping the same structure but inverting up and down spins. Therefore, on average in the real system without external magnetic field the 2DEG should not be polarized, as expected for paramagnetic spin moments. These considerations contradict the claim in Ref. 136 that a 2DEG at the interface should be seen in the XMCD spectrum at the Ti $L_{2,3}$-edge, and restore it as a plausible explanation for the puzzling paramagnetic moments observed at the Cu $L_{2,3}$-edge. For the sake of clarity we will only discuss the configuration of Fig. 5.8 in the remainder of this section, keeping in mind that spins are exchangeable.

In Fig. 5.8(b) we show the spin and orbital projected band structure. There is a striking difference between the two spin flavors: we find a single down spin d_{xy} band crossing the Fermi level, whereas we observe for the up spin two split bands of a mixed Cu d_{xy}/d_{z^2} character. The orbital mixing and the bands shape are analogous to the SOC-and-distortion-induced splitting of the Ir *d* bands in Sr_2IrO_4 [285], although it is remarkable that in our case only the up spin electrons are concerned. If the splitting of the up spin band is due to the structural distortions similarly to Sr_2IrO_4, the band mixing however is due to the C_4 symmetry breaking, not SOC. We note that the bands at the Fermi energy have a small bandwidth $W_{\uparrow/\downarrow} \simeq 300$meV, hence being sign of a low-mobility 2DEG.

In order to better understand the spin up/down difference, we show in Fig. 5.10 the spin-density at the interface CuO-1 layer around its initial Z_0 position. We observe a large distortion: the spin

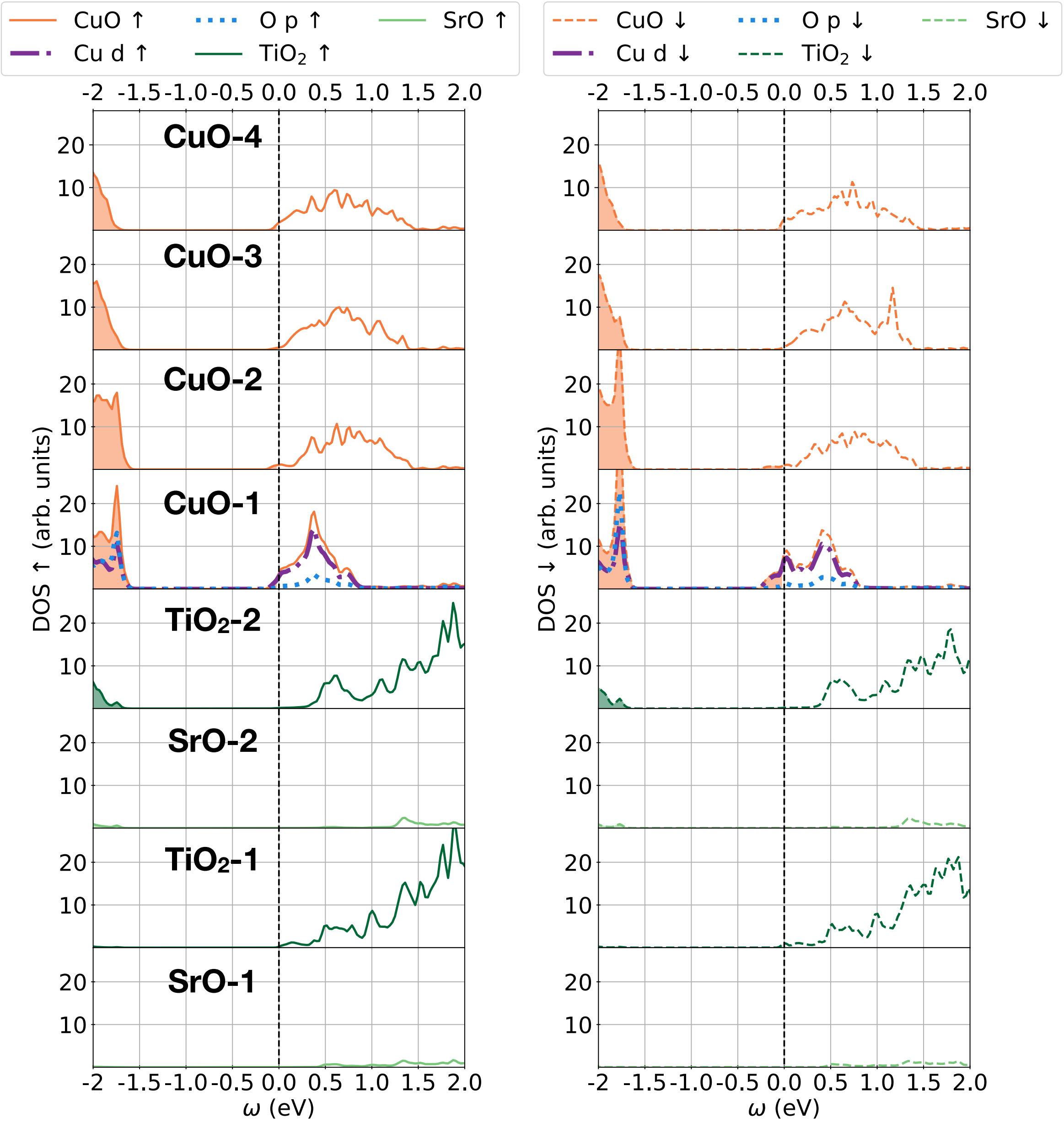

Figure 5.9: Layer-resolved DOS for up (*left*) and down (*right*) spins in the case of a vacancy in the TiO_2-2 layer. We used the same structure as in Fig. 5.8(a) but up and down spin stripes have been swapped.

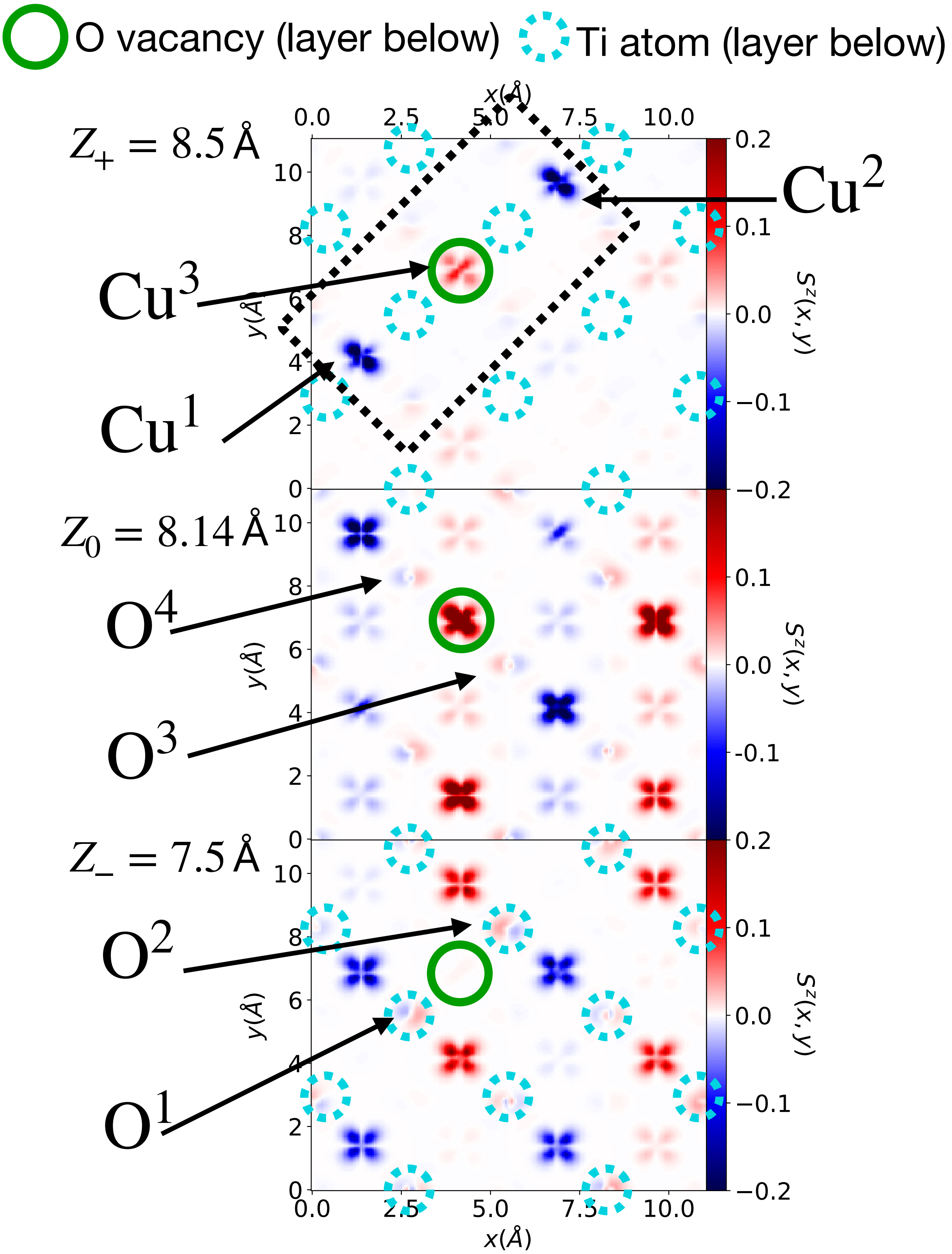

Figure 5.10: Spin density map of the interface CuO-1 layer above (*top*), at (*center*), and below (*bottom*) the initial position Z_0. As a guide to the eyes, the position of the O vacancy and the Ti atoms in the TiO$_2$-2 layer below is shown. The black frame highlight the three Cu atom on which is focused Fig. 5.11(b).

density for the same layer is non zero over more than 1Å along the c axis. Two $\mathrm{Cu}^{1,2}$ atoms belonging to the down spin stripe, see the *top* panel, show a breaking of the local C_4 symmetry due to the extra electrons coming from the TiO_2-2 layer below, similarly to the four NN Cu sites in the previous section. Interestingly, these charges are not located on the Cu^3 site just above the vacancy, but rather on the $\mathrm{Cu}^{1,2}$ sites. This is caused by the large buckling induced by the introduction of the vacancy, as can be seen in Fig. 5.11(a). The average displacement along the c axis per layer is evaluated as follow:

$$d_{layer} = \frac{1}{N_{layer}} \sum_{i \in layer} |d_i| = \frac{1}{N_{layer}} \sum_{i \in layer} |z_i - z_{avg}| \tag{5.1}$$

where N_{layer} is the number of atom per layer, z_i the z position of the atom, and z_{avg} the average z position of the layer. It is larger at the CuO-1 interface layer, and is of the order of 0.5Å. It is interesting to note that the distortions are larger than for the bare interface and the case of a vacancy in the CuO-1 layer, although here the defect is located in the TiO_2-2 layer below. Moreover, the overall distortion follows the sublattice decoupling observed experimentally [126, 134, 135], that we have explained in the previous chapter by means of CDMFT [267]. Note that the upturn in the atomic displacement in STO as going towards the first layer is due to the vacuum below the unit cell since the whole cell is optimized. It remains significantly smaller than the buckling in the CuO-1 layer. Such displacement induces large changes in the Cu-O bonds, especially around the Cu^3 located above the vacancy, see Fig. 5.11(b). Since the latter has no O neighbor below and its in-plane Cu-O distances are smaller than for the two surrounding $\mathrm{Cu}^{1,2}$ atoms, the splitting between the d_{xy} and d_{z^2} orbitals is expected to be enhanced. The d_{xy} energy in the two neighboring $\mathrm{Cu}^{1,2}$ sites is lower because their Cu-O distance is larger, i.e. the in-plane crystal field acting on d_{xy} is reduced, while the d_{z^2} is higher in energy because of the O below. Therefore, the extra charges from the TiO_2-2 layer will occupy the $\mathrm{Cu}^{1,2}$ sites belonging to the down-spin stripe since they are more favorable in energy. Note that the $\mathrm{Cu}^{1,2}$ atoms are two of the four NNN of Cu^3, and it is not trivial why those two sites would prevail the two other NNN and even the four NN Cu sites. The reason is that for all these sites, their Cu-O bonds are shorter than the ones of $\mathrm{Cu}^{1,2}$ because they remain closer to their O neighbors, as can be seen in the *middle* and *bottom* panels of Fig. 5.10, i.e. the same argument applies.

Since all the d orbitals but d_{xy} are filled, and the d_{xy} is already occupied with a down spin electron, the extra electrons have an up spin such that the electron gas is polarized. The breaking of the local C_4 symmetry induces the mixing of the d_{xy} and d_{z^2} orbitals, which are furthermore closer in energy on the $\mathrm{Cu}^{1,2}$ sites. Finally, the splitting Δ of the bands in the up spin DOS is due to a dimerization: the neighboring $\mathrm{Cu}^{1,2}$ sites couple and contribute equally to the band above and below the Fermi energy, resulting in the doubling of the unit cell for the up spin electrons, in contrast to the Cu^3 site above the vacancy which solely contributes to the single down spin band crossing the Fermi energy. Δ is however significantly smaller (Fig. 5.8(b)) that in the previous case (Fig. 5.5(e)): a Wannierization of the up spin bands using only the two neighboring sites gives an intra-unit-cell hopping $t_{in} \simeq 0.035$eV, and a inter-unit-cell hopping of the same order of magnitude $t_{out} \simeq t_{in}$.

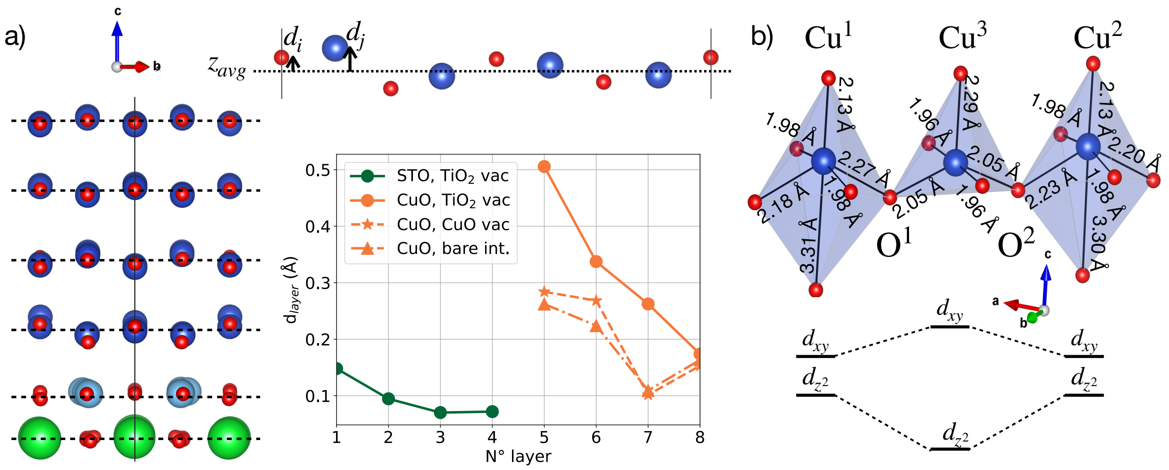

Figure 5.11: (a) Buckling on a portion of the crystal structure (*left*), illustration of how are evaluated the displacement d_i (*top right*) and evaluation of the average buckling for each layer for the three first scenarios (*bottom right*) following Eq. 5.1. (b) View of the three $Cu^{1,2,3}$ atoms highlighted in Fig. 5.10 with a schematic representation of the crystal field splitting of the d_{xy} and d_{z^2} orbitals.

An important difference with the case of a vacancy in the CuO-1 layer is that in the latter case the C_4 symmetry around the vacancy is conserved (although locally it is broken on the NN Cu site). Here, however, the global C_4 symmetry is broken as can be seen in the *bottom* panel of Fig. 5.10: among the four $O^{1,2,3,4}$ atoms located in the CuO-1 layer around the vacancy position, only two of them ($O^{1,2}$) are located above Ti sites. Those two atoms are pulled down during the relaxation process, weakening the Cu-O-Cu bond between the three $Cu^{1,2,3}$ sites highlighted by the dotted frame in Fig. 5.10. Hence, in contrast with the previous case, the four NNN Cu sites around the vacancy position are not equivalent, and the extra electrons are hosted by only two of them ($Cu^{1,2}$), leading to a breaking of the global unit cell C_4 symmetry.

If the magnetization points out-of-plane, so is the orbital moment and it is *blind* to the in-plane symmetry breaking, such that the system is equivalent to the case where a vacancy is inserted in the CuO-1 layer. Indeed, the orbital moment remains proportional and collinear to the spin one, and is therefore reduced on the two $Cu^{1,2}$ sites: on most of the Cu sites $m_{spin} \simeq \pm 0.70\mu_B$ and $m_{orb} \simeq \pm 0.14\mu_B$, while on the two NNN ones $m_{spin} \simeq -0.36\mu_B$ and $m_{orb} \simeq -0.08\mu_B$. This leads to a non-zero out-of plane orbital moment in the unit-cell, as illustrated in Fig. 5.12 where are also plotted the Wannier orbitals obtained by fitting the two split bands in the up spin band structure as well as the lonely band crossing the Fermi energy in the down spin sector. Hence, in the real material where we would have a random superposition of vacancies giving rise to up and down spin polarized 2DEG, the out-of-plane component of the orbital moment should also average to zero.

If the magnetization is in-plane instead, we observe again a pinning of the in-plane orbital moment component on the three aforementioned sites, as shown in Fig. 5.12. In our configuration, the two $Cu^{1,2}$ sites are aligned along (1,1,0), such that the magnetization axis along (1,1,0) and (1,-

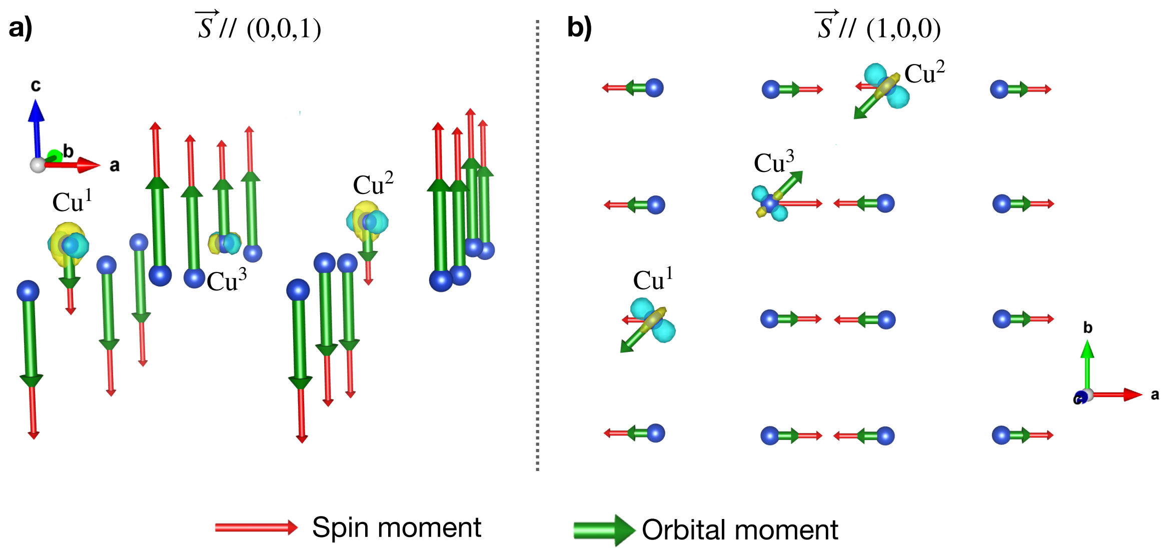

Figure 5.12: Schematic representation of the orbital momentum orientation for two different magnetization axis: (a) (0,0,1), (b) (1,0,0). The length of the vectors illustrates the variation of the absolute value of the moments. For the sake of clarity the isovalue of the Wannier orbitals was set to relatively high value (0.43), preventing from the appearance of surfaces elsewhere in the unit cell.

1,0) are no longer equivalent (contrary to the case of a vacancy in the CuO layer, see Fig. 5.6). We observe that, if we choose the magnetization axis along (1,1,0), the orbital moment is increased in absolute value on these two Cu^{1,2} sites ($m_{orb} \simeq -0.09\mu_B$ instead of $m_{orb} \simeq \pm0.05\mu_B$ on the other sites) although they have a reduced spin-moment with respect to the other sites ($m_{spin} \simeq -0.36\mu_B$ instead of $m_{spin} \simeq \pm0.70\mu_B$). Again, if the magnetization axis is along (1,0,0) or (0,1,0), the in-plane orbital moment on all the Cu atoms is collinear with the spin moment, unless for the two Cu^{1,2} atoms for which it is pinned along (-1,-1,0), as well as the Cu^3 site above the vacancy for which it is pinned along (1,1,0). The sum of the three pinned in-plane components is non-zero and positive in this configuration.

Therefore, we have shown that a 2DEG appears in the CuO-1 interface layer when creating a vacancy in the TiO$_2$-2 layer, which is invisible to XMCD at the Ti $L_{2,3}$ edge. Around the vacancy, the orbital moment is locally pinned along (1,1,0) direction and can be non-collinear with the spin moments, with an overall non-zero value. If we swap the stripes, we obtain a non-zero orbital moment of opposite sign, i.e. a random superposition should average to zero if the magnetization axis is the same. Also, the same effect could be seen in a (1,-1,0) configuration, in which case the orbital moment would be pinned along (1,-1,0) direction. If we consider a random distribution of these four configurations ((1,1,0) or (1,-1,0) and up and down spin polarized), and also consider that they all share the same magnetization axis, then the global orbital momentum should average to zero.

However, if the magnetization axis is different at the different vacancy sites, then it is possible to obtain a non-zero orbital moment because the of pinning, while the average spin moment remains zero. The striking difference here is that one vacancy gives rise to a non-zero pinned orbital momentum, and it is possible to consider a distribution of vacancies resulting in an average zero magnetization but non-zero orbital moment, whereas in the previous section it is impossible since the orbital momentum is locally averaged to zero because of the global C_4 symmetry conservation around the vacancy site. This is a key feature of this scenario that should apply on similar types of monoxide/dioxide junctions: inserting a vacancy in the dioxide interface layer induces a C_4 symmetry breaking in the monoxide layer above which could be at the origin of a non-zero pinned orbital moment. Most importantly, only the in-plane component of the orbital moment is pinned, whereas the out-of-plane part is collinear and proportional to the spin, in excellent agreement with the XMCD measurements finding no out-of-plane pinning [136].

Finally, one may have noticed that with our choice of on-site interaction $U = 6$eV, and in the absence of vacancies, we obtain a gap for t-CuO of roughly 1.5eV, much weaker than the ARPES lower bound $\Delta > 2.35$eV [134] and the STM upper bound $\Delta < 3.68$eV [126]. Since we get a gap of about 2eV for STO, then with our choice of U value the first empty states available are in the t-CuO interface layer and we obtain the physics we have described above. By choosing a higher U value, say to better reproduce the experiments, the t-CuO first available states would be pushed to higher energies, such that they could be replaced by the STO states at some critical value of the on-site interaction. In such a case, upon the formation of vacancies we could expect that the extra charges would remain in the TiO_2-2 interface layer, in contradiction with the results we have drawn in this chapter. However, PBE also underestimates the gap of STO, which is found experimentally to be $\Delta_{STO} \simeq 3.3$ [315], i.e. larger than the ARPES lower bound and of the same order than the STM upper bound for t-CuO. Given that STM overestimates the gap values due to the band bending phenomenon [316], especially in the case of insulators with a large gap, it is reasonable to consider that the gap configuration we obtain in our calculations is similar to that of the real system, albeit an overall underestimation of both gap values. In other words, at the interface, the first available states to be filled upon inserting vacancies in the TiO_2-2 interface layer should be located in the CuO-1 layer, and our observations apply.

5.6 TWO VACANCIES IN THE TiO_2 INTERFACE LAYER

An important question is whether this scenario still holds at a higher concentration of vacancies in the TiO_2-2 layer. For instance in $SrVO_3$ two neighboring oxygen vacancies, instead of a single one, are needed to reproduce the additional spectral weight seen in photoemission [317]. Fig. 5.13 shows the layer- and spin-resolved DOS obtained for a larger concentration of oxygen vacancies with two different configurations (see Fig. 5.4(c)): either two vacancies still far from each other, or forming a pair around a single Ti atom. Both configurations induce an electron gas in the interface CuO-1 layer while the TiO_2-2 layer is still insulating. Since we doubled the number of vacancies, there is an additional charge transfer to the interface CuO-1 layer which translates into a larger DOS below the Fermi level. Similarly to the previous section, the additional states at the Fermi level are almost purely of Cu *d* character.

When the vacancies form a pair around the same Ti atom, the latter is not able to totally transfer

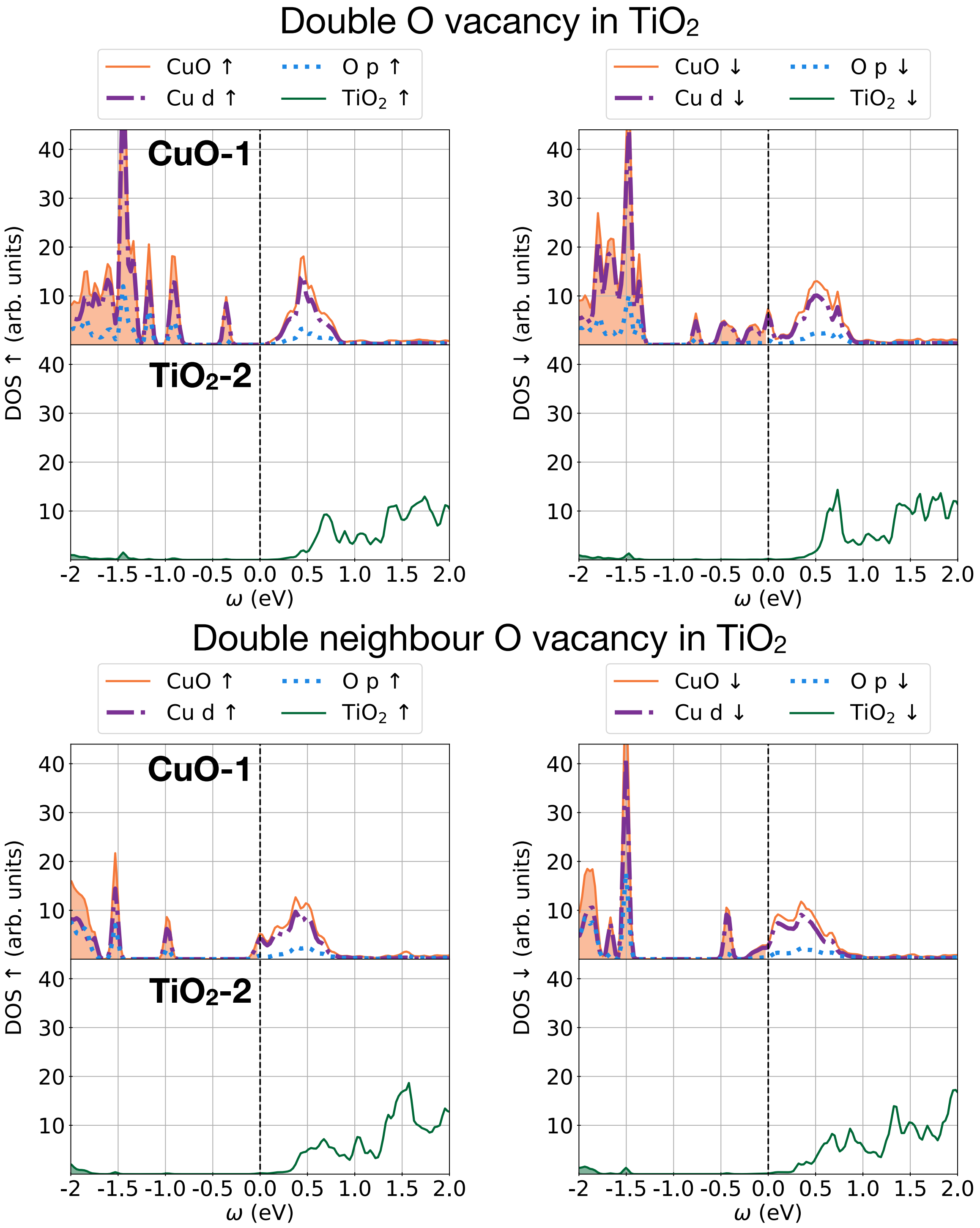

Figure 5.13: Layer-resolved DOS for the two interface layers in case of higher concentration of vacancies.

the excess charges and becomes slightly spin-polarized ($m_{spin} \simeq -0.42\mu_B$), contrary to the case in which the vacancies are still apart from each other for which no spin moment is observed on the Ti atom. Such a spin moment on the Ti atoms is not consistent with the XMCD measurements since it would be detected at the Ti $L_{2,3}$ edge, and allows us to discard the scenario of oxygen vacancies pairing around the same Ti atom. In contrast, when the two vacancies do not combine around the same Ti atom, the 2DEG remains invisible at the Ti $L_{2,3}$ edge, and we observe an in-plane pinning of the orbital moment in the CuO-1 layer.

5.7 CONCLUSION

To summarize, performing DFT+U calculations on large supercells including oxygen vacancies at the t-CuO/STO interface, we are able to identify a scenario compatible with the puzzling XMCD measurements of Ref. 136. Namely, we show that oxygen vacancies in the TiO_2-2 layer induce a 2DEG confined in the CuO-1 layer at the interface, which would explain the experimental findings: we observe no valence change nor non-zero magnetic moment at the interface Ti sites, i.e. the 2DEG is invisible at the Ti $L_{2,3}$ edge, and show that a vacancy induces the appearance of paramagnetic metallic states with a mixed d_{xy}/d_{z^2} character. We identify the breaking of both the *local* and *global* C_4 symmetries in the CuO-1 layer above the vacancy as being a mechanism for the emergence of an in-plane pinned orbital moment, in excellent agreement with the nature of the pinned moment observed in XMCD [136]. Such phenomenon is not restricted to the case of t-CuO/STO junctions since it simply stems from the stacking of a monoxide layer above a dioxide and should then generalize to other heterostructures. We moreover show that if the oxygen vacancies form pairs around a single Ti atom, the latter becomes spin polarized and is therefore not invisible anymore in XMCD.

This scenario also provides an understanding of the apparent inconsistency between the previous experimental observations and the XMCD measurements. Indeed, if the moments and the 2DEG live at the interface, as we argue in this chapter, then ARPES would not be able to resolve them since the probing depth is of the order of 2nm at the photon energy used in Ref. 134 and the t-CuO films were ~ 3.6nm-thick. In contrast, XMCD in total electron yield mode has a probing depth of $5-10$nm [318] and would therefore be sensitive to the interface. The RIXS measurements were performed on t-CuO samples synthesized on Nb-doped STO substrates [135]. Such Nb-doped substrates are metallic and would most probably change drastically the interface properties as compared to the t-CuO/STO junctions measured in XMCD. Moreover, even in the case of an undoped STO substrate, RIXS is not suited for observing paramagnetic spin moments, neither pinned orbital moments, especially when the measurements are performed without external magnetic field.

It would therefore be crucial to further investigate the interface properties of t-CuO/STO both experimentally and theoretically. Local probes like STM would be good candidates in order to study specifically the interface layers. Another possibility would be to generate vacancies with irradiation, as was done for $SrVO_3$ [317], although one would need to create them specifically at the t-CuO/STO interface. Since t-CuO was successfully synthesized up to 10 unit cells [126], it might be possible to use the small probing depth of XMCD in total electron yield to suppress, or enhance, the interface contribution to the spectrum, as was done in Ref. 149 for $LaAlO_3$/STO. Changing the termination of the STO substrate could also be a way to suppress the 2DEG, so the paramagnetic spin moment, as it was shown for instance that the AlO_2/STO interface becomes insulating when STO is SrO-terminated [306]. Finally, we show that the orientation of the magnetization axis should play an important role in the emergence of the pinned orbital moment so that its experimental determination is an important step in the understanding of the observed magnetic moments.

PART V

CONCLUSION

Throughout this thesis, we studied the rich and complex physics of strongly correlated copper oxide systems by focusing on two different compounds: $Ca_{2-x}Na_xCuO_2Cl_2$ (NaCCOC) and tetragonal CuO (t-CuO). These two materials are particularly interesting since they have a simple crystal structure, even without charge reservoir layers for t-CuO, which makes the comparison between the cuprates' low-energy effective models [30–33, 38, 263] and experiments easier. We explored their spectral and magnetic properties by means of state-of-the art numerical techniques, density function theory (DFT)(+U) [158, 159] and cluster dynamical mean-field theory (CDMFT) [42, 43, 49–51] with 2×2 and 8–site clusters, that were systematically compared to experimental results from the literature and from our two angle-resolved photoemission spectroscopy (ARPES) measurement campaigns, the first performed at the Photon Factory (Tsukuba, Japan), and the second one at SOLEIL (Saint-Aubin, France).

For the low energy properties of both NaCCOC and t-CuO, we used a single-band Hubbard model [35–37] based on the Zhang-Rice singlets (ZRS) picture [38]. The framework of CDMFT naturally gives access to the spectral function which can be directly compared to the ARPES measurements. We found an excellent agreement for NaCCOC at $x = 0$, $x = 0.05$ and $x = 0.1$, despite a missing quasiparticle peak at the nodal point [92] in the ARPES measurements at $x = 0.05$ and $x = 0.1$. The theoretical spectrum captures the waterfall feature [24, 86] at the nodal point $(\pi/2, \pi/2)$ with both cluster sizes, with the kink at the right position in momentum and energy, both for the undoped and doped systems. We interpreted this spectral feature as a cross-over between a high-energy part where the correlations are purely local and which is well described by the Hubbard-I approximation [35], and a low-energy part where electrons are dressed by the antiferromagnetic spin correlations and form spin polarons [95–98]. This result already underlines the uttermost necessity of including non-local correlations when treating the cuprates' low energy models, since the purely local Hubbard-I picture fails to describe the physics close to the Fermi level. Moreover, especially with the 8–site cluster we were able to reproduce the two-peak structure observed at the nodal point [91, 92], which consists of a sharp nodal quasiparticle peak at the Fermi level emerging from a less coherent dispersive feature at around -0.2eV.

In the spectral function of NaCCOC, we observed the opening of a pseudogap (PG) upon hole doping, both in our calculations and ARPES measurements, in agreement with previous experimental [12, 14, 24, 26, 90–94] and theoretical works [104, 107, 111–114, 246]. In the latter, the PG was traced back to short-range spin fluctuations. Our analysis of the simple 2×2 cluster results is in line with this interpretation: the state histogram obtained from the impurity solver revealed that it is dominated by only three groups of states. The leading contribution is the singlet state $|N = 4, S = 0\rangle$, which is the most probable state from $x = 0$ until $x \sim 0.12$. Within our new choice of basis, this state involves a spin singlet between the $D13$, $D42$ orbitals of the plaquette cluster (as defined in Sec. 3.4), which induces the suppression of the zero-energy excitations when the system is connected to a bath of non-interacting electrons [121]. The flat dispersion, i.e. the van Hove singularity, at the nodal point, which would jump at the Fermi level upon hole-doping, is therefore split into two subbands below and above the Fermi level since the first remaining photoemission channel is a transition from the singlet state $|N = 4, S = 0\rangle$ to the triplet $|N = 4, S = 1\rangle$.

Interestingly, in the state $|N = 4, S = 1\rangle$ the $D13, D42$ orbitals are in a spin triplet state: we therefore interpreted the formation of the PG in the spectral function as stemming from the breaking of the singlets into triplets due to the cancelling of the zero-energy photoemission channel [121]. This is intimately related to the short-range spin fluctuations, which provides the non-degenerate singlet nature of $|N = 4, S = 0\rangle$. Furthermore, we showed that this is not a special feature of the 2×2 plaquette cluster since the 8−site cluster also opens a PG. While the $(\pm\pi/2, \pm\pi/2)$ orbitals included in this cluster could be expected to behave similarly to the $D13, D42$ orbitals, we argued that their hybridization to the bath is larger both at the non-interacting and interacting level. An isolated ground state on the cluster is no longer a good approximation for the $(\pm\pi/2, \pm\pi/2)$ orbitals, such that there is no suppression of the quasi-particle peak at the nodal point.

We therefore showed that the waterfall feature and the opening of the PG in NaCCOC, and cuprates in general, can be understood under the same framework of short-range spin fluctuations. Short-range correlations are also essential to find the origin of the sublattice decoupling in t-CuO, which can not be captured with purely local fluctuations. Indeed, we demonstrated with two different impurity solvers that it is induced by the suppression of the inter-sublattice self-energy component, which leaves the hopping t_d bare while the NNN hopping term t is renormalized by a factor ~ 2 by the correlations. Because it is energetically favorable to form bonds between sites linked with the leading order hopping term, and that all hopping processes involving t only connect sites from the same sublattice, the CuO planes can be thought of as two weakly coupled CuO_2 sublattices in agreement with the experimental observations [134, 135]. We made use of this finding to motivate the construction of a super-cluster, allowing to improve the momentum resolution of our calculations. We obtained a spectral function reproducing astonishingly well the ARPES measurements [134], both using the continuous-time quantum Monte Carlo (CTQMC) [60, 62, 116] solver working at finite temperature used by the author, and the matrix-product state (MPS)-based [56–58, 141–144] solver working directly on the real frequency and at zero temperature used by M. Bramberger and M. Grundner. Combining these different solvers is extremely useful for it allows to connect and compare the finite to zero temperature results and properties.

From calculations at finite temperature, we showed that there exist two different insulating regimes in t-CuO: a paramagnetic regime at high temperature in which the self-energy shows a momentum dependent divergence at $\omega_n \rightarrow 0$, and a magnetically ordered regime at low temperature characterized by a static spin dependent shift in the self-energy. The transition between these different phases yields drastic transformations of the spectral functions: when decreasing the temperature, the lower Hubbard band (LHB) originally composed of a single broad dispersive feature turns into two split sub-bands. Only the spectral function calculated at low-temperature with the CTQMC solver corresponds to the one computed with the MPS-based solver at effectively zero temperature, and so to the ARPES measurements [134]. This underlines the effects of the spin fluctuations on the spectral properties of cuprates, which are further confirmed by the fact that the low-energy subband at low temperature is well accounted for by a self-consistent Born approximation (SCBA) calculation, similarly to NaCCOC. We moreover identified an intriguing enhancement of the spin dependent shift in the real part of the self-energy at the transition temperature, that can be explained at the local mean-field level as a combination of spin and thermal fluctuations at the transition, based on a simple effective model derived by the author .

To further understand the behavior of one-particle quantities like the spectral function, it is useful to study the two-particle observables. From the analysis of the dynamical spin structure factor (DSSF) in NaCCOC, we confirmed the predominance of the spin-fluctuations at $\mathbf{Q} = (\pi, \pi)$ at all dopings, in agreement with early quantum Monte Carlo (QMC) calculations [111], with the fluctuation diagnostic method applied to dynamical cluster approximation (DCA) [112] and diagrammatic Monte Carlo [113, 114] calculations, as well as the dual boson expansion around the DMFT solution [75]. Most interestingly, we identified a freezing of the spin-spin correlation function upon hole doping at long times $\tau = \beta/2$ and low temperatures $\beta \geq 40$, in line with recent findings [122, 123]. It can be explained by relating $\mathcal{S}(\tau)$ to its real frequency counterpart, which directly shows that the finite value at $\tau = \beta/2$ is related to the presence of low-energy spin excitations. At $x \neq 0$, the DSSF's gap closes: a low-energy and almost doping independent spectral weight appears, leading to a doping independent increase of $\mathcal{S}(\tau = \beta/2)$ with respect to the undoped system. At too large doping, however, the freezing disappears due to the weakening of the spin fluctuations [123]. Moreover, we showed that the value of the correlation function at $\tau = \beta/2$ does not depend on the inter-site distance. While this was observed with the small plaquette cluster, we argued that it should hold for larger systems given that the DSSF peak at (π, π) is broad in momentum and finite at low-frequency. This is an intriguing result that motivates for further investigations with larger system sizes.

Although most of the results in this thesis could not be obtained with DFT, it remains a necessary technique to be kept in the theoreticians' toolkit for the study of strongly correlated systems' ground state properties. The t-CuO/STO interface is a good example, since DFT+U is the only possible framework to investigate the emergence of paramagnetic spin and pinned orbital moments observed with x-ray magnetic circular dichroïsm (XMCD) at the Cu $L_{2,3}$ edge [136]. Using PBE+U [151–153], we showed that the formation of O vacancies in the TiO_2 interface layer can induce the formation of a 2D electron gas (2DEG), which can explain the measurement of a paramagnetic spin moment. Above all, this 2DEG would be invisible at the Ti $L_{2,3}$ edge since the valence of the Ti atoms in the TiO_2 interface layer remains unchanged, which is consistent with the experimental observations [136]. The large structural distortions, as well as the mismatch of the monoxide CuO and the dioxide TiO_2 layer induce the breaking of *both* local and global C_4 symmetries at the interface, which in turn leads to the in-plane pinning of the orbital moment. We emphasized that only the out-of-plane component is not pinned, in agreement with the XMCD measurements [136]. Therefore, using PBE+U we were able to construct a scenario that reconciles the XMCD observations with the physics of t-CuO/STO.

These findings remain to be confirmed experimentally, and would probably require the use of experimental techniques that can include or exclude at will the influence of the interface. Since XMCD is always performed in total electron yield for these kind of systems, a surface dependent mode, one could grow thin films of t-CuO of varying thickness and study the dependence of the magnetic moments, similarly to Ref. 149. If the sample is thick enough, the XMCD becomes insensitive to the interface, and, according to our model, the spin and orbital moments should disappear. Another way would be to change the TiO_2 termination of STO to SrO, which could for instance prevent the formation of a 2DEG at the interface as is observed at the AlO_2/STO interface [306, 319].

Further works are to be carried out on the doped phase of t-CuO, which has not yet been realized experimentally, and has not yet been investigated theoretically apart from the variational cluster approximation (VCA) calculations presented in this thesis [267]. It would be interesting to further study the possible consequences of the sublattice decoupling, other than the unusual d_{xy} superconducting order parameter, on the expected phases of cuprates like the PG, or charge density wave (CDW).

For the PG phase, based on the conclusions we drew from the study of NaCCOC, questions arise about the behavior of the spin-freezing phenomenon: how does it evolve as a function of the cluster size, how does it behave at the transition with superconductivity ? For the effect of cluster size, it would be extremely interesting to confirm the observation of the spin-freezing in a 8−site DCA cluster [123] with CDMFT, especially since we would directly have access to the inter-site correlation functions. This question opens a more general perspective on other techniques than quantum cluster methods [52], such as diagrammatic expansions around the DMFT solution [71–76]. A great advantage of these techniques is that they include long-range correlations, and allow to obtain a much better momentum resolution for the one- and two-particle quantities. On different grounds, computationally cheaper techniques like the two-particle self-consistent method [320, 321], or the fluctuating local field [322, 323], would be useful tools to study large systems while still including collective effects non-perturbatively.

In this thesis, we confronted the rich and non-trivial parent cuprate compound as well as the PG phase. This is only a limited part of the zoo of phenomena observed in this class of materials [14, 24]. While we have shown the importance of spin fluctuations, one should not forget that they live and interact with other types of fluctuations, as the charge channel which is for instance highlighted by the observation of CDW [25–29]. This complicates even more the understanding of copper oxides, and most notably the origin of superconductivity which remains elusive. For all these reasons, copper oxide systems are among the most interesting materials under study nowadays. One should therefore think twice before throwing an old oxidized saucepan to the trash, for it might yield an unexpected behavior.

PART VI

APPENDIX

A

PROBING THE ELECTRONIC STRUCTURE: ANGLE-RESOLVED PHOTOEMISSION SPECTROSCOPY

Angle-resolved photoemission spectroscopy (ARPES) is one of the most powerful experimental techniques to probe the momentum-resolved electronic structure of materials. It relies on the photoelectric effect, discovered by Hertz [324], Hallwachs [325] and Lenard [326], and explained by Einstein [327] in 1905, which was first used to experimentally measure atomic binding energies in 1957 by Siegbahn [328]. The principle is simple, and sketched in Fig. A.1: when a beam of light is shone on a sample, the electrons of the solid can be emitted into the vacuum by absorbing a photon. The measure of the emission angles (ϕ, θ) and the kinetic energy E_{kin} of the photoelectrons in the analyzer allows to reconstruct the momentum-resolved electronic structure. In this appendix, we briefly present the ARPES cross-section and how it is linked to the Green's function that we calculate using the many-body methods presented in Chap. 2. We also show how to transform the raw experimental data, which is obtained as a function of angles (ϕ, θ), back to the momentum space. We do not aim at going into the details of the technique, for which we refer the interested reader to the reviews of Damascelli [24] and Moser [258].

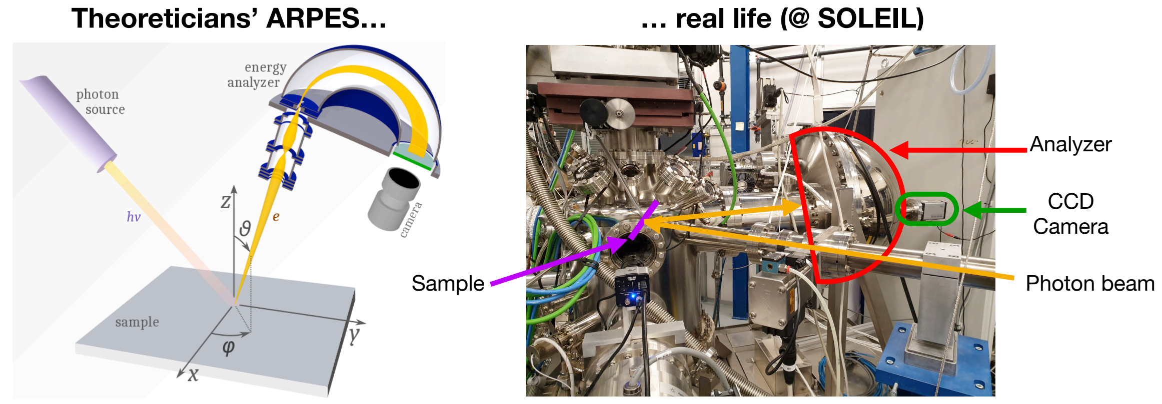

Figure A.1: Sketch (*left*) of the ARPES experimental setup, and photography of the setup at SOLEIL (Saint-Aubin, France) synchrotron (*right*).

A.1 THE PHOTOEMISSION CROSS-SECTION AND THE GREEN'S FUNCTION

In a simplified notation, we can write the Hamiltonian of the material as:

$$H = \frac{1}{2m_e}\hat{\mathbf{p}}^2 + \hat{V}, \tag{A.1}$$

where $\hat{\mathbf{p}}$ is the momentum operator, $\hat{V}$ the potential, we set $\hbar = 1$, and the bold characters denote the vector quantities. When light is shone on the sample, the momentum operator $\hat{\mathbf{p}}$ has to be replaced as follows:

$$\hat{\mathbf{p}} \to \hat{\mathbf{p}} - e\mathbf{A}, \tag{A.2}$$

where $\mathbf{A}$ is the vector potential. The Hamiltonian is therefore transformed:

$$\begin{aligned}\tilde{H} =& \frac{1}{2m_e}(\hat{\mathbf{p}} - e\mathbf{A})^2 + \hat{V} \\ =& \underbrace{\frac{1}{2m_e}\hat{\mathbf{p}}^2 + \hat{V}}_{H} - \underbrace{\frac{e}{m_e}\mathbf{A}\cdot\hat{\mathbf{p}}}_{H_{int}} - \frac{e}{2m_e}(-i\nabla\mathbf{A}) + \frac{e^2}{2m_e}\mathbf{A}^2.\end{aligned} \tag{A.3}$$

The third term is equal to zero except possibly at the surface, it is then neglected in the following. Similarly for the fourth term which describes two-photon processes, and can be ignored for the range of photon energies used in ARPES [24, 258]. We get to the approximate Hamiltonian

$$\tilde{H} \simeq H + H_{int}, \tag{A.4}$$

with H_{int} encoding the light-matter interaction. It induces optical excitations from a N-electron ground state $|\psi^N_{GS}\rangle$ to a final state $|\psi^N_f\rangle$ containing $N-1$ electrons and one photoelectron. H_{int} can be considered as a weak perturbation to H, such that Fermi's golden rule can be used to account for the transition probability:

$$w_f = 2\pi\left|\left\langle\psi^N_f\middle|H_{int}\middle|\psi^N_{GS}\right\rangle\right|^2 \delta\left(E^N_f - E^N_{GS} - \nu\right), \tag{A.5}$$

where E^N_f and E^N_{GS} are the final and ground state energies, and ν is the photon energy. We assume to be at zero-temperature, such that the initial many-body state is conveniently restricted to the ground state $|\psi^N_{GS}\rangle$.

At this stage, there are two possibilities to calculate the transition probability. The most rigorous one is the *one-step* model, in which the photon absorption, electron removal and detection are treated as a single coherent process [329]. This treatment is extremely complex, and out of the scope of this appendix. We rather consider the phenomenological *three-step* model, in which the photoemission is divided into three separated steps:

(i) Creation of a photoelectron in the solid by the absorption of a photon,
(ii) Travel to the surface,
(iii) Emission into vacuum.

The second step (*ii*) is described by an effective mean-free path proportional to the probability of the electron to reach the surface with no change in momentum and energy, i.e without scattering. Inelastic processes are also possible, and result as a broad background in the ARPES spectrum which we can ignore in this discussion. The third step (*iii*) is related to the transmission probability for an electron to escape from the solid into vacuum. Hence, it is mainly the first step (*i*) that leads to the features of interest in the photoemission intensity. This step is described by Eq. A.5: w_f measures the probability of the optical excitation of a bulk electron.

In order to connect the transition probability to the spectral function, and hence to the Green's function of the solid, H_{int} may be re-written within second quantization:

$$\begin{aligned} H_{int} &= \sum_{\substack{f=\{m_f,\mathbf{k}_f\}\\ i=\{m,\mathbf{k}\}}} \mathbf{M}_{fi} c_f^\dagger c_i \\ \mathbf{M}_{fi} &= -\frac{e}{m_e}\langle \phi_{m_f,\mathbf{k}_f}|\mathbf{A}\cdot\hat{\mathbf{p}}|\phi_{m,\mathbf{k}}\rangle, \end{aligned} \tag{A.6}$$

where $f = \{m_f, \mathbf{k}_f\}$ and $i = \{m, \mathbf{k}\}$ denote the orbital and momentum of the photoelectron $\left|\phi_{m_f,\mathbf{k}_f}\right\rangle$ and the initial electron $|\phi_{m,\mathbf{k}}\rangle$. Note that the $\{|\phi_{m,\mathbf{k}}\rangle\}$ are single-particle wavefunctions, and not many-body ones. Within the context of the effective Hubbard model that we use throughout this thesis, they can be thought of as the Fourier transformation of the localized Wannier orbitals [258] (i.e as Bloch bands):

$$|\phi_{m,\mathbf{k}}\rangle = \sum_{\mathbf{R}} \mathrm{e}^{i\mathbf{k}\mathbf{R}}|w_{m\mathbf{R}}\rangle. \tag{A.7}$$

This shows that the matrix elements $\mathbf{M}_{fi}$ are dependent on the symmetry of the material, and the orbital m of the electron that absorbed the incoming photon. It is moreover a function of the light polarization and the angles (θ, ϕ) due to the vector potential $\mathbf{A}$. Upon further transforming the transition probability, it will become clear that these matrix-elements lead to additional suppressions of the measured intensity not related to many-body effects [258].

Using the second quantized form of H_{int}, the transition probability now reads

$$w_f = 2\pi \sum_{\substack{f'=\{m'_f,\mathbf{k}'_f\}\\ i=\{m,\mathbf{k}\}}} |\mathbf{M}_{f'i}|^2 \left|\langle \psi_f^N | c_{f'}^\dagger c_i \, |\psi_{GS}^N\rangle\right|^2 \delta\big(E_f^N - E_{GS}^N - \nu\big). \tag{A.8}$$

The final state $\left|\psi_f^N\right\rangle$ is *a priori* difficult to describe since it accounts for a many-body system of $N-1$ electrons plus a photoexcited electron, which may interact with the hole created via the photon absorption, and with the rest of the $N-1$ electrons. However, at the photon energies available in synchrotron facilities, roughly about 20 – 200eV, we can assume the optical excitation to be fast, and the energy of the photoelectron well separated from that of the bulk electrons, such that the final state can be written as a product state

$$\left|\psi_f^N\right\rangle \simeq c_{m_f,\mathbf{k}_f}^\dagger \left|\psi_n^{N-1}\right\rangle \tag{A.9}$$

where $|\psi_n^{N-1}\rangle$ is a $N-1$ electron state, and $c^\dagger_{m_f,\mathbf{k}_f}$ is the creation operator of a photoelectron of orbital m_f and momentum $\mathbf{k}_f$. This is the so-called *sudden approximation* [24, 258]. For ARPES measurements using low-energy incident photons, like laser-ARPES, this assumption may break down. The energy of this product state can be conveniently written

$$E_f^N = E_{kin} + E_n^{N-1}, \tag{A.10}$$

where E_{kin} is the kinetic energy of the photoelectron and E_n^{N-1} the energy of the $N-1$ many-body state $|\psi_n^{N-1}\rangle$. This form of the final state can now be injected in Eq. A.8 by summing over all the possible $N-1$ final states $\{|\psi_n^{N-1}\rangle\}$ [258]:

$$\begin{aligned} w_f =& 2\pi \sum_{\substack{f'=\{m'_f,\mathbf{k}'_f\}\\ i=\{m,\mathbf{k}\}}} \sum_n \left|\mathbf{M}_{f'i}\right|^2 \left|\langle\psi_n^{N-1}|c_{m_f,\mathbf{k}_f} c^\dagger_{f'} c_i\,|\psi_{GS}^N\rangle\right|^2 \delta(E_n^{N-1} + E_{kin} - E_{GS}^N - \nu) \\ =& 2\pi \sum_{m,\mathbf{k}} \left|\mathbf{M}_{\substack{\{m_f,\mathbf{k_f}\}\\ \{m,\mathbf{k}\}}}\right|^2 \sum_n \left|\langle\psi_n^{N-1}|c_{m,\mathbf{k}}|\psi_{GS}^N\rangle\right|^2 \delta(E_n^{N-1} + E_{kin} - E_{GS}^N - \nu) \\ =& 2\pi \sum_{m,\mathbf{k}} \left|\mathbf{M}_{\substack{\{m_f,\mathbf{k_f}\}\\ \{m,\mathbf{k}\}}}\right|^2 A^-_{mm}(\mathbf{k},\omega), \end{aligned} \tag{A.11}$$

where the $\{A^-_{mm}(\mathbf{k},\omega)\}$ are the diagonal components of the one-electron removal spectral function corresponding to the orbital m and momentum $\mathbf{k}$, and $\mathbf{M}_{\substack{\{m_f,\mathbf{k_f}\}\\ \{m,\mathbf{k}\}}}$ are the matrix elements of the photoelectron of orbital m_f and momentum $\mathbf{k_f}$. As mentioned above, these matrix elements lead to additional suppressions not linked to the many-body effects encoded in the spectral function $A^-_{mm}(\mathbf{k},\omega)$. Although they could be naively viewed as a curse, the matrix elements can in fact be extremely useful to highlight some features in the spectrum [258], or for instance to determine the orbital character of certain unknown states [305]. For a more detailed discussion of matrix-elements effects, we refer the interested reader to the review of Moser [258].

So far, we have linked the transition probability, i.e the photocurrent measured in ARPES to the one-electron removal spectral function $A^-_{mm}(\mathbf{k},\omega)$, which is defined as follows (at zero temperature):

$$A^-_{mm}(\mathbf{k},\omega) = \sum_n \left|\langle\psi_n^{N-1}|c_{m,\mathbf{k}}|\psi_{GS}^N\rangle\right|^2 \delta(E_n^{N-1} + E_{GS}^N - \omega) \tag{A.12}$$

In order to directly see the connection to the Green's function calculated in CDMFT, it is convenient to write the retarded Green's function at zero temperature in Lehmann's representation

$$\begin{aligned} G_{mm}(\mathbf{k},\omega) &= G^-_{mm}(\mathbf{k},\omega) + G^+_{mm}(\mathbf{k},\omega) \\ &= \sum_n \frac{\left|\langle\psi_n^{N-1}|c_{m,\mathbf{k}}|\psi_{GS}^N\rangle\right|^2}{\omega + E_n^{N-1} - E_{GS}^N + i\eta} + \sum_n \frac{\left|\langle\psi_n^{N+1}|c^\dagger_{m,\mathbf{k}}|\psi_{GS}^N\rangle\right|^2}{\omega - E_n^{N+1} + E_{GS}^N + i\eta} \end{aligned} \tag{A.13}$$

where $G^{-}_{mm}(\mathbf{k},\omega)$, $G^{+}_{mm}(\mathbf{k},\omega)$ are respectively the one-electron removal and addition Green's function, and η is a small finite number. Using the relation

$$\frac{1}{x+i\eta} \rightarrow_{\eta\rightarrow 0^{+}} \mathcal{P}(\frac{1}{x}) - i\pi\delta(x), \tag{A.14}$$

one can relate the electron removal spectral function to $G^{-}_{mm}(\mathbf{k},\omega)$:

$$-\frac{1}{\pi}Im[G^{-}_{mm}(\mathbf{k},\omega)] = \sum_{n}\left|\langle\psi^{N-1}_{n}|c_{m,\mathbf{k}}|\psi^{N}_{GS}\rangle\right|^{2}\delta(\omega+E^{N-1}_{n}-E^{N}_{GS}). \tag{A.15}$$

Therefore, the photocurrent measured in ARPES can be directly related to the occupied part of the CDMFT spectrum !

A.2 FROM ANGLES TO MOMENTUM

While in the formalism above we related the transition probability to the momentum-dependent spectral function, in the experimental measurements one can only have a direct access to the emission angles (ϕ,θ) of the photoelectrons. Therefore, we need to reconstruct the momentum dependence of the spectrum based on its angle dependence.

First, we can make the approximation that the momentum transfer from the electron is small, such that it can be neglected. This means that the photoelectron in the solid has the momentum $\mathbf{k}_{f} = \mathbf{k}$. When escaping from the material, the overall momentum of the electron is modified, i.e $\mathbf{k} \neq \mathbf{p}$, with $\mathbf{k}$ ($\mathbf{p}$) the momentum inside (outside) the solid. Due to the conservation of the in-plane (x, y) symmetry when crossing the solid/vacuum interface, the in-plane component of the momentum is conserved, i.e $\mathbf{k}_{\parallel} = \mathbf{p}_{\parallel}$ [24, 258]. However, the out-of plane component is not conserved since the photoelectron crosses a step-like potential when leaving the material:

$$\begin{aligned} V(z) &= -V \quad \text{inside the solid} \\ &= 0 \quad\quad \text{outside,} \end{aligned} \tag{A.16}$$

where V is the potential inside the solid. Within a simple free-electron picture, the non-conservation of the out-of-plane component can be written as [258]:

$$\frac{\mathbf{k}^{2}_{\perp}}{2m_{e}} = \frac{\mathbf{p}^{2}_{\perp}}{2m_{e}} + V. \tag{A.17}$$

The kinetic energy of the photoelectron in the vacuum, which is measured in the analyzer, is simply given by $E_{kin} = \frac{p^{2}}{2m_{e}}$. It is also related to the binding energy E_{B} via $E_{kin} = \nu - E_{B} - \Phi$, with Φ the work function, i.e the energy necessary for the electron to escape into the vacuum. Hence, following the angle notations of Fig. A.1, we can relate the momentum $\mathbf{k}$ to the angle θ by the following relations [24, 258]:

$$\begin{aligned} \mathbf{k}_{\parallel} &= \sqrt{2m_{e}E_{kin}}\sin(\theta) \\ \mathbf{k}_{\perp} &= \sqrt{2m\Big(E_{kin}\cos(\theta)^{2} + V\Big)}. \end{aligned} \tag{A.18}$$

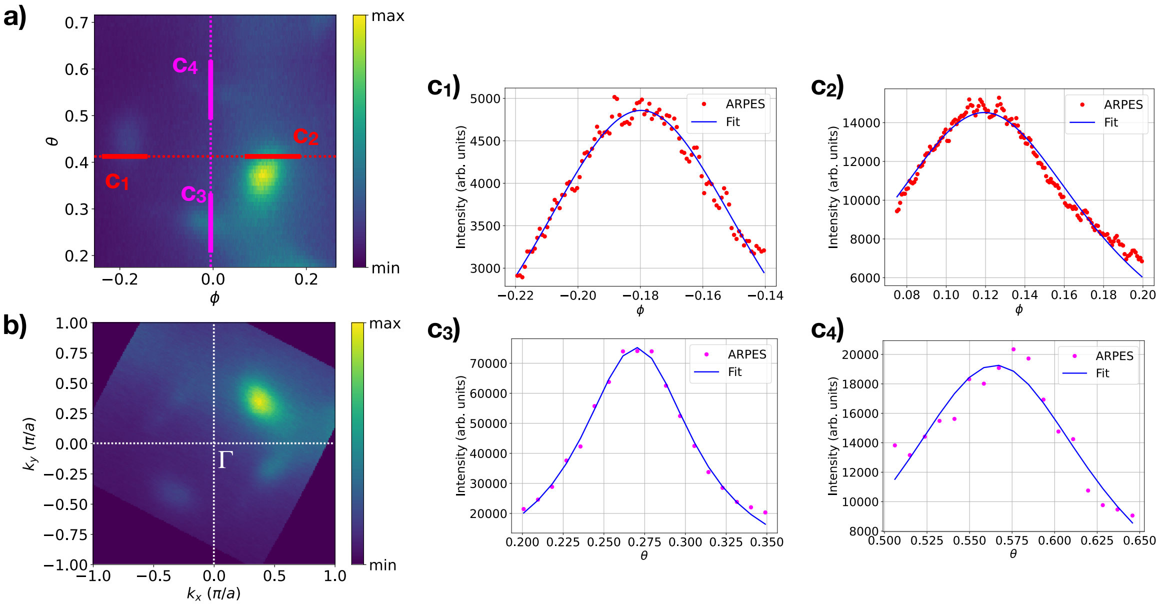

Figure A.2: (a) Angle-dependent Fermi surface obtained by integrating the spectrum over a narrow region of frequency around the Fermi level, and (b) its transformation to momentum-space. (c1)-(c4) A series of fits for the determination of the Γ point from the angle-dependent spectrum in the specific regions highlighted in (a).

Note that due to the V term in the expression of $\mathbf{k}_\perp$, the absolute value of the latter is not known *a priori*. One of the methods to determine $\mathbf{k}_\perp$ is to vary the photon energy and observe the periodicity of the spectrum at $\mathbf{k}_\parallel = 0$ [24]. We notice also that as the angle θ varies, $\mathbf{k}_\perp$ changes accordingly. This means that, in principle, for a given angle-dependent spectral function map, the out-of-plane component $\mathbf{k}_\perp$ is not constant as a function of the angles (θ, ϕ). Since we have seen in the band structures of NaCCOC and t-CuO that the low-energy ZRS band displays a weak dispersion along $\mathbf{k}_z$, we can safely ignore this complication here.

With the relations of Eq. A.18, we can now transform a typical angle-dependent spectrum as shown in Fig. A.2(a), to its momentum counterpart shown in Fig. A.2(b). To perform such transformation, we used the pyARPES package [257] that the author adapted to import the data from SOLEIL synchrotron (for the Photon Factory data the Igor software was used). It is required to locate the Γ high-symmetry point, since it serves as a center of rotation to align the axis $\mathbf{k}_x$ and $\mathbf{k}_y$. We find Γ from the Fermi surface, since it is in the middle of the four Fermi arcs that can be seen in Fig. A.2(a). Lorentzian fits can be used (see Fig. A.2(c)) to determine the precise position of each Fermi arc, from which Γ is then extracted. Once the Γ point is found as a function of the angles (ϕ, θ), the momentum-resolved spectrum can be obtained by estimating the rotation of the axis $\mathbf{k}_x$ and $\mathbf{k}_y$, as shown in Fig. A.2(b). The data is then ready for further analysis and comparison to the theoretical momentum-resolved spectrum (albeit the matrix-element effects).

ACKNOWLEDGMENTS

As we have seen in this thesis, materials are cool. Guess what, humans too, especially colleagues, friends, and family, with whom I spent quite some time in those last three years, and who deserve at least a one-and-a-half special page here.

First things first, I would like to thank the secretaries of the lab, without whom we would not do anything, as well as the computer support team.

I would like to thank Silke for welcoming me in her group, and offering me the opportunity to do this thesis. I am more than happy to have learned so much about physics, research in general, as well as singing techniques through our discussions. Benjamin (Lenz, not me), you deserve a few lines in here for all the time you spent guiding and helping me with all the sorts of problem and questions I had, although you were ”slightly” busy with your new *Maître de Conférences* position. I warmly thank you for all the knowledge you brought me, as well as the collaboration opportunities that I'm glad I could participate to. And let's not forget about the many lunches at Jussieu!

Having mentioned collaborations, I would like to thank Matteo d'Astuto who kindly accepted the dangerous task to embark theoreticians onto two ARPES beam times. These were probably two of the best physics experiences of this PhD, which by the way almost convinced me to turn to experimental physics. During the beam time in SOLEIL, it was the occasion to meet Chafic and Hervé who I would like to thank for all the nice discussions. A special mention to Chafic for the nights spent a SOLEIL with the photon flux going crazy, and who also saved us by ordering pizza since the canteen had rejected us. Talking about food (would have been strange to not discuss this topic in thesis written by a french), a second thank-you goes to both Chafic and Matteo, for the nice libanese dessert and the amazing asparagus risotto.

We're not done with collaborators yet: thanks to Martin, Sebastian, and Max from whom I learned a lot, both in terms of stories and physics. I have a special thought for Max, and all the nice writing sessions. I hope that you liked the *confit de canard*. And good luck to Sebastian, for taking care of at least 14 bachelor students at the same time.

A warm thanks goes to Steffen: in fact you would deserve the title (*officieux*) of co-supervisor. Thank you for all the time you spent answering my (often stupid) questions, helping me solving all kinds of technical problems, as well as for the nice mushroom hunt during which we found the nicest boletus I've ever eaten, and the amazing Christmas riddle. I hope that everything goes well in Japan! Thanks also to all the nice people I met at the lab and who made life enjoyable there: Jean-Baptiste, Louis, Julien who shared his writing experience that I can relate to right now, Jakob, Sumanta, Marcello, Anna, Erik for bringing so much life to the group and especially for the *caramel* tea, Adrian who should now enjoy the heatwave in France, Maria for the best (almost improvised) lecture on Feynman diagrams I attended to, Alaska for the sometimes heated discussions, Jan for the coffee and language expertise, and Zhenya for destroying unintentionally an innocent master's student presenting his results.

Life at the lab was not only about research, but also teaching. I must say that I was extremely lucky to be asked to do the superconductivity *modal* with Yannis, Aurélien and Renaud. Thank you to all three of you, for all the nice discussions about physics, flamenco, and others, as well as our small end-of-modal parties. And also the lab visits to discover Yannis' and Aurélien's setups.

Enough with physics, it's now time to greet all my friends, from Cachan or before, with who I spent amazing times during these three years. They are too many of you and I would forget about some names, so to avoid any disrespectful omission I will simply give a warm thanks to all of you, since without all the good times we spent together I would not have made it to this point.

A special thanks goes to the militant association *Droit au logement*, with which I spent quite some time during these last two years to fight for housing rights. I am in debt with all the militants I met there, who taught me everything I know about housing, and with whom I walked a few kilometers in Paris' streets to fight against savage evictions, rental abuses, denied access to social housing, etc. *Un toit, c'est un droit*!

Finally, the last paragraph is devoted to my closest family, who brought me so much support and love. Marie, of course. My sister, you were always present when needed, and you paved me the way towards the PhD. My father, especially for your patience and help each time we moved in a new apartment, and finally my mother who, although she could not make it to read this, surely immensely contributed to provide me the chance to do this thesis.

ACRONYMS

μ-SR	muon spin resonance. 8, 121
2DEG	2D electron gas. 9, 10, 122–125, 131, 133, 136, 139, 145, 146
AIM	Anderson's impurity model. 28, 32, 33
ARPES	angle-resolved photoemission spectroscopy. 6–9, 23, 40, 63, 65–67, 70, 71, 73–76, 87, 95, 98, 100, 104, 106, 108, 114, 119, 121, 137, 143, 144, 149–153
BZ	Brillouin zone. 4, 7, 25, 26, 38, 39, 58, 63, 66, 73, 76, 98, 100, 101, 106, 108, 109
CDMFT	cluster dynamical mean-field theory. 5–7, 9, 10, 22, 38–41, 44, 46, 51, 53, 55, 59, 64, 67–69, 71–73, 75–79, 83, 84, 86, 87, 89, 94–96, 98, 99, 101, 102, 104–106, 111–114, 117, 119, 121, 133, 143, 146, 152, 153
CDW	charge density wave. 4, 6, 38, 40, 63, 97, 146
CTQMC	continuous-time quantum Monte Carlo. 6, 9, 32, 41, 45, 46, 69, 98, 101, 111, 144
DCA	dynamical cluster approximation. 6, 7, 38, 64, 78, 92, 145, 146
DFT	density functional theory. 4, 8, 10, 13, 14, 17, 21–25, 27, 33, 67, 68, 97, 100, 101, 111, 121–123, 125, 139, 143, 145
DMFT	dynamical mean-field theory. 5–7, 10, 22, 24, 27, 28, 32, 34, 36–38, 41, 46, 55, 64, 110, 145, 146
DOS	density of states. 29, 40, 66, 67, 84, 86, 101, 123–127, 129–132, 135, 137–139
DSSF	dynamical spin structure factor. 8, 65, 69, 70, 87–96, 145
ED	exact diagonalization. 93
EDC	energy distribution curve. 75, 76, 78, 79, 86, 87
GGA	generalised gradient approximation. 18, 19
LDA	local density approximation. 4, 18–22, 24, 25, 38, 66–68, 100, 108, 123

LHB	lower Hubbard band. 3, 71, 73, 74, 81, 114, 144
LSDA	local spin density approximation. 18–21
MEM	maximum entropy method. 48–54, 88
MLWF	maximally localized Wannier functions. 26, 27, 68
MPS	matrix-product state. 6, 9, 32, 98, 101, 103, 104, 106–112, 144
MQEM	maximum quantum entropy method. 48, 53, 54, 69, 71
NaCCOC	$Ca_{2-x}Na_xCuO_2Cl_2$. 3–8, 10, 14, 18, 19, 24, 25, 27, 44, 46, 57, 59, 63–69, 71, 73, 74, 76, 89, 95, 97, 99, 100, 143–146, 154
NN	nearest-neighbor. 5, 8, 24, 30, 54, 55, 57, 68, 80, 89–93, 98, 100, 104, 105, 126, 128, 129, 133, 135
NNN	next-NN. 8, 30, 58, 68, 88–93, 98, 100, 101, 104, 126, 133, 135, 144
NNNN	next-NNN. 27, 58, 68, 126
PBE	Perdew–Burke–Ernzerhof. 123, 124, 128, 137, 145
PG	pseudogap. 4, 6–8, 39, 63–65, 67–69, 71, 74–79, 81, 82, 84, 86, 87, 91–93, 95, 96, 143, 144, 146
QMC	quantum Monte Carlo. 7, 64, 145
RIXS	resonant inelastic x-ray scattering. 8, 65, 68, 80, 87–89, 98, 100, 121
RVB	resonating valence bond. 80, 83, 86, 96
SCBA	self-consistent Born approximation. 7, 9, 10, 56, 57, 59, 65, 72, 73, 75, 78, 82, 95, 108, 113, 114, 144
SCOC	$Sr_2CuCl_2O_2$. 98
SOC	spin-orbit coupling. 121, 124, 128, 133
STM	scanning tunneling microscopy. 71, 137, 139
STO	$SrTiO_3$. 8–10, 21, 97, 121–126, 133, 137, 139, 140, 145, 146
t-CuO	tetragonal CuO. 3, 5, 6, 8–10, 18, 19, 21, 39, 40, 46, 51, 53, 54, 57, 97–101, 104, 111, 114, 118–125, 137, 139, 140, 143–146, 154
TB	tight-binding. 23–25, 27, 67, 68
TMO	transition metal oxides. 8, 18–20, 23, 98
UHB	upper Hubbard band. 3, 114
UHV	ultra high vacuum. 70
VASP	Vienna *ab initio* simulation package. 67, 123–125

VCA	variational cluster approximation. 6, 9, 99, 102, 118, 119, 146
XMCD	x-ray magnetic circular dichroïsm. 9, 10, 121–123, 125, 129, 131, 136, 137, 139, 145, 146
ZRS	Zhang-Rice singlets. 5, 23, 24, 27, 63, 67, 98, 108, 126, 143, 154

BIBLIOGRAPHY

[1] J. G. Bednorz and K. A. Müller. *Z. Physik B - Condensed Matter* 64.2 (1986), pp. 189–193. ISSN: 1431-584X. DOI: `10.1007/BF01303701` (cit. on p. 7).

[2] A. Schilling, M. Cantoni, J. D. Guo, and H. R. Ott. *Nature* 363 (1993), pp. 56–58. ISSN: 0028-0836. DOI: `10.1038/363056a0` (cit. on p. 7).

[3] J. Bardeen, L. N. Cooper, and J. R. Schrieffer. *Phys. Rev.* 108.5 (1957), pp. 1175–1204. DOI: `10.1103/PhysRev.108.1175` (cit. on p. 7).

[4] Nikolay Plakida. Vol. 166. Springer Series in Solid-State Sciences. Berlin, Heidelberg: Springer Berlin Heidelberg, 2010. ISBN: 978-3-642-12632-1 978-3-642-12633-8. DOI: `10.1007/978-3-642-12633-8` (cit. on pp. 7, 8).

[5] Daniel Khomskii. Cambridge University Press, 2014. ISBN: 978-1-107-02017-7 (cit. on pp. 7, 27).

[6] C. C. Tsuei and J. R. Kirtley. *Rev. Mod. Phys.* 72.4 (2000), pp. 969–1016. DOI: `10.1103/RevModPhys.72.969` (cit. on pp. 7, 8).

[7] A. I. Lichtenstein and M. L. Kulić. *Physica C: Superconductivity* 245.1 (1995), pp. 186–192. ISSN: 0921-4534. DOI: `10.1016/0921-4534(95)00085-2` (cit. on p. 7).

[8] Michael R. Norman. *Science* 332.6026 (2011), pp. 196–200. ISSN: 0036-8075, 1095-9203. DOI: `10.1126/science.1200181` (cit. on p. 7).

[9] B. Keimer, S. A. Kivelson, M. R. Norman, S. Uchida, and J. Zaanen. *Nature* 518.7538 (2015), pp. 179–186. ISSN: 1476-4687. DOI: `10.1038/nature14165` (cit. on pp. 7, 8).

[10] Patrick A. Lee, Naoto Nagaosa, and Xiao-Gang Wen. *Rev. Mod. Phys.* 78.1 (2006), pp. 17–85. ISSN: 0034-6861, 1539-0756. DOI: `10.1103/RevModPhys.78.17` (cit. on p. 7).

[11] M R Norman and C Pépin. *Rep. Prog. Phys.* 66.10 (2003), pp. 1547–1610. ISSN: 0034-4885, 1361-6633. DOI: `10.1088/0034-4885/66/10/R01` (cit. on p. 7).

[12] Tom Timusk and Bryan Statt. *Rep. Prog. Phys.* 62.1 (1999), pp. 61–122. ISSN: 0034-4885. DOI: `10.1088/0034-4885/62/1/002` (cit. on pp. 7, 8, 11, 67, 68, 151).

[13] Subir Sachdev. *Rev. Mod. Phys.* 75.3 (2003), pp. 913–932. ISSN: 0034-6861, 1539-0756. DOI: `10.1103/RevModPhys.75.913` (cit. on p. 7).

[14] Cyril Proust and Louis Taillefer. *Annu. Rev. Condens. Matter Phys.* 10.1 (2019), pp. 409–429. ISSN: 1947-5454, 1947-5462. DOI: `10.1146/annurev-conmatphys-031218-013210`. arXiv: `1807.05074 [cond-mat]` (cit. on pp. 7, 8, 67, 151, 154).

[15] N. F. Mott and R. Peierls. *Proc. Phys. Soc.* 49.4S (1937), pp. 72–73. ISSN: 0959-5309. DOI: `10.1088/0959-5309/49/4S/308` (cit. on pp. 8, 9, 23).

[16] N. F. Mott. *Proc. Phys. Soc. A* 62.7 (1949), pp. 416–422. ISSN: 0370-1298. DOI: `10.1088/0370-1298/62/7/303` (cit. on pp. 8, 9, 23).

[17] P. W. Anderson. *Phys. Rev.* 115.1 (1959), pp. 2–13. DOI: `10.1103/PhysRev.115.2` (cit. on pp. 8, 117).

[18] P. W. Anderson. *Phys. Rev.* 124.1 (1961), pp. 41–53. DOI: `10.1103/PhysRev.124.41` (cit. on pp. 8, 32).

[19] D. Vaknin, S. K. Sinha, D. E. Moncton, D. C. Johnston, J. M. Newsam, C. R. Safinya, and H. E. King. *Phys. Rev. Lett.* 58.26 (1987), pp. 2802–2805. DOI: `10.1103/PhysRevLett.58.2802` (cit. on p. 8).

[20] Sudip Chakravarty, Bertrand I. Halperin, and David R. Nelson. *Phys. Rev. Lett.* 60.11 (1988), pp. 1057–1060. DOI: `10.1103/PhysRevLett.60.1057` (cit. on p. 8).

[21] H. Alloul, T. Ohno, and P. Mendels. *Phys. Rev. Lett.* 63.16 (1989), pp. 1700–1703. DOI: `10.1103/PhysRevLett.63.1700` (cit. on pp. 8, 11, 68).

[22] W. W. Warren, R. E. Walstedt, G. F. Brennert, R. J. Cava, R. Tycko, R. F. Bell, and G. Dabbagh. *Phys. Rev. Lett.* 62.10 (1989), pp. 1193–1196. DOI: `10.1103/PhysRevLett.62.1193` (cit. on pp. 8, 11, 68).

[23] T. Ito, K. Takenaka, and S. Uchida. *Phys. Rev. Lett.* 70.25 (1993), pp. 3995–3998. DOI: `10.1103/PhysRevLett.70.3995` (cit. on pp. 8, 11, 68).

[24] Andrea Damascelli, Zahid Hussain, and Zhi-Xun Shen. *Rev. Mod. Phys.* 75.2 (2003), pp. 473–541. DOI: `10.1103/RevModPhys.75.473` (cit. on pp. 8, 10, 11, 67, 68, 80, 151, 154, 157, 158, 160–162).

[25] T. Hanaguri, C. Lupien, Y. Kohsaka, D.-H. Lee, M. Azuma, M. Takano, H. Takagi, and J. C. Davis. *Nature* 430.7003 (2004), pp. 1001–1005. ISSN: 0028-0836, 1476-4687. DOI: `10.1038/nature02861` (cit. on pp. 8, 67, 154).

[26] K. M. Shen. *Science* 307.5711 (2005), pp. 901–904. ISSN: 0036-8075, 1095-9203. DOI: `10.1126/science.1103627` (cit. on pp. 8, 11, 67, 80, 151, 154).

[27] W. D. Wise, M. C. Boyer, Kamalesh Chatterjee, Takeshi Kondo, T. Takeuchi, H. Ikuta, Yayu Wang, and E. W. Hudson. *Nature Phys* 4.9 (2008), pp. 696–699. ISSN: 1745-2473, 1745-2481. DOI: `10.1038/nphys1021` (cit. on pp. 8, 67, 154).

[28] Suchitra E. Sebastian and Cyril Proust. *Annu. Rev. Condens. Matter Phys.* 6.1 (2015), pp. 411–430. ISSN: 1947-5454, 1947-5462. DOI: `10.1146/annurev-conmatphys-030212-184305` (cit. on pp. 8, 154).

[29] Riccardo Comin and Andrea Damascelli. *Annu. Rev. Condens. Matter Phys.* 7.1 (2016), pp. 369–405. ISSN: 1947-5454, 1947-5462. DOI: `10.1146/annurev-conmatphys-031115-011401` (cit. on pp. 8, 154).

[30] O.K. Andersen, A.I. Liechtenstein, O. Jepsen, and F. Paulsen. *Journal of Physics and Chemistry of Solids* 56.12 (1995), pp. 1573–1591. ISSN: 00223697. DOI: `10.1016/0022-3697(95)00269-3` (cit. on pp. 8, 151).

[31] Motoaki Hirayama, Youhei Yamaji, Takahiro Misawa, and Masatoshi Imada. *Phys. Rev. B* 98.13 (2018), p. 134501. DOI: `10.1103/PhysRevB.98.134501` (cit. on pp. 8, 9, 28, 151).

[32] J. Zaanen, G. A. Sawatzky, and J. W. Allen. *Phys. Rev. Lett.* 55.4 (1985), pp. 418–421. ISSN: 0031-9007. DOI: `10.1103/PhysRevLett.55.418` (cit. on pp. 9, 151).

[33] V. J. Emery. *Phys. Rev. Lett.* 58.26 (1987), pp. 2794–2797. ISSN: 0031-9007. DOI: `10.1103/PhysRevLett.58.2794` (cit. on pp. 9, 151).

[34] C. M. Varma, S. Schmitt-Rink, and Elihu Abrahams. *Solid State Communications* 62.10 (1987), pp. 681–685. ISSN: 0038-1098. DOI: `10.1016/0038-1098(87)90407-8` (cit. on p. 9).

[35] J. Hubbard and Brian Hilton Flowers. *Proceedings of the Royal Society of London. Series A. Mathematical and Physical Sciences* 276.1365 (1963), pp. 238–257. DOI: `10.1098/rspa.1963.0204` (cit. on pp. 9, 23, 28, 46, 48, 69, 72, 77, 106, 123, 151).

[36] Martin C. Gutzwiller. *Phys. Rev. Lett.* 10.5 (1963), pp. 159–162. DOI: `10.1103/PhysRevLett.10.159` (cit. on pp. 9, 23, 28, 72, 106, 151).

[37] Junjiro Kanamori. *Progress of Theoretical Physics* 30.3 (1963), pp. 275–289. ISSN: 0033-068X. DOI: `10.1143/PTP.30.275` (cit. on pp. 9, 23, 28, 72, 106, 151).

[38] F. C. Zhang and T. M. Rice. *Phys. Rev. B* 37.7 (1988), pp. 3759–3761. DOI: `10.1103/PhysRevB.37.3759` (cit. on pp. 9, 27, 67, 71, 104, 114, 134, 151).

[39] A. Macridin, M. Jarrell, Th. Maier, and G. A. Sawatzky. *Phys. Rev. B* 71.13 (2005), p. 134527. DOI: `10.1103/PhysRevB.71.134527` (cit. on p. 9).

[40] Mi Jiang, Mirko Moeller, Mona Berciu, and George A. Sawatzky. *Phys. Rev. B* 101.3 (2020), p. 035151. DOI: `10.1103/PhysRevB.101.035151` (cit. on pp. 9, 104).

[41] A. A. Aligia. *Phys. Rev. B* 102.11 (2020), p. 117101. DOI: `10.1103/PhysRevB.102.117101` (cit. on pp. 9, 104).

[42] Antoine Georges and Gabriel Kotliar. *Phys. Rev. B* 45.12 (1992), pp. 6479–6483. DOI: `10.1103/PhysRevB.45.6479` (cit. on pp. 9, 28, 32, 36, 151).

[43] Antoine Georges, Gabriel Kotliar, Werner Krauth, and Marcelo J. Rozenberg. *Rev. Mod. Phys.* 68.1 (1996), pp. 13–125. DOI: `10.1103/RevModPhys.68.13` (cit. on pp. 9, 28, 32, 36, 40, 58, 151).

[44] Walter Metzner and Dieter Vollhardt. *Phys. Rev. Lett.* 62.3 (1989), pp. 324–327. DOI: `10.1103/PhysRevLett.62.324` (cit. on pp. 9, 32, 33, 35).

[45] Walter Metzner. *Z. Physik B - Condensed Matter* 77.2 (1989), pp. 253–266. ISSN: 1431-584X. DOI: `10.1007/BF01313669` (cit. on pp. 9, 32, 34, 35).

[46] Walter Metzner. *Phys. Rev. B* 43.10 (1991), pp. 8549–8563. DOI: `10.1103/PhysRevB.43.8549` (cit. on pp. 9, 32, 39, 40).

[47] Dieter Vollhardt. *AIP Conference Proceedings* 1297.1 (2010), p. 339. ISSN: 0094-243X. DOI: `10.1063/1.3518901` (cit. on pp. 9, 32, 33).

[48] H. Park, K. Haule, and G. Kotliar. *Phys. Rev. Lett.* 101.18 (2008), p. 186403. DOI: `10.1103/PhysRevLett.101.186403` (cit. on pp. 9, 41, 85, 119).

[49] A. I. Lichtenstein and M. I. Katsnelson. *Phys. Rev. B* 57.12 (1998), pp. 6884–6895. DOI: `10.1103/PhysRevB.57.6884` (cit. on pp. 9, 11, 13, 28, 30, 42, 104, 151).

[50] A. I. Lichtenstein and M. I. Katsnelson. *Phys. Rev. B* 62.14 (2000), R9283–R9286. DOI: `10.1103/PhysRevB.62.R9283` (cit. on pp. 9, 11, 13, 42, 59, 104, 107, 126, 151).

[51] Gabriel Kotliar, Sergej Y. Savrasov, Gunnar Pálsson, and Giulio Biroli. *Phys. Rev. Lett.* 87.18 (2001), p. 186401. DOI: `10.1103/PhysRevLett.87.186401` (cit. on pp. 9, 11, 13, 42, 45, 104, 107, 151).

[52] Thomas Maier, Mark Jarrell, Thomas Pruschke, and Matthias H. Hettler. *Rev. Mod. Phys.* 77.3 (2005), pp. 1027–1080. DOI: `10.1103/RevModPhys.77.1027` (cit. on pp. 9–11, 13, 41, 42, 59, 104, 107, 154).

[53] Michel Caffarel and Werner Krauth. *Phys. Rev. Lett.* 72.10 (1994), pp. 1545–1548. DOI: `10.1103/PhysRevLett.72.1545` (cit. on pp. 10, 36).

[54] Qimiao Si, M. J. Rozenberg, G. Kotliar, and A. E. Ruckenstein. *Phys. Rev. Lett.* 72.17 (1994), pp. 2761–2764. DOI: `10.1103/PhysRevLett.72.2761` (cit. on pp. 10, 36).

[55] O. Sakai and Y. Kuramoto. *Solid State Communications* 89.4 (1994), pp. 307–311. ISSN: 0038-1098. DOI: `10.1016/0038-1098(94)90589-4` (cit. on pp. 10, 36).

[56] U. Schollwöck. *Rev. Mod. Phys.* 77.1 (2005), pp. 259–315. DOI: `10.1103/RevModPhys.77.259` (cit. on pp. 10, 13, 36, 104, 152).

[57] Ulrich Schollwöck. *Annals of Physics*. January 2011 Special Issue 326.1 (2011), pp. 96–192. ISSN: 0003-4916. DOI: `10.1016/j.aop.2010.09.012` (cit. on pp. 10, 13, 36, 104, 152).

[58] F. Alexander Wolf, Ian P. McCulloch, Olivier Parcollet, and Ulrich Schollwöck. *Phys. Rev. B* 90.11 (2014), p. 115124. DOI: `10.1103/PhysRevB.90.115124` (cit. on pp. 10, 13, 36, 104, 107, 112, 126, 152).

[59] F. Alexander Wolf, Ara Go, Ian P. McCulloch, Andrew J. Millis, and Ulrich Schollwöck. *Phys. Rev. X* 5.4 (2015), p. 041032. ISSN: 2160-3308. DOI: `10.1103/PhysRevX.5.041032` (cit. on pp. 10, 13, 36, 107, 110).

[60] A. N. Rubtsov, V. V. Savkin, and A. I. Lichtenstein. *Phys. Rev. B* 72.3 (2005), p. 035122. ISSN: 1098-0121, 1550-235X. DOI: `10.1103/PhysRevB.72.035122` (cit. on pp. 10, 13, 36, 45, 50, 73, 104, 107, 152).

[61] Philipp Werner, Armin Comanac, Luca de' Medici, Matthias Troyer, and Andrew J. Millis. *Phys. Rev. Lett.* 97.7 (2006), p. 076405. DOI: `10.1103/PhysRevLett.97.076405` (cit. on pp. 10, 13, 36, 45, 50, 71, 73, 107).

[62] Emanuel Gull, Andrew J. Millis, Alexander I. Lichtenstein, Alexey N. Rubtsov, Matthias Troyer, and Philipp Werner. *Rev. Mod. Phys.* 83.2 (2011), pp. 349–404. DOI: `10.1103/RevModPhys.83.349` (cit. on pp. 10, 13, 36, 45, 50, 73, 104, 107, 152).

[63] M. H. Hettler, A. N. Tahvildar-Zadeh, M. Jarrell, T. Pruschke, and H. R. Krishnamurthy. *Phys. Rev. B* 58.12 (1998), R7475–R7479. DOI: `10.1103/PhysRevB.58.R7475` (cit. on pp. 10, 43).

[64] M. H. Hettler, M. Mukherjee, M. Jarrell, and H. R. Krishnamurthy. *Phys. Rev. B* 61.19 (2000), pp. 12739–12756. DOI: `10.1103/PhysRevB.61.12739` (cit. on pp. 10, 43).

[65] C. Huscroft, M. Jarrell, Th. Maier, S. Moukouri, and A. N. Tahvildarzadeh. *Phys. Rev. Lett.* 86.1 (2001), pp. 139–142. DOI: `10.1103/PhysRevLett.86.139` (cit. on pp. 10, 11, 43, 68).

[66] Claudius Gros and Roser Valentí. *Phys. Rev. B* 48.1 (1993), pp. 418–425. DOI: `10.1103/PhysRevB.48.418` (cit. on p. 10).

[67] D. Sénéchal, D. Perez, and M. Pioro-Ladrière. *Phys. Rev. Lett.* 84.3 (2000), pp. 522–525. DOI: `10.1103/PhysRevLett.84.522` (cit. on pp. 10, 44, 73).

[68] M. Potthoff, M. Aichhorn, and C. Dahnken. *Phys. Rev. Lett.* 91.20 (2003), p. 206402. DOI: `10.1103/PhysRevLett.91.206402` (cit. on pp. 10, 13, 105, 108, 125).

[69] David Sénéchal. *2008 22nd International Symposium on High Performance Computing Systems and Applications*. Quebec city, QC, Canada: IEEE, 2008, pp. 9–15. ISBN: 978-0-7695-3250-9. DOI: `10.1109/HPCS.2008.18` (cit. on pp. 10, 13, 108, 125).

[70] M. Potthoff. e-print, 2014 (cit. on pp. 10, 13, 108, 125).

[71] A. N. Rubtsov, M. I. Katsnelson, and A. I. Lichtenstein. *Phys. Rev. B* 77.3 (2008), p. 033101. DOI: `10.1103/PhysRevB.77.033101` (cit. on pp. 10, 41, 154).

[72] A. N. Rubtsov, M. I. Katsnelson, and A. I. Lichtenstein. *Annals of Physics* 327.5 (2012), pp. 1320–1335. ISSN: 0003-4916. DOI: `10.1016/j.aop.2012.01.002` (cit. on pp. 10, 41, 154).

[73] Thomas Ayral and Olivier Parcollet. *Phys. Rev. B* 92.11 (2015), p. 115109. DOI: `10.1103/PhysRevB.92.115109` (cit. on pp. 10, 41, 154).

[74] G. Rohringer, H. Hafermann, A. Toschi, A. A. Katanin, A. E. Antipov, M. I. Katsnelson, A. I. Lichtenstein, A. N. Rubtsov, and K. Held. *Rev. Mod. Phys.* 90.2 (2018), p. 025003. DOI: `10.1103/RevModPhys.90.025003` (cit. on pp. 10, 154).

[75] Evgeny A. Stepanov, Lars Peters, Igor S. Krivenko, Alexander I. Lichtenstein, Mikhail I. Katsnelson, and Alexey N. Rubtsov. *npj Quant Mater* 3.1 (2018), pp. 1–7. ISSN: 2397-4648. DOI: `10.1038/s41535-018-0128-x` (cit. on pp. 10, 11, 68, 82, 84, 90, 93, 94, 100, 101, 153, 154).

[76] E. A. Stepanov, V. Harkov, and A. I. Lichtenstein. *Phys. Rev. B* 100.20 (2019), p. 205115. DOI: `10.1103/PhysRevB.100.205115` (cit. on pp. 10, 41, 154).

[77] Hidekazu Mukuda, Sunao Shimizu, Akira Iyo, and Yoshio Kitaoka. *J. Phys. Soc. Jpn.* 81.1 (2012), p. 011008. ISSN: 0031-9015, 1347-4073. DOI: `10.1143/JPSJ.81.011008` (cit. on pp. 10, 103).

[78] V. Oliviero, S. Benhabib, I. Gilmutdinov, B. Vignolle, L. Drigo, M. Massoudzadegan, M. Leroux, G. L. J. A. Rikken, A. Forget, D. Colson, D. Vignolles, and C. Proust. *Nat Commun* 13.1 (2022), p. 1568. ISSN: 2041-1723. DOI: `10.1038/s41467-022-29134-6` (cit. on pp. 10, 103).

[79] So Kunisada, Shunsuke Isono, Yoshimitsu Kohama, Shiro Sakai, Cédric Bareille, Shunsuke Sakuragi, Ryo Noguchi, Kifu Kurokawa, Kenta Kuroda, Yukiaki Ishida, Shintaro Adachi, Ryotaro Sekine, Timur K. Kim, Cephise Cacho, Shik Shin, Takami Tohyama, Kazuyasu Tokiwa, and Takeshi Kondo. *Science* 369.6505 (2020), pp. 833–838. ISSN: 0036-8075, 1095-9203. DOI: `10.1126/science.aay7311` (cit. on pp. 10, 11, 103).

[80] Z. Hiroi, N. Kobayashi, and M. Takano. *Nature* 371.6493 (1994), pp. 139–141. ISSN: 1476-4687. DOI: `10.1038/371139a0` (cit. on pp. 10, 67).

[81] Hiroi, N. Kobayashi, and M. Takano. *Physica C: Superconductivity* 266.3 (1996), pp. 191–202. ISSN: 0921-4534. DOI: `10.1016/0921-4534(95)00535-8` (cit. on pp. 10, 67).

[82] S. Adachi, T. Tatsuki, C. -Q. Jin, X. -J. Wu, A. Tokiwa-Yamamoto, T. Tamura, Y. Moriwaki, and K. Tanabe. *J Low Temp Phys* 105.5 (1996), pp. 1505–1510. ISSN: 1573-7357. DOI: `10.1007/BF00753913` (cit. on pp. 10, 67).

[83] Yuhki Kohsaka, Masaki Azuma, Ikuya Yamada, Takao Sasagawa, Tetsuo Hanaguri, Mikio Takano, and Hidenori Takagi. *J. Am. Chem. Soc.* 124.41 (2002), pp. 12275–12278. ISSN: 0002-7863, 1520-5126. DOI: `10.1021/ja026680i` (cit. on pp. 10, 67, 74).

[84] Kazuki Ohishi, Ikuya Yamada, Akihiro Koda, Wataru Higemoto, Shanta R. Saha, Ryosuke Kadono, Kenji M. Kojima, Masaki Azuma, and Mikio Takano. *J. Phys. Soc. Jpn.* 74.9 (2005), pp. 2408–2412. ISSN: 0031-9015, 1347-4073. DOI: `10.1143/JPSJ.74.2408` (cit. on pp. 10, 11, 67, 73, 97).

[85] F. Ronning. *Science* 282.5396 (1998), pp. 2067–2072. DOI: `10.1126/science.282.5396.2067` (cit. on pp. 10, 23, 67, 69, 77, 78).

[86] F. Ronning, K. M. Shen, N. P. Armitage, A. Damascelli, D. H. Lu, Z.-X. Shen, L. L. Miller, and C. Kim. *Phys. Rev. B* 71.9 (2005), p. 094518. ISSN: 1098-0121, 1550-235X. DOI: `10.1103/PhysRevB.71.094518` (cit. on pp. 10, 67–69, 75–77, 151).

[87] K. M. Shen, F. Ronning, W. Meevasana, D. H. Lu, N. J. C. Ingle, F. Baumberger, W. S. Lee, L. L. Miller, Y. Kohsaka, M. Azuma, M. Takano, H. Takagi, and Z.-X. Shen. *Phys. Rev. B* 75.7 (2007), p. 075115. ISSN: 1098-0121, 1550-235X. DOI: `10.1103/PhysRevB.75.075115` (cit. on pp. 10, 67, 69).

[88] Cheng Hu, Jian-Fa Zhao, Ying Ding, Jing Liu, Qiang Gao, Lin Zhao, Guo-Dong Liu, Li Yu, Chang-Qing Jin, Chuang-Tian Chen, Zu-Yan Xu, and Xing-Jiang Zhou. *Chinese Phys. Lett.* 35.6 (2018), p. 067403. ISSN: 0256-307X, 1741-3540. DOI: `10.1088/0256-307X/35/6/067403` (cit. on pp. 10, 67, 69).

[89] Cun Ye, Peng Cai, Runze Yu, Xiaodong Zhou, Wei Ruan, Qingqing Liu, Changqing Jin, and Yayu Wang. *Nat Commun* 4.1 (2013), p. 1365. ISSN: 2041-1723. DOI: `10.1038/ncomms2369` (cit. on pp. 10, 67, 75).

[90] F. Ronning, T. Sasagawa, Y. Kohsaka, K. M. Shen, A. Damascelli, C. Kim, T. Yoshida, N. P. Armitage, D. H. Lu, D. L. Feng, L. L. Miller, H. Takagi, and Z.-X. Shen. *Phys. Rev. B* 67.16 (2003), p. 165101. ISSN: 0163-1829, 1095-3795. DOI: `10.1103/PhysRevB.67.165101` (cit. on pp. 11, 67, 68, 74, 80, 151).

[91] Yuhki Kohsaka, Takao Sasagawa, Filip Ronning, Teppei Yoshida, Changyoung Kim, Tetsuo Hanaguri, Masaki Azuma, Mikio Takano, Zhi Xun Shen, and Hidenori Takagi. *J. Phys. Soc. Jpn.* 72.5 (2003), pp. 1018–1021. ISSN: 0031-9015, 1347-4073. DOI: `10.1143/JPSJ.72.1018` (cit. on pp. 11, 67–69, 77, 78, 80, 81, 83, 151).

[92] K. M. Shen, F. Ronning, D. H. Lu, W. S. Lee, N. J. C. Ingle, W. Meevasana, F. Baumberger, A. Damascelli, N. P. Armitage, L. L. Miller, Y. Kohsaka, M. Azuma, M. Takano, H. Takagi, and Z.-X. Shen. *Phys. Rev. Lett.* 93.26 (2004), p. 267002. ISSN: 0031-9007, 1079-7114. DOI: `10.1103/PhysRevLett.93.267002` (cit. on pp. 11, 67–69, 80, 81, 83, 151).

[93] T. Sasagawa, F. Ronning, Y. Kohsaka, K.M. Shen, T. Yoshida, M. Azuma, M. Takano, Z.-X. Shen, and H. Takagi. *Physica C: Superconductivity* 388–389 (2003), pp. 307–308. ISSN: 09214534. DOI: `10.1016/S0921-4534(02)02462-0` (cit. on pp. 11, 67, 80, 151).

[94] Jian-Qiao Meng, M. Brunner, K.-H. Kim, H.-G. Lee, S.-I. Lee, J. S. Wen, Z. J. Xu, G. D. Gu, and G.-H. Gweon. *Phys. Rev. B* 84.6 (2011), p. 060513. ISSN: 1098-0121, 1550-235X. DOI: `10.1103/PhysRevB.84.060513` (cit. on pp. 11, 67, 151).

[95] Gerardo Martinez and Peter Horsch. *Phys. Rev. B* 44.1 (1991), pp. 317–331. DOI: `10.1103/PhysRevB.44.317` (cit. on pp. 11, 59, 61, 68, 69, 77, 100, 151).

[96] Efstratios Manousakis. *Phys. Rev. B* 75.3 (2007), p. 035106. DOI: `10.1103/PhysRevB.75.035106` (cit. on pp. 11, 68, 69, 77, 100, 151).

[97] Alexandru Macridin, M. Jarrell, Thomas Maier, and D. J. Scalapino. *Phys. Rev. Lett.* 99.23 (2007), p. 237001. DOI: `10.1103/PhysRevLett.99.237001` (cit. on pp. 11, 68, 69, 77, 100, 151).

[98] Y. Wang, K. Wohlfeld, B. Moritz, C. J. Jia, M. van Veenendaal, K. Wu, C.-C. Chen, and T. P. Devereaux. *Phys. Rev. B* 92.7 (2015), p. 075119. ISSN: 1098-0121, 1550-235X. DOI: `10.1103/PhysRevB.92.075119` (cit. on pp. 11, 68, 69, 77, 100, 151).

[99] Masanori Kohno. *Phys. Rev. Lett.* 108.7 (2012), p. 076401. DOI: `10.1103/PhysRevLett.108.076401` (cit. on pp. 11, 68).

[100] Masanori Kohno. *Phys. Rev. B* 90.3 (2014), p. 035111. DOI: `10.1103/PhysRevB.90.035111` (cit. on pp. 11, 68).

[101] R. Preuss, W. Hanke, and W. von der Linden. *Phys. Rev. Lett.* 75.7 (1995), pp. 1344–1347. DOI: `10.1103/PhysRevLett.75.1344` (cit. on pp. 11, 68).

[102] C. Gröber, R. Eder, and W. Hanke. *Phys. Rev. B* 62.7 (2000), pp. 4336–4352. DOI: `10.1103/PhysRevB.62.4336` (cit. on pp. 11, 68).

[103] M. Civelli, M. Capone, S. S. Kancharla, O. Parcollet, and G. Kotliar. *Phys. Rev. Lett.* 95.10 (2005), p. 106402. DOI: `10.1103/PhysRevLett.95.106402` (cit. on pp. 11, 68, 104, 119).

[104] B. Kyung, S. S. Kancharla, D. Sénéchal, A.-M. S. Tremblay, M. Civelli, and G. Kotliar. *Phys. Rev. B* 73.16 (2006), p. 165114. DOI: `10.1103/PhysRevB.73.165114` (cit. on pp. 11, 68, 82, 84, 100, 104, 151).

[105] Shiro Sakai, Yukitoshi Motome, and Masatoshi Imada. *Phys. Rev. Lett.* 102.5 (2009), p. 056404. DOI: `10.1103/PhysRevLett.102.056404` (cit. on pp. 11, 68, 104).

[106] G. Sordi, P. Sémon, K. Haule, and A.-M. S. Tremblay. *Phys. Rev. Lett.* 108.21 (2012), p. 216401. DOI: `10.1103/PhysRevLett.108.216401` (cit. on pp. 11, 68, 69, 104).

[107] Alexandru Macridin, M. Jarrell, Thomas Maier, P. R. C. Kent, and Eduardo D'Azevedo. *Phys. Rev. Lett.* 97.3 (2006), p. 036401. DOI: `10.1103/PhysRevLett.97.036401` (cit. on pp. 11, 68, 82, 84, 100, 151).

[108] Michel Ferrero, Pablo S. Cornaglia, Lorenzo De Leo, Olivier Parcollet, Gabriel Kotliar, and Antoine Georges. *Phys. Rev. B* 80.6 (2009), p. 064501. DOI: `10.1103/PhysRevB.80.064501` (cit. on pp. 11, 68, 119).

[109] Philipp Werner, Emanuel Gull, Olivier Parcollet, and Andrew J. Millis. *Phys. Rev. B* 80.4 (2009), p. 045120. DOI: `10.1103/PhysRevB.80.045120` (cit. on pp. 11, 68).

[110] E. Gull, M. Ferrero, O. Parcollet, A. Georges, and A. J. Millis. *Phys. Rev. B* 82.15 (2010), p. 155101. DOI: `10.1103/PhysRevB.82.155101` (cit. on pp. 11, 68, 82).

[111] R. Preuss, W. Hanke, C. Gröber, and H. G. Evertz. *Phys. Rev. Lett.* 79.6 (1997), pp. 1122–1125. DOI: `10.1103/PhysRevLett.79.1122` (cit. on pp. 11, 68, 82, 84, 93, 100, 151, 153).

[112] O. Gunnarsson, T. Schäfer, J. P. F. LeBlanc, E. Gull, J. Merino, G. Sangiovanni, G. Rohringer, and A. Toschi. *Phys. Rev. Lett.* 114.23 (2015), p. 236402. DOI: `10.1103/PhysRevLett.114.236402` (cit. on pp. 11, 59, 68, 82, 84, 90, 93, 99, 100, 151, 153).

[113] Wei Wu, Michel Ferrero, Antoine Georges, and Evgeny Kozik. *Phys. Rev. B* 96.4 (2017), p. 041105. DOI: `10.1103/PhysRevB.96.041105` (cit. on pp. 11, 59, 68, 82, 84, 90, 93, 97, 99, 100, 151, 153).

[114] Riccardo Rossi, Fedor Šimkovic, and Michel Ferrero. *EPL* 132.1 (2020), p. 11001. ISSN: 0295-5075. DOI: `10.1209/0295-5075/132/11001` (cit. on pp. 11, 68, 82, 84, 90, 100, 151, 153).

[115] A.-M. S. Tremblay, B. Kyung, and D. Sénéchal. *Low Temperature Physics* 32.4 (2006), p. 424. ISSN: 1063-777X. DOI: `10.1063/1.2199446` (cit. on p. 11).

[116] Hiroshi Shinaoka, Michele Dolfi, Matthias Troyer, and Philipp Werner. *J. Stat. Mech.* 2014.6 (2014), P06012. ISSN: 1742-5468. DOI: `10.1088/1742-5468/2014/06/P06012` (cit. on pp. 11, 13, 45, 50, 73, 92, 93, 104, 107, 110, 112, 117, 152).

[117] Hiroshi Shinaoka, Yusuke Nomura, and Emanuel Gull. *Computer Physics Communications* 252 (2020), p. 106826. ISSN: 0010-4655. DOI: `10.1016/j.cpc.2019.06.016` (cit. on pp. 11, 50, 73, 92).

[118] A. Gaenko, A.E. Antipov, G. Carcassi, T. Chen, X. Chen, Q. Dong, L. Gamper, J. Gukelberger, R. Igarashi, S. Iskakov, M. Könz, J.P.F. LeBlanc, R. Levy, P.N. Ma, J.E. Paki, H. Shinaoka, S. Todo, M. Troyer, and E. Gull. *Computer Physics Communications* 213 (2017), pp. 235–251. ISSN: 00104655. DOI: `10.1016/j.cpc.2016.12.009` (cit. on pp. 11, 50, 73, 104, 107, 110, 112, 117).

[119] Priyanka Seth, Igor Krivenko, Michel Ferrero, and Olivier Parcollet. *Computer Physics Communications* 200 (2016), pp. 274–284. ISSN: 0010-4655. DOI: `10.1016/j.cpc.2015.10.023` (cit. on pp. 11, 45, 73, 84).

[120] Olivier Parcollet, Michel Ferrero, Thomas Ayral, Hartmut Hafermann, Igor Krivenko, Laura Messio, and Priyanka Seth. *Computer Physics Communications* 196 (2015), pp. 398–415. ISSN: 0010-4655. DOI: `10.1016/j.cpc.2015.04.023` (cit. on pp. 11, 55, 73, 84, 119).

[121] J. Merino and O. Gunnarsson. *Phys. Rev. B* 89.24 (2014), p. 245130. DOI: `10.1103/PhysRevB.89.245130` (cit. on pp. 12, 69, 73, 84, 85, 87, 90, 91, 151, 152).

[122] Philipp Werner, Shintaro Hoshino, and Hiroshi Shinaoka. *Phys. Rev. B* 94.24 (2016), p. 245134. DOI: `10.1103/PhysRevB.94.245134` (cit. on pp. 12, 94, 97, 153).

[123] Philipp Werner, Xi Chen, and Emanuel Gull. *Phys. Rev. Research* 2.2 (2020), p. 023037. DOI: `10.1103/PhysRevResearch.2.023037` (cit. on pp. 12, 71, 94, 96, 97, 153, 154).

[124] Wolter Siemons, Gertjan Koster, Dave H. A. Blank, Robert H. Hammond, Theodore H. Geballe, and Malcolm R. Beasley. *Phys. Rev. B* 79.19 (2009), p. 195122. ISSN: 1098-0121, 1550-235X. DOI: `10.1103/PhysRevB.79.195122` (cit. on pp. 12, 23, 103, 104, 117, 129).

[125] D. Samal, Haiyan Tan, Y. Takamura, W. Siemons, Jo Verbeeck, G. Van Tendeloo, E. Arenholz, C. A. Jenkins, G. Rijnders, and Gertjan Koster. *EPL* 105.1 (2014), p. 17003. ISSN: 0295-5075, 1286-4854. DOI: `10.1209/0295-5075/105/17003` (cit. on pp. 12, 103, 129, 131).

[126] Yong Zhong, Ziyuan Dou, Rui-Feng Wang, Yan-Feng Lv, Sha Han, Hang Yan, Can-Li Song, Xu-Cun Ma, and Qi-Kun Xue. *Appl. Phys. Lett.* 119.17 (2021), p. 172602. ISSN: 0003-6951, 1077-3118. DOI: `10.1063/5.0069356` (cit. on pp. 12, 103, 106, 129, 142, 145, 148).

[127] B. X. Yang, T. R. Thurston, J. M. Tranquada, and G. Shirane. *Phys. Rev. B* 39.7 (1989), pp. 4343–4349. ISSN: 0163-1829. DOI: `10.1103/PhysRevB.39.4343` (cit. on pp. 12, 104).

[128] Giovanni Peralta, Danilo Puggioni, Alessio Filippetti, and Vincenzo Fiorentini. *Phys. Rev. B* 80.14 (2009), p. 140408. ISSN: 1098-0121, 1550-235X. DOI: `10.1103/PhysRevB.80.140408` (cit. on pp. 12, 14, 103, 104, 117, 129, 131).

[129] Xing-Qiu Chen, C. L. Fu, C. Franchini, and R. Podloucky. *Phys. Rev. B* 80.9 (2009), p. 094527. ISSN: 1098-0121, 1550-235X. DOI: `10.1103/PhysRevB.80.094527` (cit. on pp. 12, 14, 103, 104, 106, 117, 129, 131).

[130] C Franchini, Xing-Qiu Chen, and R Podloucky. *J. Phys.: Condens. Matter* 23.4 (2011), p. 045004. ISSN: 0953-8984, 1361-648X. DOI: `10.1088/0953-8984/23/4/045004` (cit. on pp. 12, 103, 129, 131, 132).

[131] Fang-Fang Wang, Peng-Yue Wei, Xue-Yong Ding, Xian-Ran Xing, and Xing-Qiu Chen. *Chinese Phys. Lett.* 31.2 (2014), p. 027402. ISSN: 0256-307X, 1741-3540. DOI: `10.1088/0256-307X/31/2/027402` (cit. on pp. 12, 14, 103, 104, 129, 131).

[132] Paul M Grant. *J. Phys.: Conf. Ser.* 129 (2008), p. 012042. ISSN: 1742-6596. DOI: `10.1088/1742-6596/129/1/012042` (cit. on pp. 12, 103).

[133] Giovanni Drera, Alessio Giampietri, Alfredo Febbrari, Maddalena Patrini, Maria Cristina Mozzati, and Luigi Sangaletti. *Phys. Rev. B* 99.7 (2019), p. 075124. ISSN: 2469-9950, 2469-9969. DOI: `10.1103/PhysRevB.99.075124` (cit. on pp. 12, 103, 131–133).

[134] S. Moser, L. Moreschini, H.-Y. Yang, D. Innocenti, F. Fuchs, N. H. Hansen, Y. J. Chang, K. S. Kim, A. L. Walter, A. Bostwick, E. Rotenberg, F. Mila, and M. Grioni. *Phys. Rev. Lett.* 113.18 (2014), p. 187001. ISSN: 0031-9007, 1079-7114. DOI: `10.1103/PhysRevLett.113.187001` (cit. on pp. 12, 13, 44, 104, 106, 110, 112–114, 126, 129, 133, 142, 145, 147, 152).

[135] S. Moser, N. E. Shaik, D. Samal, S. Fatale, B. Dalla Piazza, M. Dantz, J. Pelliciari, P. Olalde-Velasco, T. Schmitt, G. Koster, F. Mila, H. M. Rønnow, and M. Grioni. *Phys. Rev. B* 92.14 (2015), p. 140404. ISSN: 1098-0121, 1550-235X. DOI: `10.1103/PhysRevB.92.140404` (cit. on pp. 12, 14, 44, 104, 106, 126, 129, 142, 147, 152).

[136] N. Ortiz Hernández, Z. Salman, T. Prokscha, A. Suter, J. R. L. Mardegan, S. Moser, A. Zakharova, C. Piamonteze, and U. Staub. *Phys. Rev. B* 103.22 (2021), p. 224429. ISSN: 2469-9950, 2469-9969. DOI: `10.1103/PhysRevB.103.224429` (cit. on pp. 12–14, 23, 44, 129, 130, 137, 139, 145, 147, 153).

[137] K. S. Rabinovich, L. L. Samoilenko, A. S. Zhuravleva, and A. G. Shneider. *Appl. Phys. Lett.* 104.18 (2014), p. 182406. ISSN: 0003-6951, 1077-3118. DOI: `10.1063/1.4875042` (cit. on pp. 12, 104, 117).

[138] Nils-Oliver Linden, Manuel Zingl, Claudius Hubig, Olivier Parcollet, and Ulrich Schollwöck. *Phys. Rev. B* 101.4 (2020), p. 041101. ISSN: 2469-9950, 2469-9969. DOI: `10.1103/PhysRevB.101.041101` (cit. on pp. 13, 107, 110).

[139] Jonathan Karp, Max Bramberger, Martin Grundner, Ulrich Schollwöck, Andrew J. Millis, and Manuel Zingl. *Phys. Rev. Lett.* 125.16 (2020), p. 166401. ISSN: 0031-9007, 1079-7114. DOI: `10.1103/PhysRevLett.125.166401` (cit. on pp. 13, 107).

[140] Max Bramberger, Jernej Mravlje, Martin Grundner, Ulrich Schollwöck, and Manuel Zingl. *Phys. Rev. B* 103.16 (2021), p. 165133. ISSN: 2469-9950, 2469-9969. DOI: `10.1103/PhysRevB.103.165133` (cit. on pp. 13, 107, 110).

[141] F. Alexander Wolf, Ian P. McCulloch, and Ulrich Schollwöck. *Phys. Rev. B* 90.23 (2014), p. 235131. DOI: `10.1103/PhysRevB.90.235131` (cit. on pp. 13, 104, 107, 112, 126, 152).

[142] Martin Grundner, Max Bramberger, Paeckel Sebastian, Ulrich Schollw\"ock, and Sam Mardazad. *in preparation* (2022) (cit. on pp. 13, 104, 107, 112, 126, 152).

[143] Daniel Bauernfeind, Manuel Zingl, Robert Triebl, Markus Aichhorn, and Hans Gerd Evertz. *Phys. Rev. X* 7.3 (2017), p. 031013. DOI: `10.1103/PhysRevX.7.031013` (cit. on pp. 13, 104, 107, 112, 126, 152).

[144] Daniel Bauernfeind, Robert Triebl, Manuel Zingl, Markus Aichhorn, and Hans Gerd Evertz. *Phys. Rev. B* 97.11 (2018), p. 115156. DOI: `10.1103/PhysRevB.97.115156` (cit. on pp. 13, 104, 107, 112, 126, 152).

[145] David Sénéchal, P.-L. Lavertu, M.-A. Marois, and A.-M. S. Tremblay. *Phys. Rev. Lett.* 94.15 (2005), p. 156404. ISSN: 0031-9007, 1079-7114. DOI: `10.1103/PhysRevLett.94.156404` (cit. on pp. 13, 59, 108, 126).

[146] M. Capone and G. Kotliar. *Phys. Rev. B* 74.5 (2006), p. 054513. DOI: `10.1103/PhysRevB.74.054513` (cit. on pp. 13, 59, 126).

[147] S. S. Kancharla, B. Kyung, D. Sénéchal, M. Civelli, M. Capone, G. Kotliar, and A.-M. S. Tremblay. *Phys. Rev. B* 77.18 (2008), p. 184516. DOI: 10.1103/PhysRevB.77.184516 (cit. on pp. 13, 59, 126).

[148] A. Foley, S. Verret, A.-M. S. Tremblay, and D. Sénéchal. *Phys. Rev. B* 99.18 (2019), p. 184510. DOI: 10.1103/PhysRevB.99.184510 (cit. on pp. 13, 59, 126).

[149] J.-S. Lee, Y. W. Xie, H. K. Sato, C. Bell, Y. Hikita, H. Y. Hwang, and C.-C. Kao. *Nature Mater* 12.8 (2013), pp. 703–706. ISSN: 1476-4660. DOI: 10.1038/nmat3674 (cit. on pp. 14, 130, 148, 154).

[150] J. R. L. Mardegan, D. V. Christensen, Y. Z. Chen, S. Parchenko, S. R. V. Avula, N. Ortiz-Hernandez, M. Decker, C. Piamonteze, N. Pryds, and U. Staub. *Phys. Rev. B* 99.13 (2019), p. 134423. DOI: 10.1103/PhysRevB.99.134423 (cit. on pp. 14, 130).

[151] Vladimir I. Anisimov, Jan Zaanen, and Ole K. Andersen. *Phys. Rev. B* 44.3 (1991), pp. 943–954. DOI: 10.1103/PhysRevB.44.943 (cit. on pp. 14, 23–25, 131, 153).

[152] Vladimir I. Anisimov, F. Aryasetiawan, and A. I. Lichtenstein. *J. Phys.: Condens. Matter* 9.4 (1997), pp. 767–808. ISSN: 0953-8984. DOI: 10.1088/0953-8984/9/4/002 (cit. on pp. 14, 23, 24, 28, 30, 131, 153).

[153] A. I. Liechtenstein, V. I. Anisimov, and J. Zaanen. *Phys. Rev. B* 52.8 (1995), R5467–R5470. ISSN: 0163-1829, 1095-3795. DOI: 10.1103/PhysRevB.52.R5467 (cit. on pp. 14, 23–25, 131, 153).

[154] S. Cottenier. 2002-2013 (2nd edition). ISBN: 978-90-807215-1-7 (freely available at http://www.wien2k.at/reg user/textbooks) (cit. on p. 17).

[155] Walter Kohn (1999). DOI: https://www.nobelprize.org/uploads/2018/06/kohn-lecture.pdf (cit. on pp. 17, 18).

[156] Chris J. Pickard, Ion Errea, and Mikhail I. Eremets. *Annu. Rev. Condens. Matter Phys.* 11.1 (2020), pp. 57–76. ISSN: 1947-5454, 1947-5462. DOI: 10.1146/annurev-conmatphys-031218-013413 (cit. on p. 17).

[157] J. C. Slater. *Phys. Rev.* 34.10 (1929), pp. 1293–1322. DOI: 10.1103/PhysRev.34.1293 (cit. on p. 18).

[158] P. Hohenberg and W. Kohn. *Phys. Rev.* 136.3B (1964), B864–B871. DOI: 10.1103/PhysRev.136.B864 (cit. on pp. 18, 151).

[159] W. Kohn and L. J. Sham. *Phys. Rev.* 140.4A (1965), A1133–A1138. DOI: 10.1103/PhysRev.140.A1133 (cit. on pp. 19, 22, 151).

[160] Mel Levy. *Phys. Rev. A* 26.3 (1982), pp. 1200–1208. DOI: 10.1103/PhysRevA.26.1200 (cit. on p. 19).

[161] John P. Perdew, Robert G. Parr, Mel Levy, and Jose L. Balduz. *Phys. Rev. Lett.* 49.23 (1982), pp. 1691–1694. DOI: 10.1103/PhysRevLett.49.1691 (cit. on p. 21).

[162] Ulrike Salzner and Roi Baer. *J. Chem. Phys.* 131.23 (2009), p. 231101. ISSN: 0021-9606. DOI: 10.1063/1.3269030 (cit. on p. 21).

[163] John P. Perdew, Kieron Burke, and Matthias Ernzerhof. *Phys. Rev. Lett.* 77.18 (1996), pp. 3865–3868. ISSN: 0031-9007, 1079-7114. DOI: `10.1103/PhysRevLett.77.3865` (cit. on pp. 23, 131).

[164] John P. Perdew, Kieron Burke, and Matthias Ernzerhof. *Phys. Rev. Lett.* 78.7 (1997), pp. 1396–1396. ISSN: 0031-9007, 1079-7114. DOI: `10.1103/PhysRevLett.78.1396` (cit. on pp. 23, 131).

[165] Axel D. Becke. *The Journal of Chemical Physics* 98.2 (1993), pp. 1372–1377. ISSN: 0021-9606, 1089-7690. DOI: `10.1063/1.464304` (cit. on pp. 23, 117, 131).

[166] B. W. Lebert, M. P. M. Dean, A. Nicolaou, J. Pelliciari, M. Dantz, T. Schmitt, R. Yu, M. Azuma, J.-P. Castellan, H. Miao, A. Gauzzi, B. Baptiste, and M. d'Astuto. *Phys. Rev. B* 95.15 (2017), p. 155110. ISSN: 2469-9950, 2469-9969. DOI: `10.1103/PhysRevB.95.155110` (cit. on pp. 23, 63, 69, 71–73, 92, 93, 100).

[167] B.H. Brandow. *Advances in Physics* 26.5 (1977), pp. 651–808. ISSN: 0001-8732. DOI: `10.1080/00018737700101443` (cit. on p. 23).

[168] Baird Brandow. *Narrow-Band Phenomena—Influence of Electrons with Both Band and Localized Character*. Ed. by J. C. Fuggle, G. A. Sawatzky, and J. W. Allen. NATO ASI Series. Boston, MA: Springer US, 1988, pp. 97–109. ISBN: 978-1-4684-5559-5. DOI: `10.1007/978-1-4684-5559-5_16` (cit. on p. 23).

[169] Walter A. Harrison. *Phys. Rev. B* 29.6 (1984), pp. 2917–2925. DOI: `10.1103/PhysRevB.29.2917` (cit. on p. 23).

[170] A. Svane and O. Gunnarsson. *Phys. Rev. Lett.* 65.9 (1990), pp. 1148–1151. DOI: `10.1103/PhysRevLett.65.1148` (cit. on p. 23).

[171] Masatoshi Imada, Atsushi Fujimori, and Yoshinori Tokura. *Rev. Mod. Phys.* 70.4 (1998), pp. 1039–1263. DOI: `10.1103/RevModPhys.70.1039` (cit. on pp. 23, 26).

[172] F. Hund. *Z. Physik* 33.1 (1925), pp. 855–859. ISSN: 0044-3328. DOI: `10.1007/BF01328373` (cit. on p. 25).

[173] Dr Karlheinz Schwarz (), p. 295 (cit. on pp. 28, 106, 132).

[174] Peter Blaha, Karlheinz Schwarz, Fabien Tran, Robert Laskowski, Georg K. H. Madsen, and Laurence D. Marks. *J. Chem. Phys.* 152.7 (2020), p. 074101. ISSN: 0021-9606, 1089-7690. DOI: `10.1063/1.5143061` (cit. on pp. 28, 106, 132).

[175] S. Y. Savrasov, G. Kotliar, and E. Abrahams. *Nature* 410.6830 (2001), pp. 793–795. ISSN: 1476-4687. DOI: `10.1038/35071035` (cit. on p. 30).

[176] E. Pavarini, S. Biermann, A. Poteryaev, A. I. Lichtenstein, A. Georges, and O. K. Andersen. *Phys. Rev. Lett.* 92.17 (2004), p. 176403. DOI: `10.1103/PhysRevLett.92.176403` (cit. on p. 30).

[177] Wei Ku, H. Rosner, W. E. Pickett, and R. T. Scalettar. *Phys. Rev. Lett.* 89.16 (2002), p. 167204. DOI: `10.1103/PhysRevLett.89.167204` (cit. on p. 30).

[178] V. I. Anisimov, D. E. Kondakov, A. V. Kozhevnikov, I. A. Nekrasov, Z. V. Pchelkina, J. W. Allen, S.-K. Mo, H.-D. Kim, P. Metcalf, S. Suga, A. Sekiyama, G. Keller, I. Leonov, X. Ren, and D. Vollhardt. *Phys. Rev. B* 71.12 (2005), p. 125119. DOI: `10.1103/PhysRevB.71.125119` (cit. on p. 30).

[179] Markus Aichhorn, Leonid Pourovskii, Veronica Vildosola, Michel Ferrero, Olivier Parcollet, Takashi Miyake, Antoine Georges, and Silke Biermann. *Phys. Rev. B* 80.8 (2009), p. 085101. DOI: `10.1103/PhysRevB.80.085101` (cit. on p. 30).

[180] B. Amadon, F. Lechermann, A. Georges, F. Jollet, T. O. Wehling, and A. I. Lichtenstein. *Phys. Rev. B* 77.20 (2008), p. 205112. DOI: `10.1103/PhysRevB.77.205112` (cit. on p. 30).

[181] Nicola Marzari and David Vanderbilt. *Phys. Rev. B* 56.20 (1997), pp. 12847–12865. DOI: `10.1103/PhysRevB.56.12847` (cit. on pp. 30, 31, 72).

[182] Ivo Souza, Nicola Marzari, and David Vanderbilt. *Phys. Rev. B* 65.3 (2001), p. 035109. DOI: `10.1103/PhysRevB.65.035109` (cit. on pp. 30, 31, 72).

[183] Arash A. Mostofi, Jonathan R. Yates, Young-Su Lee, Ivo Souza, David Vanderbilt, and Nicola Marzari. *Computer Physics Communications* 178.9 (2008), pp. 685–699. ISSN: 0010-4655. DOI: `10.1016/j.cpc.2007.11.016` (cit. on pp. 30, 31, 72, 136).

[184] Arash A. Mostofi, Jonathan R. Yates, Giovanni Pizzi, Young-Su Lee, Ivo Souza, David Vanderbilt, and Nicola Marzari. *Computer Physics Communications* 185.8 (2014), pp. 2309–2310. ISSN: 0010-4655. DOI: `10.1016/j.cpc.2014.05.003` (cit. on pp. 30, 31, 72, 136).

[185] Eva Pavarini, Dieter Vollhardt, Erik Koch, and Alexander Lichtenstein. Tech. rep. PreJuSER-17645. Forschungszenrum Jülich GmbH Zentralbibliothek, Verlag, 2011 (cit. on p. 31).

[186] F. Aryasetiawan, M. Imada, A. Georges, G. Kotliar, S. Biermann, and A. I. Lichtenstein. *Phys. Rev. B* 70.19 (2004), p. 195104. DOI: `10.1103/PhysRevB.70.195104` (cit. on p. 31).

[187] F. Aryasetiawan, K. Karlsson, O. Jepsen, and U. Schönberger. *Phys. Rev. B* 74.12 (2006), p. 125106. DOI: `10.1103/PhysRevB.74.125106` (cit. on p. 31).

[188] O. Gunnarsson, O. K. Andersen, O. Jepsen, and J. Zaanen. *Phys. Rev. B* 39.3 (1989), pp. 1708–1722. DOI: `10.1103/PhysRevB.39.1708` (cit. on p. 31).

[189] M. R. Norman and A. J. Freeman. *Phys. Rev. B* 33.12 (1986), pp. 8896–8898. DOI: `10.1103/PhysRevB.33.8896` (cit. on p. 31).

[190] I. V. Solovyev and P. H. Dederichs. *Phys. Rev. B* 49.10 (1994), pp. 6736–6740. DOI: `10.1103/PhysRevB.49.6736` (cit. on p. 31).

[191] Elliott H. Lieb and F. Y. Wu. *Exactly Solvable Models of Strongly Correlated Electrons*. Vol. Volume 18. Advanced Series in Mathematical Physics. WORLD SCIENTIFIC, 1994, pp. 9–12. ISBN: 978-981-02-1534-7. DOI: `10.1142/9789812798268_0001` (cit. on p. 32).

[192] Pierre Weiss. *J. Phys. Theor. Appl.* 6.1 (1907), pp. 661–690. ISSN: 0368-3893, 2507-6485. DOI: `10.1051/jphystap:019070060066100` (cit. on p. 32).

[193] Fusayoshi J. Ohkawa. *J. Phys. Soc. Jpn.* 60.10 (1991), pp. 3218–3221. ISSN: 0031-9015. DOI: `10.1143/JPSJ.60.3218` (cit. on pp. 32, 36).

[194] J. E. Hirsch. *Phys. Rev. Lett.* 54.12 (1985), pp. 1317–1320. DOI: `10.1103/PhysRevLett.54.1317` (cit. on p. 36).

[195] M. Jarrell. *Phys. Rev. Lett.* 69.1 (1992), pp. 168–171. DOI: `10.1103/PhysRevLett.69.168` (cit. on p. 36).

[196] V. Janiš. *Z. Physik B - Condensed Matter* 83.2 (1991), pp. 227–235. ISSN: 1431-584X. DOI: `10.1007/BF01309423` (cit. on p. 36).

[197] V. Janiš and D. Vollhardt. *Int. J. Mod. Phys. B* 06.05n06 (1992), pp. 731–747. ISSN: 0217-9792. DOI: `10.1142/S0217979292000438` (cit. on p. 36).

[198] Gordon Baym and Leo P. Kadanoff. *Phys. Rev.* 124.2 (1961), pp. 287–299. DOI: `10.1103/PhysRev.124.287` (cit. on p. 36).

[199] G. Kotliar, S. Y. Savrasov, K. Haule, V. S. Oudovenko, O. Parcollet, and C. A. Marianetti. *Rev. Mod. Phys.* 78.3 (2006), pp. 865–951. DOI: `10.1103/RevModPhys.78.865` (cit. on p. 36).

[200] Michael Edward Peskin and Daniel V. Schroeder. The Advanced Book Program. Boca Raton London New York: CRC Press, Taylor & Francis Group, 2019. ISBN: 978-0-367-32056-0 978-0-201-50397-5 (cit. on p. 37).

[201] J. Hubbard and Brian Hilton Flowers. *Proceedings of the Royal Society of London. Series A. Mathematical and Physical Sciences* 281.1386 (1964), pp. 401–419. DOI: `10.1098/rspa.1964.0190` (cit. on pp. 40, 123).

[202] David Sénéchal. 2010. DOI: `10.48550/arXiv.0806.2690`. arXiv: `0806.2690 [cond-mat]` (cit. on pp. 42–44).

[203] S. Verret, J. Roy, A. Foley, M. Charlebois, D. Sénéchal, and A.-M. S. Tremblay. *Phys. Rev. B* 100.22 (2019), p. 224520. DOI: `10.1103/PhysRevB.100.224520` (cit. on pp. 42, 45).

[204] Tudor D. Stanescu and Gabriel Kotliar. *Phys. Rev. B* 74.12 (2006), p. 125110. DOI: `10.1103/PhysRevB.74.125110` (cit. on p. 45).

[205] Steffen Backes. PhD thesis. 2017 (cit. on p. 47).

[206] H. Terletska, J. Vučičević, D. Tanasković, and V. Dobrosavljević. *Phys. Rev. Lett.* 107.2 (2011), p. 026401. DOI: `10.1103/PhysRevLett.107.026401` (cit. on p. 48).

[207] R. de L. Kronig. *J. Opt. Soc. Am., JOSA* 12.6 (1926), pp. 547–557. DOI: `10.1364/JOSA.12.000547` (cit. on pp. 50, 51).

[208] H. A. Kramers. *Atti Cong. Intern. Fisica (Transactions of Volta Centenary Congress) Como* 2 (1927), pp. 545–557 (cit. on pp. 50, 51).

[209] H. J. Vidberg and J. W. Serene. *J Low Temp Phys* 29.3 (1977), pp. 179–192. ISSN: 1573-7357. DOI: `10.1007/BF00655090` (cit. on p. 52).

[210] O. Gunnarsson, M. W. Haverkort, and G. Sangiovanni. *Phys. Rev. B* 82.16 (2010), p. 165125. DOI: `10.1103/PhysRevB.82.165125` (cit. on p. 52).

[211] Anders W. Sandvik. *Phys. Rev. B* 57.17 (1998), pp. 10287–10290. DOI: `10.1103/PhysRevB.57.10287` (cit. on p. 52).

[212] Jiani Fei, Chia-Nan Yeh, and Emanuel Gull. *Phys. Rev. Lett.* 126.5 (2021), p. 056402. DOI: `10.1103/PhysRevLett.126.056402` (cit. on p. 52).

[213] R. N. Silver, D. S. Sivia, and J. E. Gubernatis. *Phys. Rev. B* 41.4 (1990), pp. 2380–2389. DOI: `10.1103/PhysRevB.41.2380` (cit. on pp. 52–54).

[214] Mark Jarrell and J. E. Gubernatis. *Physics Reports* 269.3 (1996), pp. 133–195. ISSN: 0370-1573. DOI: `10.1016/0370-1573(95)00074-7` (cit. on pp. 52–54).

[215] Gernot J. Kraberger, Robert Triebl, Manuel Zingl, and Markus Aichhorn. *Phys. Rev. B* 96.15 (2017), p. 155128. DOI: `10.1103/PhysRevB.96.155128` (cit. on pp. 52, 55, 56, 112, 119).

[216] Gernot J. Kraberger and Manuel Zingl (2018). DOI: `https://github.com/TRIQS/maxent` (cit. on pp. 52, 55, 56, 112, 119).

[217] Jae-Hoon Sim and Myung Joon Han. *Phys. Rev. B* 98.20 (2018), p. 205102. DOI: `10.1103/PhysRevB.98.205102` (cit. on pp. 52, 57, 58, 73, 75).

[218] R. K. Bryan. *Eur Biophys J* 18.3 (1990), pp. 165–174. ISSN: 1432-1017. DOI: `10.1007/BF02427376` (cit. on p. 54).

[219] Dominic Bergeron and A.-M. S. Tremblay. *Phys. Rev. E* 94.2 (2016), p. 023303. DOI: `10.1103/PhysRevE.94.023303` (cit. on p. 54).

[220] Ryan Levy, J. P. F. LeBlanc, and Emanuel Gull. *Computer Physics Communications* 215 (2017), pp. 149–155. ISSN: 0010-4655. DOI: `10.1016/j.cpc.2017.01.018` (cit. on pp. 54, 74, 93).

[221] Jan Martin Tomczak. PhD thesis. Ecole Polytechnique X, 2007 (cit. on p. 55).

[222] Oscar Nájera Ocampo. These de Doctorat. Université Paris-Saclay (ComUE), 2017 (cit. on pp. 56, 57).

[223] Nicolas Kowalski, Sidhartha Shankar Dash, Patrick Sémon, David Sénéchal, and André-Marie Tremblay. *Proc. Natl. Acad. Sci. U.S.A.* 118.40 (2021), e2106476118. ISSN: 0027-8424, 1091-6490. DOI: `10.1073/pnas.2106476118` (cit. on pp. 59, 104).

[224] LN Bulaevski, EL Nagaev, and DI Khomskiĭ. *Sov. Phys. JETP* 27 (1968), p. 836 (cit. on p. 59).

[225] V. J. Emery. *Phys. Rev. B* 14.7 (1976), pp. 2989–2994. DOI: `10.1103/PhysRevB.14.2989` (cit. on p. 59).

[226] C. Gros, R. Joynt, and T. M. Rice. *Phys. Rev. B* 36.1 (1987), pp. 381–393. DOI: `10.1103/PhysRevB.36.381` (cit. on p. 59).

[227] F. Grusdt, M. Kánasz-Nagy, A. Bohrdt, C. S. Chiu, G. Ji, M. Greiner, D. Greif, and E. Demler. *Phys. Rev. X* 8.1 (2018), p. 011046. ISSN: 2160-3308. DOI: `10.1103/PhysRevX.8.011046` (cit. on pp. 59, 60).

[228] Fabian Grusdt, Annabelle Bohrdt, and Eugene Demler. *Phys. Rev. B* 99.22 (2019), p. 224422. ISSN: 2469-9950, 2469-9969. DOI: `10.1103/PhysRevB.99.224422` (cit. on pp. 59, 60).

[229] Annabelle Bohrdt, Eugene Demler, Frank Pollmann, Michael Knap, and Fabian Grusdt. *arXiv:2001.05509 [cond-mat, physics:quant-ph]* (2020). arXiv: `2001.05509 [cond-mat, physics:quant-ph]` (cit. on pp. 59, 60).

[230] Gerald D. Mahan. Springer Science & Business Media, 2013. ISBN: 978-1-4757-5714-9 (cit. on p. 59).

[231] J. Appel. Academic Press, 1968. ISBN: 978-0-08-086485-3 (cit. on p. 59).

[232] S. Schmitt-Rink, C. M. Varma, and A. E. Ruckenstein. *Phys. Rev. Lett.* 60.26 (1988), pp. 2793–2796. DOI: `10.1103/PhysRevLett.60.2793` (cit. on pp. 59, 61).

[233] C. L. Kane, P. A. Lee, and N. Read. *Phys. Rev. B* 39.10 (1989), pp. 6880–6897. DOI: `10.1103/PhysRevB.39.6880` (cit. on pp. 59, 61).

[234] T. Holstein and H. Primakoff. *Phys. Rev.* 58.12 (1940), pp. 1098–1113. DOI: `10.1103/PhysRev.58.1098` (cit. on p. 60).

[235] J.-Y. P. Delannoy, M. J. P. Gingras, P. C. W. Holdsworth, and A.-M. S. Tremblay. *Phys. Rev. B* 79.23 (2009), p. 235130. ISSN: 1098-0121, 1550-235X. DOI: `10.1103/PhysRevB.79.235130` (cit. on pp. 63, 73, 98).

[236] R. Coldea, S. M. Hayden, G. Aeppli, T. G. Perring, C. D. Frost, T. E. Mason, S.-W. Cheong, and Z. Fisk. *Phys. Rev. Lett.* 86.23 (2001), pp. 5377–5380. ISSN: 0031-9007, 1079-7114. DOI: `10.1103/PhysRevLett.86.5377` (cit. on pp. 63, 73).

[237] I. Yamada, A. A. Belik, M. Azuma, S. Harjo, T. Kamiyama, Y. Shimakawa, and M. Takano. *Phys. Rev. B* 72.22 (2005), p. 224503. ISSN: 1098-0121, 1550-235X. DOI: `10.1103/PhysRevB.72.224503` (cit. on p. 67).

[238] T. Tatsuki, S. Adachi, M. Itoh, T. Tamura, X. -J. Wu, C. -Q. Jin, N. Koshizuka, and K. Tanabe. *Physica C: Superconductivity* 255.1 (1995), pp. 61–64. ISSN: 0921-4534. DOI: `10.1016/0921-4534(95)00587-0` (cit. on p. 67).

[239] Yuji Zenitani, Teruhiko Suzuki, Hirokazu Kawashima, and Jun Akimitsu. *Physica C: Superconductivity* 419.1 (2005), pp. 32–40. ISSN: 0921-4534. DOI: `10.1016/j.physc.2004.12.002` (cit. on p. 67).

[240] T. Hanaguri, Y. Kohsaka, J. C. Davis, C. Lupien, I. Yamada, M. Azuma, M. Takano, K. Ohishi, M. Ono, and H. Takagi. *Nature Phys* 3.12 (2007), pp. 865–871. ISSN: 1745-2473, 1745-2481. DOI: `10.1038/nphys753` (cit. on p. 67).

[241] Şerban Smadici, Peter Abbamonte, Munetaka Taguchi, Yuhki Kohsaka, Takao Sasagawa, Masaki Azuma, Mikio Takano, and Hidenori Takagi. *Phys. Rev. B* 75.7 (2007), p. 075104. ISSN: 1098-0121, 1550-235X. DOI: `10.1103/PhysRevB.75.075104` (cit. on p. 67).

[242] L. Chaix, B. Lebert, H. Miao, A. Nicolaou, F. Yakhou, H. Cercellier, S. Grenier, N. B. Brookes, A. Sulpice, S. Tsutsui, A. Bosak, L. Paolasini, D. Santos-Cottin, H. Yamamoto, I. Yamada, M. Azuma, T. Nishikubo, T. Yamamoto, M. Katsumata, M. P. M. Dean, and M. d'Astuto. *Phys. Rev. Research* 4.3 (2022), p. 033004. DOI: `10.1103/PhysRevResearch.4.033004` (cit. on p. 67).

[243] A. G. Loeser, Z.-X. Shen, D. S. Dessau, D. S. Marshall, C. H. Park, P. Fournier, and A. Kapitulnik. *Science* 273.5273 (1996), pp. 325–329. DOI: `10.1126/science.273.5273.325` (cit. on p. 68).

[244] H. Ding, T. Yokoya, J. C. Campuzano, T. Takahashi, M. Randeria, M. R. Norman, T. Mochiku, K. Kadowaki, and J. Giapintzakis. *Nature* 382.6586 (1996), pp. 51–54. ISSN: 1476-4687. DOI: `10.1038/382051a0` (cit. on p. 68).

[245] M. R. Norman, H. Ding, M. Randeria, J. C. Campuzano, T. Yokoya, T. Takeuchi, T. Takahashi, T. Mochiku, K. Kadowaki, P. Guptasarma, and D. G. Hinks. *Nature* 392.6672 (1998), pp. 157–160. ISSN: 1476-4687. DOI: `10.1038/32366` (cit. on p. 68).

[246] Wei Wu, Mathias S. Scheurer, Shubhayu Chatterjee, Subir Sachdev, Antoine Georges, and Michel Ferrero. *Phys. Rev. X* 8.2 (2018), p. 021048. DOI: `10.1103/PhysRevX.8.021048` (cit. on pp. 68, 72, 82, 84, 100, 151).

[247] Kristjan Haule and Gabriel Kotliar. *Phys. Rev. B* 76.10 (2007), p. 104509. DOI: `10.1103/PhysRevB.76.104509` (cit. on pp. 69, 73, 85, 88).

[248] W. S. Lee, J. J. Lee, E. A. Nowadnick, S. Gerber, W. Tabis, S. W. Huang, V. N. Strocov, E. M. Motoyama, G. Yu, B. Moritz, H. Y. Huang, R. P. Wang, Y. B. Huang, W. B. Wu, C. T. Chen, D. J. Huang, M. Greven, T. Schmitt, Z. X. Shen, and T. P. Devereaux. *Nature Phys* 10.11 (2014), pp. 883–889. ISSN: 1745-2481. DOI: `10.1038/nphys3117` (cit. on pp. 71, 92, 94, 100, 101).

[249] L. Chaix, E. W. Huang, S. Gerber, X. Lu, C. Jia, Y. Huang, D. E. McNally, Y. Wang, F. H. Vernay, A. Keren, M. Shi, B. Moritz, Z.-X. Shen, T. Schmitt, T. P. Devereaux, and W.-S. Lee. *Phys. Rev. B* 97.15 (2018), p. 155144. DOI: `10.1103/PhysRevB.97.155144` (cit. on pp. 71, 92, 94, 100, 101).

[250] Davide Betto, Roberto Fumagalli, Leonardo Martinelli, Matteo Rossi, Riccardo Piombo, Kazuyoshi Yoshimi, Daniele Di Castro, Emiliano Di Gennaro, Alessia Sambri, Doug Bonn, George A. Sawatzky, Lucio Braicovich, Nicholas B. Brookes, José Lorenzana, and Giacomo Ghiringhelli. *Phys. Rev. B* 103.14 (2021), p. L140409. DOI: `10.1103/PhysRevB.103.L140409` (cit. on pp. 71, 92, 94, 100, 101).

[251] K. Waku, T. Katsufuji, Y. Kohsaka, T. Sasagawa, H. Takagi, H. Kishida, H. Okamoto, M. Azuma, and M. Takano. *Phys. Rev. B* 70.13 (2004), p. 134501. DOI: `10.1103/PhysRevB.70.134501` (cit. on pp. 71, 72).

[252] G. Kresse and J. Hafner. *Phys. Rev. B* 47.1 (1993), pp. 558–561. ISSN: 0163-1829, 1095-3795. DOI: `10.1103/PhysRevB.47.558` (cit. on pp. 71, 131).

[253] G. Kresse and J. Hafner. *Phys. Rev. B* 49.20 (1994), pp. 14251–14269. ISSN: 0163-1829, 1095-3795. DOI: `10.1103/PhysRevB.49.14251` (cit. on pp. 71, 131).

[254] G. Kresse and J. Furthmüller. *Computational Materials Science* 6.1 (1996), pp. 15–50. ISSN: 09270256. DOI: `10.1016/0927-0256(96)00008-0` (cit. on pp. 71, 131).

[255] G. Kresse and J. Furthmüller. *Phys. Rev. B* 54.16 (1996), pp. 11169–11186. ISSN: 0163-1829, 1095-3795. DOI: `10.1103/PhysRevB.54.11169` (cit. on pp. 71, 131).

[256] Wei Wu, Mathias S. Scheurer, Michel Ferrero, and Antoine Georges. *Phys. Rev. Research* 2.3 (2020), p. 033067. DOI: `10.1103/PhysRevResearch.2.033067` (cit. on p. 72).

[257] Conrad Stansbury and Alessandra Lanzara. *SoftwareX* 11 (2020), p. 100472. ISSN: 2352-7110. DOI: `10.1016/j.softx.2020.100472` (cit. on pp. 75, 162).

[258] Simon Moser. *Journal of Electron Spectroscopy and Related Phenomena* 214 (2017), pp. 29–52. ISSN: 03682048. DOI: `10.1016/j.elspec.2016.11.007` (cit. on pp. 75, 114, 157–161).

[259] Eva Pavarini, Erik Koch, Richard Scalettar, Richard Martin, Institute for Advanced Simulation, and German Research School for Simulation Sciences, eds. Schriften Des Forschungszentrums Jülich. Reihe Modeling and Simulation Band 7. Jülich: Forschungszentrum, Zentralbibliothek, 2017. ISBN: 978-3-95806-224-5 (cit. on p. 77).

[260] B. J. Kim, H. Koh, E. Rotenberg, S.-J. Oh, H. Eisaki, N. Motoyama, S. Uchida, T. Tohyama, S. Maekawa, Z.-X. Shen, and C. Kim. *Nature Phys* 2.6 (2006), pp. 397–401. ISSN: 1745-2481. DOI: `10.1038/nphys316` (cit. on p. 78).

[261] G. Sordi, P. Sémon, K. Haule, and A.-M. S. Tremblay. *Sci Rep* 2.1 (2012), p. 547. ISSN: 2045-2322. DOI: `10.1038/srep00547` (cit. on p. 82).

[262] Alice Moutenet, Antoine Georges, and Michel Ferrero. *Phys. Rev. B* 97.15 (2018), p. 155109. DOI: `10.1103/PhysRevB.97.155109` (cit. on p. 85).

[263] P. W. Anderson, G. Baskaran, Z. Zou, and T. Hsu. *Phys. Rev. Lett.* 58.26 (1987), pp. 2790–2793. DOI: `10.1103/PhysRevLett.58.2790` (cit. on pp. 85, 151).

[264] Chunjing Jia, Krzysztof Wohlfeld, Yao Wang, Brian Moritz, and Thomas P. Devereaux. *Phys. Rev. X* 6.2 (2016), p. 021020. DOI: `10.1103/PhysRevX.6.021020` (cit. on p. 92).

[265] Phillip Weinberg and Marin Bukov. *SciPost Physics* 2.1 (2017), p. 003. ISSN: 2542-4653. DOI: `10.21468/SciPostPhys.2.1.003` (cit. on p. 98).

[266] Phillip Weinberg and Marin Bukov. *SciPost Physics* 7.2 (2019), p. 020. ISSN: 2542-4653. DOI: `10.21468/SciPostPhys.7.2.020` (cit. on p. 98).

[267] Max Bramberger, Benjamin Bacq-Labreuil, Martin Grundner, Silke Biermann, Ulrich Schollwöck, Sebastian Paeckel, and Benjamin Lenz. *arXiv:2203.07880 [cond-mat]* (2022). arXiv: `2203.07880 [cond-mat]` (cit. on pp. 103, 105, 109, 113, 115, 116, 118, 125, 129, 142, 154).

[268] H. Eskes, L. H. Tjeng, and G. A. Sawatzky. *Phys. Rev. B* 41.1 (1990), pp. 288–299. ISSN: 0163-1829, 1095-3795. DOI: `10.1103/PhysRevB.41.288` (cit. on p. 103).

[269] S. Åsbrink and L.-J. Norrby. *Acta Cryst B* 26.1 (1970), pp. 8–15. ISSN: 0567-7408. DOI: `10.1107/S0567740870001838` (cit. on p. 103).

[270] Lichen Wang, Guanhong He, Zichen Yang, Mirian Garcia-Fernandez, Abhishek Nag, Ke-Jin Zhou, Matteo Minola, Matthieu Le Tacon, Bernhard Keimer, Yingying Peng, and Yuan Li. 2020. DOI: `10.48550/arXiv.2011.05029`. arXiv: `2011.05029 [cond-mat]` (cit. on p. 104).

[271] Giorgio Levy, Maayan Yaari, Tom Z. Regier, and Amit Keren. 2021. DOI: `10.48550/arXiv.2107.09181`. arXiv: `2107.09181 [cond-mat]` (cit. on p. 104).

[272] S. M. O'Mahony, Wangping Ren, Weijiong Chen, Yi Xue Chong, Xiaolong Liu, H. Eisaki, S. Uchida, M. H. Hamidian, and J. C. Seamus Davis. 2022. DOI: `10.48550/arXiv.2108.03655`. arXiv: `2108.03655 [cond-mat]` (cit. on p. 104).

[273] Clemens P. J. Adolphs, Simon Moser, George A. Sawatzky, and Mona Berciu. *Phys. Rev. Lett.* 116.8 (2016), p. 087002. DOI: `10.1103/PhysRevLett.116.087002` (cit. on p. 104).

[274] I. J. Hamad, L. O. Manuel, and A. A. Aligia. *Phys. Rev. Lett.* 120.17 (2018), p. 177001. ISSN: 0031-9007, 1079-7114. DOI: `10.1103/PhysRevLett.120.177001` (cit. on pp. 104, 114).

[275] C. Dahnken, M. Aichhorn, W. Hanke, E. Arrigoni, and M. Potthoff. *Phys. Rev. B* 70.24 (2004), p. 245110. ISSN: 1098-0121, 1550-235X. DOI: `10.1103/PhysRevB.70.245110` (cit. on p. 108).

[276] M. Aichhorn, E. Arrigoni, M. Potthoff, and W. Hanke. *Phys. Rev. B* 74.2 (2006), p. 024508. ISSN: 1098-0121, 1550-235X. DOI: `10.1103/PhysRevB.74.024508` (cit. on p. 108).

[277] Matthias Balzer and Michael Potthoff. *Phys. Rev. B* 82.17 (2010), p. 174441. ISSN: 1098-0121, 1550-235X. DOI: `10.1103/PhysRevB.82.174441` (cit. on p. 108).

[278] Roland W Freund. Bai, Zhaojun and Demmel, James and Dongarra, Jack and Ruhe, Axel and van der Vorst, Henk. SIAM, 2000 (cit. on p. 108).

[279] David Sénéchal. *Strongly Correlated Systems*. Ed. by Adolfo Avella and Ferdinando Mancini. Vol. 171. Berlin, Heidelberg: Springer Berlin Heidelberg, 2012, pp. 341–371. ISBN: 978-3-642-21830-9 978-3-642-21831-6. DOI: `10.1007/978-3-642-21831-6_11` (cit. on p. 108).

[280] M. Charlebois, D. Sénéchal, A.-M. Gagnon, and A.-M. S. Tremblay. *Phys. Rev. B* 91.3 (2015), p. 035132. DOI: `10.1103/PhysRevB.91.035132` (cit. on p. 112).

[281] B. Pahlevanzadeh, P. Sahebsara, and David Sénéchal. *SciPost Physics* 11.1 (2021), p. 017. ISSN: 2542-4653. DOI: `10.21468/SciPostPhys.11.1.017` (cit. on p. 112).

[282] N. Nücker, H. Romberg, X. X. Xi, J. Fink, B. Gegenheimer, and Z. X. Zhao. *Phys. Rev. B* 39.10 (1989), pp. 6619–6629. ISSN: 0163-1829. DOI: `10.1103/PhysRevB.39.6619` (cit. on p. 114).

[283] M. Takigawa, P. C. Hammel, R. H. Heffner, Z. Fisk, K. C. Ott, and J. D. Thompson. *Phys. Rev. Lett.* 63.17 (1989), pp. 1865–1868. ISSN: 0031-9007. DOI: `10.1103/PhysRevLett.63.1865` (cit. on p. 114).

[284] M. Oda, C. Manabe, and M. Ido. *Phys. Rev. B* 53.5 (1996), pp. 2253–2256. ISSN: 0163-1829, 1095-3795. DOI: `10.1103/PhysRevB.53.2253` (cit. on p. 114).

[285] B Lenz, C Martins, and S Biermann. *J. Phys.: Condens. Matter* 31.29 (2019), p. 293001. ISSN: 0953-8984, 1361-648X. DOI: `10.1088/1361-648X/ab146a` (cit. on pp. 116, 139).

[286] Alessio Filippetti and Nicola A. Spaldin. *Phys. Rev. B* 67.12 (2003), p. 125109. DOI: `10.1103/PhysRevB.67.125109` (cit. on p. 117).

[287] Aliaksandr V. Krukau, Oleg A. Vydrov, Artur F. Izmaylov, and Gustavo E. Scuseria. *J. Chem. Phys.* 125.22 (2006), p. 224106. ISSN: 0021-9606. DOI: `10.1063/1.2404663` (cit. on p. 117).

[288] J. H. Van Vleck. *J. Chem. Phys.* 9.1 (1941), pp. 85–90. ISSN: 0021-9606. DOI: 10.1063/1.1750830 (cit. on p. 117).

[289] Nathascia Lampis, Cesare Franchini, Guido Satta, Alessandra Geddo-Lehmann, and Sandro Massidda. *Phys. Rev. B* 69.6 (2004), p. 064412. DOI: 10.1103/PhysRevB.69.064412 (cit. on p. 117).

[290] N. D. Mermin and H. Wagner. *Phys. Rev. Lett.* 17.22 (1966), pp. 1133–1136. DOI: 10.1103/PhysRevLett.17.1133 (cit. on p. 119).

[291] E. A. Stepanov, S. Brener, F. Krien, M. Harland, A. I. Lichtenstein, and M. I. Katsnelson. *Phys. Rev. Lett.* 121.3 (2018), p. 037204. ISSN: 0031-9007, 1079-7114. DOI: 10.1103/PhysRevLett.121.037204 (cit. on pp. 119, 121).

[292] M. Potthoff, T. Wegner, and W. Nolting. *Phys. Rev. B* 55.24 (1997), pp. 16132–16142. DOI: 10.1103/PhysRevB.55.16132 (cit. on p. 119).

[293] Andrea Paradisi, Johan Biscaras, and Abhay Shukla. *Appl. Phys. Lett.* 107.14 (2015), p. 143103. ISSN: 0003-6951, 1077-3118. DOI: 10.1063/1.4932572 (cit. on p. 127).

[294] Edoardo Sterpetti, Johan Biscaras, Andreas Erb, and Abhay Shukla. *Nat Commun* 8.1 (2017), p. 2060. ISSN: 2041-1723. DOI: 10.1038/s41467-017-02104-z (cit. on p. 127).

[295] Yong Zhong, Yang Wang, Sha Han, Yan-Feng Lv, Wen-Lin Wang, Ding Zhang, Hao Ding, Yi-Min Zhang, Lili Wang, Ke He, Ruidan Zhong, John A. Schneeloch, Gen-Da Gu, Can-Li Song, Xu-Cun Ma, and Qi-Kun Xue. *Science Bulletin* 61.16 (2016), pp. 1239–1247. ISSN: 20959273. DOI: 10.1007/s11434-016-1145-4 (cit. on p. 127).

[296] Y. Wang, K. Wohlfeld, B. Moritz, C. J. Jia, M. van Veenendaal, K. Wu, C.-C. Chen, and T. P. Devereaux. *Phys. Rev. B* 97.19 (2018), p. 199903. ISSN: 2469-9950, 2469-9969. DOI: 10.1103/PhysRevB.97.199903 (cit. on p. 127).

[297] H. Y. Hwang, Y. Iwasa, M. Kawasaki, B. Keimer, N. Nagaosa, and Y. Tokura. *Nature Mater* 11.2 (2012), pp. 103–113. ISSN: 1476-4660. DOI: 10.1038/nmat3223 (cit. on p. 129).

[298] Divine P. Kumah, Joseph H. Ngai, and Lior Kornblum. *Advanced Functional Materials* 30.18 (2020), p. 1901597. ISSN: 1616-3028. DOI: 10.1002/adfm.201901597 (cit. on p. 129).

[299] M. Salluzzo, S. Gariglio, D. Stornaiuolo, V. Sessi, S. Rusponi, C. Piamonteze, G. M. De Luca, M. Minola, D. Marré, A. Gadaleta, H. Brune, F. Nolting, N. B. Brookes, and G. Ghiringhelli. *Phys. Rev. Lett.* 111.8 (2013), p. 087204. ISSN: 0031-9007, 1079-7114. DOI: 10.1103/PhysRevLett.111.087204 (cit. on p. 130).

[300] Y. Hotta, T. Susaki, and H. Y. Hwang. *Phys. Rev. Lett.* 99.23 (2007), p. 236805. DOI: 10.1103/PhysRevLett.99.236805 (cit. on p. 130).

[301] Y. Z. Chen, N. Bovet, F. Trier, D. V. Christensen, F. M. Qu, N. H. Andersen, T. Kasama, W. Zhang, R. Giraud, J. Dufouleur, T. S. Jespersen, J. R. Sun, A. Smith, J. Nygård, L. Lu, B. Büchner, B. G. Shen, S. Linderoth, and N. Pryds. *Nat Commun* 4.1 (2013), p. 1371. ISSN: 2041-1723. DOI: 10.1038/ncomms2394 (cit. on p. 130).

[302] P. Schütz, D. V. Christensen, V. Borisov, F. Pfaff, P. Scheiderer, L. Dudy, M. Zapf, J. Gabel, Y. Z. Chen, N. Pryds, V. A. Rogalev, V. N. Strocov, C. Schlueter, T.-L. Lee, H. O. Jeschke, R. Valentí, M. Sing, and R. Claessen. *Phys. Rev. B* 96.16 (2017), p. 161409. DOI: `10.1103/PhysRevB.96.161409` (cit. on p. 130).

[303] D. V. Christensen, Y. Frenkel, P. Schütz, F. Trier, S. Wissberg, R. Claessen, B. Kalisky, A. Smith, Y. Z. Chen, and N. Pryds. *Phys. Rev. Applied* 9.5 (2018), p. 054004. DOI: `10.1103/PhysRevApplied.9.054004` (cit. on p. 130).

[304] T. C. Rödel, J. Dai, F. Fortuna, E. Frantzeskakis, P. Le Fèvre, F. Bertran, M. Kobayashi, R. Yukawa, T. Mitsuhashi, M. Kitamura, K. Horiba, H. Kumigashira, and A. F. Santander-Syro. *Phys. Rev. Materials* 2.5 (2018), p. 051601. DOI: `10.1103/PhysRevMaterials.2.051601` (cit. on p. 130).

[305] A. F. Santander-Syro, O. Copie, T. Kondo, F. Fortuna, S. Pailhès, R. Weht, X. G. Qiu, F. Bertran, A. Nicolaou, A. Taleb-Ibrahimi, P. Le Fèvre, G. Herranz, M. Bibes, N. Reyren, Y. Apertet, P. Lecoeur, A. Barthélémy, and M. J. Rozenberg. *Nature* 469.7329 (2011), pp. 189–193. ISSN: 1476-4687. DOI: `10.1038/nature09720` (cit. on pp. 130, 160).

[306] J. Mannhart, D.H.A. Blank, H.Y. Hwang, A.J. Millis, and J.-M. Triscone. *MRS Bull.* 33.11 (2008), pp. 1027–1034. ISSN: 0883-7694, 1938-1425. DOI: `10.1557/mrs2008.222` (cit. on pp. 130, 148, 154).

[307] F. Gunkel, D. V. Christensen, Y. Z. Chen, and N. Pryds. *Appl. Phys. Lett.* 116.12 (2020), p. 120505. ISSN: 0003-6951. DOI: `10.1063/1.5143309` (cit. on p. 130).

[308] Michael Sing, Harald O. Jeschke, Frank Lechermann, Roser Valentí, and Ralph Claessen. *Eur. Phys. J. Spec. Top.* 226.11 (2017), pp. 2457–2475. ISSN: 1951-6401. DOI: `10.1140/epjst/e2017-70059-7` (cit. on p. 130).

[309] Roman Wahl, Doris Vogtenhuber, and Georg Kresse. *Phys. Rev. B* 78.10 (2008), p. 104116. DOI: `10.1103/PhysRevB.78.104116` (cit. on p. 131).

[310] Lixin Cao, E. Sozontov, and J. Zegenhagen. *physica status solidi (a)* 181.2 (2000), pp. 387–404. ISSN: 1521-396X. DOI: `10.1002/1521-396X(200010)181:2<387::AID-PSSA387>3.0.CO;2-5` (cit. on p. 131).

[311] G. Kresse and D. Joubert. *Phys. Rev. B* 59.3 (1999), pp. 1758–1775. DOI: `10.1103/PhysRevB.59.1758` (cit. on p. 131).

[312] J. Padilla and David Vanderbilt. *Phys. Rev. B* 56.3 (1997), pp. 1625–1631. DOI: `10.1103/PhysRevB.56.1625` (cit. on p. 133).

[313] J. Padilla and David Vanderbilt. *Surface Science* 418.1 (1998), pp. 64–70. ISSN: 0039-6028. DOI: `10.1016/S0039-6028(98)00670-0` (cit. on p. 133).

[314] P. Audehm, M. Schmidt, S. Brück, T. Tietze, J. Gräfe, S. Macke, G. Schütz, and E. Goering. *Sci Rep* 6.1 (2016), p. 25517. ISSN: 2045-2322. DOI: `10.1038/srep25517` (cit. on p. 136).

[315] K. van Benthem, C. Elsässer, and R. H. French. *Journal of Applied Physics* 90.12 (2001), pp. 6156–6164. ISSN: 0021-8979. DOI: `10.1063/1.1415766` (cit. on p. 145).

[316] R. M. Feenstra, Y. Dong, M. P. Semtsiv, and W. T. Masselink. *Nanotechnology* 18.4 (2006), p. 044015. ISSN: 0957-4484. DOI: `10.1088/0957-4484/18/4/044015` (cit. on p. 145).

[317] S. Backes, T. C. Rödel, F. Fortuna, E. Frantzeskakis, P. Le Fèvre, F. Bertran, M. Kobayashi, R. Yukawa, T. Mitsuhashi, M. Kitamura, K. Horiba, H. Kumigashira, R. Saint-Martin, A. Fouchet, B. Berini, Y. Dumont, A. J. Kim, F. Lechermann, H. O. Jeschke, M. J. Rozenberg, R. Valentí, and A. F. Santander-Syro. *Phys. Rev. B* 94.24 (2016), p. 241110. ISSN: 2469-9950, 2469-9969. DOI: `10.1103/PhysRevB.94.241110` (cit. on pp. 145, 147).

[318] J. Stöhr and H. C. Siegmann. Springer. Springer Series in Solid-State Sciences. 2006 (cit. on p. 147).

[319] A. Ohtomo and H. Y. Hwang. *Nature* 427.6973 (2004), pp. 423–426. ISSN: 1476-4687. DOI: `10.1038/nature02308` (cit. on p. 154).

[320] Y. M. Vilk, Liang Chen, and A.-M. S. Tremblay. *Phys. Rev. B* 49.18 (1994), pp. 13267–13270. DOI: `10.1103/PhysRevB.49.13267` (cit. on p. 154).

[321] Y. M. Vilk and A.-M. S. Tremblay. *J. Phys. I France* 7.11 (1997), pp. 1309–1368. ISSN: 1155-4304, 1286-4862. DOI: `10.1051/jp1:1997135` (cit. on p. 154).

[322] Alexey N. Rubtsov. *Phys. Rev. E* 97.5 (2018), p. 052120. DOI: `10.1103/PhysRevE.97.052120` (cit. on p. 154).

[323] Alexey N. Rubtsov, Evgeny A. Stepanov, and Alexander I. Lichtenstein. *Phys. Rev. B* 102.22 (2020), p. 224423. DOI: `10.1103/PhysRevB.102.224423` (cit. on p. 154).

[324] H. Hertz. *Annalen der Physik* 267.8 (1887), pp. 983–1000. ISSN: 1521-3889. DOI: `10.1002/andp.18872670827` (cit. on p. 157).

[325] Wilhelm Hallwachs. *Annalen der Physik* 269.2 (1888), pp. 301–312. ISSN: 1521-3889. DOI: `10.1002/andp.18882690206` (cit. on p. 157).

[326] P. Lenard. *Annalen der Physik* 307.6 (1900), pp. 359–375. ISSN: 1521-3889. DOI: `10.1002/andp.19003070611` (cit. on p. 157).

[327] A. Einstein. *Annalen der Physik* 322.6 (1905), pp. 132–148. ISSN: 1521-3889. DOI: `10.1002/andp.19053220607` (cit. on p. 157).

[328] C. Nordling, E. Sokolowski, and K. Siegbahn. *Physical Review* 105.5 (1957), pp. 1676–1677. ISSN: 0031-899X. DOI: `10.1103/PhysRev.105.1676` (cit. on p. 157).

[329] G. D. Mahan. *Phys. Rev. B* 2.11 (1970), pp. 4334–4350. DOI: `10.1103/PhysRevB.2.4334` (cit. on p. 158).

DOCTORAL SCHOOL

Titre : Propriétés spectrales et magnétiques des oxydes de cuivre : vers une description théorique par les premiers principes

Mots clés : Cuprates, Système à électrons fortement corrélés, Théorie du Champ Moyen Dynamique, Théorie de la fonctionnelle de la densité, Spectroscopie par photoémission résolue en angle

Résumé : Si l'oxydation du cuivre peut être une malédiction pour les anciennes casseroles, c'est bénédiction pour le monde scientifique puisqu'elle est à l'origine de la famille des cuprates. Un champ entier de recherche s'est lancé pour comprendre pourquoi leur température critique supraconductrice est si élevée, découvrant au passage un diagramme de phase riche et complexe. Cependant, malgré les immenses efforts déployés par la communauté scientifique, un compréhension théorique globale fait toujours défaut. Dans cette thèse nous nous intéressons aux propriétés spectrales et magnétiques de deux oxydes de cuivres : $Ca_{2-x}Na_xCuO_2Cl_2$ (NaCCOC) et CuO tétragonal (t-CuO), en combinant la théorie fonctionelle de la densité, la théorie du champ moyen dynamique appliquée aux amas (CDMFT), et la spectroscopie par photoémission résolue en angle.

Nous montrons d'abord le rôle essentiel des fluctuations antiferromagnétiques de spin dans les propriétés spectrales de NaCCOC non-dopé et dopé en trou. Le phénomène de ”cascade” peut en effet être compris comme un croisement entre une physique de polaron de spin et d'électrons localisés. Pour la gamme de dopage faible à intermédiaire, où nous observons un pseudogap, nous prouvons qu'il s'agit du produit de la suppression des excitations à basse énergie de l'amas dans le bain électronique autocohérent dû à des interférences destructives.

t-CuO est composé de plans CuO 2D, de symétrie tétragonale, qui se superposent au dessus d'un substrat de $SrTiO_3$ (STO). Nous démontrons que la forte répulsion de Coulomb locale est à l'origine du découplage des plans CuO en deux sous-réseaux CuO_2, phénomène observé expérimentallement mais encore inexpliqué. Dans le système dopé en trou, le découplage se traduit par un paramètre d'ordre supraconducteur ayant une symétrie d_{xy} contrastant avec la symétrie $d_{x^2-y^2}$ usuelle pour les cuprates.

Enfin, nous montrons que la formation de lacunes en oxygène à l'interface t-CuO/STO peut expliquer les, a priori mystérieux, moments de spin paramagnétique et ceux orbitaux fixes observés en expérience.

Title: Spectral and magnetic properties of copper oxides: towards a theoretical description from first principles

Keywords: Cuprates, Strongly correlated systems, Dynamical Mean-Field Theory, Density Functional Theory, Angle-Resolved Photoemission Spectroscopy

Abstract: The oxidation of copper does not only lead to an unusable saucepan, but also to one of the most fascinating family of materials: the cuprates. Their large superconducting critical temperature first attracted the scientific community's attention, which led to the discovery of a rich and complex phase diagram. However a complete theoretical understanding is still missing. In this thesis, we investigate the spectral and magnetic properties of two copper oxide systems: $Ca_{2-x}Na_xCuO_2Cl_2$ (NaCCOC) and tetragonal CuO (t-CuO) using a combination of density functional theory, cellular dynamical mean-field theory (CDMFT) and angle- resolved photoemission spectroscopy.

We study the spectral properties of the undoped and hole-doped NaCCOC, and show that the antiferromagnetic spin fluctuations play a key role. We show that the waterfall feature observed experimentally and captured by our CDMFT calculations can be understood as a cross-over between a spin-polaron and a localized electrons physics. At low to intermediate dopings, we argue that the pseudogap opens due to destructive interference of the low-energy excitations of the embedded cluster.

t-CuO is composed of two-dimensional CuO planes with a tetragonal symmetry, stacked above a $SrTiO_3$ (STO) substrate. We rationalize the experimentally observed decoupling of each of its CuO planes into two weakly-coupled CuO_2 sublattices as a consequence of the strong on-site Coulomb interaction. This translates upon doping into an unusual superconducting order parameter symmetry of type d_{xy} instead of the usual $d_{x^2-y^2}$ found in cuprates.

Finally, we show that the formation of oxygen vacancies at the t-CuO/STO interface can explain the seemingly abnormal paramagnetic spin and pinned orbitals moments observed experimentally.

Institut Polytechnique de Paris
91120 Palaiseau, France